Radio properties of a complete sample of nearby groups of galaxies

Konstantinos Kolokythas

Department of Physics

University of Birmingham

This dissertation is submitted for the degree of

Doctor of Philosophy

October 2014

My parents have always told me to aim high. Therefore i turned my head to the sky and since then, never wanted to take my eyes down. I would like to dedicate this Thesis to my loving parents and sister who supported me throughout the long trip of chasing my dream: Become an astrophysicist.

Declaration

I hereby declare that except where specific reference is made to the work of others, the contents of this dissertation are original and have not been submitted in whole or in part for consideration for any other degree or qualification in this, or any other University. This dissertation is the result of my own work and includes nothing which is the outcome of work done in collaboration, except where specifically indicated in the text. This dissertation contains less than 50,000 words including appendices, bibliography, footnotes, tables and equations and has less than 150 figures.

Konstantinos Kolokythas
October 2014

Paper publications

1. **New insights into the evolution of the FR I radio galaxy 3C 270 (NGC 4261) from low frequency GMRT radio observations**
   Konstantinos Kolokythas, Ewan O'Sullivan, Simona Giacintucci, Somak Raychaudhury, C.H. Ishwara-Chandra, Diana M. Worrall and Mark Birkinshaw
   Material covered in Chapter 3. This paper is accepted for publication in the Monthly Notices of the Royal Astronomical Society (MNRAS). The citation for the article is: Monthly Notices of the Royal Astronomical Society 2015 450 (2): 1732-1744doi: 10.1093/mnras/stv665.
   In this work that involved the collaboration of many people I performed the analysis of the radio data, the calculations for the age, internal pressure and lobe energy estimations and was the only author that wrote the entire material of the paper, which of course was subject to corrections and suggestions by the co-authors. Dr Ewan O'Sullivan performed the calculation of the inverse-Compton contribution from the X-rays (bottom of page 106) and contributed only in the writting of this paragraph. Fig. 3.11 was also done by Dr. Ewan O'Sullivan. The model fit of the spectral index distribution in the lobes (JP model) of Figs. 3.8 and 3.9, in order to calculate the age of the radio source in the lobes, was performed by Dr. Simona Giacintucci. The same model fit of the integrated spectrum (Fig. 3.4) was also performed by Dr. Simona Giacintucci. The inspiration for the paper was from Prof. Somak Raychaudhury who along with Prof. Mark Birkinshaw and Prof. Diana Worrall contributed in the correction of the text. Finally Dr. Ishwara-Chandra helped in the demanding radio data analysis of this system.

2. **Radio properties of nearby groups of galaxies**
   Konstantinos Kolokythas, Ewan O'Sullivan, Somak Raychaudhury, C.H. Ishwara-Chandra, and Nimisha Kantharia
   Material covered in Chapter 4. This appeares in the proceedings of The Metrewavelength Sky (MWSKY) conference held at NCRA-TIFR, Pune, from 9-13 December

2013 (arXiv:1402.5109).
This is a conference proceeding paper I wrote where I briefly summarize the first radio results of the CLoGS project and show some of the interesting systems and radio images. The X-ray characteristics of each system, the energy outputs and any X-ray results I refer to were calculated by Dr. Ewan O'Sullivan.

3. **First Results from the Complete Local-Volume Groups Sample**
Ewan O'Sullivan, Konstantinos Kolokythas, Somak Raychaudhury, Jan M. Vrtilek and Nimisha Kantharia
Material partially covered in Chapter 4. This appeares in the proceedings of The Metrewavelength Sky (MWSKY) conference held at NCRA-TIFR, Pune, from 9-13 December 2013 (arXiv:1402.4676). This proceeding was written entirely by Dr. Ewan O'Sullivan.

4. **The radio properties of the central group galaxies in the Complete Local-Volume Groups Sample (CLoGS)**
Normal author list: *Konstantinos Kolokythas, Ewan O'Sullivan, Somak Raychaudhury, Nimisha Kantharia and Simona Giacintucci*
Paper in prep. This is the material covered in Chapter 4.

5. **Star formation and AGN in the Complete Local-Volume Groups Sample (CLoGS) from multiwavelength analysis**
Normal author list: *Konstantinos Kolokythas, Ewan O'Sullivan, Somak Raychaudhury and Nimisha Kantharia*
Paper in prep. This is the material covered in Chapter 5.

Konstantinos Kolokythas
October 2014

Acknowledgements

During this period of my life that I was passing through the 'doctorate' path, I see many people whose help and support must be acknowledged. Friends, parents and colleagues, they made these few years much easier than they could have been. At the top of this list is my supervisor, Prof. Somak Raychaudhury. He is a wonderful person and a charismatic scientistic as well. He always had good advice and great insight, without which I wouldn't be able to move on. I will be always grateful for being selected and trusted in order to accomplish the dificult task of this project. Especially grateful for all these trips to India, where I learned a new culture and interacted with new people (although I never liked curry and spicy food in general). He is, as we say in my country, my spiritual father. Special thanks and enormous gratitute to Dr. Ewan O'Sullivan, for all his help with every aspect of my phd. He was always there to support, help and guide in every step of my phd. His advice helped me get through some tough times. I really thank him for all the long telecons and discussions we had every time a problem came up or I wasn't understanding something. Without his help, I could not have completed a huge part of my work. His support and help, especially for my first publication was invaluable. I would also like to thank two people specifically: Ishwara Chandra, who taught me everything about the radio data analysis and David Stops for the help with all these mysterious (to me) computer and software problems but also for his interesting discussions at the coffee lounge. What would I do without my friends? I wanted to thank Charlotte, Trevor, Chris, Mark, Rory, Nikos and Richard. They helped make the hard times easier, the happy times happier and all the other times in between, enjoyable. I would like to extend thanks to Prof. Trevor Ponman, for many useful discussions applying his critical thinking in my Thesis and the invaluable help in organising it and for the job applications.

None of this would have been possible without my mother Athina Siatira and my father, Athanasios Kolokythas, who encouraged me to go for research and to travel abroad to study. My parents and my sister Vana, have always supported me in all my endeavors, inspite of opposition from other quarters. I want to thank them for always believing in me. Last but not the least, I want to thank Maira Mitrou, for her unwavering support and encouragement

and all the things she cheerfully put up with on a day to day basis as I raced to finish. This research has made extensive use of the NASA/IPAC Extragalactic Database (NED) which is operated by the Jet Propulsion Laboratory, California Institute of Technology, under contract with the National Aeronautics and Space Administration. This research has made use of NASA's Astrophysics Data System Bibliographic Services.

Abstract

Much of the evolution of galaxies takes place in groups where feedback has the greatest impact on galaxy formation. By using an optically selected, statistically complete sample of 53 nearby groups (CLoGS), observed at radio (GMRT) and X-ray (Chandra and XMM-Newton) frequencies, we aim to characterise the radio-AGN population in groups and examine their impact on the intra-group gas and member galaxies. In this dissertation, low-frequency GMRT radio images of the nearby (<80 Mpc) central brightest group ellipticals from the high richness CLoGS sub-sample are presented for the first time at 235 and 610 MHz. Using the sensitivity to older electron populations at 235 MHz and the resolution of 610 MHz as a key to identify past and current AGN activity, a detailed analysis of the radio properties for each of the central group radio sources is performed, with the results being in addition combined with findings from the X-ray observations.

Using models of spectral ageing, we report an age of $\sim$29-36 Myr for the radio source 3C 270 in NGC 4261, concluding that the expansion of the radio jet underwent several outbursts during the lifetime of the source.

From the entire sample, we find that 13/26 systems (50%) have a group-scale X-ray emission that reach beyond 65 kpc (X-ray bright), with 5/13 (39%) of these X-ray bright systems presenting radio emission in the form of small/large scale jet. Furthermore, 5/13 (39%) are radio point sources and 3/13 (22%) host diffuse radio emission with no particular orientation. The largest radio sources which are currently active or have been so in the recent past, lie in X-ray bright cool-core groups, while the systems that do not present radio emission at any frequency appear in the X-ray faint systems. Central radio galaxies that reside in the most massive groups (with masses $> 10^{14}$ $M_{\odot}$) are found to be able to balance the cooling of gas with a transition point at 2×10^{13} $M_{\odot}$ above which massive groups are able to overcome cooling.

In a total of 690 galaxies we detect $\sim$12% (85 out of 690) at 610 MHz, $\sim$14% (97 out of 690) at 235 MHz and $\sim$7% (49 out of 690) at both 610 and 235 MHz. The detection rate for our sample galaxies in any form of radio emission is observed to be slightly higher for late-type (spiral) galaxies ($\sim$53%) than early-types ($\sim$36%) with the ones detected of

unknown morphology having a detection rate of $\sim$11%. Of the radio detected galaxies, 17% are found to be radio-loud ($L_{1.4GHz} > 10^{22}$ W Hz^{-1}). Finally, by calculating the star formation using different indicators across the electromagnetic spectrum, we find that the star formation rates in CLoGS groups do not exhibit a gradient with group-centric distance for both early and late type galaxies.

Contents

List of Figures

List of Tables

Chapter 1

Radio emission from Galaxy groups and clusters

1.1 Galaxy groups and clusters

1.1.1 Introduction (What are groups of galaxies?)

The Universe as seen in its large–scale structure appears to be a vast network which is made up of walls, filaments, knots and voids (Gregory & Thompson, 1978; Jõeveer et al., 1978; Zeldovich, 1982). In the large-scale structure of the Universe, the galaxies can be found in a range of different environments based on their spatial density: from rich clusters, with hundreds of galaxies within a system one or two megaparsecs across, to groups, with tens of galaxies within a similar volume, all the way down to the low-density field, on filaments and sheets on the cosmic web, or on the surfaces of voids. The richer and more luminous groups along with the rich clusters are located in the highest density regions, at the intersections of walls and filaments. A system of clusters and associated filaments and groups is usually

known as Supercluster of galaxies, which represent the largest bound system that exiss in the Universe today (Croft et al., 2012; Einasto et al., 2003, 2005; Porter & Raychaudhury, 2005).

In contrast, the galaxies that reside in the 'field' are somewhat 'lonely' galaxies which have no neighbours for many megaparsecs. In this scenario of the structure formation of the Universe, galaxy groups represent an environment that is intermediate between the two extreme ones described earlier (Forbes et al., 2006). There are numerous approaches to defining a group of galaxies. In more recent approaches, it is argued that a group of galaxies is a structure that has 3-10 members with a magnitude of $M_v < -19$ and within a radius of 0.5 Mpc or a group could be an ensemble that has only a few members with a velocity dispersion of $200\text{kms}^{-1}<\sigma<400\text{kms}^{-1}$ (Dariush et al., 2010). In the context of modern cosmological simulations groups are defined by their halo masses from where groups can be defined as structures that are in the mass range of 10^{12} - 10^{14} $M_{\odot}$ (Eke et al., 2004).

1.1.2 Why study groups of galaxies?

Despite the small number of galaxies a typical group contains compared to a cluster, the role of galaxy groups in the construction of large-scale structures is fundamental, as in time, galaxies get assembled into groups, and in turn groups may merge together to form richer groups and clusters, in the hierarchical nature of structure formation in the Universe. The study of groups is therefore essential in order to acquire a complete understanding of the evolution of galaxies along with the environmental processes involved. There are several reasons that support the importance of such studies (Forbes et al., 2006). To begin with, with approximately 70% of galaxies located in groups (Tully, 1987), they are the most common environment in the local Universe (Eke et al., 2005; Geller & Huchra, 1983). Taking into

account the dominant scenario of structure formation, the groups that are seen at the present are the precursors of future galaxy clusters. For this reason, the early evolution of rich cluster galaxies (e.g. Bekki et al., 1999; Moss & Whittle, 2000) is closely connected with the evolution of galaxies in groups. As groups come together, collapse and merge to form in time larger systems, the logical result would be that they are a scaled-down picture of galaxy clusters, but in-depth studies of individual systems, based on the multi-wavelength observations, show that indeed this is not the case (e.g. Mulchaey, 2000; Ponman et al., 2003; Voit et al., 2005).

Another reason for the study of groups to be interesting is that they are the ideal laboratory to study the most efficient processes in the morphological transformation of galaxies: merging (e.g. Toomre & Toomre, 1972). Mamon (2000) showed that groups merge a couple of orders of magnitude times more often than rich clusters do. As groups represent less deep potential wells, gravity plays an important role due to the close proximity of members, given the reasonably high galaxy density of groups. More crucial in this context is that the velocity dispersion of these systems is lower than in clusters, and thus groups are better environments for enhanced tidal interactions and mergers, and it is in these environments that most of the galaxy metamorphosis in morphology and star formation rates will occur (e.g. Hashimoto & Oemler, 2000; Mulchaey & Zabludoff, 1998).

Recent large surveys, such as the 2dFGRS (Lewis et al., 2002) have shown that star formation is suppressed on group level densities. The increased incidence of quenched star formation in galaxy groups can be strongly linked with the reduction of the mean star formation rate of the Universe moving to redshift 0 (Laganá et al., 2013). As noted in Hou et al. (2013) the interactions between galaxies, which are more common in a group environment, initially give rise to star formation (Cox et al., 2006; Sanders et al., 1988;

Teyssier et al., 2010), that consumes the available supply of cold gas and prompts the ceasing of star formation, if no more gas is accreted into the galaxy. For that reason, processes such as merging and interactions rely on the stage of the evolution at which a galaxy is observed and play a decisive role in boosting or cutting off star formation. Considering only the galaxies that reside in rich groups or clusters with masses of $M_{halo} > 10^{13}$ h^{-1} $M_{\odot}$, Hou et al. (2013) reports that approximately 40% is believed to be preprocessed (i.e. with star formation suppressed) before their accretion into the system (De Lucia et al., 2012; McGee et al., 2009). The physical mechanism for this 'pre-processing' of galaxies in groups is currently an open issue and not properly understood (e.g. Fujita et al., 2003), but this scenario provides a plausible explanation for the observed continuous reduction of the global star forming rate as a function of the time of the Universe (e.g. Cowie et al., 1999; Cooper et al., 2008).

Another significant characteristic of galaxy groups is that they contain a large fraction of the hot gas that is seen in the Universe (Forbes et al., 2006). Compared to clusters, most groups appear to have a similar amount of hot gas. Given the abundance of groups of galaxies, these systems thus significantly contribute to the baryonic component of the Universe (Fukugita et al., 1998). However, the matter content in groups differs significantly from one system to another. If we examine groups in more detail, the baryon composition in groups and clusters can be divided into two major components: i) the hot gas between galaxies, and ii) the stars in them. The amount between hot gas and stars in groups of galaxies can either be equal (Laganá et al., 2011) or in some cases the amount of hot gas can be lower than the stellar mass component (e.g. Giodini et al., 2009). In clusters, the baryon component which is always dominant is the hot gas. Hence, groups give the very rare opportunity to study the origin and nature of this important mass component and its

very close relation with galaxies and their evolution (Forbes et al., 2006).

Finally, our own environment in which our Galaxy exists, is a small group with a few tens of galaxies. As the environments that correspond to galaxy groups range from systems that have collapsed very early (fossil groups) to those with density only a little higher than that in the 'field', in order to understand what are the implications of the evolution in our Local Group environment we need to study in more detail systems of nearby galaxy groups. While in clusters of galaxies early-type galaxies had the majority of stars created at very early epochs, (e.g. Tanaka et al., 2005; Terlevich & Forbes, 2002), star formation occurs in a wider variety of systems in groups of galaxies (Terlevich & Forbes, 2002). For this reason, the detailed examination and multi-wavelength study of nearby groups of galaxies, taking advantage of their proximity, is essential in order to examine the extent to which star formation in galaxies is related to the state of evolution in these abundant systems, keeping in mind that much of the early evolution of galaxies occurs in the group environment (Forbes et al., 2006).

1.1.3 Properties of galaxies with distance from the group centre

In a group of galaxies, it is important to study the difference in properties such as star formation and galaxy morphology of the central galaxies, if any, and the non-central galaxies of similar mass, and to examine the dependence of these properties on the distance of the galaxies from the centre of the group.

In order to achieve this, it is thus very important to identify the position of the centre of a group. Usually, when the group exhibits a group is very important in order to accurately study the implications of these properties in relation to their distance from the group centre. Usually, when the group exhibits large scale diffuse X-ray emission there are two types of

X-ray morphologies of groups: the X-ray luminous ($L_X \geq 10^{42}$ h_{100}^{-2} erg s^{-1}) and those of lower luminosity (Mulchaey, 2000). In the case of X-ray luminous systems, the centre can obviously be defined as the position of the centroid peak of the detected diffuse X-ray emission, representing the inter-galactic medium (IGM) at the bottom of the gravitational potential well of the dark matter halo of the group. The position of the centre does not necceserily need to be a position of a galaxy, but in these systems the peak of the X-ray emission usually coincides with a luminous early-type galaxy, which lies in the centre of the group potential and also might as well be the optically luminous group member (Ebeling et al., 1994; Mulchaey & Zabludoff, 1998; Mulchaey et al., 1996).

On the other hand, if the group does not have high-luminosity Xray emission, the emission may appear 'clumpy' and not centered on a specific galaxy, but rather extended including several galaxies (Mulchaey, 2000). In this case, from the optical image, a luminosity weighted centre of the group members, where the membership is ascertained from redshift, may be calculated, which may or may not coincide with one of the major galaxies. From the group centre defined in this way, a group-centric radius can be defined (e.g. Li et al., 2012).

As we move from the centre of the group outwards (group-centric radius rises) the population of optically fainter, active star forming blue and late type morphology galaxies goes up while the fraction of early-type galaxies decreases (e.g. Brough et al., 2006; Goto et al., 2004). The most likely galaxies to be found at the outskirts of a group are therefore late type galaxies and this radial trend, as shown in Weinmann et al. (2006), is not independent of the mass of the halo in which the galaxies are embedded. It is important to break this degeneracy: is it the environment that the galaxies are into or the halo mass that causes this trend. Blanton et al. (2005) and later using the zCosmos sample Kovač et al. (2010), find that there is a dependence on mass of these properties that is superposed on the environmental effect.

The properties of the galaxies in a group therefore depend strongly on the properties of the central galaxies and the mass of the group. In more recent extensive studies such as Vulcani et al. (2015), it is shown from observations that the incidence of red galaxies increases with increasing mass, and, for galaxy masses below $10^{10.7}M_{\odot}$, red galaxies decrease toward the group outskirts. They conclude that almost all the variation in the galaxy properties can be attributed to a dependence on mass rather than on the environment. In some semi-analytic models, it is seen that the fraction of early type galaxies rises with increase of the halo mass, assuming a fixed luminosity, but is also higher for an early type central galaxy halo, than for a central galaxy which is of late type morphology at the same halo mass (Weinmann et al., 2006). Furthermore, the fraction of early type galaxies increases with the increase of luminosity while for late type galaxies the opposite happens. This luminosity dependence appears to be stronger for central galaxies than in satellites.

In order to fully comprehend the connection between different types of groups, their evolution and the effect of the group environment on galaxies it is important to adopt a multi-wavelength approach. The true nature of groups can only then be revealed especially in groups which are undergoing evolutionary stages of gas and energy transitions (Forbes et al., 2006).

1.2 The origin of radio emission from galaxies

The radio emission that is detected in galaxies is a synthesis of sources that are either related to the active galactic nuclei (AGN) or originate from star formation (for a review see Condon 1992). In the first case, the source of energy, the so called *central engine*, is thought to be associated with the AGN, the emission originating in the central few parsecs[1] of an

[1] 1 parsec = 3.26 light years

active galaxy. The concept is that the AGN is surrounded by an accretion disk and is fuelled by the accretion of gas onto a massive collapsed object, a supermassive black hole (Blandford & Rees , 1974). AGN emit mostly radiation that is not according to the typical blackbody spectra of stars but the nature of the emitted radiation is non-thermal (Rosswog & Bruggen, 2007). The main non-thermal process here is synchrotron emission (see 2.2.2). The production of synchrotron radiation comes from flows of charged relativistic particles, expelled from the AGN due to acceleration in a magnetic field (Burbidge, 1956; Begelman, Blandford & Rees , 1984; Blandford & Rees , 1974; De Young, 2001; Harris & Krawczynski, 2006). The transportation of energy is taking place through a highly collimated beam of relativistic particles in two oppositely directed beams that are called jets. The interaction of these jets with the interstellar/intergalactic medium on kpc-Mpc scales creates the radio structures that we see on scales ranging from arcsec to a few degrees (Hardcastle, 2009). Radio sources emit synchrotron radiation throughout the whole range of radio wavelengths with non-thermal emission starting to dominate the spectrum of radio emission below 30 GHz (Condon, 1992).

On the other hand, there are two possible origins for the continuum radio emission that can be attributed to star formation, as noted also in Bell et al. (2003): The first one is the thermal bremsstrahlung radiation which is mostly found in HII regions (e.g., Caplan & Deharveng, 1986) and the second one, is the non-thermal synchrotron emission that originates from either electrons or protons that travel relativistically and emit radiation trapped in the magnetic field of the galaxy (Condon, 1992). Only massive stars that are $\sim$8 $M_{\odot}$ or over are able to ionize the H II regions as well as to produce the Type II or Type Ib supernovae whose remnants (SNRs) (which also include dust and cosmic rays) are believed to be responsible for the acceleration of the relativistic electrons or protons. While thermal (free–free) radio

emission exhibits a flat spectrum with a spectral index of $\alpha = 0.1$ where $S_\nu = \nu^{-\alpha}$, non-thermal emission has a steeper radio spectrum of $\alpha \sim 0.8$, but with the note that the spectral index is possible to vary even with frequency (Condon, 1992). Owing to this intrinsic difference in the spectrum of the two emissions, there is a frequency dependence on their relative contributions with the nonthermal radiation almost completely dominating at frequencies $\leq$5 GHz and with the thermal emission starting to take over at frequencies $\geq$10 GHz (Price & Duric, 1992). In fact, Condon (1992) mentions that $\sim$90% of the radio continuum flux of luminous spiral galaxies at 1.4 GHz, is attributed to nonthermal emission.

Furthermore, there is also a dependence of the relative ratios of thermal and nonthermal emission on the mass of the host galaxy. Despite the fact that estimation of the balance between thermal and nonthermal radio emission is extremely complex and can be uncertain for even very well studied galaxies at a factor of 5 (Condon, 1992), it seems that dwarf galaxies have a lower nonthermal-to-thermal emission ratio than normal spiral galaxies (Klein et al., 1984, 1991; Mayya & Rengarajan, 1997; Rengarajan et al., 1997; Roychowdhury & Chengalur, 2012). This difference in the fraction of thermal and nonthermal emission between dwarf and larger galaxies could be explained due to the higher confinement efficiency that cosmic-rays exhibit in naturally more massive galaxies (e.g., Bourne et al., 2011; Chi and Wolfendale, 1990; Lacki & Thompson, 2010; Price & Duric, 1992).

1.3 Evolution of radio emission in galaxies

The evolution of radio emission in galaxies is closely related to the evolution of the galaxy itself. As the growth of supermassive black holes, as is evident from studies in the local Universe, is closely connected with the spheroid/halo in which they are embedded (Fabian, 1999; King, 2003; Robertson et al., 2006), much evidence supports the crucial role of the

AGN activity in the evolution of the host galaxy with outflows from the AGN, regulating, or completely terminating, star-formation (e.g. Cattaneo et al., 2009)

In general, the star formation rate over time within galaxies is reduced, with galaxy colors shifting from blue to red. As spiral galaxies evolve, their most obvious characteristic, the spiral arms, progressively becomes less dominant and eventually fade away (Li et al., 2012). Initially a star forming galaxy will emit as discussed earlier (§ 1.2), at radio wavelengths, for as long it could sustain its star forming regions. After that, the consequences of the quenching of the star formation in a galaxy is the complete absence of radio emission, if the gas is depleted, and there is no other source of radio emission (e.g. AGN) after a period of 10^8 yrs. Then as galaxies undergo the transition of becoming S0 type or ellipticals through merging, an initial starburst period will again trigger star formation and thus radio emission. Eventually if the galaxy hosts a supermassive black hole with enough gas to accrete, there will be radio emission from the AGN for $10^7 - 10^8$ yrs. Overall studies have shown that $\sim 30\%$ of the galaxies (the most massive ones), exhibit radio continuum emission (e.g., Best et al., 2005; Shabala et al., 2008).

1.3.1 The structure of a radio source

The basic model of the generation and evolution of luminous extragalactic radio sources was developed by Blandford & Rees (1974); Scheuer (1974). In this model a cool flow of high collimation and speed was created in the region near or within the AGN. This flow afterwards spreads to the ends of the radio-emitting lobes, where it shocks and stops, changing most of its kinetic energy into relativistic electrons and magnetic fields. This model explains in a simple way the structure of extragalactic radio sources and a large variety of observational evidence strongly supports it.

Recent progress in the theory of relativistic jet production, indicates that such jets may be launched with a spine/sheath flow structure, having a much higher velocity close to the axis and a lower one away from it. Relativistic jets are presumed to obtain much of their energy from the infall of matter into a supermassive black hole. Therefore models of accretion flows are now considering the production of a jet by that flow (Meier, 2003).

In the review of Worrall & Birkinshaw (2006) the twisting of the magnetic field connected to the accretion disk is considered to be the most plausible mechanism for the extraction of energy from the jet system. The most propable contents of the jets are considered to be electrons and positrons, or electrons and protons, although electromagnetic (Poynting flux) jets (e.g., Rees 1971) and proton-dominated jets are also proposed (e.g., Mannheim and Biermann 1989). In the resulting magnetohydrodynamic flow much of the momentum would be carried by particles, although Poynting flux may carry a significant fraction of the total energy. An electron-positron pair plasma is a natural consequence of the high energy density near the centres of active galaxies, and hence it might be expected that electrons and positrons would be an important, and perhaps dominant, component of the jet outflow (Worrall & Birkinshaw, 2006).

Radio galaxies can be divided into two subclasses known as Fanaroff and Riley type I (FRI), and type II (FRII) (see fig. 1.1) (Fanaroff & Riley, 1974). Although this classification is based on morphology, Fanaroff & Riley (1974) found that most sources with radio luminosity at 170 MHz below $2\times10^{2}5$W Hz^{-1} sr^{-1} are FRI and the rest are FRII.

- **Fanaroff-Riley type I (FRI):** These sources are brightest near the centre of the active nucleus of the galaxy, as can be seen in the right side of fig 1.1. Until the point where the lobes terminate, these sources become gradually fainter, and their spectra steeper (explained later in spectral ageing). FRI jets show a range of morphologies, from

straight symmetrical two-sided jets to the bent 'head-tail' sources. This type is not as powerful as FRII galaxies because their jets are not highly collimated (Rosswog & Bruggen, 2007).

- **Fanaroff-Riley type II (FRII):** These sources present strong, collimated jets, showing quite often hotspots that can be several kpc away (Rosswog & Bruggen, 2007) The jet ends at the beam head (radio hotspot, see fig 1.1) where the fluid of the jet goes through a shock to give rise to a cocoon of radio-emitting plasma. The ambient gas is heated from the bow shock created in front of the jet termination shock, which then fills an area surrounding the lobe of radio-emitting plasma. The observational result on kpc scales is radio emission from jets that power edge brightened lobes.

The difference between these two FR types is mainly on the velocity of the jet front. In FRI type, the jets travel subsonically through the ambient medium due to decceleration by entrainment of external material (Ledlow & Owen, 1996) dissipating much of their energy without developing a well-defined beam head, and in FRII the jets travel supersonically, transporting energy efficiently to the ends of the lobes where they stop causing shocks which are thought to create the observed radio hotspots without much deceleration (Bicknell, 1995).

The structure of a typical radio galaxy includes a core associated with the AGN, oppositely collimated jets coming up from the core, and lobes that rise from the jet terminals. In more detail:

- **Core:** It is unresolved and corresponds to the nucleus of the galaxy, from which the collimated flow arises (Carilli et al., 1991)

- **Jets:** A highly collimated beam of relativistic particles -sometimes two oppositely

orientated beams- coming directly from the nucleus and going to the lobes. This radio-emitting narrow beam reveals the flow which transmits mass, momentum, energy, and electromagnetic field as it passes through the empty lobes (Carilli et al., 1991)

- **Lobes:** Double, often symmetrical, approximately ellipsoidal structures positioned on each side of the active nucleus. These radio-emitting structures contain the outflow from the shock. Sometimes some low-luminosity sources show structures usually known as *plumes* which are much more 'stretched' (Blandford & Rees , 1974; Scheuer, 1974)

- **Hotspots:** Bright structures that point where the cool flow, coming from the nucleus, is shocked and heated upon colliding with the external medium. The momentum of the jet afterwards moves the hotspots forward into the surrounding medium and the lobes grow in size and luminosity (Blandford & Rees , 1974; Scheuer, 1974)

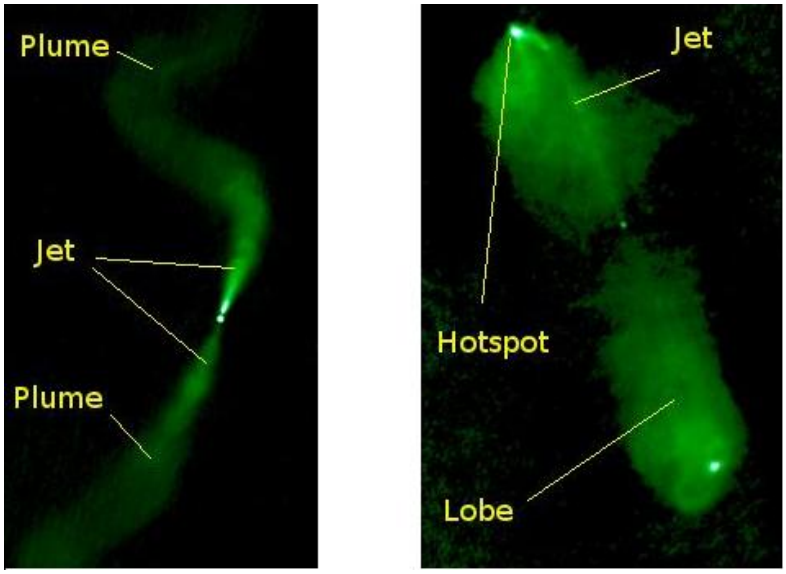

Figure 1.1 The structure of FRI and FRII galaxies: pseudo-colour images of the large-scale radio structure of the FRII radio galaxy 3C98 on the right and the FRI radio galaxy 3C31 on the left. [http://upload.wikimedia.org/wikipedia/en/4/42/3C31 & 3C98.png].

1.3.2 Classification and modes of Active Galactic Nuclei

In the recent review by (Heckman and Best, 2014) the activity of an AGN is divided in two different modes: i) The 'radiative-mode' (or quasar mode as called in earlier reviews) and ii) the 'jet-mode' (or radio mode). In the first case, the radiative-mode AGN are associated with populations of lower-mass black holes ($10^6 - 10^8$ $M_\odot$) that are fed by material that is accreted from a radiatively-efficient accretion disk (e.g., Shakura & Sunyaev, 1973) which is thin in geometry and thick when observed in optical wavebands (Best & Heckman, 2012). The radiation emitted covers a large range of the electromagnetic spectrum (UV, optical, and near-IR permitted emission-lines) having their host galaxies, sometimes also related to star formation (e.g., Kauffmann et al., 2003). The fact that the AGN is related to central star-formation implies that feedback from massive stars will be present but its efficiency is not well quantified (Heckman and Best, 2014).

The class of AGN that usually comes from the radiative-mode is the *Radio-quiet AGN*. In this class the host galaxy can be a spiral, an elliptical or an irregular galaxy. Radio-quiet AGN exhibit a small scale jet and usually the radio emission that corresponds to the jets can be ignored. The main representatives of this class are Seyfert galaxies, which are spiral galaxies with very bright and unresolved nuclei that present line emission of ionized atoms that can't be produced by stars, and Radio-quiet quasars which show strong optical continuum emission, X-ray continuum emission and both broad and narrow optical emission lines (Rosswog & Bruggen, 2007). A small fraction of 'radiative-mode' AGN could become radio-loud (e.g. radio-loud QSOs or radio galaxies), exhibiting very powerful radio jets that span several kpc away from the host galaxy and can accelerate with shocks the intragroup/intracluster gas (e.g., Best et al., 2000), giving rise to winds in two opposite directions at velocities of thousands of km/s (e.g., Nesvadba et al., 2008).

In the second mode of AGN activity, the 'jet-mode', the material is accreted with low rate on to the black hole and drives small amounts of radiated energy (characteristic luminosity below about 1% of the Eddington limit), but is capable of producing radio jets of very high energy (Best & Heckman, 2012). These AGN are linked to typical radio galaxies of higher mass black holes ($>10^8$ $M_\odot$) where indirect evidence for the 'feeding' of the AGN exists by the accretion of hot gas seen in X-rays. Only the feedback from the interaction of the jets with this hot gas can be directly observed, with the details of this process remaining uncertain (Heckman and Best, 2014). These systems are at the end of their evolutionary path with the majority of the star-formation and black hole growth having occured at high-redshift.

The second class of AGN that are associated with the the 'jet-mode' AGN are the *Radio-loud AGN*. In this class the host galaxies are mainly elliptical galaxies and the emission from the jets and the lobes dominates the luminosity of the AGN. These low luminosity radio sources (usually called low-excitation radio galaxies) are fundamentally different from the radiatively efficient AGN that drive the 'radiative-mode', as they lack the emission of strong lines usually seen in powerful AGN (Hine & Longair, 1979) and the X-ray and infrared emission from the accretion activity and the torus respectively (e.g., Hardcastle et al., 2007; Heckman and Best, 2014). The geometrically-thin accretion disk is replaced here by a geometrically-thick structure (called advection-dominated or radiatively inefficient accretion flow, ADAF/RIAF) in which the inflow time is much shorter than the radiative cooling time (e.g. Ho 2008; Narayan 2005). These flows are responsible for the launch of two-sided jets.

The radio-loud AGN in the category of radiative-mode are hosted by more massive galaxies, but may also be enhanced by a boosting of the radio luminosity in Unlike 'radiative-

mode' AGN, the 'jet-mode' AGN are more likely to be found in denser environments, most probably in the central galaxies of groups and clusters, indicates an altered fueling mechanism.

The main representatives of this class are:

i) Radio-loud quasars, where all such AGN are hosted by massive elliptical galaxies with old stellar populations. Their radio source hosts are highly bulge-dominated, with a massive black hole mass,
ii) Blazars, which behave more like radio-loud quasars with the addition of a quickly changing component which is believed to originate due to a relativistic jet directed towards the line of sight of the observer (Vermeulen et al., 1995) and
iii) Radio galaxies, which show nuclear and extended radio emission as well as optical and X-ray nuclear emission which is agreeable that develops in a jet (Hardcastle, Evans, & Croston, 2006; Longair, 1979). They may be the best current candidates for AGN with radiatively inefficient accretion (Grandi & Osterbrock, 1978). The most luminous LINERs are also likely to be members of this population with the differences in host galaxy properties, black hole mass and presence of an accretion disk can also make radio galaxies radiatively efficient (e.g. high-excitation radio galaxies, Heckman and Best 2014).

The reasons that cause the differences between the two modes of radiatively efficient and inefficient AGN are still uncertain. In Hardcastle et al. (2007) it is argued that the accretion of cold gas could sustain a steady accretion disk, thus resulting in a radiatively efficient accretion, while a Bondi accretion of hot gas would favor the production of the radiatively inefficient AGN. This is also known as the Bondi-Hoyle-Lyttleton (Bondi & Hoyle, 1944; Bondi, 1952, 'Bondi') mechanism, where the accretion of gas, considered to be stationary at

infinity, occurs at a constant rate from every direction (spherical symmetry). Furthermore, McNamara et al. (2011) argues that the spin of the black hole might play a significant role in the radiative efficiency of the AGN, and this is used in many galaxy formation model simulations (e.g., Fanidakis et al., 2011). Lastly, yet another feature was noted by Narayan & Yi (1995), who argued that the radiative efficiency is closely related to the ratio of the rate of accretion of the gas on the black hole, to the Eddington limit, with the 'jet-mode' taking place when the accretion rate is much lower than the Eddington limit (Best & Heckman, 2012; Heckman and Best, 2014).

1.3.3 Astrophysical shocks

As most of the astrophysical processes include phenomena that lead to particle acceleration and energy ejection (radiation), of great importance in astrophysics is the creation of shocks. In general, a shock wave can be described as a disturbance that propagates through a medium, carrying energy faster than its signal speed, causing the compression, heating and acceleration of the medium. The properties of the medium are therefore completely altered by the passage of the shock front, but one has the ability to measure the sudden change in pressure, temperature and density of the flow (McKee & Hollenbach, 1980).

The most common sources of shock generation in astrophysics are those where supersonic compressive disturbances occur. Shocks can therefore be found in both galactic and extragalactic environments, span over a variety of processes and are divided into: a) non-relativistic shocks, such as Supernovae remnants, accretion onto hydrostatic intracluster medium (ICM, galaxy clusters), and b) relativistic shocks, such as pulsar winds, Gamma-Ray Bursts (GRBs) and radio AGN jets (Bykov & Treumann, 2011).

In Worrall & Birkinshaw (2006), it is described that in FR II radio AGN jets the interac-

tion of the supersonic propagating jet -compared to the X-ray-emitting interstellar medium (ISM)- with the intragroup/intracluster medium, gives rise to shock fronts. As the jet terminates at the radio hotspots (jet head) its fluid goes through a powerful shock in order to inflate a layer (cocoon) of radio-emitting plasma. The jet flow momentum and energy are usually keen to drive a bow shock into the surrounding medium in front of the area of the jet termination shock that heats the ambient gas as it passes through the termination shock filling an area around the lobe of radio-emitting plasma. Observations of such processes show a jet (extending several kpc) that emits in radio, inflating lobes that exhibit bright edges.

The sound speed in the gas of temperature T is

$$c_s = \sqrt{\frac{\gamma kT}{\mu m_H}} \tag{1.1}$$

where $\gamma = 5/3$ is the ratio of the specific heats, k_B is the Boltzmann constant and $\mu m_H = 0.6 m_H$ is the mass per particle with m_H being the mass of the hydrogen atom. Taking into consideration the above, the sound speed can be calculated by

$$c_s \approx 516 (k_B T / KeV)^{1/2} \,\mathrm{kms}^{-1} \tag{1.2}$$

or,

$$c_s \approx 0.54 (k_B T / KeV)^{1/2} \,\mathrm{kpc\,Myr}^{-1} \tag{1.3}$$

The general description of the Mach number of the advance speed, υ_{adv} of the bow shock in the surrounding medium is given by $\mathscr{M} = \upsilon_{\mathrm{adv}}/\mathrm{c_s}$, that can be calculated with the

appropriate units by

$$\mathrm{M} \approx 580(\upsilon_{\mathrm{adv}}/\mathrm{c_s})(\mathrm{k_B T/KeV})^{-1/2} \tag{1.4}$$

where c is the speed of light and υ_{adv} is not as fast as the bulk jet speed.

The hot, X-ray emitting intracluster/intragroup gas is related to the jets of an active galaxy. Provided that the ambient gas is in hydrostatic equilibrium, its density and temperature profile will depend on its thermal history, been largely affected by the source dynamics. In the case of a bow shock propagation from a jet, rims of shocked gas are expected to be seen surrounding the radio lobe along with the ambient gas X-ray emission (Worrall & Birkinshaw, 2006).

Applying the Rankine-Hugoniot conditions for a strong shock (Spitzer, 1978) we are able to get a relation for density, temperature and pressure respectively

$$\rho_2/\rho_1 = 4\mathscr{M}^2/(\mathscr{M}^2+3) \tag{1.5}$$

$$T_2/T_1 = (5\mathscr{M}^2-1)(\mathscr{M}^2+3)/16\mathscr{M}^2 \tag{1.6}$$

$$P_2/P_1 = (5\mathscr{M}^2-1)/4 \tag{1.7}$$

where ρ_1, $\mathrm{T_1}$, $\mathrm{P_1}$ represent the unshocked gas and ρ_2, $\mathrm{T_2}$, $\mathrm{P_2}$ the shocked gas areas at the tip of the bow shock, for a monoatomic gas. From the above equations, as an example, in the energy band 0.8-2 keV, a $\mathscr{M}$ = 4 shock, will create a contrast in the X-ray emissivity between shocked and unshocked gas a factor of 3 higher, provided that the ambient gas in the ISM of the galaxy is at a galaxy temperature of $\sim$0.3 keV (using equation 1.5 and

converting density into X-ray emissivity, Worrall & Birkinshaw 2006).

Despite the fact that low-power FR-I jets transfer a great amount of their energy without evolving a proper beam head, as they are in good contact with the external medium in which they are embedded, the above equations can also be applied to them (Worrall & Birkinshaw, 2006). A nice example is the low-power radio galaxy Cen A (Croston et al., 2009; Kraft et al., 2007, 2003), that shows such shell of X-ray emitting gas that has the geometry of a shocked ambient gas. The Mach number of the shock in the gas is calculated by assuming a temperature and density such that the combined thermal and ram pressure is in pressure equilibrium.

In addition, apart from the temperature jump seen in the ambient X-ray gas, the Mach number of a shock that a radio jet creates in the ambient gas can also be constrained from the radio observations. By using a radiative age model (Jaffe & Perola, 1973, e.g.,) the age of the source can be estimated and from the knowledge of the extend of the radio lobes (or the extend of the rim of compressed gas from the core of the galaxy) the supersonic expansion speed of the lobes can be calculated (Kolokythas et al. 2015, also see Chapter 3), resulting in an estimate of the Mach number of the shock in the medium.

In clusters of galaxies shocks could be generated from the motion of the galaxies in the cluster medium (heating of the intracluster gas through friction; Ruderman & Spiegel 1971; Hunt 1971), through gravitational infall (Miniati et al., 2000), cluster mergers with other groups or clusters (cold fronts; e.g. A3667, Vikhlinin et al. 2001), or from double radio AGN relics (Roettiger et al., 1999). Such shocks are effective in causing a sharp increase of both their temperature and density. The calculation of the density jump in the X-ray surface brightness discontinuity across the shock edge, allows a measurement of the shock's Mach number (Markevitch, 2006). Recently, X-ray surface brightness discontinuities were

discovered at the place that some radio relics exist, with the most probable explanation being that these discontinuites are shocks with Mach numbers of 2 (Finoguenov et al., 2010; Macario et al., 2011).

1.3.4 Feedback: AGN and Supernovae

Complex numerical simulations that model the variation of density in the early Universe (e.g., Springel et al., 2005) predict more than needed faint and bright galaxies with the largest of those being star forming (Benson et al., 2003). This is not what exactly is observed in nature, where the majority of the largest galaxies are found to be passive. In the recent study of Fraser-McKelvie et al. (2014) it is shown that the bulk of BCGs at $z < 0.1$ possess little or no star formation at current times thus only modest BCG growth is occurring as a result of star formation at the current epoch. However, there are studies (e.g., Liu et al. 2012; Pipino et al. 2009) that reveal BCGs with current star formation, which is suggested to be fueled by gas cooling out of the intracluster medium. The process that could give an answer to this problem is heating by AGN. Although its efficiency is unknown, the conversion of radio AGN outflow energy into heating of the circumgalactic medium is adequate to provide the needed heating in order to stop cool gas from collapsing into one point and create stars (McNamara & Nulsen, 2007). This is called *AGN feedback* and numerous processes connected with AGN phenomena for this *feedback* have been proposed. Winds directed by radiation, AGN-driven shocks and outflows of mass, quasi stellar objects and radio sources associated with AGNs have all been suggested (e.g., Sijacki et al., 2007). In general, as *feedback* is called the loop process where some form of energy is created in the core of the galaxy, that is enough to heat up the gas that flows in providing sufficient energy to supress star formation. A basic requirement to this is that this heating occurs in a time comparable

to the relevant cooling times (for a detailed review of this topic see De Young (2010) and McNamara & Nulsen 2007).

The nature of the AGN mode that a galaxy exhibits, has implication on the feedback mechanism of the host galaxy. Despite the fact that in 'radio-mode' the energy released from the jet is significantly lower than in 'quasar-mode' AGN (e.g., Cattaneo & Best, 2009), an effective feedback mechanism is most likely created from the local storage of this energy in the system (Best & Heckman, 2012). The observational evidences for such a mechanism are the bubbles and the cavities that the radio loud AGN excavates in the hot intragroup/intracluster gas in which they are embedded or the gas of the haloes of their host galaxies (Fabian et al., 2006; McNamara et al., 2000). In semi-analytic models of galaxy formation (e.g., Bower et al., 2006; Croton et al., 2006; Guo et al., 2011) the mechanism of 'radio-mode' AGN feedback has been extensively used in order to explain the lack of star formation in the most massive early-type galaxies and in addition to reproduce the shape of the galaxy luminosity function at its bright end (Best & Heckman, 2012). In Best et al. (Best06) it is shown that radio sources with 'radio-mode' AGN feedback have an average energy output per unit time that could balance the cooling of the gas in early-type galaxies.

A second mechanism that is taken into consideration in the models of galaxy formation along with AGN feedback and has an impact on the quantity of star formation rate is feedback from supernovae (Newton & Kay, 2013). More recent simulations by Booth & Schaye (2013) have shown that star formation rate, unlike to what was believed so far, is suppresed further when both AGN and supernovae feedback mechanisms are acting together rather than when treated independently. However, even the added supernovae feedback mechanism was unable to supress an initial starburst in the event of a merger. The reason behind this is the close relation of the star formation drop-off with the temperature of the heated

gas -with higher temperatures helping the gas to getaway from the star forming region- in both AGN and supernovae feedback mechanisms (Newton & Kay, 2013).

AGN feedback plays a more significant role in mergers and can supress starbursts only when the heating of the gas is powerful, whereas supernovae feedback controls the star formation suppression in disk galaxies of masses at the order of the Milky-Way (Newton & Kay, 2013). The inherent difference between the two processes is mainly due to the different regions associated with these processes. AGN activity acts in the vey central region of a galaxy, whereas supernovae occur in the entire galactic disk.

1.4 Correlation of emission in the radio in galaxies with that at other wavelengths

1.4.1 The Radio-FIR Correlation

As described earlier, the non-thermal radio emission and the far-infrared (FIR) have a common origin: high-mass luminous stars and their products called supernova remnants. Massive short lived stars provide the UV radiation which is absorbed by the optically thick interstellar dust and then re-radiated into the thermal infrared part of the spectrum at wavelengths of roughly 10-300 μm (Kennicutt, 1998). The far infrared (FIR) emission can be in principle a very good tracer of young star population and star formation rate (SFR). As described in (Haines et al., 2011), complete surveys that combine radio-continuum emission at GHz frequencies and IRAS FIR fluxes, confirm the existence of a tight correlation between the observed radio and FIR luminosities. That relation is found to be linear and extends for several orders of magnitudes (Condon, 1992). These surveys include more than 98% of the systems with FIR emission that are nearby (Yun et al., 2001), and it is believed

that this exceptionally linear relation is generally linked with 'newborn' stars (e.g. Condon et al., 1991; de Jong et al., 1985; Ivison et al., 2010). The origin of the non-thermal GHz radio continuum emission associated with star-formation, is synchrotron radiation from relativistic cosmic ray electrons and protons, accelerated in supernova explosions of the same massive young stars. The radio emission from supernova remnants does not last very long though (e.g., Vela in our galaxy is 10^4 yr old). In this case, the correlation between the radio and FIR emission, which is the re-radiated dust from the star-formation, would then require a prolongue period of starbursts, being accordingly long, in the order of 10^9 years (Haines et al., 2011). In any other case, the radio-FIR correlation would not be seen as only the dust re-radiated FIR emission would be present without any radio emission to correlate with.

The light from galaxies that currently exhibit star formation, can originate from both newly formed and older stars. In late-type star forming galaxies, where young stars in HII regions heat up dust to rather high temperatures, (with a low 100 μm to 60 μm ratio of 1) there is a correlation of the FIR luminosity with other star formation tracers such as the ultraviolet continuum and H_α luminosity. However, in early-type (S0–Sab) galaxies, high FIR luminosities are often seen along with a much cooler emission, as older stars and the far-ultraviolet (FUV) light from OB type stars in the field heat the dust to much lower temperatures (100 μm to 60 μm $\geq$5; e.g., Buat & Xu 1996; Lonsdale Persson & Helou 1987). On the contrary, there are many early-type galaxies that lack independent evidence of high star formation rates (SFRs), suggesting that active galactic nuclei (AGNs) or older stars are responsible for much of the FIR emission (Kennicutt, 1998). Thus, old stellar populations affect earlier types of galaxies more than later ones (Bell et al., 2003).

The complexity of the emission mechanisms in radio continuum and infrared light yields the existence of a conspiracy between these two components (Bell et al., 2003). The val-

idation of the relation with a scatter of only a factor of 2 arose misbeliefs for a closer examination in the radio-IR correlation. In a recent study of Lacki et al. (2010) it is shown that the hidden cause of the far-IR/radio correlation is the total energy loss of the relativistic particles and UV photons before getting away from their galaxies ('calorimetry'). Haines et al. (2011) describes that this phenomenon has greater effect in galaxies with small gas surface density, that is in normal galaxies. In these galaxies a much lower synchrotron radio emission is observed due to the great fraction of relativistic electrons that have escaped, which leads to a greater absorption of UV photons, thus lowering the infrared flux. On the other hand at the site of large star forming regions, where the average gas surface density is high, radio losses from ionization and 'braking radiation' (bremsstrahlung) are balanced by radiation from secondary electrons and protons (Haines et al., 2011, ACCESS III).

The FIR quantity could be measured by the IRAS 60 and 100 μm fluxes (Condon, 1992) by:

$$\left(\frac{FIR}{W\,m^{-2}}\right) = 1.26\times10^{-14}\left(\frac{2.58S_{60\mu m}+S_{100\mu m}}{Jy}\right), \tag{1.8}$$

where FIR is the total flux between λ ~40 μm and λ ~120 μm.

In Garn et al. (2009) the SFR can be estimated converting equation 2 from Condon (1992) to a 610 MHz equivalent assuming a spectral index of $\alpha = 0.8$ with α defined as $S_o = \nu^{-\alpha}$:

$$\left(\frac{SFR}{(M_\odot yr^{-1}}\right) = 2.84\times10^{-22}\left(\frac{L_{610}}{W\,Hz^{-1}}\right) \tag{1.9}$$

for $L_{610} \geq L_c$ where $L_c = 3.3\times10^{21} W\,Hz^{-1}$ is the luminosity at 610 MHz of a galaxy with

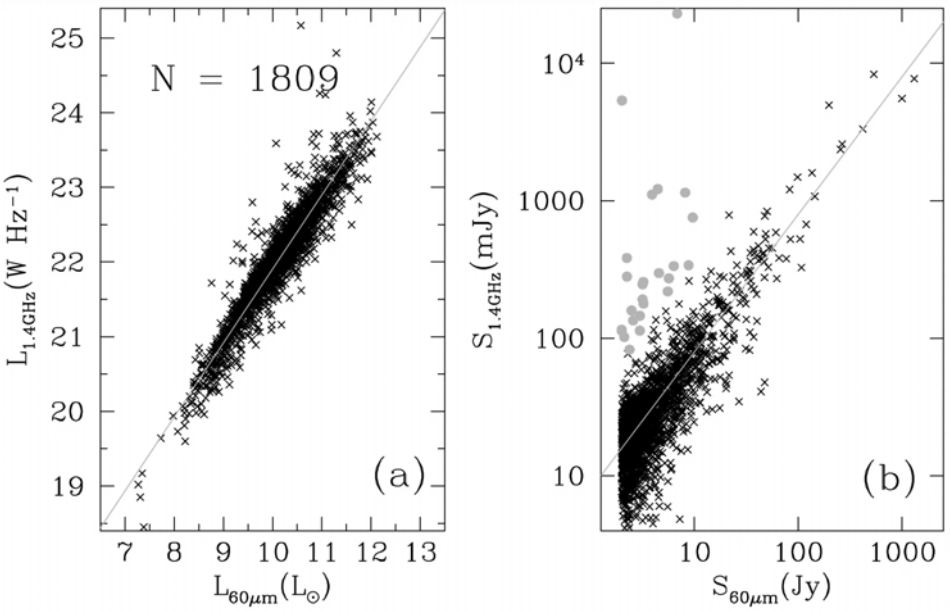

Figure 1.2 (a) Plot of 1.4 GHz radio luminosity vs IRAS 60 μm luminosity from Yun et al. (2001). The solid line represents the linear relation with a constant offset. (b) Plot of 1.4 GHz and IRAS 60 μm flux density for the IRAS 2 Jy sample. The solid line corresponds to the same linear relation shown in (a). Gray filled circles identify the radio-excess objects. The remaining 1750 objects (out of 1809) lie very close to the linear relation, with the scatter being less than 0.26

$SFR \simeq 1 M_\odot yr^{-1}$, and

$$\left(\frac{SFR}{(M_\odot yr^{-1}}\right) = \frac{2.84\times10^{-22}}{0.1+0.9(L_{610}/L_c)^0.3}\left(\frac{L_{610}}{W\,Hz^{-1}}\right) \tag{1.10}$$

for $L_{610} \leq L_c$.

A main characteristic of the far-IR/radio correlation is the dependence of its slope with galaxy luminosity. Steep radio-IR correlations have the tendency to be seen in samples that include more relatively faint galaxies ($L_{IR} \leq 10^{10} L_\odot$) (e.g., Price & Duric 1992, Xu et al. 1994), whereas slopes $\sim$1 are seen in samples with a greater representation of highly luminous galaxies ($10^{10} L_\odot \leq L_{IR} \leq 10^{12.5} L_\odot$) (e.g., Condon et al. 1991, Yun et al. 2001; Figs. 1 and 2).

The luminosity-dependent slope is explained by various studies in terms of dust re-

radiation by older stars or effects in the radio by nonthermal/thermal processes. Fitt et al. (1988) and Devereux & Eales (1989) found a linear radio-IR correlation by removing the contributions from old stellar populations (using total IR luminosity as a constraint). In Condon et al. (1991) contributions from old stellar populations were identified through by the fact that IR-overluminous galaxies were also overluminous in optical B band (4400 Å), when comparing the ratio of IR/radio fluxes with the ratio of optical B/radio fluxes. The same result was shown by the model of Xu et al. (1994) attempting to justify that the slope of the radio-IR correlation is a quantity different from unity, and some of the scatter in the relation.

In addition, the far-IR/radio correlation slope depends on the radio frequency. At high radio frequencies ($\geq$5 GHz) the slope tends to unity while in radio frequencies below 5 GHz the slope becomes steeper usually approaching values greater than unity. Similarly, Price & Duric (1992) and Niklas (1997) have investigated the significance of the nonthermal to thermal radio emission fraction on the radio-IR correlation. It was found that the thermal radio continuum radiation (which corresponds directly to SF rate) correlated linearly with the IR luminosity, while the nonthermal emission had a steeper correlation with IR luminosity. Adding these two results together, it was again concluded that the steepening of the radio-IR correlation with decreasing radio frequency at low IR luminosities, originate from old stellar population that is heating the IR toward low IR luminosities and that the relation of the nonthermal radio emission to the SF rate is nonlinear.

The case for the far-IR/radio correlation in the cores of groups and clusters is a little more complicated as the intergalactic medium plays an important role on the average gas surface density of galaxies. In a plethora of poor groups, where ram-pressure stripping is not significant due to the low relative velocities of the galaxies, there is a correlation of radio and

far-IR emission with soft X-ray emission (e.g., O'Sullivan et al., 2009). However, in the case of rich clusters these correlations are affected by tidal and gas stripping processes. In Miller & Owen (2001) 329 radio galaxies from 18 nearby clusters were investigated, and it was found that the relation holds for star forming galaxies. An excess of starforming galaxies were found towards the centre of the clusters, which enhanced the radio emission by two or three times, possibly due to magnetic field compression from ram-pressure (Haines et al., 2011, ACCESS III).

1.4.2 Ultraviolet wavelength as a star formation tracer

Ultraviolet radiation ($\sim$2000 Å) originally emitted from young stars of intermediate masses (2–5 $M_{\odot}$; Boselli et al. 2001), supplies the information needed for the recent SFR over the last 10^8 yr of a galaxy. The only disadvantage is that UV emission is highly affected by the existence of dust around these stars, reducing its emissivity (Haines et al., 2011). For that reason the ultraviolet radiation that is seen from spiral galaxies comes mainly from a little older stars (10^7 –10^8 yr) that have moved further from the highly absorbing molecular clouds of their birth areas (Calzetti et al., 2005).

As mentioned earlier, the UV radiation absorbed by dust is re-radiated into the mid-or-far-infrared giving us the opportunity to calculate the amount of the obscured star formation (e.g. Kennicutt, 1998; Kennicutt et al., 2009; Rieke et al., 2009). The level of the dust absorbed depends not only on the properties of the galaxy itself, such as mass and morphology, but also on the geometry and the relative position between the dust and the young stars. However, for the majority of galaxies, despite the factors mentioned above the fact is that more than 90% of the UV photons are absorbed by dust. For that reason the ultraviolet luminosity function requires complementary estimators of SFRs in order to provide strong

constraint on the universal SFRs in groups and clusters of galaxies. The combination of radio continuum emission and optically thin infrared estimate of SFRs, are the best candidates as they are mostly sensitive to obscured emission, which is exactly the one being missed by the ultraviolet luminosity function (Haines et al., 2011).

Thus, the fraction of infrared-to-ultraviolet as mentioned also in Haines et al. (2011) can be used as a sufficiently good tool in order to calculate the extinction of young stars at UV waveband (10^8 yr). Nevertheless, a note of caution has to be given for this fraction as the areas within a starforming region or a galaxy that correspond to the observed ultraviolet and infrared emission are either different, or are created by the stars of the same age (Calzetti et al., 2005). As mentioned in Bell (2002) the issue that still affects mostly the UV and optical SFR tracers, is the dust obscuration.

There are several relations for estimating the SFR in galaxies from the UV and FUV fluxes. In Kennicutt (1998), by assuming that the star formation rate has not changed over timescales that are long in comparison to the lifetimes of the dominant UV emitting population ($\leq 10^8$ yr) the SFR from the UV luminosity wavelengths is given by :

$$SFR(M_{\odot}yr^{-1}) = 1.4 \times 10^{-28} L_{\nu} ergss^{-1} Hz^{-1} \tag{1.11}$$

where the UV spectrum is approximately flat in L_{ν} over the wavelength range 1500–2800 Å with the equation being applicable to galaxies that exhibit constant star formation over 10^8 yr or more.

The most characteristic phenomenon in UV waveband is galactic extinction, so the best estimation possible of the FUV attenuation is important. The first method that was used to estimate the FUV attenuation is the total HI and H2 column density via the estimation of the dust content of the galaxy (e.g., Buat et al., 1989). However the studies of Buat (1992) and

Xu et al. (1997) confirmed that the geometry of the dust, the metallicity and the extinction curve added significant dispersion into the relation between gas density and extinction.

A second method that was mainly used at high redshifts for the estimation of the FUV extinction is the correlation between the UV spectral slope with the FUV extinction (Meurer et al., 1999). However, the validity of this method as a good attenuation indicator was limited only in starburst galaxies as it proved to be weak for other types of galaxies (Bell, 2002).

In principle, the most complete and robust FUV extinction indicator is the TIR/FUV ratio where TIR is the total $8-1000$ μm luminosity and $FUV = \nu F_\nu$ at $\sim$1500 Å (Bell et al., 2003). This method, which is the ratio of the direct radiation to the light hidden by young stars is independent from changes in dust extinction curve, dust geometry, and SF history (Gordon et al., 2000). This method for the estimation of the FUV attenuation has been used before numerous times, e.g., by Bell (2002) and its major limitation is that the older stellar populations are disregarded in the dust heating.

1.5 Radio properties of galaxies and their environment

Whether galaxy evolution is mainly affected by internal processes, such as feedback, or external ones, that are connected with the environment they are embedded in (e.g., ram pressure stripping; Hou et al. 2013), remains an open question. The early observations of Oemler 1974 and Dressler (1980) revealed the important role the local environment plays in the properties of galaxies. Much later, results from the Sloan Digital Sky Survey (SDSS) have confirmed that the morphological distribution of galaxies and their colour is correlated with the local density (e.g., Balogh et al., 2004; Blanton et al., 2003). The picture in the nearby Universe is that the population of red galaxies rises with local density, whereas the

star-forming galaxies can be seen in any density region, thus are almost independent of their environment (De Propris et al., 2004).

In dense environments such as clusters of galaxies, where preferentially reside elliptical and S0 (early-type) galaxies that exhibit bulge-dominated morphology, low star formation rates and less atomic/molecular gas content, can be found for many radio AGN (Ledlow & Owen, 1996). On the other hand, spiral and irregular (late-type; blue) galaxies reside in low-density regions (field environment; Blanton & Moustakas 2009; Hou et al. 2013) implying that the star formation rate becomes lower as the local galaxy density rises (Li et al., 2012).

The connection between the local environment of a galaxy and its radio emission lies in the mechanisms that are taking place in each local density and their efficiency to trigger or boost radio activity. It has been suggested that radio activity can be enhanced by merging of clusters and groups (more effective in higher density environments) or by galaxy-galaxy interactions and mergers within a group (more effective in lower density environments; Miles et al. 2004; Taylor & Babul 2005). In early type galaxies, these processes efficiently direct gas to the AGN, resulting in radio emission from a small or large-scale jet, whereas in late-type galaxies, the corresponding processes would set off or increase radio emission from star formation (see Vollmer et al., 2001). The radio luminosity of the AGN would also be affected by the interaction of the jet with the intragroup/intracluster gas (Shabala et al., 2008).

In conclusion, radio loud AGN with emission lines are the most likely to be found in regions of higher densities than the radio quiet ones (Kauffmann et al., 2008). The number of radio-selected star forming galaxies declines as the local overdensity rises whereas galaxies with AGN activity are almost independent with the local density, apart from the case of low density environments, due to the lack of existence of these objects in such environments

(Bardelli et al., 2009). Star forming galaxies are independent of their environment in distances greater than one Mpc (Kauffmann et al., 2004) while the most probable environment to regulate the AGN radio emission corresponds to groups or clusters, rather than systems consisting of isolated pairs of galaxies or companions (Best, 2004).

1.6 The Complete Local-Volume Groups Sample (CLoGS)

In order to comprehend the impact that the various forms of the feedback process have in groups of galaxies, an unbiased sample is essential. With the majority of studies to date being focused only on the obvious places where the feedback mechanism would take place, on jet/cavity systems in massive clusters of galaxies, one important environment where feedback would have the greatest impact on galaxy evolution and formation is left out: groups of galaxies.

Galaxy groups are the environment where most of the galaxies reside (e.g., Eke et al., 2004). The fact that galaxies in groups are into close proximity, ignites more easily processes such as galaxy interactions. Thus the understanding of feedback requires the close investigation of the processes involved in a variety of groups, as the governing process of galaxy dynamics in groups is still unknown (e.g., Gaspari et al., 2011; McCarthy et al., 2010; Randall et al., 2011). The gap in our knowledge for galaxy groups is also enhanced by the fact that to date there is no complete radio/X-ray sample of nearby groups making automatically the study of AGN feedback in groups a necessary, but also a very difficult, task. The samples that are considered to be the best available for galaxy groups to date, are selected in such a manner (e.g., Osmond & Ponman, 2004; Rasmussen & Ponman, 2007; Sun, 2009) that are 'vulnerable' to any potential biases that would most probably lead to a misinterpretation of any results drawn from them (O' Sullivan et al., 2014).

For example, X-ray selected samples until recently were based on the shallow observations of *ROSAT All-Sky Survey* (RASS), which is known for its bias at low luminosities to centrally-concentrated cool core systems (Eckert et al. 2011, discussion about cool-core bias in cluster samples). A similar cool-core bias manifests itself in cluster samples selected by virtue of the Sunyaev-Zel'dovich effect, since the latter preferentially picks up centrally condensed systems (Lin et al., 2015): group samples based on the S-Z effect are not feasible with current technology anyway. While the detection of diffuse X-rays ensures the presence of a substantial dark halo binding the group or cluster together, optically selected group catalogues (e.g. Berlind et al. 2006; Eke et al. 2004) suffer from the limitation that a significant fraction of the groups selected by percolation or friends-of-friends like algorithms turn out to be chance superpositions, or systems in the early stages of collapse.

The Complete Local-Volume Groups Sample (CLoGS) project targets to fill this gap for galaxy groups and become the first statistically complete survey of galaxy groups observed in the X-ray, optical and radio wavelengths (http://www.sr.bham.ac.uk/ ejos/CLoGS.html). The main science goals of this project in which I am performing the radio data analysis include:

- Investigate the X-ray temperature of groups and their hot halo filled with gas (Sanderson, Ponman, & O'Sullivan, 2006).

- Characterise the population of AGN in groups, and investigate their impact on their environment.

- Study the process of star formation, the radio activity presented in the core of central galaxies and the statistics concerning these two processes of the overall population of galaxies in groups.

1.6.1 Sample

X-ray or optical catalogues utilised by most studies of galaxy groups so far were inserting biases in their own way. Systems that were not yet verified as formed groups were most certainly included by optically selected group catalogues while the low number of galaxies that most optically selected samples had was making this method not trustworthy for safe results (O' Sullivan et al., 2014). On the other hand, the X-ray selection of samples of galaxies relies in the nearby Universe on the ROSAT All-Sky Survey (RASS), which has a preference in 'picking up' more cool core systems (Eckert et al., 2011). This bias is also obvious from the results of many statistical and representative samples of cluster galaxies. For example, in Sanderson et al. (2006) it is found that half of the galaxies in the sample are characterised as cool-core systems whereas the equivalent finest sample that exists for groups of galaxies (but non statistical), reveals that only $\sim$20% of galaxies are non cool-core (Dong et al., 2010). Lastly, most of the observations that were performed for most of the X-ray catalogues to date, were not deep enough in order to avoid the non detection of fainter X-ray systems.

The only method to certify that a group is formed, is the detection of the hot intra-group medium from the X-rays. Combining systems selected using this method with optical and radio detections, will give the opportunity for the identification and investigation of more AGN and star forming galaxies in the group environment (O' Sullivan et al., 2014).

The CLoGS sample consists of 53 candidate groups that reside in the local Universe ($\leq$80 Mpc) and aims to be the first carefully selected optical sample of groups with high-quality X-ray and radio data. X-ray data are from *Chandra* and *XMM-Newton* satellite telescopes that allow us to have accurate group temperatures and detailed information of the hot group gaseous haloes. On the other hand, the detection of older, radio AGNs, will be

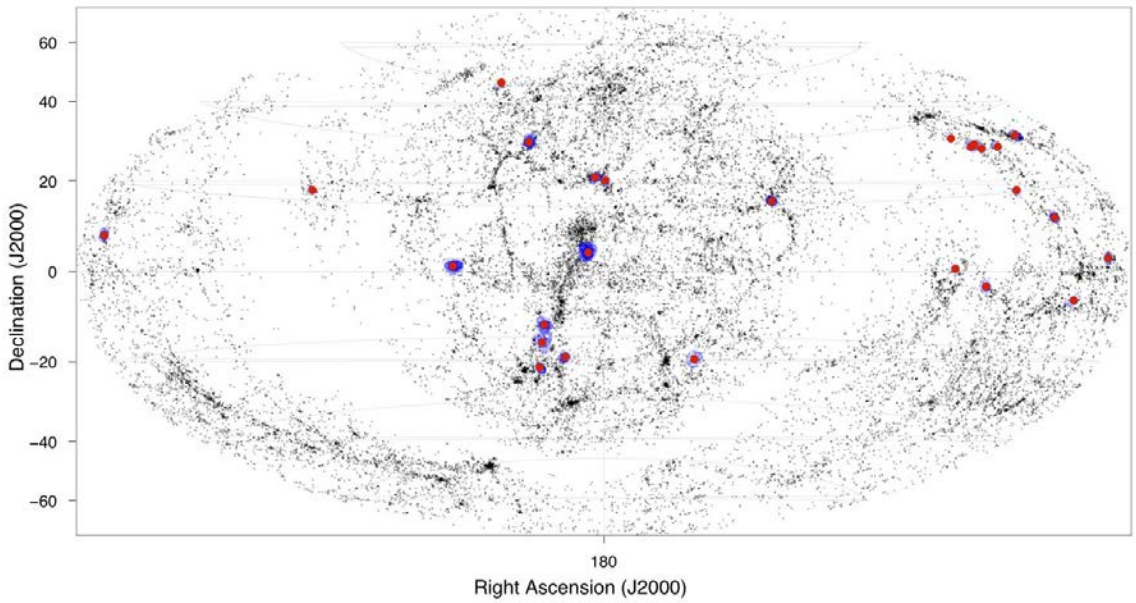

Figure 1.3 Locations of the CLoGS groups among the filamentary structures of the local volume, projected on the sky. Blue circles mark member galaxies, red points are dominant ellipticals and all other galaxies in the local volume are marked in black [http://www.sr.bham.ac.uk/ ejos/CLoGS_Sample.html].

possible with low-frequency radio data from the Giant Metrewave Radio Telescope (GMRT) that is used to observe the groups using for the observations two frequencies, at 235 and 610 MHz, with average time spent on source of 3-4 hours. The sample has also been selected to overlap with the NVSS 1.4 GHz and TGSS 150 MHz surveys so more multifrequency data will need to be analysed in the future.

In order for our sample selection to be secure we also include a threshold determined by the richness parameter R. As R we set the number of galaxies with log $L_B \geq 10.2$ within 1 Mpc and 3σ (σ=mean group velocity) of the BGE. Systems then that have richness parameter greater than 10 are excluded from our sample as they end up being clusters already known, and on the other side, six groups that have R = 1 are also excluded, as they are not rich enough to give a trustworthy determination of their physical parameters. Finally, in a total of 53 groups, we divided the CLoGS groups into two statistically complete sub-

samples: i) the 26 high richness groups sub-sample with R = 4−8 and ii) the 27 low richness groups sub-sample with R = 2−3.

Lastly, GMRT observations of the full 53-group sample have been succesfully finished, while in the X-ray only the high-richness subsample of 26 groups is observed, with a limiting sensitivity of $L_{0.5-0.7KeV} > 1.2\times10^{42}$ erg s^{-1}.

1.7 This Dissertation

For this dissertation, deep interferometric radio observations of a well-defined sample of galaxy groups, in the local Universe, were obtained over a period of three years, and analysed to address some of the goals mentioned above. The main goals of this dissertation is the characterization of radio AGN population in groups, the study of the interaction of central radio AGN with their environment, the effect of group AGN on feedback mechanism and the estimation of star formation rate in nearby groups. For the most part, observations at 235 and 610 MHz from the Giant Metrewave Radio telescope in India are analysed to measure the spectral and morphological properties of the radio detected galaxies in those groups. In one case the detailed study of the very strong FR I radio source 3C 270 includes the analysis at 1.4 and 4.8 GHz from the Very Large Array (VLA). Combination of the analysed sample of radio galaxies is performed with other multiwavelength catalogues for the calculation of star formation using different star formation indicators.

In Chapter 2 the basic principles of radioastronomy and interferometry are presented along with a detailed description of the function and technical properties of the GMRT. The process of the analysis of the radio data that is followed is also described. The analysis is performed using the Astronomical Image Processing System (AIPS) the main tasks of which are mentioned and explained.

In Chapter 3 the detailed spectral analysis of the FR I radio source 3C 270, that rises from the nearby group-central elliptical galaxy NGC 4261, that is part of the CLoGS sample, is discussed. The radio source is analysed at three frequencies: at GMRT 240 MHz and at VLA 1.55 GHz and 4.8 GHz. Their combination leads to the production of spectral index maps that reveal a constant spectral index along the jets and a gradual steepening from the ends of the jets through the backflow region into the lobes. Using the observed spectral index trend along the lobes and by fitting an ageing JP model a radiative age of ~ 29 Myr for the western lobe and ~ 36 Myr for the eastern one is found. The lobe is assumed to have passed an early supersonic phase that expanded into the ISM at approximately Mach 6 (3500 km s^{-1}), or the source underwent multiple AGN outbursts with possible large changes in jet power, or the transportation of young electrons to the back of the lobes relatively fast via a backflow mechanism. It is also discussed that the lobes are likely to contain thermal plasma from material entrained from the jets.

In Chapter 4, the radio images of the 26 rich sub-sample groups focused on the properties of the central AGN are presented. The systems are categorized according to the radio morphology that their central galaxy exhibits and in combination with the X-ray data available the nature of the processes that governs each system is revealed. The statistics of the central ellipticals detected in radio is also discussed along with their spectral index distribution. The estimation of the mechanical energy output that each system has is calculated based on its integrated radio luminosity and the available X-rays are giving an impression for the account of AGN feedback in groups.

In Chapter 5, the separation between AGN and star-forming galaxies is presented. Optical identification of galaxies (BPT diagram) is performed that leads to the distinction between AGN, composite and star-forming galaxies. The radio data analysed are combined

with various catalogues across the electromagnetic spectrum in order to reveal the star formation and AGN properties of the groups in the nearby Universe. The usage of multi-wavelength catalogues includes older radio observations (NVSS), Far-Infrared (2MASS), Ultraviolet (GALEX) and Mid-Infrared (WISE). The best star formation rate (SFR) indicator is found from colour magnitude diagrams and the radial distribution of the star formation and AGN in groups give a clear view of the co-existence and evolution of these properties in our local Universe.

Chapter 2

Radio Astronomy

2.1 Introduction

The study of the sky at radio wavelengths is the science of radio astronomy, which is the field that revealed that the properties of gas, in an astrophysical context, is influenced by magnetic fields. Compared to the more traditional optical astronomy, the 'new' astronomies such as radio astronomy, microwave astronomy and astronomy in the infrared (IR), X-ray and ultraviolet (UV) are only about 60-80 years old. The atmosphere is largely opaque to electromagnetic radiation, except for a few windows in the optical, near-infrared and radio regions. In many of the other parts of the e-m spectrum, one needs to have the telescopes above the atmosphere of the Earth. Thus, most of these new kinds of astronomy has been enabled by the capabilities of modern space technology.

Meanwhile, radiowaves (between the frequencies of 10 MHz to 300 GHz, corresponding to wavelengths of about 1 mm to 30 m) are able to pass through the whole of the Earth's atmosphere (Chengalur, Gupta & Dwarakanath, 2007) making their detection possible by ground based telescopes.

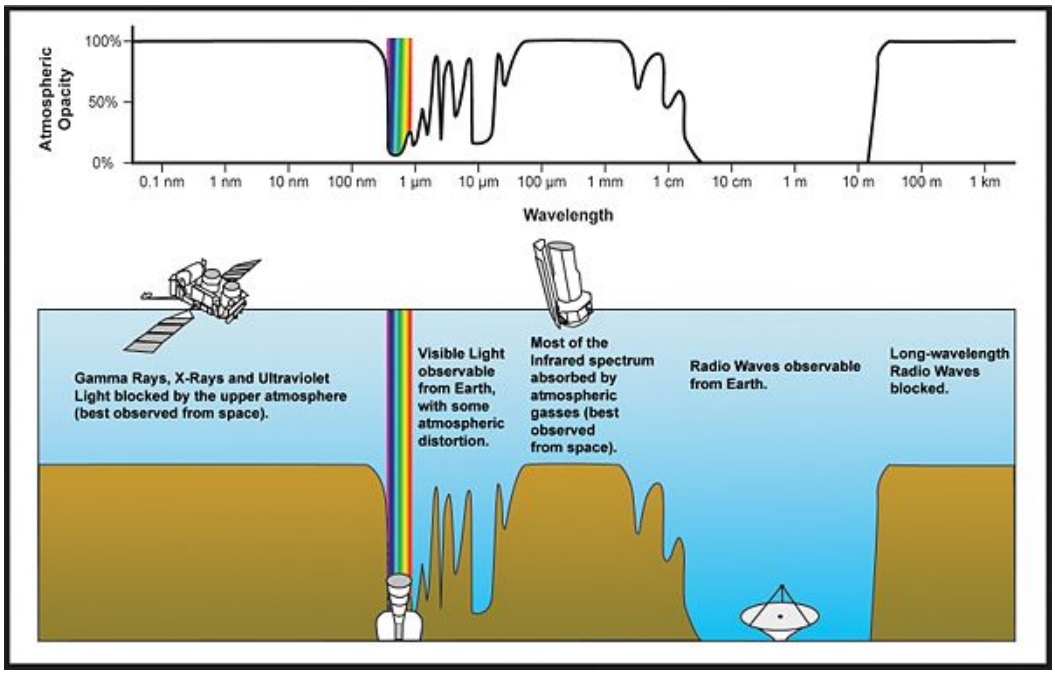

Figure 2.1 A schematic plot of the opacity of the Earth's atmosphere at various parts of the electromagnetic spectrum. Note the windows in the optical and radio regions. [http://www.ipac.caltech.edu/outreach/Edu/Windows/irwindows.html].

The field of radio astronomy originates from an experiment conducted in 1923 when Karl Jansky, while trying to reduce the noise in receivers at radio wavelengths, discovered that some of the noise was due to radiation whose origin was outside the atmosphere of the Earth. In honour of his pioneering efforts, measurements of flux density in radioastronomy are made with an unit named after Karl Jansky, which amounts to

$$1 \text{ Jansky} = 10^{-26} W m^{-2} Hz^{-1}. \tag{2.1}$$

This shows that astronomical radio sources are faint compared to terrestrial ones.

2.1.1 The Radio Sky

At various parts of the electromagnetic spectrum, celestial sources may appear very different. Thus, multi-wavelength observational astronomy is not only interesting, but essential to unlock the secrets of our Universe. Thermal sources, such as stars and gas clouds, whose temperatures are between $10^3 - 10^4$ K emit mostly at optical wavelengths. The sources of non-thermal radiation are usually weak in the optical region of the E-M spectrum, but powerful elsewhere. For example, strong emitters in the infrared are cold ($\approx$ 100 K) objects, while objects at very high temperatures ($\geq 10^5$ K) are strong emitters of X-rays and gamma-rays. Extraterrestial sources are made up of both thermal and non-thermal emitters, and so multiwavelength studies are essential in order to completely comprehend them (see e.g., Léna, Rouan, Lebrun, Mignard & Pelat 2012 Observational Astrophysics, 3rd Edition, 2012, Springer Verlag)+.

2.2 Processes of Radiation

2.2.1 Thermal and Non-thermal radiation

The main difference between thermal and non-thermal emission lies in the properties of their sources. Thermal radiation is emitted by a body because of its thermal energy and the emission is totally determined by the body's temperature. Non-thermal radiation on the other hand is not a direct result of the thermal energy of a source but depends on other parameters beyond temperature.

Thermal and non-thermal radiation differ clearly in their spectra. At the high energy end thermal radiation has a characteristic exponential drop-off. Non-thermal radiation however can have a long 'tail'at high energies represented by a power law of the form $S_\nu \propto E^{-a}$

(Rosswog & Bruggen, 2007).

Now assuming that we have the best possible emitter of thermal radiation − blackbody radiation − we can derive the specific intensity of blackbody radiation, called the Planck Law:

$$B_\nu(T) = \frac{2h\nu^3}{c^2}\frac{1}{e^{\frac{h\nu}{kT}} - 1}, \tag{2.2}$$

where $B_\nu(T)$ is the specific intensity of blackbody radiation or sky brightness of the source at ν, the observed frequency, T the temperature of the source and k is the Boltzmann's constant.

For thermal radiation the source function S_ν (or flux density) is equal to the blackbody intensity $B_\nu(T)$ (Rosswog & Bruggen, 2007)

$$B_\nu(T) = S_\nu. \tag{2.3}$$

At radio frequencies, where the energies are much lower than the typical thermal energy, that is $h\nu << kT$, Planck's Law can be well approximated by :

$$B_\nu(T) = \frac{2kT}{\lambda^2}, \tag{2.4}$$

where

$$e^{\frac{h\nu}{kT}} - 1 \approx 1 + \frac{h\nu}{kT}, \tag{2.5}$$

by MacLaurin's expansion formula. This is the Rayleigh-Jeans Limit. This is a suitable approximation for radio astronomy due to the energies involved. It is obvious though that this approximation fails to describe the high-frequency end of the spectrum, since the discrete nature of the photons have not been accounted for, when $h\nu >> kT$.

Therefore, for a source of predominantly thermal radiation, where the temperature is greater than 100 K, the flux density at radio frequencies is given by:

$$S = \frac{2kT}{\lambda^2} d\Omega, \tag{2.6}$$

where S is the flux density of the source, λ the observed wavelength, T the temperature of the source, k is Boltzmann's constant and Ω is the solid angle of the emission.

2.2.2 Synchrotron emission

One of the most important non-thermal radiation processes in astrophysics is synchrotron emission. Highly relativistic electrons that spiral around magnetic field lines generate synchrotron radiation. Only the presence of relativistic light particles like electrons and magnetic fields is revealed by synchrotron emission, with heavier charged particles, like protons, may being present but not contributing significantly to the emitted synchrotron radiation (Begelman, Blandford & Rees , 1984; Hardcastle, 2005; Harris & Krawczynski, 2006).

To maintain their spiral trajectory, the electrons experience a constant acceleration and thus emit electromagnetic radiation. The emitted radiation depends on the initial kinetic energy of the electron, and on the strength of the magnetic field. Furthermore in a process called beaming, the emitted radiation is confined in a narrow opening angle towards the direction of the motion of the particle. Synchrotron emission is a good example of non-thermal emission, since in the form described above, its flux density decreases with frequency, compared to the case of thermal emission, where the flux density increases with rise in frequency. Celestial sources that radiate synchrotron emission are thus preferably studied at low radio frequencies (Chengalur, Gupta & Dwarakanath, 2007). A diagnostic observa-

tional feature of synchrotron emission would be a smooth spectrum over a large range of wavelength (continuum), without any emission lines, accompanies by a strong polarisation ($\approx 70\%$) in a perpendicular plane to the magnetic field.

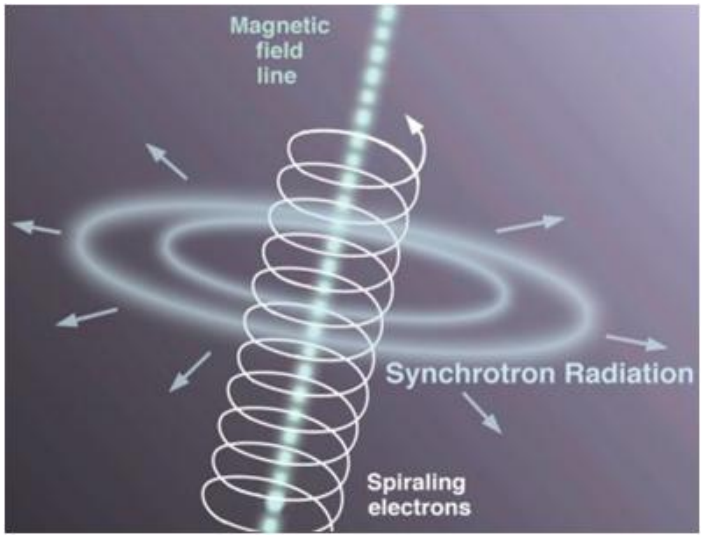

Figure 2.2 An artist's impression of the spiralling motion of an electron along magnetic field lines emitting synchrotron radiation [http://astronomyonline.org/Stars].

Synchrotron radiation can be found in various environments: in the ionized gas around hot stars (HII regions), in the remnants of supernovae and in the jets of Active Galactic Nuclei (Rosswog & Bruggen, 2007).

2.2.3 The spectrum of synchrotron emission

A simplified derivation of the most important and relevant results will be presented here (a more detailed description can be found in standard textbooks such as *Introduction to High-Energy Astrophysics* by Stephan Rosswog and Marcus Bruggen).

The spectrum of the synchrotron radiation emitted by only one electron presents an abrupt rise at approximately a frequency γ^3 times its gyro-frequency ω_{rel}, where γ is the usual Lorentz factor defined as $\gamma = \frac{c}{\sqrt{c^2-v^2}}$. The electron emits radiation over a range of

frequencies peaking at ν_c, given by

$$\nu_c = \frac{\gamma^2 Be}{2\pi m_e}, \tag{2.7}$$

where m_e is the mass of the electron, and B is the magnetic field strength. This is known as the *critical frequency*. Since the spectrum is strongly peaked, almost all the energy that escapes is near to this peculiar frequency.

As the total energy E of an electron is $E = \gamma m_e c^2$, one finds that the critical frequency

$$\nu_c \propto E^2. \tag{2.8}$$

So in an electron population of a range of energies, moving in a non-varying average magnetic field B, the electrons of higher energy will predominantly emit at higher frequencies, the latter being proportional to E^2.

The total range of frequencies that is observed is very broad compared to the small range of frequencies over which the electron deposits most of its energy. We conclude that for the ensemble of electrons in the plasma, the resultant observed power-law spectrum originates from a fundamental power-law distribution of the energy of the population of electrons (see Fig. 2.3. Therefore, the spectrum of synchrotron emission results from the combination of the radiation spectrum of one electron, with the total range of electron energies.

So, over a large range of electron energies E, it can be inferred that

$$N(E)\,dE \propto E^{-k} dE. \tag{2.9}$$

The convolution can be approximated as follows. The strongly-peaked energy distribution

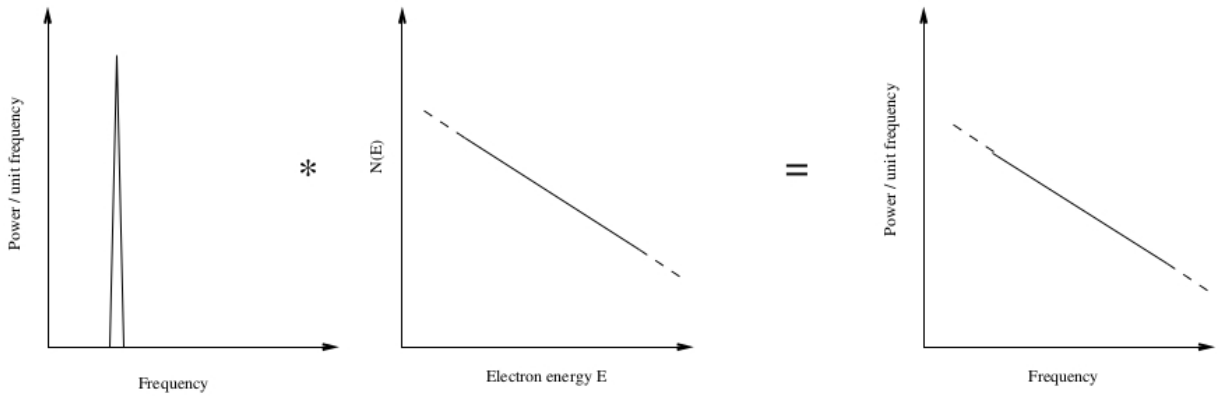

Figure 2.3 the observed spectrum of synchrotron emission results from the convolution of the radiation spectrum of a single electron, with the distribution of electron energies. [$www - astro.physics.ox.ac.uk/\ garret/teaching/lecture5-2008.pdf$].

of the radiation of a single electron is approximated by a delta function (see Fig. 2.3. The synchrotron power emitted by one electron is $P(E) \propto E^2 B^2$, and the critical frequency of the electron radiation is also proportional to E^2 (Eq. 2.8). The radiated power in the frequency range ν to $\nu + d\nu$ is the same as that between the energies E and $E + dE$. We make a simple assumption, that each electron radiates all of its power

$$P = -\frac{dE}{dt} = \frac{4}{3}\sigma_T \beta^2 \gamma^2 c U_B \tag{2.10}$$

at the single frequency

$$\nu \approx \gamma^2 \nu_G, \tag{2.11}$$

where ν_{G} is the frequency of a synchrotron pulse (gyrofrequency) and U_{B} in equation 2.10 is the magnetic field energy density. The emission coefficient of the synchrotron radiation by an ensemble of electrons then is

$$\varepsilon_\nu d_\nu = -\frac{dE}{dt} N(E) dE \tag{2.12}$$

where,

$$E = \gamma m_e c^2 \approx \frac{\nu}{\nu_{\rm G}}^{1/2} m_e c^2. \tag{2.13}$$

Differentiating E gives

$$\frac{dE}{d\nu} \approx \frac{m_e c^2 \nu_{\rm G}^{-1/2}}{2\nu_{\rm G}^{1/2}} \tag{2.14}$$

so we have

$$\varepsilon_\nu \approx (\frac{4}{3}\sigma_T \beta^2 \gamma^2 c U_B)(E^{-k})(\frac{m_e c^2 \nu_{\rm G}^{-1/2}}{2\nu_{\rm G}^{1/2}}) \tag{2.15}$$

By ignoring all the physical constants and eliminating E in favor of $\nu/\nu_{\rm G}$ results to

$$\varepsilon_\nu \propto (\frac{\nu}{\nu_G})B^2(\frac{\nu}{\nu_G})^{-k/2}(\nu\nu_G)^{-1/2} \tag{2.16}$$

since $\nu_{\rm G} \propto$ B,

$$\varepsilon_\nu \propto (\frac{\nu}{B})B^2(\frac{\nu}{B})^{-k/2}(\nu B)^{-1/2} \tag{2.17}$$

Eventually we get:

$$\varepsilon_\nu \propto B^{(k+1)/2}\nu^{(1-k)/2} \tag{2.18}$$

This implies that, for the powerlaw spectrum that one sees, $\nu^{-\alpha} \propto \nu^{(1-k)/2}$, the spectral index of the emitting radiation is given by

$$\alpha = (k-1)/2. \tag{2.19}$$

2.2.4 Low-frequency cutoff: synchrotron self-absorption

So far, to estimate the synchrotron spectrum of a population of electrons, we have accepted that all of the emitted synchrotron radiation is observed without any losses. In reality,

however, what happens is that a photon on its way out of the source propagating through the plasma may bounce away one of the other synchrotron-emitting electrons, leading to a process known as *synchrotron self-absorption*. If a photon has to be scattered many times before it can escape, the photons that can easily get out without much scattering are those near the surface of the source. So the observer only detects specific emission from the source that originates from the most upper area. The cross-section of the absorption of a low-energy photon and a synchrotron electron is greater at lower frequencies. At higher frequencies, one observes photons from deeper layers, i.e. those which are further away from the surface, resulting in a larger total flux density. Eventually we reach the point where one can observe right through the ionised gas. The frequency higher than this point gives us the basic power-law distribution.

Despite the fact that the energy spread of the particles in this case is not thermal, an effective temperature can be defined as

$$k_B T_{\text{eff}} \approx \gamma m_e c^2, \tag{2.20}$$

and since the electrons emit at a critical frequency, it is

$$k_B T_{\text{eff}} \propto E \propto \nu^{1/2}. \tag{2.21}$$

The most efficient radiation is that of a black body. So if T_{eff} is used from Eq. 2.13 in the Planck formula (Eq. 2.12), it will give the highest feasible brightness for a synchrotron plasma, i.e.,

$$B_\nu \propto \nu^{5/2}. \tag{2.22}$$

So as the observing frequency is lowered, there is a steep rise of the spectrum, to the point

one reaches frequencies where the length of the average collision-free successive scattering becomes similar to the one needed to escape from the emitting area.

2.2.5 High-frequency cutoff and the synchrotron spectral ageing.

The maximum energy a particle can gain by Fermi acceleration (Fermi, 1949) depends on the characteristics of the shock it is imbedded. Such acceleration is commonly seen in astrophysical plasmas eg. acceleration of electrons in a jet, or a plasma, or possibly from a collision between galaxies or clusters.

As a first-order Fermi mechanism, we call the sequential diffusion of particles back and forth across a shock or any region of a concentrated flow. The very simple version of this process leads to a rise in particle velocity so that multiple times crossing through the shock ends up to significant acceleration (Baring, 1997; Petrosian and Bykov, 2008). The energy gains in this case are always positive allowing via spatial diffusion the dissipation of the shock energy to a non-thermal particle population. As a second-order Fermi process we call the random scattering that particles of a certain velocity v undergo, while moving along the magnetic field lines (strength B) and a pitch angle θ, by different moving agents of velocity u. As the energy gaining collisions are more probable than the energy losing ones, on average, the particles can gain energy at a rate proportional to $(u/v)^2 D_{\rm m}$ where $D_{\rm m}$ is the pitch angle diffusion rate. This is also known as stochastic acceleration (Baring, 1997; Petrosian and Bykov, 2008).

Once the energies of the electrons are in such levels where the gyro-radius is bigger than the area over which the particles are being accelerated, they stop scattering up to still higher energies. The energy losses of the particles in the lobes of a radio source leads to an abrupt cut-off in its spectrum, which means that the synchrotron radiation ‘consumes’ all

their initial energy they gained at the shock.

If the electron loses energy predominantly through synchrotron radiation, then for highly relativistic electrons,

$$-\frac{dE}{dt} \propto E^2 B^2. \tag{2.23}$$

As time passes, the electrons that radiate away their energy faster, will be those having the higher energy. The time taken then by a synchrotron electron with energy E to do this can be calculated by,

$$\tau = \frac{E}{dE/dt}. \tag{2.24}$$

This is the lifetime of a synchrotron-emitting electron, and is defined as the time it takes to 'consume' the total amount of the available energy it has. If we thus consider a plasma which predominantly emits via synchrotron radiation a time τ after it was accelerated, just the electrons that last longer than τ will exist, irrespective of the highest energies of the electrons in the original synchrotron population.

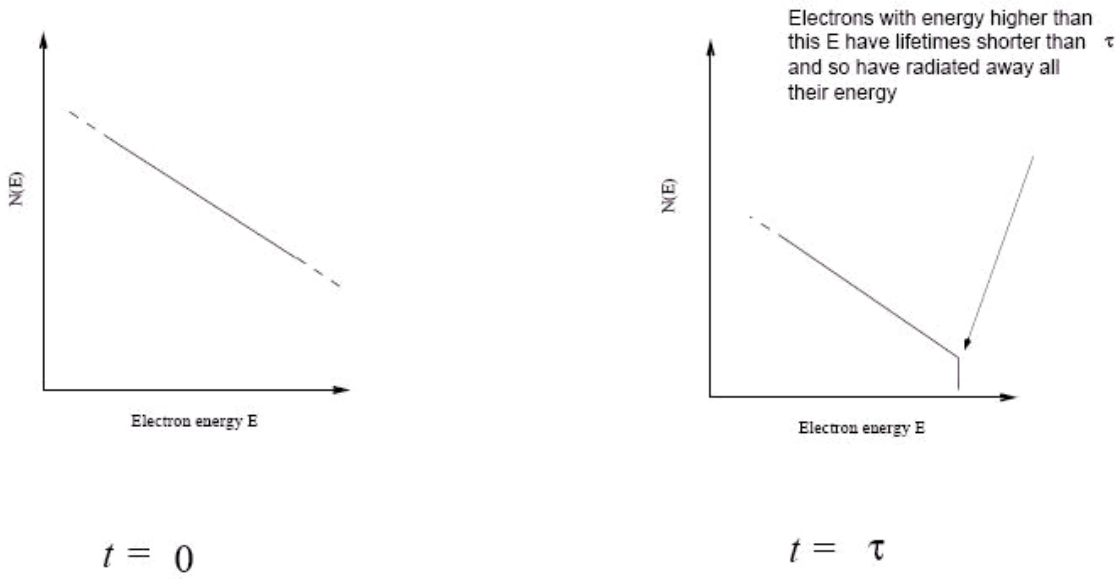

Figure 2.4 The high-frequency cutoff in the spectrum of synchrotron emission [www-astro.physics.ox.ac.uk/ garret/teaching/lecture6-2008.pdf].

This shows that there is a cutoff at the high frequency end of the synchrotron radiation emitted by the lobes of a radio source, due to the absence of the highest-energy electrons. This is known as synchrotron spectral ageing (Jaffe & Perola, 1973; Kardashev, 1962; Myers & Spangler, 1985; Pacholczyk, 1970) and the frequency above which the high-energy electrons no longer exist is called the *break frequency*.

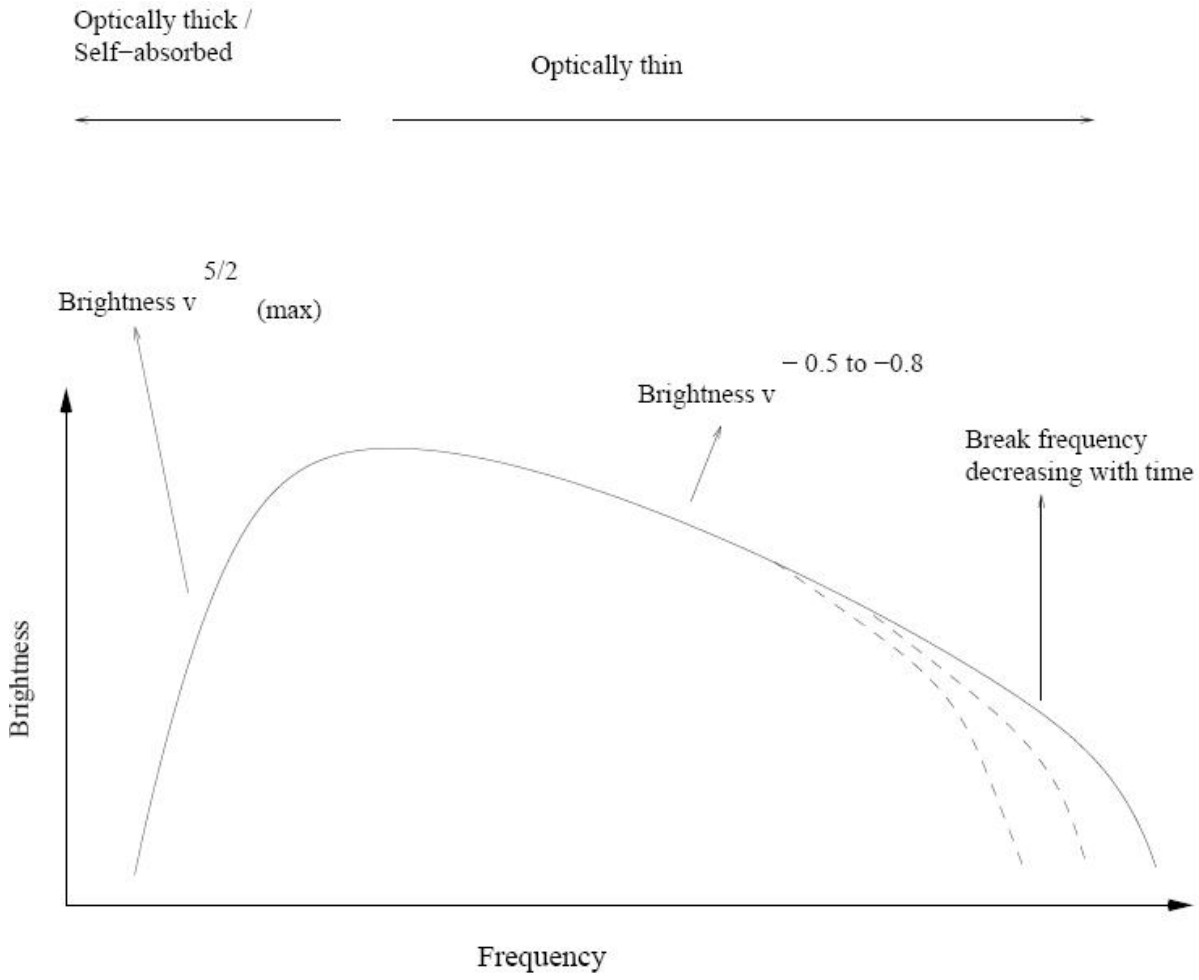

Figure 2.5 The cutoff and low and high frequencies in the spectrum of synchrotron emission from a radio-emitting astrophysical plasma [http://www-astro.physics.ox.ac.uk/ garret/teaching/lecture6-2008.pdf].

This feature (Fig. 2.5) of the synchrotron spectrum of a radio-emitting astrophysical plasma enables us to estimate the source ages associated with jets. Apart from the knowl-

edge of the *break frequency*, one needs to make certain assumptions on the magnetic field (either uniform e.g. Jaffe & Perola 1973; Kardashev 1962; Pacholczyk 1970 or varying e.g. Tribble 1993) and estimate it first via the equipartition assumption before an ageing modelling could be perfomed.

If a jet, in a source, terminates in a strong shock as it interacts with the intergalactic medium (e.g. at the position of hotspot), by estimating first the magnetic field using the equipartition assumption, the age of the source can be estimated by measuring the break frequency at various points along the lobe, starting from the nucleus all the way up to the hotspot, assuming here that the plasma is accelerated for the last time at the hotspot. Furthermore, the magnetic flux density in the lobes can be estimated from the net synchrotron luminosity measured in this exercise.

While investigating the phenomenon of synchrotron ageing in radiogalaxies, one of the main difficulties encountered is that the steepening of the spectrum, at the higher frequency end, that is expected due to synchrotron radiation losses, occurs over a broad range of frequencies (Carilli et al., 1991). This is why radio observations are needed over several frequencies.

2.3 GMRT and Radio Interferometry

2.3.1 The Giant Metrewave Radio Telescope (GMRT)

The Giant Metrewave Radio Telescope (GMRT) is an array, situated about 80 km north of Pune in central India, consisting of 30 huge steerable parabolic antennas of 45m diameter each, with their maximum distance reaching up to 25 km. It has been designed to function at a range of frequencies from 50 MHz to 1450 MHz. The antennae have been built using

an original technique in which their reflecting surface is made of panels of wire mesh in a parabolic configuration. Due to the design each antenna has minor wind loading, as well as a very low total weight. Hence the entire array of GMRT could be constructed at a relatively low cost, compared to traditional designs.

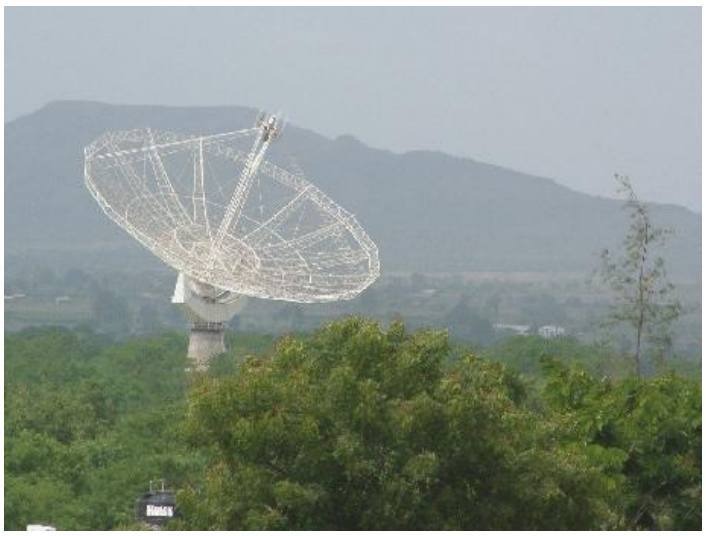

Figure 2.6 One of the 30 GMRT antennas (Chengalur, Gupta & Dwarakanath, 2007).

Chengalur, Gupta & Dwarakanath (2007) notes that as a radio source is observed by a GMRT antenna, a fluctuating voltage is generated, varying with the same frequency as the astrophysical electromagnetic (E/M) wave detected. We call this the the Radio Frequency (RF). As in all modern radio observatories, the front-end of the GMRT interferometric system relies entirely on digital electronic techniques to process the detected signals.

The celestial radio signal is very faint indeed, typically of the order of 10^{-29} to 10^{-27} W m^{-2}. The original fluctuating voltage thus has to be significantly amplified by the RF amplifier, which is part of the front-end electronics. It is of utmost importance that the noise introduced at this stage is kept to the minimum possible, since the original signal is weak. After the amplifier is a mixer, which alters the frequency of the signal, usually down to a base-band (BB) frequency in a heterodyne receiver system. This is then sampled, close

to the Nyquist limit. At the same time, an integrator records the average of the signal to enhance the signal-to-noise ratio. Further details are summarised in Chengalur, Gupta & Dwarakanath (2007).

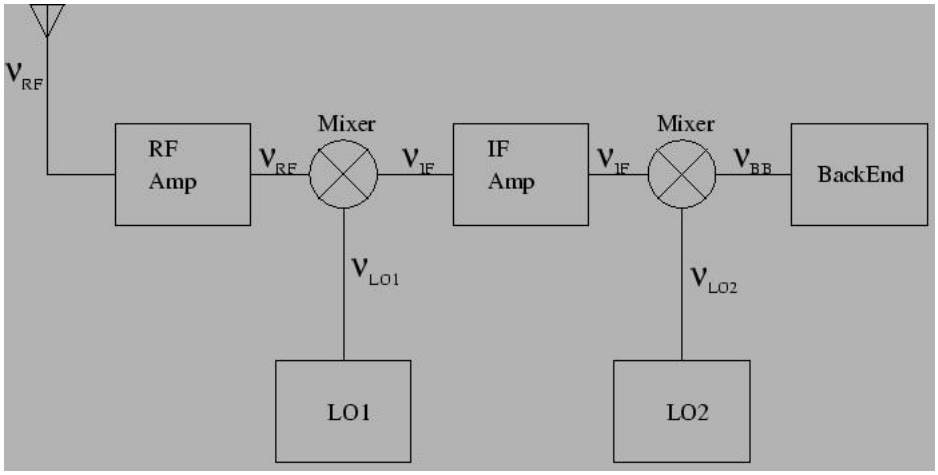

Figure 2.7 Schematical diagram of a single dish radio telescope (Chengalur, Gupta & Dwarakanath, 2007).

2.4 Polarisation and the Stokes parameters

The waves arriving from a cosmic source due to their huge distance from the observers can be assumed as plane waves. We can also assume that the wave is essentially monochromatic since with a radio telescope, we observe in a narrow frequency band around the RF (Chengalur, Gupta & Dwarakanath, 2007).

The two components of the electric field of a plane monochromatic electromagnetic wave are given by

$$\begin{aligned} E_X &= A_X \cos(2\pi\nu t + \phi_X) \\ E_Y &= A_Y \cos(2\pi\nu t + \phi_Y), \end{aligned} \tag{2.25}$$

where A_X, A_Y, ϕ_X, ϕ_Y are constants. Since electromagnetic waves are transverse, both components of the electric field E must lie in the plane normal to the direction of propagation (say X-Y), and thus the time-varying electric field can be written as

$$E(t) = A_X \cos(2\pi\nu t)\,\widehat{e}_X + A_Y \cos(2\pi\nu t + \phi)\,\widehat{e}_Y. \tag{2.26}$$

If the field just has just one component travelling along the Y axis ($A_X = 0$), going from $-A_Y$ to $+A_Y$ within a single cycle, then it is defined as linearly polarised along the Y axis. The manner in which the electric field of a wave changes at a specific point in space with time is often characterized by its polarisation. The state of polarisation is quantified by the Stokes parameters, which for a monochromatic plane wave are given by

$$\begin{aligned} I &= E_x^2 + E_y^2 \\ Q &= E_x^2 - E_y^2 \\ U &= 2E_xE_y cos(\phi) \\ V &= 2E_xE_y sin(\phi). \end{aligned} \tag{2.27}$$

Here Q and U are quantities describing linear polarisation, and V measures circular polarisation. I is a measure of the total intensity of the wave (For more details see Chapter 16 Low Frequency Radio Astronomy, Third Edition Chengalur, Gupta & Dwarakanath 2007).

2.5 Single aperture radio telescopes

2.5.1 Signal to noise ratio (SNR)

As a radio wave arrives at an antenna, the power P that is absorbed per unit frequency is often represented in terms of an "antenna temperature"

$$T_A = \frac{P}{k}, \tag{2.28}$$

where k is the Boltzmann constant. It must be noted that this antenna temperature is not related to the actual temperature of the antenna Chengalur, Gupta & Dwarakanath 2007.

In a similar vein, the integrated power at a radio receiver is specified as the "system temperature"

$$T_{sys} = \frac{\text{Total power referred to receiver inputs}}{k}. \tag{2.29}$$

The system temperature is the total random noise in the system when looking at blank sky and hence we want to minimise it. The main components of noise, from the the various constituent subsystems of the radio telescope that add up linearly to form a total T_{sys}, according to Chengalur, Gupta & Dwarakanath (2007) are mainly a) the contribution of the background sky brightness b) the stray radiation from the ground picked up by the antenna feed and finally c) the noise from the receiver. Most important of all contribution to the noise is the terrestial radio frequency interference (RFI), which is explained in more detail later.

Since the celestial signals detected by a radio telescope are random, the detector will also record variations in power which are random in nature. Imagine a telescope with system temperature $T_{\rm sys}$ and gain G, observing an astrophysical source within a bandwidth $\Delta\nu$. In

Chengalur, Gupta & Dwarakanath (2007) it is noted that it is well known when a power detector observes for τ seconds a signal over a bandwidth of $\Delta\nu$ Hz, the rms of the signal is $T_{sys}/\sqrt{\Delta\nu\tau}$, where the rms of the detector is T_{sys}. The net increase in the system temperature is just $G \times \sigma$, where σ is the flux density of the astrophysical object. Hence, the signal-to-noise ratio is given by

$$SNR = \frac{G\sigma\sqrt{\Delta\nu\tau}}{T_{\rm sys}}. \tag{2.30}$$

This represents the fundamental equation for the observer, giving the sensitivity of a single dish antenna. If the signal-to-noise ratio remains large, the certainty of detecting the source is high. We must remark here that the noise accounted for in the signal-to-noise ratio here refers only to the various sources of 'thermal noise', i.e. stray radiation from the ground, sky temperature, noise from lossy elements etc (Chengalur, Gupta & Dwarakanath, 2007).

2.5.2 Antenna patterns

The effective aperture of a single component of a radio telescope, i.e. an antenna is given by

$$A_e = \frac{\text{Power density available at antenna terminals}}{\text{Flux density of wave incident on the antenna}}, \tag{2.31}$$

where the units are $\frac{W/Hz}{W/m^2/Hz} = m^2$.

Since the ability of the antenna to absorb the incoming radiation is better in certain directions compared to others, this measure of effective area depends on the direction of the incident wave. Thus we should write this quantity as a function of azimuthal angles

$$A_e = A_e(\theta, \phi). \tag{2.32}$$

This characteristic of the antenna is known as its *power pattern*, which is defined as the effective area, but normalized to be unity at its maximum,

$$P(\theta,\phi) = \frac{A_e(\theta,\phi)}{A_e^{\max}}. \tag{2.33}$$

In Fig. 2.8 is shown the normal shape of an antenna regarding its power. Chengalur, Gupta & Dwarakanath 2007 discusses that the principal maximum is called the *main lobe*. In addition, typically it has several secondary maxima, known as *side lobes*. The angular distance between the two points at Half Power is called the Half Power Beamwidth (HPBW). For radio astronomical observations the HPBW is desired to be as minimum as possible, and the sidelobes are to be kept to a minimum (to minimise unwanted radiation from stray sources being incorporated in the main observation).

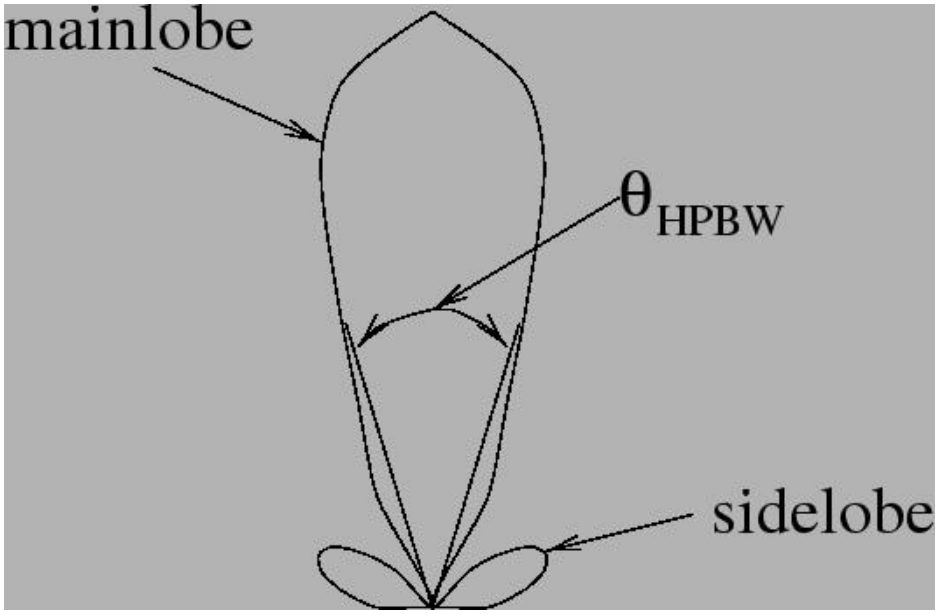

Figure 2.8 A typical schematic power pattern of an antenna (Chengalur, Gupta & Dwarakanath, 2007).

Whatever the use of the antenna, transmitting or receiving, its pattern remains the same. This means that if an antenna efficiently transmits in certain directions, it will also efficiently

receive in those directions. This property of an antenna is known as reciprocity.

2.6 The need for interferometry

Radioastronomers observe at longer wavelengths than do optical astronomers. Since the angular resolution is expressed by Rayleigh's criterion

$$\theta \approx \lambda / D \tag{2.34}$$

where D is the aperture size and λ is the wavelength of observation, a single radio dish typically has very poor resolution.

Chengalur, Gupta & Dwarakanath (2007) states that the necessity to reach better angular resolution at radio frequencies has resulted in the development of large instruments that work at smaller wavelengths. Higher resolutions can be accomplished either with the increase of the telescope's diameter (which is not functional) or with the decrease of the observing wavelength. Due to the second option, radio telescopes working in the wavelength range of cm to mm achieve higher resolution (Chengalur, Gupta & Dwarakanath, 2007). However, to achieve resolutions comparable to optical telescopes, the radio aperture have to be $>$ 100 km in size.

Radio interferometry can be approached via the Van Cittert-Zernike theorem (See Chengalur, Gupta & Dwarakanath (2007) for a derivation), which describes how the spatial coherence function

$$V(r_1, r_2) = \langle E(r_1) E^*(r_2) \rangle \tag{2.35}$$

is related to the spatial distribution of the intensity of the approaching radiation, $I(s)$. The theorem establishes that that if all the measurements are in a plane, then the spatial correla-

tion function $V(r_1, r_2)$ is just the Fourier transform of the spatial distribution of the intensity of the source

$$V(r_1, r_2) = F\{I(s)\}. \tag{2.36}$$

Radioastronomers often refer to the spatial correlation function $\langle E(P_1)E^*(P_2)\rangle$ as the "visibility"

$$V(u, \upsilon, w) = \int I(l,m) e^{-i2\pi[lu+m\upsilon+nw]} \frac{dldm}{\sqrt{1-l^2-m^2}} \tag{2.37}$$

This relation between the source intensity distribution, which a radioastronomer is trying to map, and the visibility, which s/he observes, is the fundamental relation of radio interferometry and is known in the literature as the Van Cittert-Zernike theorem. The above equation is not a Fourier transform relation between the visibility and the brightness distribution as the visibility here is a function of three variables (u,v,w) and the brightness distribution is a function of only two variables, $(l\&m)$. For observations in the U-V plane (coplanar array), a coordinate system can be chosen such as $w = 0$, and the above equation turns out to be a 2-D Fourier relation, reducing to

$$V(u, \upsilon) = \int \frac{I(l,m)}{\sqrt{1-l^2-m^2}} e^{-i2\pi[lu+m\upsilon]}\, dldm, \tag{2.38}$$

implying that the visibility $V(u, \upsilon, w)$ is nothing but the Fourier transform of the source (modified) brightness distribution

$$\frac{I(l,m)}{\sqrt{1-l^2-m^2}}, \tag{2.39}$$

where (u, υ) defines the co-ordinates system of antenna spacings, (l,m) defines cosines in the (u, υ) co-ordinates system. Further details can be found in standard textbooks (Chen-

galur, Gupta & Dwarakanath, 2007, e.g.).

2.7 Aperture synthesis

As we saw previously, the measured visibility obtained by a radioastronomer is simply the Fourier transform of the source brightness distribution $I(\theta,\phi)$. A single Fourier component of $I(\theta,\phi)$ is obtained from correlating the voltage picked by any two of the radio antennae of the interferometer (Chengalur, Gupta & Dwarakanath, 2007). If we have an adequate number of observations from independent pairs of antennae, the source brightness distribution may be acquired by Fourier inversion, resulting in a "map" of the sky (Chengalur, Gupta & Dwarakanath, 2007).

The radio sky, apart from a few exceptions, is constant with time. This means that all the Fourier components are not required to be measured at the same time. Thus what can be done is to calculate all the Fourier components that are needed with only two antennae: one could be fixed and the other movable, or both movable. This method of assembling all the Fourier components needed to reconstruct the image the source is called "*aperture synthesis*" (Chengalur, Gupta & Dwarakanath, 2007). In practice, the fact that the Earth rotates is used to model the U-V plane: the vector joining two antennas as seen from a distant cosmic source, is continuously changing (see Figure 2.9) progressively sampling the U-V plane. In an actual observation, one measures the Fourier components up to a certain length of baseline, and then an image can be created with an effective aperture size corresponding to the longest baseline.

Short baselines can create a low resolution image, which can be used to image large-scale structures in the source, while longer baselines, which can create a high resolution, are sensitive to fine-scale structure. This is a result from the inverse relationship of Fourier

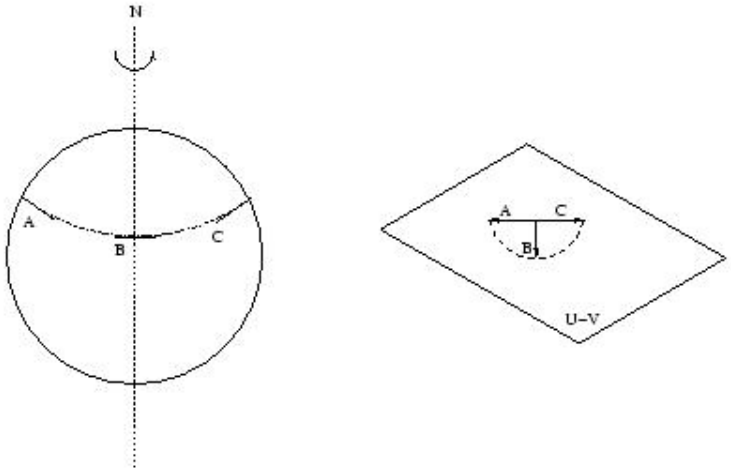

Figure 2.9 The trace in the U-V plane of the vector joining two antennae situated along East-West, due to the Earth's rotation (Chengalur, Gupta & Dwarakanath, 2007).

compound variables (Chengalur, Gupta & Dwarakanath, 2007). To create an image which has both large-scale and finer features, one thus needs a combination of observations corresponding to a whole range of baselines.

2.8 Radio Frequency Interference

Radio Frequency Interference (RFI) is the most inhibiting source of difficulty for radio-astronomical observations at low frequencies. There are two types: broadband and narrowband. Broadband RFI covers a wide range in frequencies and is commonly caused as a secondary effect of electrical objects. Power transmission lines and electric motors are two causes of broadband RFI. This type of RFI is most damaging to observations as it covers most of the observational band and is more difficult to remove from data.

On the other hand, narrowband RFI is usually more powerful and affects only a small frequency range. Examples of narrowband RFI are from intentional transmissions such as radio, TV stations and mobile phones.

2.9 Radio imaging at low frequencies with GMRT

The data taken from GMRT were reduced using the NRAO Astronomical Image Processing System (AIPS) package. The recorded observations have initially to be converted into a format applicable to AIPS. GMRT data, written in the Long Term Accumulation format (LTA format), contain the visibility data from each antenna. Then this is converted to the Flexible Image Transport System (FITS) format which is on average at the size of three GB for a six hour observation time with an integration time per visibility of 16.9 sec. The FITS file afterwards can be imported into AIPS and the great advantage of the data analysis here is that the original FITS file remains as it is. This means that the editing we will explain that is done, does not alter the original FITS file but is applied on the file through separate 'tables' that one creates. The data set that will be used afterwards as an example, is the analysis that was done for the galaxy NGC 5982.

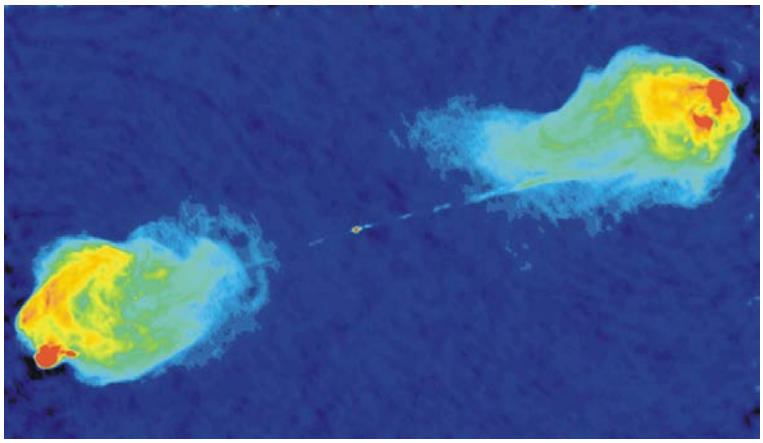

Figure 2.10 Radio image of the jet and lobes in the ultra-luminous radio galaxy Cygnus A at 5 GHz from VLA. This is a false colour image: red represents regions with the brightest radio emission, and the bluer regions are fainter. [http://images.nrao.edu/AGN/Radio_Galaxies/260].

The case that we deal with here is radio emission from individual galaxies residing in groups. By concentrating on low-frequency radio properties, past as well as present activity can be seen. As galaxies properties change in time and according to their environment, the

results of the radio emission analysis vary. A detection of huge jet is possible (Fig. 2.10), diffuse radio emission from star forming regions as well as a very small scale jet seen in radio emission. The best case of radio detection is shown in Fig. 2.10 where Cygnus A, a powerful radiogalaxy in the Cygnus A cluster is a typical Fanaroff-Riley type II radio source. The very narrow jets and enormous distinct lobes can be clearly seen. Particles are accelerated in diffusive shocks in the huge hotspots (Carilli et al., 1991). Combination with X-rays reveals the interaction with the intergalactic medium.

2.10 Primary flux and phase calibrators

The observations at GMRT are done with a periodical switch between the source and the calibrators (see Figure 2.11). It is very important to find the right calibrators because information such as the flux density of our source and the effects of ionosphere in our data can be calculated. Calibrator observations are not only used to reveal instrumental phase and gain changes, ionospheric gain and phase variations, but also for tracking the quality of the data and the random gain and phase alterations.

In the reduction of interferometric data at radio frequencies, one needs to employ observations of two kinds of calibration sources: phase calibrators and flux calibrators (see Figure 2.11). These are chosen to be near the source being observed, so that frequent calibration observations can be made during the scientific observation. There are a handful of flux calibrators, which are usually 3C sources which are constant with time, or in the worst scenario vary only very slowly compared to the duration of the observation. These are sources for which fluxes are known to a great degree of accuracy, and also such that they are not resolved into multiple sources by the standard arrays. (A good example is 3C 286, which is well-measured and not variable, but is resolved by the VLA).

The antenna based complex gains can vary on timescales of tens of minutes. The relative phase and amplitude variations between the antennas, therefore, have to be corrected so that the phase and amplitude of all the antennas of the array being usedm is constant over the many hours of observation. These slow variations are measured and corrected using periodic observations of secondary calibrator, which are known as phase calibrator. These observations have to be done very often. In our observations, we have taken flux calibrator observations at the beginning and end of each observing session, but phase calibrator observations every half an hour.

```
                                                                  Source summary
Scan      Source      Qual  Calcode Sub         Timerange          FrqI   Velocity type = 'TOPOCENT'    Definition = 'RADIO   '
D
   1 3C147          : 0000           1  1/13:28:42 -   1/14:00:38         ID Source          Qual  Calcode RA(2000.0)     Dec(2000.0)  No. vis
1                                                                          1 3C147          : 0000          05:42:36.1298  49:51:07.164   52200
   2 1311-222       : 0000           1  1/14:10:18 -   1/14:14:36         2 1311-222       : 0000          13:11:39.3343 -22:16:41.725   69600
1                                                                          3 ESO507-25      : 0000          12:51:31.8042 -26:27:07.026  269700
   3 ESO507-25      : 0000           1  1/14:18:37 -   1/14:59:58         4 NGC5153        : 0000          13:27:54.3044 -29:37:05.024  271440
1                                                                          5 3C286          : 0000          13:31:08.2443  30:30:32.530   16095
  25 NGC5982        : 0000           1  1/23:13:38 -   1/23:55:15         6 1449+632       : 0000          14:49:21.7252  63:16:14.440   46980
1                                                                          7 NGC5982        : 0000          15:38:39.8050  59:21:20.953  384540
  26 1449+632       : 0000           1  1/23:56:51 -   2/00:01:25         8 3C48           : 0000          01:37:41.3139  33:09:35.174   42630
1
  27 NGC5982        : 0000           1  2/00:04:55 -   2/00:46:31         ID Source          Freq(GHz) Velocity(Km/s) Rest freq (GHz)
1                                                                          1 3C147             0.6290         0.0000          0.0000
  28 1449+632       : 0000           1  2/00:47:52 -   2/00:52:25         2 1311-222          0.6290         0.0000          0.0000
1                                                                          3 ESO507-25         0.6290         0.0000          0.0000
  29 NGC5982        : 0000           1  2/00:56:11 -   2/01:16:35         4 NGC5153           0.6290         0.0000          0.0000
1                                                                          5 3C286             0.6290       -62.0628          0.0000
  30 1449+632       : 0000           1  2/01:18:44 -   2/01:23:34         6 1449+632          0.6290         0.0000          0.0000
1                                                                          7 NGC5982           0.6290         0.0000          0.0000
  31 NGC5982        : 0000           1  2/01:24:54 -   2/02:14:02         8 3C48              0.6290       -31.0330          0.0000
```

Figure 2.11 Task 'listr' in AIPS showing the total time of observation, the visibilities and the coordinates of the sources and the calibrators that were used.

In Figure 2.11 we can see that in the start of the observation for NGC 5982 the primary flux calibrator 3C147 that was used, is observed for ≈ 30 minutes before the phase calibrator and target source are changed back and forth. The number of visibilities for the primary flux calibrator in this case are 52200 and for the target source 384540. We see that our observation ends up with a different flux calibrator, 3C48, because obviously the previous one has set.

2.11 Flagging & Calibration

One of the most important procedures in radio data analysis is 'flagging'. This is the process of marking bad data such as RFI, so that they are not included in our image in the final product. 'Flagging' begins by deleting the visibilities that have great phase difference in the flux calibrator and is then applied to the phase calibrator and our source of interest. As visibilities, we call the Fourier transform of the sky brightness distribution. This is repeated with the phase calibrator. If bad data exist in the observations of the calibrators, this means that they will also exist in our source observations as well. The same procedure is followed by checking the amplitude data. Data with huge amplitude difference in an antenna are also flagged here.

Phase difference between successive visibilities is used as a task of 'goodness' of our data. If an antenna is working properly the phase will be stable -an actual value of it- but the difference must be close to 0. On the other hand if an antenna is not working, the actual phase will be random -noise- so the phase difference will also be random and $\neq 0$. This condition cannot be applied to actual sources but only to calibrators, because they are point sources. The task where we can spot and delete bad data is called 'TVFLG' (see Fig. 2.12). In tvflg usually we have 256 or 512 channels and flagging is applied immediately to all channels. It is preferable while flagging to delete as many bad data as you can even if that means deleting many good data as well.

After the initial flagging of the data is finished, in the order we mentioned, they are calibrated. The task 'CALIB' is first used on the observation of the flux calibrator, which yields the conversion factor between the observed quantity of the flux calibrator and its known absolute flux. The same task is then applied on the phase calibrator. The task 'CALIB' is used to create phase and amplitude solutions for the observed data set, and to quantify the

unwanted features that were added to the signal by the atmosphere and the environment of the instruments. These solutions are stored in an SN (solution) table, and eventually will be applied to the data in a CL (calibration) table. There are various solution types and the solution interval can vary as well. For the solution type we used (L1R) the weighted sum of the moduli of the residuals is minimized with robust iteration. This way the computed gain solutions are less influenced by 'bad' data points, but there is some loss of statistical efficiency. A big solution interval (e.g. 1 min) means that the variance in ionosphere might not be tracked, and too small leads to bad signal-to-noise ratio. The solution mode used was for both amplitude and phase (A&P). The tool that we can use here to check our calibration is the 'SNPLT' (solution plot). The 'SNPLT' tool is used in order to see that the phase slope

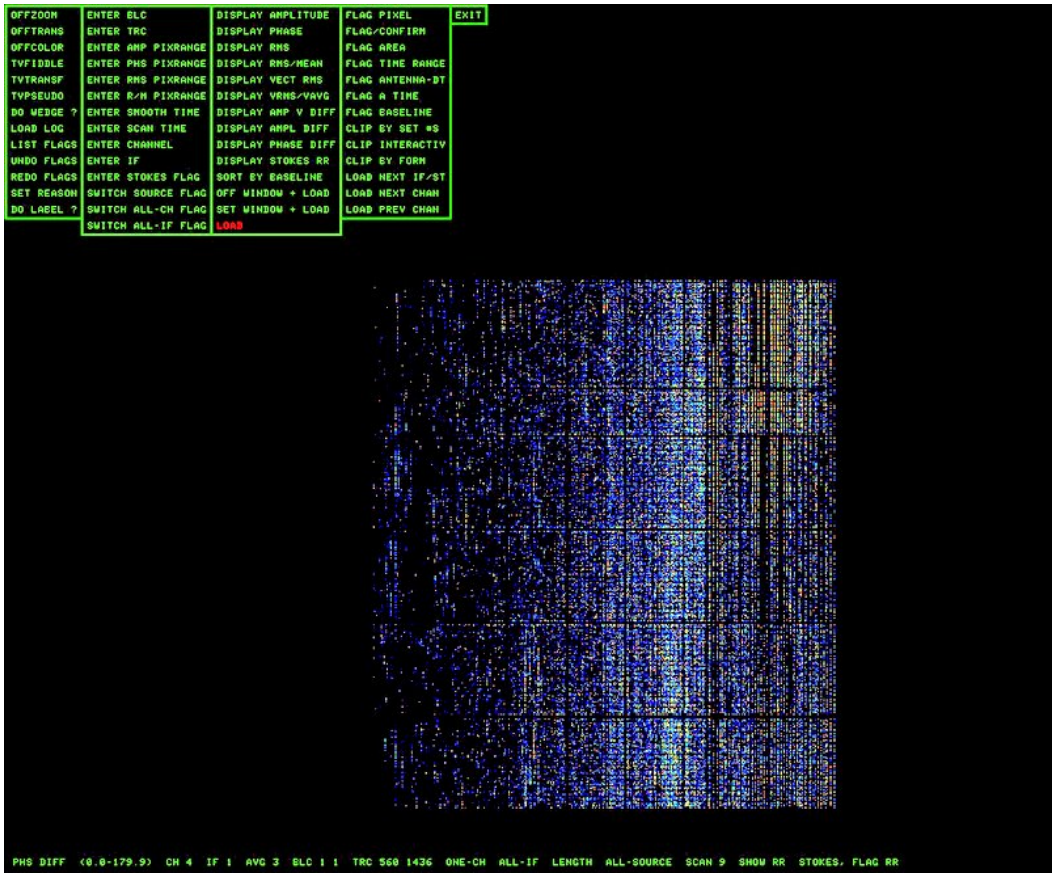

Figure 2.12 Interactive flagging tool, 'TVFLG'. The difference between phase and the average over a small period of time is plotted. Phase difference here is high thus flagging is required.

is horizontal. If it is, then the calibration applied is acceptable (see Fig. 2.13).

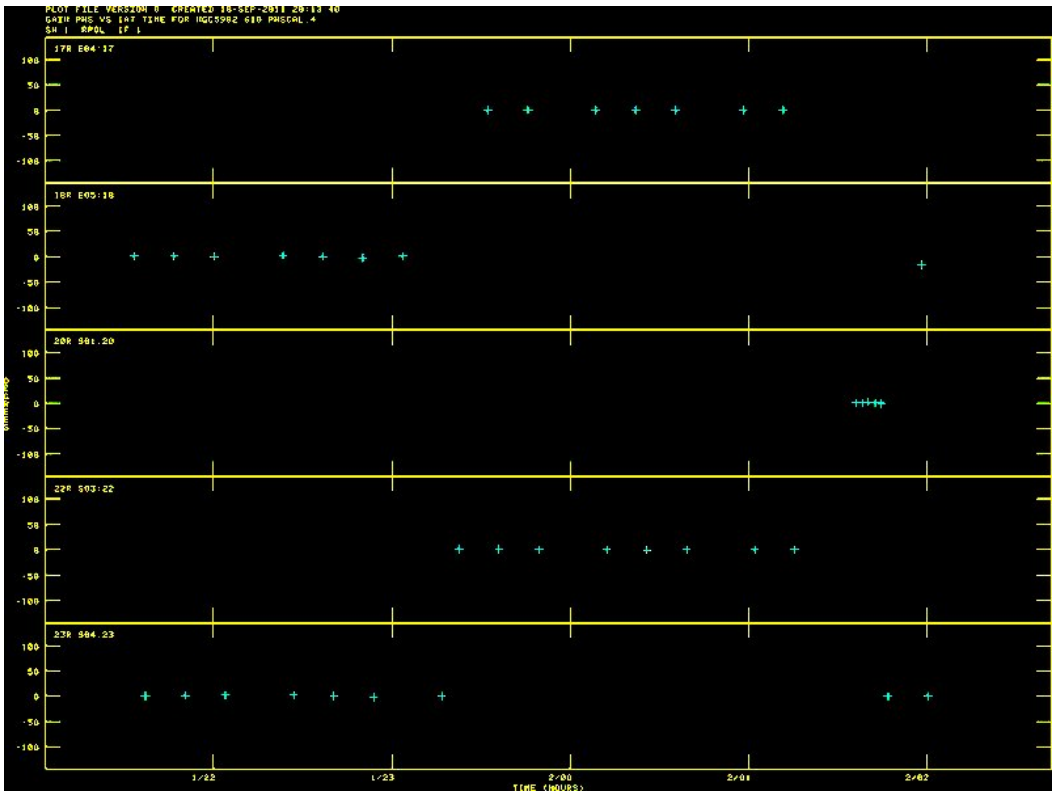

Figure 2.13 The 'SNPLT' tool with a solution interval of 0.5 min. Phase is shown on the y-axis and time on the x-axis. Only the target source NGC 5982 is shown here.

Afterwards the task 'GETJY' is run in order to derive the flux of the phase calibrator. Then this flux is compared to the VLA Calibrator Manual where there is a list of fluxes of the different phase calibrators [1]. Then a bandpass is created which is the relative gain of an antenna -baseline- as a function of frequency. What the bandpass table does is normalise the visibilities so that each frequency channel can be compared easily. This actually means relating the amplitude difference between all the channels according to the one that was calibrated. The ideal case is a completely linear relation but any channels with large spikes due to strong RFI at a specific frequency can be easily seen and flagged (see Fig. 2.14). The plot seen in Figure 2.14 is after flagging the bad channels. Many spikes can be seen on each

[1] http://www.vla.nrao.edu/astro/calib/manual/csource.html

channel, but this is normal because as we can see the variations here in amplitude are in the order of 4 mJy.

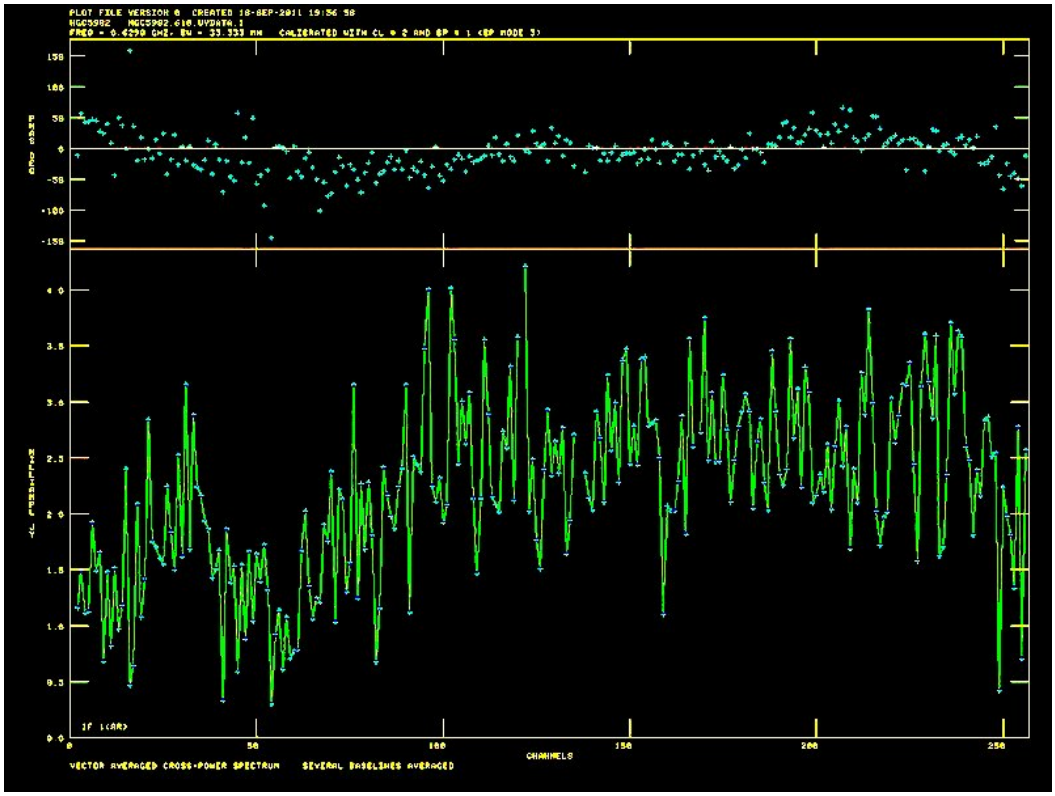

Figure 2.14 Observations across the whole bandwidth: the Channel number is on the x-axis and amplitude is on the y-axis. Amplitude variation is insignificant here, and phase is, as seen on top plot, very smooth as well.

Subsequently, the 256 or 512 channels that we have, of 125 KHz each, are averaged so as to increase the signal-to-noise ratio. So we end up having usually 8 channels of $\sim$2 MHz each. Attention must be given to the number of the collapsed channels here. If too many channels are collapsed then we will have a bandwidth smearing. Bandwidth smearing is an effect that occurs because in this process, one assumes for visibility data that the observations were made at one frequency ν_o, namely the central frequency of the band, instead of a frequency range $\Delta\nu$. So for the rest of the frequencies one gets different (u,v) values, and averaging them is equivalent to averaging visibilities in the radial direction

of the (u,v) plane. This affects the sources which are located far from the centre of the image. These sources at the edges of the image are radially smeared with some of their flux distributed throughout the image, increasing the noise. Finally these collapsed channels are calibrated as previously until there are good solutions. Once the u-v data have been merged and calibrated, the imaging stage can begin.

2.12 Imaging

In an aperture synthesis array there are a finite numbers of antennas. This means that there are also a finite number of points for the visibilities to be measured in the uv-plane (Chengalur, Gupta & Dwarakanath, 2007). The Fourier transforms (FT) of the visibilities are used to obtain the *Dirty Map*, and the Fourier transform of the weighted uv-sampling function is used to obtain the Dirty Beam (Chengalur, Gupta & Dwarakanath, 2007). To do this in a reasonable amount of time, an efficient FFT algorithm needs to be employed.

In Chengalur, Gupta & Dwarakanath (2007) it is shown that in an aperture synthesis interferometer, the relation between the measured visibility V and the sky brightness distribution of the source I is

$$V \cdot S \rightleftharpoons I, \tag{2.40}$$

where $\rightleftharpoons$ corresponds to the FT and S is the uv-sampling function.

Since in reality there is only a specific number of antennas, the uv-plane is sampled at a discrete number of values and Eq. 2.32 has to be recast as

$$V \rightleftharpoons I * DB(= I^D), \tag{2.41}$$

where I^D is the *Dirty Map*, representing the raw image. Also, I is the actual brightness

distribution, *DB* is the *Dirty Beam*, representing the transfer equation of the telescope used as an imaging device. *S* is the sampling function in the *uv*-plane, given by

$$S(u,v) = \sum_k \delta(u-u_k, v-v_k), \tag{2.42}$$

where u_k, v_k are the measured (u,v) points.

Simply put, Chengalur, Gupta & Dwarakanath (2007) explains that the *Dirty Map* is a product of the combination of the true brightness distribution of the source and the *Dirty Beam* of the telescope. The resultant I^D is not the desired result, because if there is a strong source in the field, side-lobe artefacts resulting from diffraction patterns will appear as a consequence of the unsampled points in the uv-plane. This means that the flux in the *Dirty Map* is not where it should be and de-convolution is needed. The final de-convolution is the process that effectively attempts to estimate I from I^D, so that the quantity $(I-I^D)*DB$ is minimised, without changing the noise characteristics in the map (Chengalur, Gupta & Dwarakanath, 2007).

What is actually done is that everytime a box is put on a local flux maximum in the dirty map it removes 10% of the flux of the peak the box was put on. Then this flux is placed to a new 'clean table' and the same thing is repeated until the stage that nothing is left behind. This way, by removing the flux of your 'brightest sources' you end up 'seeing' more noise -lower flux signals- until you are left with just noise. Then one has an array of point sources, which are known as the CLEAN components (CC). These, all gathered in a so called CC table, when convolved with the dirty beam, will result to the dirty map. Finally, each point is put in the place of a so-called 'CLEAN' beam (Gaussian), which is implying that the sky brightness, convolved with this beam, has been obtained (Chengalur, Gupta & Dwarakanath, 2007).

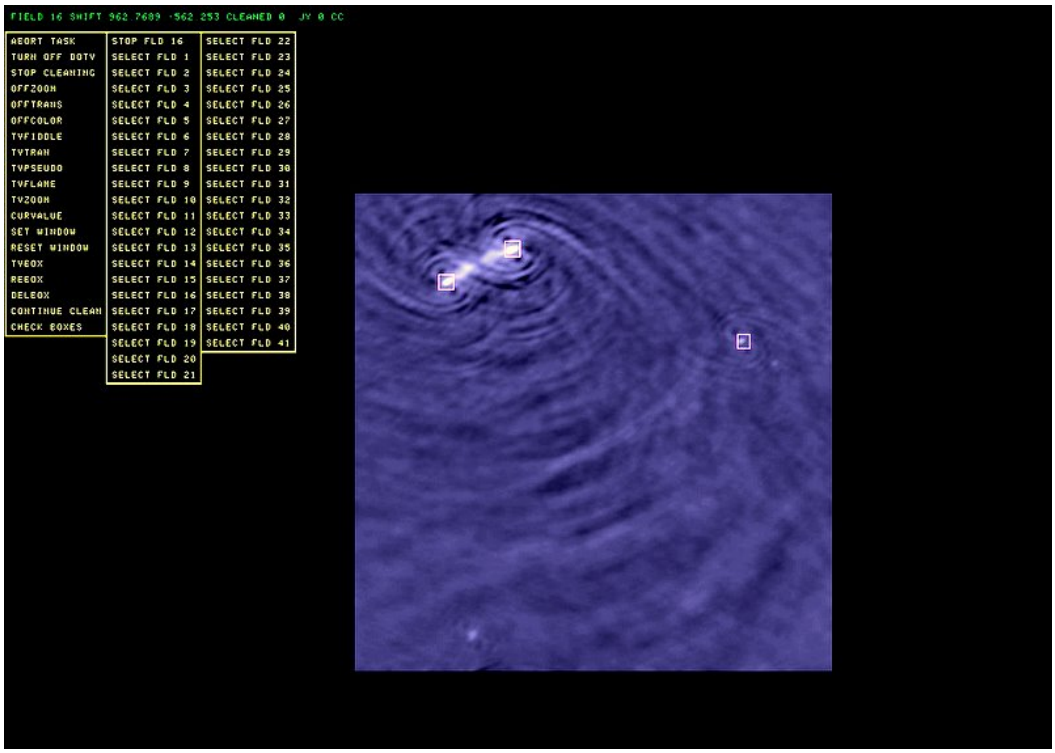

Figure 2.15 Interactive imaging task ‘IMAGR’. The boxes drawn around the visible sources are seen.

The only imaging task in AIPS used is called ‘IMAGR’ and the algorithm that was described earlier and is used is the CLEAN algorithm. In Fig. 2.15, the use of the task ‘IMAGR’ and the use of the CLEAN algorithm described.

In the case where different, widely-spaced frequencies constitute a single image, the differences in the primary beam size can vary significantly with frequency. This rises a problem in ‘cleaning’ objects away from the pointing center causing the subtraction of the combined model from the visibility data at the different frequencies to be incorrect due to the variations in the primary beam. For this reason residuals will appear in the visibility data that cannot be cleaned properly as the data does not correspond to a possible sky brightness distribution. By using the correction control parameters (IMAGRPRM(1) > 0) a correction is made in the subtraction to remove the effects of the frequency dependence of the primary

beam.

2.13 Self-calibration

Self-calibration uses the image just created in IMAGR as a model to help derive the telescope gains and hence minimise the differences between the model's visibilities and the observed ones. So self-calibration involves minimising

$$S = \sum_{k} \sum_{i,j,i\neq j} \left| V_{ij}(t_k) - g_i(t_k) g_j^*(t_k) \cdot V_{ij}^M(t_k) \right|^2, \tag{2.43}$$

where S is the Fourier transform of the source, g_i, g_j are the telescope gains, $V_{ij}(t_k)$ the observed visibilities and M the number of the antennas.

Self-calibration in AIPS is done by using the task 'CALIB' whereas imaging and selfcal iterations are repeated until a satisfactory final image is produced. In order to have a better image used for the model, one can flag again from 'TVFLG' only the source and use new amplitudes in order to get rid of any residual noise. So high amplitudes in tvflg'TVFLG' will show remaining RFI in the data.

As a summary, the steps that are theoretically used for self-calibration are:

1) Create an initial model of the source using preliminary calibration and acceptable source structures.

2) Solutions for complex gains are found using Eq. 2.35.

3) Find the corrected visibility $V_{ij,corr}(t) = \frac{V_{ij}(t)}{g_i(t) g_j^*(t)}$.

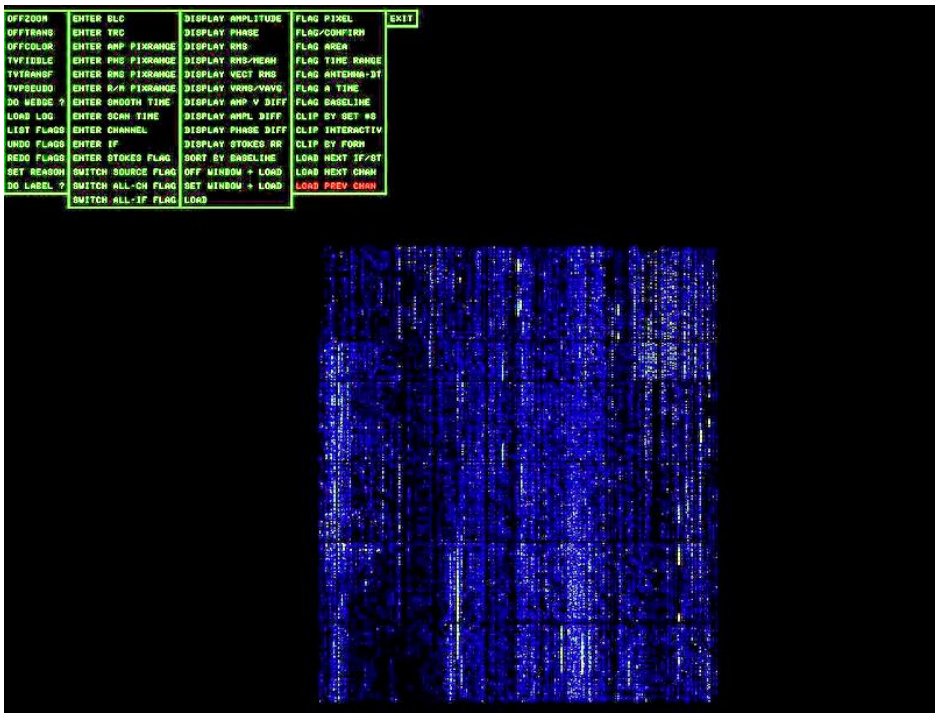

Figure 2.16 Here amplitudes are shown, where one obvious RFI spike can be spotted. Baselines are on the *x*-axis, amplitudes in *y*-axis and the colour is related to the amplitude.

4) Form a new model from the image made from the corrected data.

5) Repeat from 2 unless satisfied.

(Source:Radio Astronomy School (RAS) lectures notes ‘Self-calibration in Radio astronomy’ by Subhashis Roy)

Chapter 3

New insights into the evolution of the FR I radio galaxy 3C 270 (NGC 4261) from low frequency GMRT radio observations

Author: Konstantinos Kolokythas et al.

Konstantinos Kolokythas,[1] **Ewan O'Sullivan,**[2,1] **Simona Giacintucci,**[3,4] **Somak Raychaudhury,**[5,1] **C.H. Ishwara-Chandra,**[6] **Diana M. Worrall**[7,2] **and Mark Birkinshaw**[7,2]

[1]*School of Physics and Astronomy, University of Birmingham, Birmingham B15 2TT, UK*

[2]*Harvard-Smithsonian CfA, 60 Garden Street, Cambridge, MA 02138, USA*

[3]*Department of Astronomy, University of Maryland, College Park, MD, 20742-2421, USA*

[4]*Joint Space-Science Inst., University of Maryland, College Park, MD, 20742-2421, USA*

[5]*Department of Physics, Presidency University, 86/1 College Street, 700 073 Kolkata, India*

[6]*National Centre for Radio Astrophysics, TIFR, Ganeshkhind, Pune 411 007, India*

[7]*HH Wills Physics Laboratory, University of Bristol, Tyndall Avenue, Bristol BS8 1TL, UK*

(The work that is presented in this Chapter is from the study of 3C 270 radio source that has been submitted for publication in the Monthly Notices of the Royal Astronomical Society (MNRAS) with archive id number: MN-14-1422-MJ. The JP model fitting for this analysis was perfomed by the co-author Dr. Simona Giacintucci using the package Synage.)

3.1 Abstract

We present *Giant Metrewave Radio Telescope* (GMRT) 240 MHz observations of the nearby luminous FR I radio source 3C 270, in the group-central elliptical NGC 4261. Combining these data with reprocessed *Very Large Array* (VLA) 1.55 and 4.8 GHz observations, we produce spectral index maps that reveal a constant spectral index along the jets and a gradual steepening from the ends of the jets through the lobes towards the nucleus. A Jaffe & Perola (JP) model fitted to the integrated spectrum of the source gives an asymptotic low-frequency index of $\alpha_{inj} = 0.53^{+0.01}_{-0.02}$, while JP models fitted to the observed spectral index trend along the lobes allow us to estimate radiative ages of ~ 29 Myr and ~ 37 Myr for the west and east lobes respectively. Our age estimates are a factor of two lower than the 75-Myr upper limit derived from X-ray data (O'Sullivan et al., 2011). We find unlikely the scenario of an early supersonic phase in which the lobe expanded into the ISM at approximately Mach 6 (3500 km s^{-1}), and suggest that either the source underwent multiple AGN outbursts with possible large changes in jet power, or possibly that the source age that we find is due to a backflow that transports young electrons in the lobes towards the nucleus relatively quickly. We calculate that in the lobes the energy ratio of non-radiating to radiating particles is $\sim 4-24$ indicating significant gas entrainment. If the lobes are in pressure balance with their surroundings, the total energy required to heat the entrained material is 10^{58} erg, $\sim$40% of the total enthalpy of the lobes.

3.2 Introduction

The study of radio galaxies has become increasingly important as they appear to be natural laboratories uniquely suited to the study of one of the most energetic phenomena in the

Universe: relativistic jets arising from the associated active galactic nuclei (AGN). The reason this phenomenon is so important is that radio-loud activity of the central AGN is now considered to be the most likely source of the heating mechanism injecting energy into the hot gaseous halos of groups and clusters of galaxies, thereby balancing the effects of radiative cooling (Fabian 2012; McNamara & Nulsen 2007; Peterson & Fabian 2006).

The evolution of radio galaxies is commonly accepted to pass through three phases as described in Kraft et al. (2007). In the beginning, the inflation of the lobes surrounding the jets is highly supersonic as the lobes appear to be significantly over-pressured in relation to the ambient medium. After this early, in most sources short-lived, supersonic phase, the expansion of the lobes continues and the pressure in the lobes drops, approaching equilibrium with the ambient gas, with the weak shock of the lobe expansion sometimes observable in the X-ray emission as a surface brightness discontinuity (e.g. in 3C 310, Kraft et al. 2012 and PKS B2152-699, Worrall et al. 2012). In the final phase the bubble eventually becomes unobservable due to energy loss via adiabatic expansion and perhaps thermal conduction.

The effects of the complex interactions between the relativistic plasma of the radio lobes and the thermal, X-ray emitting gas of the intra-cluster or intra-group medium (IGM) are very evident in our local Universe. In several cases the environments of radio galaxies observed in groups and clusters show X-ray disturbances in the IGM by driving shocks (Nulsen et al. 2005; Fabian et al. 2006; Forman et al. 2007; David et al. 2011) and inflating cavities (e.g. Bîrzan et al. 2008; O'Sullivan et al. 2011; Fabian 2012).

Present knowledge of the physical processes acting behind this phenomenology is still rather poor. In order to understand how AGN feedback works, the combination of high-quality X-ray data and high-sensitivity radio observations is essential. X-ray observations provide information on the physical properties of the environment surrounding the radio

source, most notably the pressure of the IGM that the radio lobes are expanding into, and allow dynamical estimates of the expansion timescale and AGN power output. Multi-frequency radio data provide information on the cycle of jet activity, including independent estimates of the source expansion timescale and indications of the physical mechanisms of energy injection (Giacintucci et al., 2008, 2012).

With this aim we have chosen to examine NGC 4261, a nearby galaxy which has an active galactic nucleus that contains a supermassive black hole of $(4.9\pm1.0)\times10^8 M_\odot$ (Ferrarese, Ford & Jaffe, 1996) and hosts the low-power FR I radio source 3C 270. It is the brightest elliptical in a poor group (Forbes et al., 2006) projected onto the outskirts of the nearby Virgo cluster. Its proximity means that its features can be observed with good sensitivity and linear resolution, allowing detailed study of the energetics of lobe inflation.

3C 270 is composed of highly symmetric kiloparsec-scale twin jets (Birkinshaw & Davies, 1985) with previous jet modelling studies indicating they lie close to the plane of the sky ($64^\circ - 76^\circ$; Piner et al. 2001, Laing & Bridle 2014), extending also on a scale of tens of kiloparsecs into the intragroup medium (IGM) (Worrall et al., 2010). The jets emanate from a compact radio core coincident with the optical nucleus of the galaxy (Jones & Wehrle, 1997), where optical spectroscopy revealed a low-ionization nuclear emission-line region (Ho, Filippenko & Sargent, 1997). In addition, a nearly edge-on nuclear disk (100-pc-scale) rich in dust, molecular and atomic gas (Jaffe et al., 1993), lies orthogonal to the orientation of the radio jets (Tremblay et al., 2009). In Laing & Bridle (2013) the average spectral index at the base of the main jets is found to be steepening from $\sim$0.55 to $\sim$0.7 in a distance between $9-12''$ from the nucleus.

In the X-ray band, ROSAT images of the NGC 4261 group show diffuse thermal emission and a non-thermal nuclear component at low energies (Worrall & Birkinshaw, 1994).

Chandra observations reveal the existence of internal X-ray jets (at the order of a few kpc) enclosed by the radio jets (Gliozzi, Sambruna & Brandt, 2003; O'Sullivan et al., 2011; Zezas et al., 2005) suggesting that the cause of jet X-ray emission is synchrotron radiation which exhibits along the jet, areas of low surface brightness (Worrall et al., 2010).

More recent analysis of the *Chandra* and *XMM-Newton* data in O'Sullivan et al. (2011) shows a lot of systematic organisation in the gas in which the galaxy resides. O'Sullivan et al. (2011) notes that the AGN jets gave rise to two lobes, generating cavities in the IGM and constructing peripheral lines of compressed hot gas that nearly completely surround the lobes. The cavity peripheral lines (rims) consist of material that has been picked up and compressed by the expansion of the lobes, weakly heated by compression with no evidence of shock heating (O'Sullivan et al., 2011). NGC 4261 hosts a small cool core with radius $\sim$ 10 kpc and a temperature of $\sim$ 0.6 keV, with the IGM temperature in the group being $\sim$ 1.6 keV (Humphrey et al., 2009). The structure of the core has been obviously changed by the inflation of the radio lobes and is not spherically symmetric (O'Sullivan et al., 2011), with wedge-shaped surface-brightness decrements that suggest the jets have driven out the IGM gas from conical regions around their first few kiloparsecs (Worrall et al., 2010).

Proof of a non-isotropical distribution in the globular cluster of NGC 4261 is noted to be seen by many previous studies (e.g., Giordano et al. 2005, Bonfini et al. 2012, D'Abrusco et al. 2013) while the study of optical wavelengths has exposed the existence of a weak emission in the rear end to the north-west and a fan to the southeast of the galaxy (Tal et al., 2009). The aforementioned characteristics suggest that NGC 4261 went through merging or tidal interactions with another system in the near past (1-2 Gyr) (O'Sullivan et al., 2011).

In this paper we present a detailed low-radio-frequency spectral study of the galaxy NGC 4261. Previous studies have left the question of the radiative age of the source unclear

Table 3.1 Details of the GMRT radio observations

Project Code	Observation date	Frequency (MHz)	Bandwidth (MHz)	Integration time (min)	HPBW[a], PA (full array, $''\times''$, $^\circ$)	rms mJy b^{-1}
15KMH01	2009 Feb 15	610	32	270	7.32×4.77, 76.62	1
15KMH01	2009 Feb 15	240	16	270	15.30×11.00, 67.17	1.6

[a]Using uniform weighting

and with our study will try to resolve this problem. Our work is based on archival data from the Giant Metrewave Radio Telescope (GMRT) at 610 MHz and 240 MHz and the Very Large Array (VLA) at 1.55 GHz and 4.8 GHz. The primary targets of this work include the estimation of the radiative age of 3C 270 and the understanding of the energetics and dynamics that govern the interaction between the relativistic plasma of the source's radio lobes and the X-ray emitting gas following O'Sullivan et al. (2011). The paper is organised as follows. In Sections 2 and 3 we describe the GMRT and VLA archival data used and the data reduction approach. The radio images are presented in Section 4. In Section 5 we derive its physical parameters. In Section 6 we discuss the X-ray properties of the galaxy's environment in the context of its radio properties. The summary and conclusions are finally presented in Section 7.

We adopt a distance to NGC 4261 of 31.3 Mpc, which gives an angular scale of $1'' = 0.151$ kpc. This is consistent with the distance adopted by Worrall et al. (2010) and negligibly different from the distance adopted by O'Sullivan et al. (2011) who used an angular scale of $1'' = 0.153$ kpc for their X-ray analysis. When correcting for redshift we adopt a value of z=0.007378 (Cappellari et al., 2011). The radio spectral index α is defined according to $S_\nu \propto \nu^{-\alpha}$, where S_ν is the flux density at the frequency ν.

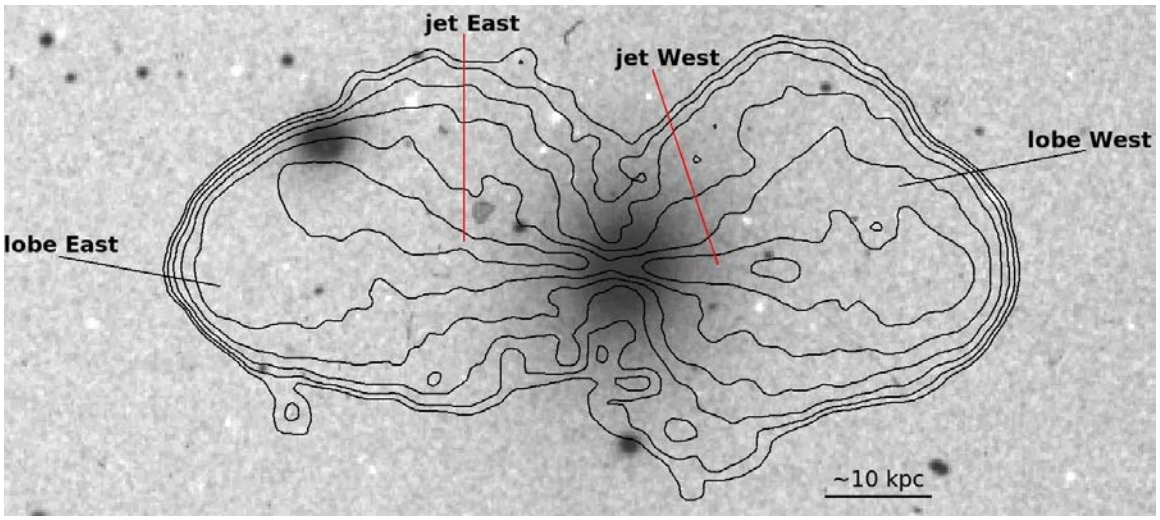

Figure 3.1 GMRT 240 MHz radio contours of 3C 270, overlaid on the r band optical image from the Digitized Sky Survey (DSS). The contour levels (black) start at 4σ and rise by factor of 2. The 1σ level in the radio image is ~ 1.6 mJy beam^{-1}. Labels indicate the individual components of the radio source. Restoring beam: $\sim 15.30 \times 11.00$, P.A.= 67.17°.

3.3 GMRT observations and data reduction

NGC 4261 was observed using the GMRT at 240 MHz and 610 MHz with total integration time of 4.5 hours in each band. At 610 MHz the data were recorded using the lower and upper side bands (LSB and USB respectively) for an observing bandwidth of 16 MHz each. For the 240 MHz data only one correlator was used to record the data in a total observing bandwidth of 16 MHz where only half of the data were useful. Data for both frequencies were collected with 256 channels at a spectral resolution of 125 kHz per channel. The data were analysed and reduced using the NRAO Astronomical Image Processing System (AIPS) package. We summarize the details of the observations in Table 1, where we report the observing date, frequency, total observing bandwidth, total time on source, half-power beamwidth (HPBW) of the full array and rms level (1 σ) at full resolution.

The data were edited to remove bad antennas and other obvious defects. Initially the phase and flux calibrators were checked and the data with extreme phase difference were

removed. This procedure was also applied to our source. The flux density scale was set to the best VLA values (2010) using the task SETJY. Then the data were calibrated and the flux density scale was defined using the amplitude calibrators 3C 286 and 3C 147. The point source 1330+251 was used as phase calibrator for both 610 and 240 MHz. Bandpass calibration based on 3C 147 was applied, which relates the amplitude difference between all channels according to the one clean channel that was calibrated, with channels that presented amplitude 'spikes' removed. At 610 MHz about 25% of the data were edited out. In order to increase signal-to-noise while limiting the effects of bandwidth smearing, the channels were averaged into 6 of $\sim$2 MHz each at 610 MHz, and 4 of $\sim$1.5 MHz each at 240 MHz.

Due to the large field of view of the GMRT, the field was split into multiple facets for imaging. 56 facets were created at 610 MHz (with cellsize $1.5''$) and 85 facets were created at 240 MHz (with cellsize $3''$) so that in each facet the imaging field still approximates a plane surface. When recombined for our final image these give a field of view of $\sim 1.2^\circ \times 1.2^\circ$ at 610 MHz and $\sim 3^\circ \times 3^\circ$ at 240 MHz. After editing again the averaged data, repeated cycles of deconvolution were performed along with careful phase-only self-calibration in order to image the data. Most of the remaining noise in our final images arises from confusion and calibration undertainties. At the lowest frequencies the phase errors are expected to originate from rapidly varying ionospheric delays.

The final images were corrected for the primary beam pattern of the GMRT using the task PBCOR in AIPS. The full resolution of the GMRT is $\sim 13''$ at 240 MHz and $\sim 5''$ at 610 MHz with the u-v range at 240 MHz being $\sim 0.05 - 21$ kλ and $\sim 0.1 - 50$ kλ at 610 MHz. The rms noise level (1σ) achieved in the final full resolution images is 1 mJy at 610 MHz, and 1.6 mJy at 240 MHz (see Table 1). There are also various elements of imprecision in the flux density measurement. These include uncertainty in the overal flux calibration scale.

The imprecision in the flux density scale is estimated to be $\sim$ 5% at 610 MHz and $\sim$ 8% at 240 MHz (Chandra, Ray & Bhatnagar, 2004). These estimates include an uncertainty in the measuring of the flux of the flux calibrator plus systematic uncertainties introduced by the telescope hardware. In addition (Chandra, Ray & Bhatnagar, 2004) quote an elevation dependent error on the scale of 2-4%. We therefore set our flux densities to the Perley & Butler (2013) flux density scale and accept that the flux calibration scale is uncertain at that level. Comparing our flux calibrators values to the Scaife & Heald (2012) flux density scale we find a change at the order of $\sim$1%.

The resulting maps of the 610-MHz data showed ghost images containing $\sim$10% of the flux of the main image to the N and S of the true radio structure, presumably because of residual delay and amplitude errors, though no attempt to improve these corrections was successful. We considered the possibility that the ghost images are caused by residual amplitude and phase errors due to the brightness of the source with the deconvolution ('CLEAN' algorithm) not accounting for the spectral gradients. Amplitude errors show up if the delays can't be fitted and an amplitude self-calibration would be needed. We tested the effect of amplitude self-calibration but found no improvement. Several other tests with different methods were performed, i.e. imaging only one side band or performing one round of self calibration only. The 610-MHz image is not qualitatively different from the image at similar angular resolution from the VLA (Sec. 3), but we choose to use the 610 MHz data only for the total source flux estimation for the integrated spectrum and not to use it for the point-by-point spectral analyses later because of unreliability in the image reconstruction.

We imaged the phase and flux calibrators to check the integrity of the calibrations. While these were as expected, the flux densities derived for 8 background sources in the 3C 270 field were found to be systematically low by about 20% at 240 and 610 MHz as compared

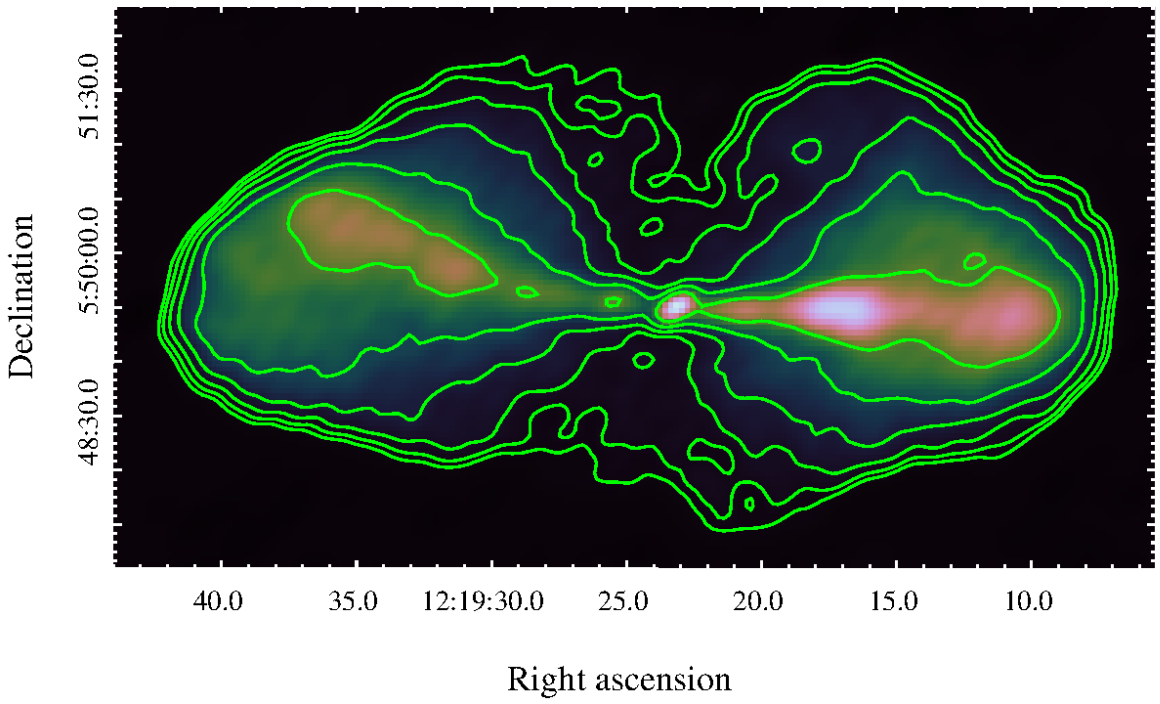

Figure 3.2 VLA 1.55 GHz radio contours of 3C 270 overlaid on the radio emission in grey. The 1 σ rms noise is $\sim$ 0.8 mJy beam^{-1} with contour levels starting at 4σ and rise by factor of 2. Flux Density: 18.3 Jy, Restoring beam: $\sim$ 15.78 $\times$ 10.69, P.A.= -57.44°.

with expectations based on literature measurements. At 240 MHz all source structures appeared normal, and it was considered appropriate to increase all flux densities, including those for 3C 270, by 20% using the task MATH in AIPS. The same procedure was applied for the total flux density of 3C 270 at 610 MHz.

3.4 Archival VLA observations

From the VLA public archive we acquired and reanalysed the radio observations listed in Table 2. The data were calibrated and imaged in AIPS. In order to achieve the best possible noise level for the 1.55 GHz and 4.86 GHz VLA archival data, several datasets were combined for mapping, to obtain the best uv coverage for image reconstruction. Individual observations were analysed separately until the stage where the source and calibrator uv data

Table 3.2 Summary of the archival VLA observations

Project	Observation date	Array	Frequency (GHz)	Bandwidth (MHz)	Integration time (min)
AP0077	1984 Apr 23	C	1.55	2×50	25
AV0088	1984 Jun 05	C	1.49	2×50	16
AH0343 A	1989 Mar 15	B	1.57	2×50	10
AH0343 B	1989 Jul 28	BnC	1.57	2×50	10
AL0693 B	2007 Mar 18	D	4.86	2×50	81

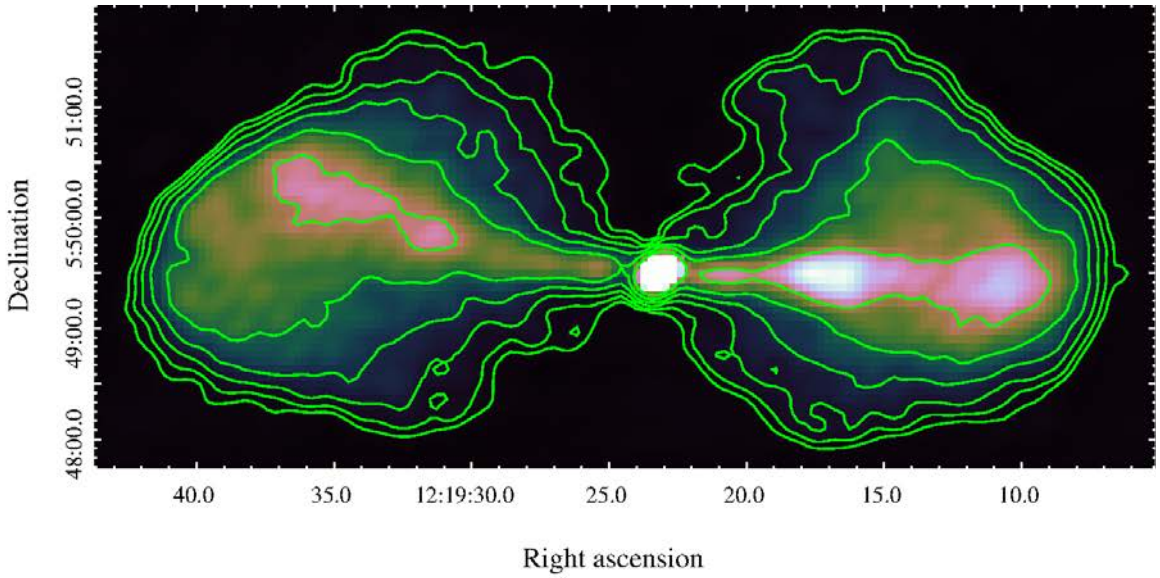

Figure 3.3 VLA 4.86 GHz radio contours of 3C 270 overlaid on the radio emission in grey. The 1 σ rms noise is $\sim$ 0.4 mJy beam^{-1} with contour levels starting at 4σ and rise by factor of 2. Flux Density: 8.3 Jy, Restoring beam: $\sim 19.01'' \times 11.17''$, P.A.= -55.35°.

were separated. The SPLIT files were combined using DBCON and the analysis proceeded with phase-only self-calibration and imaging. For the 1.55 GHz data, as can be seen in Table 2, four different observations were combined together (AP0077, AV0088, AH0343 A and AH0343 B) in order to produce the final image with a total integration time of 61 mins and an rms noise level of 0.8 mJy (DBCON 1 in Table 3). At 4.86 GHz only the D-array observation was used and analysed as it was sufficiently long and has a resolution comparable to the 1.55 GHz image. The properties of the resulting maps are given in Table 3.

Table 3.3 Results of the archival VLA data

	Array	Frequency (GHz)	Integration time (min)	HPBW, PA (Typical full array, $''\times''$, $^\circ$)	rms mJy beam^{-1}
DBCON 1	B&C	1.55	61	$\sim 19.01 \times 11.17$, -55.35	0.8
AL0693 B	D	4.86	81	$\sim 15.78 \times 10.69$, -57.44	0.4

Table 3.4 Radio properties of NGC 4261

Components	S_{240} MHz (Jy)	$S_{1.55}$ GHz (Jy)	$S_{4.8}$ GHz (Jy)	$\alpha_{1.55\mathrm{GHz}}^{240\mathrm{MHz}}$ ($\pm$0.09)	$\alpha_{4.8\mathrm{GHz}}^{1.55\mathrm{GHz}}$ ($\pm$0.14)	LS (kpc)
Total	48.50$\pm$3.21	18.30$\pm$0.92	8.3$\pm$0.42	0.41	1.01	80×40
Core	0.48$\pm$0.04	0.36$\pm$0.02	0.37$\pm$0.02	0.16	0.03	-
West jet..	10.60$\pm$0.85	3.80$\pm$0.19	1.38$\pm$0.20	0.47	0.90	37×7
East jet..	8.00$\pm$0.64	2.80$\pm$0.14	1.13$\pm$0.06	0.56	0.80	43×8

The task LGEOM was also used in order to rotate the data where needed, to match the VLA and GMRT observations for the spectral index maps. Finally the images were corrected for the primary beam response using the task PBCOR. Both images have spatial resolution similar to that of the GMRT 240 MHz image. The flux densities are set to the flux density scale of the Perley & Butler (2013) with the flux density scale errors being $\sim$5%. Using the Scaife & Heald (2012) flux density density scale would alter the results by $\sim$1%.

3.5 Radio images

Figure 3.1 presents the GMRT 240 MHz radio image of 3C 270 at a resolution of $15.3'' \times 11.0''$ overlaid on the optical image from the Digitized Sky Survey. The contour levels start at 4σ and rise by a factor of 2. The most prominent components of the source, that is, the two symmetrical bright jets and their surrounding lobes, are shown. The jets are more prominent on the higher-frequency maps. The VLA images at 1.55 GHz and 4.8 GHz are shown in Figures 3.2 and 3.3, respectively, where the radio contours at each frequency can be seen.

The radio jets extend in opposite directions for several tens of kpc from the host galaxy of NGC 4261, having a similar morphology at all frequencies and at different restoring beams. The two bright jets are continuous and inflate two fairly round radio lobes that surround the jets. However, as expected, the relative brightness of the compact core changes with frequency, and is clearly detected at 1.55 and 4.86 GHz, but not at 240 MHz.

There are two morphological differences between the two jets: first, the eastern jet is bent whereas the western one is straight with no distortion but has a point where it noticeably broadens; second, the difference in the actual size of the lobes, with the western lobe being less extended than the eastern one. These differences may be caused by interactions with their surroundings, but we see no evidence of a denser environment on either side in the X-ray. In O'Sullivan et al. (2011) it is noted that the alteration of the jet orientation could be misleading, since we are viewing a projected image of a three-dimensional structure.

Table 4 summarises the most relevant properties of the source and its components including flux density, the spectral index in the 240 MHz$-$1.55 GHz frequency range and the linear size (LS). The largest linear size of the source at all frequencies is $\sim$80 kpc, with a total angular extent of $\sim 530''$ along the east/west axis. The jets have similar flux density and size, with the eastern jet being about 2 kpc more extended, while the western jet flux density is $\sim$10% greater than the eastern one. The radio lobes appear symmetrical with similar size and shape. An interesting characteristic of this radio source is that the expansion of the eastern jet exhibits a bend towards the north before the jet diffuses into the lobe. As is evident from Figures 1 to 3, at lower frequencies the lobes tend to grow and connect north and south of the core. This is the first clear indication of the strong spectral gradients present in the radio emission of NGC 4261.

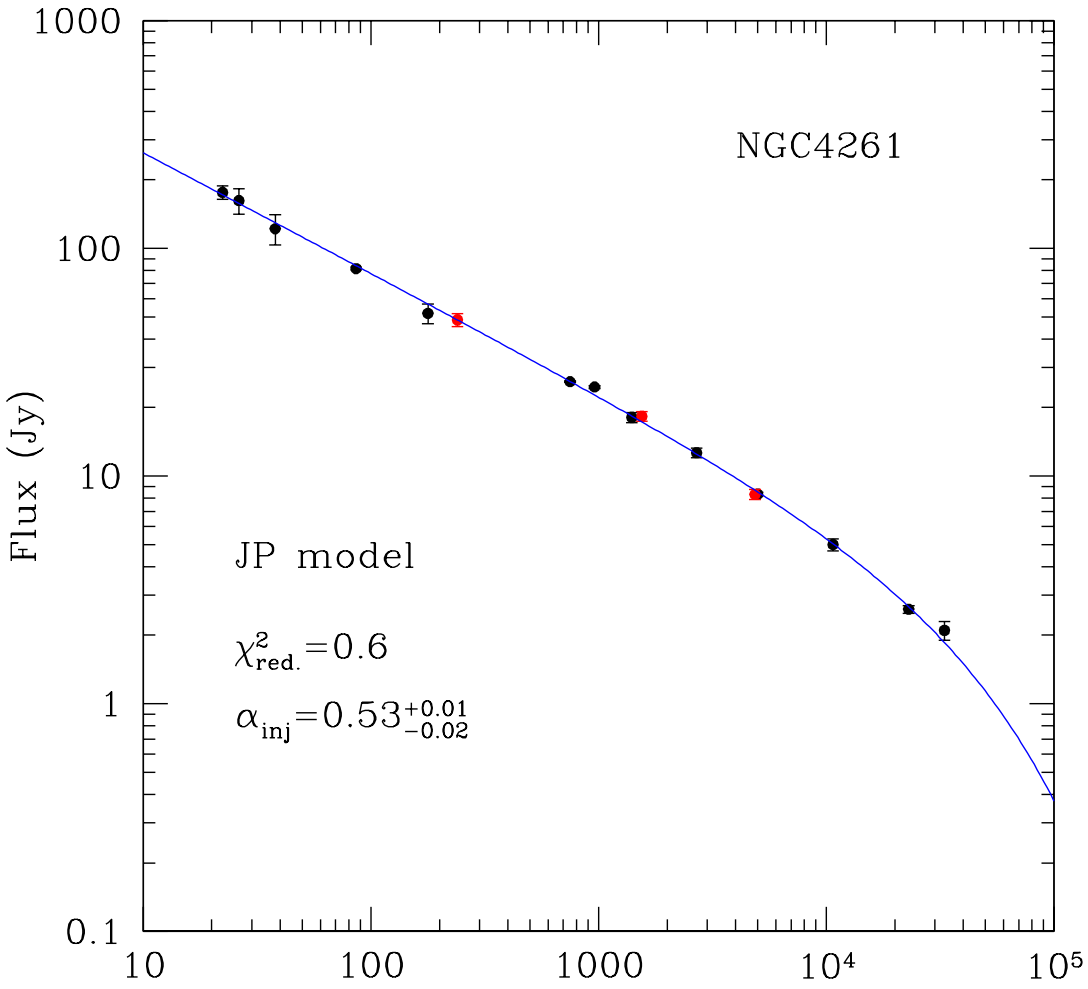

Figure 3.4 Radio spectrum of NGC 4261 between 22 MHz and 33 GHz. The black points are literature data, (see Table 5), and the red points are the VLA 4.86 GHz and 1.55 GHz, and the GMRT 240 MHz analysed in this paper. The best-fit curve is a Jaffe-Perola (JP) model applied to the data. The best fitting values of α are given as well as the reduced χ^2 value from the fit. Model fit performed by co-author Dr. Simona Giacintucci

Table 3.5 Literature data for NGC 4261

ν MHz	Flux Density (Jy)	References [a]
22.3	176 ± 12	1
26.3	162 ± 21	2
38	122 ± 18.3	3
86	81.5 ± 1.1	4
178	51.8 ± 5.2	3
750	25.96 ± 0.22	5
960	24.60 ± 0.33	1
1400	18.1 ± 0.91	3
2695	12.65 ± 0.63	3
5000	8.32 ± 0.16	6
10700	5.0 ± 0.3	7
23000	2.6 ± 0.1	8
33000	2.1 ± 0.2	8

[a]REFERENCES.-(1) Roger et al. (1969); (2) Viner & Erickson (1975); (3) Kellermann et al. (1969); (4) Artyukh et al. (1969); (5) Pauliny-Toth et al. (1966); (6) Pauliny-Toth & Kellermann (1968); (7) NRAO image, Kellermann & Pauliny-Toth (1973); (8) WMAP image, Bennett et al. (2003)

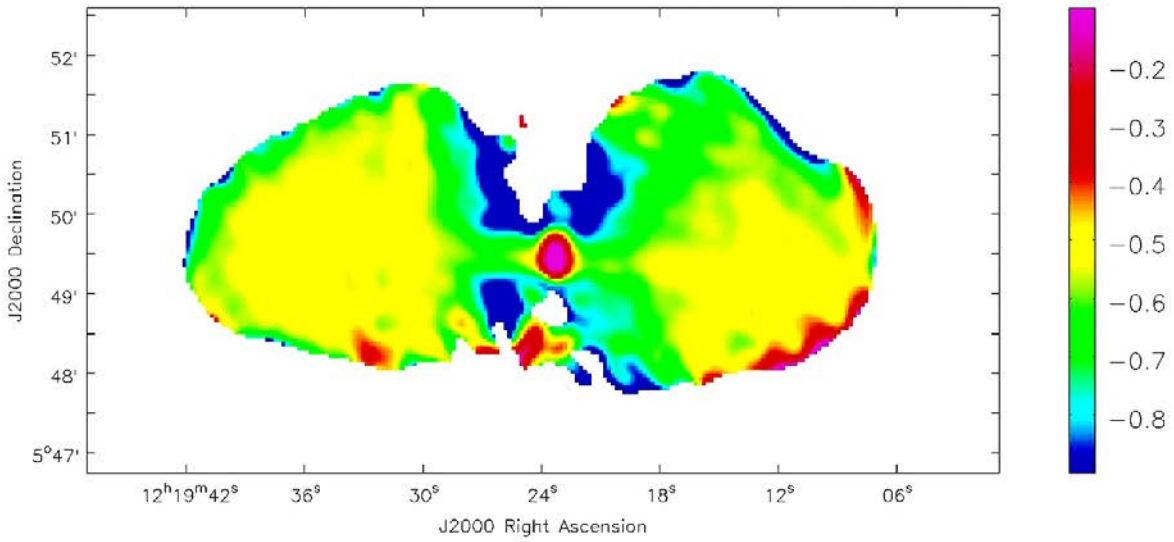

Figure 3.5 Colour-scale image of the spectral index distribution between 240 MHz GMRT and 1.55 GHz VLA over 3C 270. The image was produced from images with a restoring beam of $20'' \times 20''$.

3.6 Radio spectral analysis and physical parameters

The archival GMRT and VLA radio data were coupled with data from the literature in order to calculate the integrated radio spectrum of 3C 270. The physical parameters of 3C 270 were then calculated using the spectral index distribution of the source. The analysis described below was performed using the Synage++ package (Murgia, 2000).

3.6.1 Spectral analysis

The integrated radio spectrum between 22 MHz and 33 GHz for 3C 270 is shown in Figure 3.4. The flux densities compiled from the literature, as listed in NASA/IPAC Extragalactic Database (ned.ipac.caltech.edu/), along with the VLA measurements that were used for the derivation of the integrated radio spectrum, are shown in Table 5. The GMRT data points are both in good agreement with the source-integrated fit. The VLA 1.55 and 4.86 GHz data points lie close to the fit and are both in good agreement with previous VLA measurements.

The integrated radio spectrum between 22 MHz and 33 GHz for 3C 270 is shown in Figure 3.4. Table 3.5 lists the literature flux densities used in the spectrum, and the source of each measurement. Adding our VLA measurements to the literature data, we fit a (Jaffe & Perola, 1973) (JP) model to the integrated spectrum. Our aim in fitting this model is firstly to determine whether the low-frequency data can be well modelled as a power-law, whose slope will approximate the injection spectral index, and secondly to allow us to compare our GMRT flux density measurements with the well-calibrated data from other frequencies. The model assumes that the radiative timescale of the electrons is much longer than their timescale for continuous isotropisation. The resulting fit describes the low frequency data well, with an asymptotic low-frequency index of $\alpha_{inj} = 0.53^{+0.01}_{-0.02}$, typical of FR I jets

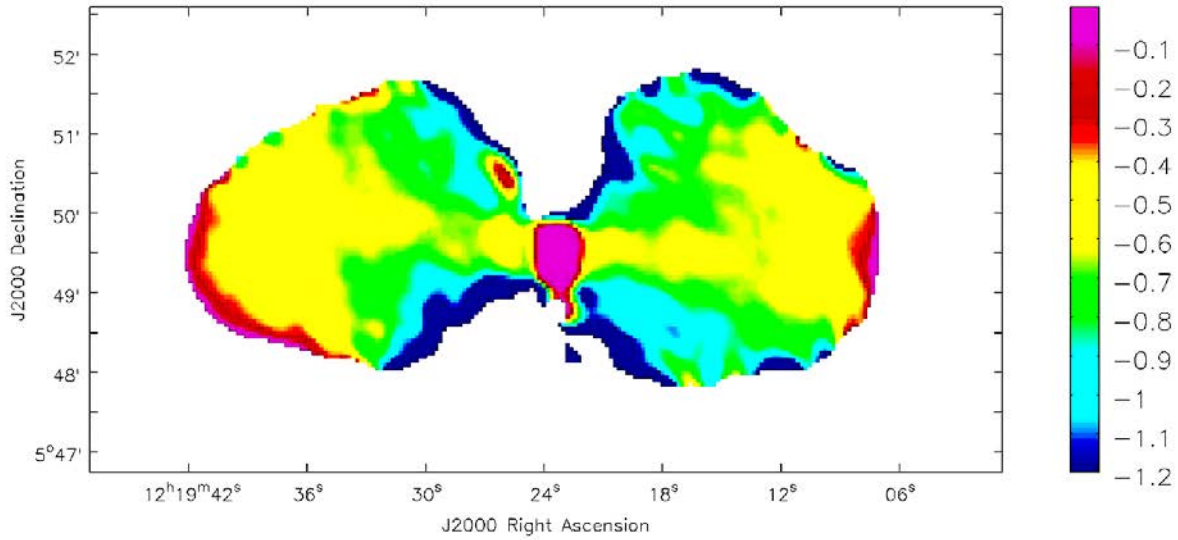

Figure 3.6 Colour-scale image of the spectral index distribution between 1.55 GHz and 4.8 GHz over 3C 270.The image was produced from images with a restoring beam of $20'' \times 20''$.

(Young et al., 2005). The slope steepens above ∼5 GHz, with a break frequency of ∼85 GHz, though this is likely driven to a high value owing to the high luminosity of the relatively young plasma in the jets and core. We note that a continuous-injection (CI) model gives an identical fit.

Later, a point-to-point spectral analysis was performed using two different frequency intervals in order to study the spectral index distribution of the source. In the first one the GMRT 240 MHz image was combined with the VLA 1.55 GHz image while in the second one the VLA 1.55 GHz image was coupled with the VLA 4.86 GHz to obtain the spectral index image. Each set of images was produced using the same *u-v* range and cellsize using matched *u-v* scales directly from IMAGR i.e. same Gaussian taper. The synthesized beams were adjusted from their slightly different values (because of different *uv* sample) to a $20''$ circular beam by a final convolution step, corrected for the primary beam, and aligned. Spectral images were created where the flux density in both images is greater than

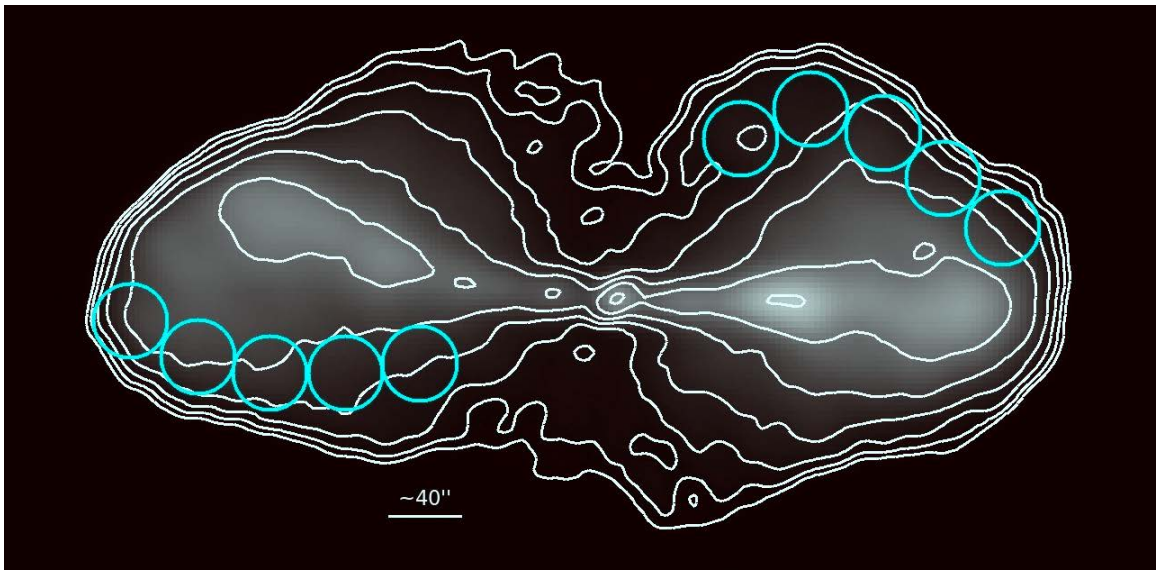

Figure 3.7 1.55 GHz image in grey scale. Overlaid are the 1.55 GHz contour levels starting at 3.2 mJy beam^{-1} and rising by factor of 2 until 204.8 mJy beam^{-1}. The cyan circles indicate the lobe regions used for the source's age estimation using the spectral index profile method.

3σ significant. The choice of $20''$ was based on the lowest resolution image of 1.55 GHz. Finally the images were combined using the task COMB in AIPS to obtain the spectral images presented in Figures 3.5 and 3.6 for the 240 MHz - 1.55 GHz and 1.55 GHz - 4.86 GHz frequency ranges respectively.

In Figure 3.5, the unresolved core of the radio source can be seen. It has a spectral index $\alpha_{240}^{1550} \sim 0.16 \pm 0.09$ mostly as a result of self-absorption (as indicated by the lack of an obvious core in the 240 MHz image – Fig. 3.1) since the spectral index is rather frequency-dependent (high curvature). Moving outwards the spectral index becomes steeper and a constant value of $\alpha \sim 0.50 \pm 0.09$ can be seen in the jets, while the lobes that dominate the total index in the lower-frequency band, appear with constant but slightly steeper value ($\alpha \sim 0.60 \pm 0.09$) (for results see Table 3.4). In Figure 3.6 the core is obvious with a flat spectral index $\alpha_{1550}^{4860} \sim 0.03 \pm 0.09$. The steepening of the spectral index within the lobes is much clearer in this image as a spectral index of $\sim 0.9 - 1$ can be seen above and below the

beginning of the jets. In the jets, the spectral index at the point where they are surrounded by the lobes is $\sim 0.5-0.6$ and remains constant throughout. The spectrum gradually steepens at the back of the lobes reaching values of $\sim 1-1.2$ with some parts of the lobes reaching $\sim 1.20\pm0.09$. In both Figures 3.5 and 3.6, the features in the spectral-index maps at the edges of the source, and particularly at the ends of the lobes, are likely to be spurious and induced by residual reconstruction errors in regions of steep intensity gradient.

As NGC 4261 hosts an extended radio source with active jets, we performed a fit of the observed spectral index trend only along the region of the lobes as done in Murgia (2003). This was done for the 1.55 GHz − 4.86 GHz frequency range. The spectral index trend was determined by averaging the flux densities of each frequency in $40''$ diameter circular regions starting at the end of the source's jet and then moving back from the jet head along the path that we would expect to be followed by back-flowing plasma (see Fig 3.7). The circular regions were chosen to be larger than the beam size so that the measurements of the spectral index are independent. The produced $1.55-4.86$ GHz spectral index distribution as a function of the distance along the west lobe is shown in Figure 3.8 and for the eastern one in Figure 3.9.

The trends in the west and east lobe were fitted using also a JP model (Jaffe & Perola, 1973). By assuming a simple constant source expansion velocity ($d \propto t$), the transport speed of the plasma in the back flow in the lobes of the source can be calculated by also assuming that the break frequency is $\nu_{break} \propto d^{-2}$, where d is the distance from the end of the jet. The best fit for the observed spectral trend in west and east lobe of the source can be seen as a solid line in Figures 3.8 and 3.9, respectively. We note that the model provides a reasonable description of the spectral index trend in both lobes, suggesting that our assumption of constant expansion velocity is not unreasonable. The model provided similar values of α_{inj}

Table 3.6 Results of the point-to-point analysis. The value marked * were fixed during fitting.

Region	$\alpha_{\rm inj}$	$\nu_{\rm break}$ (GHz)	$\tau_{\rm rad}$ (10^6 yrs)	$\upsilon_{\rm trans}$ c
West lobe	$0.56^{+0.04}_{-0.03}$	$12.4^{+4.3}_{-2.7}$	~ 29	$\sim 0.004c$
East lobe	0.50^{*}	$7.5^{+0.3}_{-0.4}$	~ 36	$\sim 0.004c$

and ν_{break} for both lobe regions. In the west lobe the calculated injection spectral index from the model was $\alpha_{inj} \sim 0.56$ with a break frequency of $\nu_{break} \sim 12.4$ GHz while in the east lobe we used a fixed injection spectral index of $\alpha_{inj} = 0.5$ and got a $\nu_{break} \sim 7.5$ GHz (see also Table 3.6). These results change little if the injection indices in the two lobe heads are assumed to be the same - either 0.5 or 0.56, as in fits shown in Figs. 3.8 and 3.9.

3.6.2 Physical parameters of 3C 270

To calculate the key physical parameters of 3C 270, we have to make certain assumptions. Firstly, the relativistic particle and magnetic field energy densities were assumed to be uniformly distributed over the volume occupied by the radio source and in approximate energy equipartition. A low energy cut-off γ_{min} (where γ is the electron Lorentz factor) was introduced in the energy distribution of the radiating electrons rather than the fixed 10 MHz $-$ 100 GHz frequency interval used in the classic equipartition equations (Pacholczyk, 1970). We assumed that the magnetic field is unordered along the line of sight and used $\gamma_{min} = 100$ in the electron energy distribution, which corresponds to ~ 50 MeV.

We used an injection spectral index $\alpha_{inj} = 0.5$, derived from the west lobe using a JP model, which is broadly in agreement with the injection spectral index of the lobes (Table 3.6). The model assumes that the radiative timescale of the electrons is much longer than their timescale for continuous isotropisation. Furthermore, the flux density at 240 MHz (Table 3.7) was used to calculate the radio luminosity of the source, since among the fre-

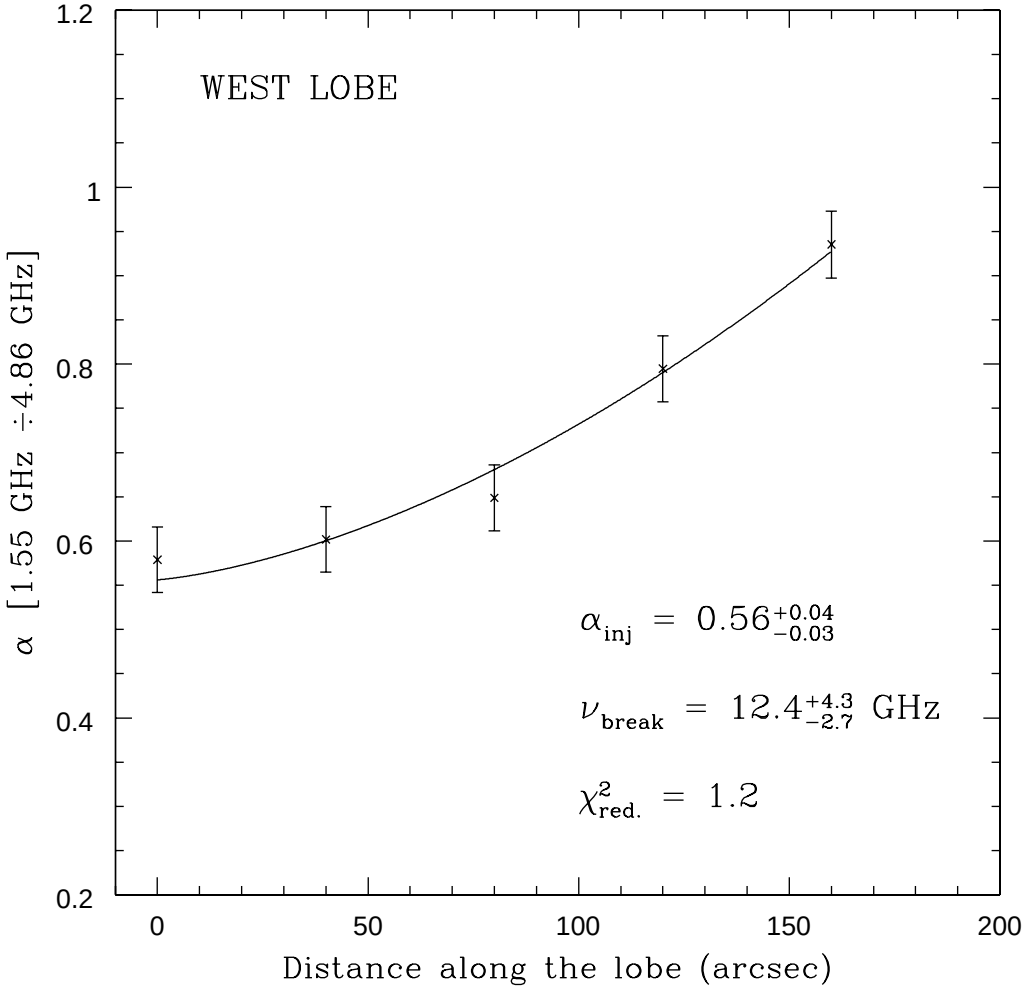

Figure 3.8 Spectral-index distribution along the west lobe of the source calculated from the 1.55 and 4.86 GHz frequencies, derived using the circular regions shown in Fig. 3.7. The solid line represents the best JP model fit. The values of α_{inj} and ν_{break} along with the reduced χ^2 from the fit are reported here. Model fit performed by co-author Dr. Simona Giacintucci

Table 3.7 Physical parameters of 3C 270 in the lobe regions chosen. In this Table is shown the size of each region, the flux densitites at 240 and 1550 MHz, teh observed spectral index and the results from the model fit performed by Dr. Giacintucci for the luminosity at 1550 MHz teh equipartition magnetic field and the radio power

Region	r_{min} ($''$)	r_{max} ($''$)	V_{tot} (kpc^3)	S_{240} (mJy)	S_{1550} (mJy)	α_{obs}	L_{1550} (10^{22} W/Hz)	B_{eq} (μG)	P_{radio} [a]
West Lobe									
1	10	33	1724	998 ± 80	316 ± 16	0.62	3.6	5.0	1.42
2	33	63	3861	2067 ± 165	650 ± 33	0.62	7.3	4.9	1.36
3	63	168	12081	8741 ± 700	3138 ± 157	0.55	35	5.5	1.73
4	168	242	2551	2262 ± 181	897 ± 45	0.50	10	6.0	2.06
East Lobe									
5	10	33	1056	408 ± 33	146 ± 7	0.55	1.6	4.6	1.21
6	33	63	1646	976 ± 78	287 ± 14	0.66	3.2	4.9	1.39
7	63	168	9753	5868 ± 469	2310 ± 116	0.50	26	5.3	1.64
8	168	282	4668	5755 ± 460	2202 ± 110	0.52	25	6.5	2.43

[a] 10^{-12} dyn cm^{-2}

quencies used in this work it is least affected by electron spectral ageing. In Fig. 3.10 one can see the different regions in which the lobes of the source were divided in order to estimate their volumes. We assumed cylindrical geometry for each subregion, a filling factor $\phi = 1$ and equal energy in relativistic protons and electrons. We also assume that the axis of the radio galaxy is in the plane of the sky. If the jet axis is oriented at 76° to the plane of the sky (as suggested by the most recent modelling from Laing & Bridle 2014), our estimated volume will increase by $\sim$10%, altering our estimate of the minimum pressure of the relativistic plasma by $\sim$10%. The regions numbered 1-8 were also used because their distance from the core is matched to the radii used in the X-ray pressure profile. The jets, as being overpressured, were excluded from this analysis. The results are summarized in Table 3.7 where we have estimated for each region (sum of n subregions) the magnetic field, the minimum and maximum radius of the cylinder assumed, the total volume, the flux den-

sity at 240 and 1550 MHz, the observed spectral index α, the radio luminosity calculated at 1550 MHz using the observed α, the equipartition magnetic field and the pressure. We found a similar magnitude for B_{eq} $\sim$5 μG for both eastern and western lobes. For the total source, we found an average magnetic field of $\sim$6.4 μG. For this field (see later), electrons at γ_{min}=100 radiate at $\sim$5 MHz.

3.6.3 Radiative age

When considering the development of the radio jets and lobes, we adopt a simple conceptual model, in which at any given time plasma is rapidly transported out from the central engine to the tip of the jet. At this point the jet flow is halted by contact with the IGM, and the plasma driven out of the jet moves out radially to form the lobe. In this model, the age of the lobe plasma is linked to the distance along the jet; the back of the lobes (close to the nucleus) formed when the jet only extended a few kiloparsecs, while the tips of the lobes have only formed recently. In principle, backflows could develop, transporting younger plasma away from the jet tips into regions of the lobe formed at earlier times. However, in the absence of such a flow, or external forces causing reacceleration, plasma in the lobes is expected to age passively, with the high-frequency break in its spectral index falling to lower frequencies over time.

The radiative age of the radio source of NGC 4261 can be calculated if the break frequency of the source is known (e.g. Myers & Spangler, 1984). As break frequency is called the frequency above which there is no synchrotron radiation emitted by the lobes of a radio source, due to the absence of the highest-energy electrons. The magnetic field is considered to be uniform and constant over the whole of the source's lifetime when radiative losses dominate over expansion losses. Neglecting reacceleration processes, the radiative age,

which is the time since the last period of injection of relativistic electrons began, can be obtained as

$$t_{\rm rad} = 1590 \frac{B_{\rm eq}^{0.5}}{B_{\rm eq}^2 + B_{\rm CMB}^2} [(1+z)\nu_{\rm break}]^{-0.5} \text{ Myr}, \tag{3.1}$$

where $\nu_{\rm break}$ is expressed in GHz, and $B_{\rm eq}$ and $B_{\rm CMB}$ in μG (Parma et al., 2007). $B_{\rm eq}$ is the equipartition magnetic field and $B_{\rm CMB} = 3.2$ is the equivalent magnetic field strength of the cosmic microwave background (CMB) radiation at zero redshift, and equation (1) thus includes both inverse Compton and synchrotron losses.

Using Equation 3.1 and data in Table 3.7, we estimated a radiative age of $\sim$29 Myr for the western lobe and $\sim$36 Myr for the eastern one (Figs 3.8 and 3.9). We also derived an estimate of the plasma transport velocity to the back of the lobes, $\upsilon_{\rm trans}$/c, where c is the speed of light. This velocity was calculated as $\upsilon_{\rm trans}$= LD/$\tau_{\rm rad}$, assuming a simple constant velocity and using the linear distance (LD) from the tip of the jet to the back of the lobe as measured from the radio images in Section 4. We found that for both lobes $\upsilon_{\rm trans} \sim 0.004$c ($\sim$1250 km s^{-1} for the western lobe and $\sim$1170 km s^{-1} for the eastern one).

By comparison, the sound speed in the IGM in the environment around NGC 4261, estimated from the measured X-ray temperature, increases from about 380 km s^{-1} near the core to 590 km s^{-1} outside 100$''$ from the core, and the Alfven speed in the lobe is about 96000 km s^{-1} (using the lobe density deduced in Sec. 6.2). That is, the back-flow speed from the jet head is strongly sub-Alfvenic, and so will not excite magnetic shocks in the lobes. The internal characteristic speed of the waves in the magnetized plasma were calculated from

$$\upsilon_A = \frac{B_{\rm eq}}{\sqrt{\mu_o \rho}}, \tag{3.2}$$

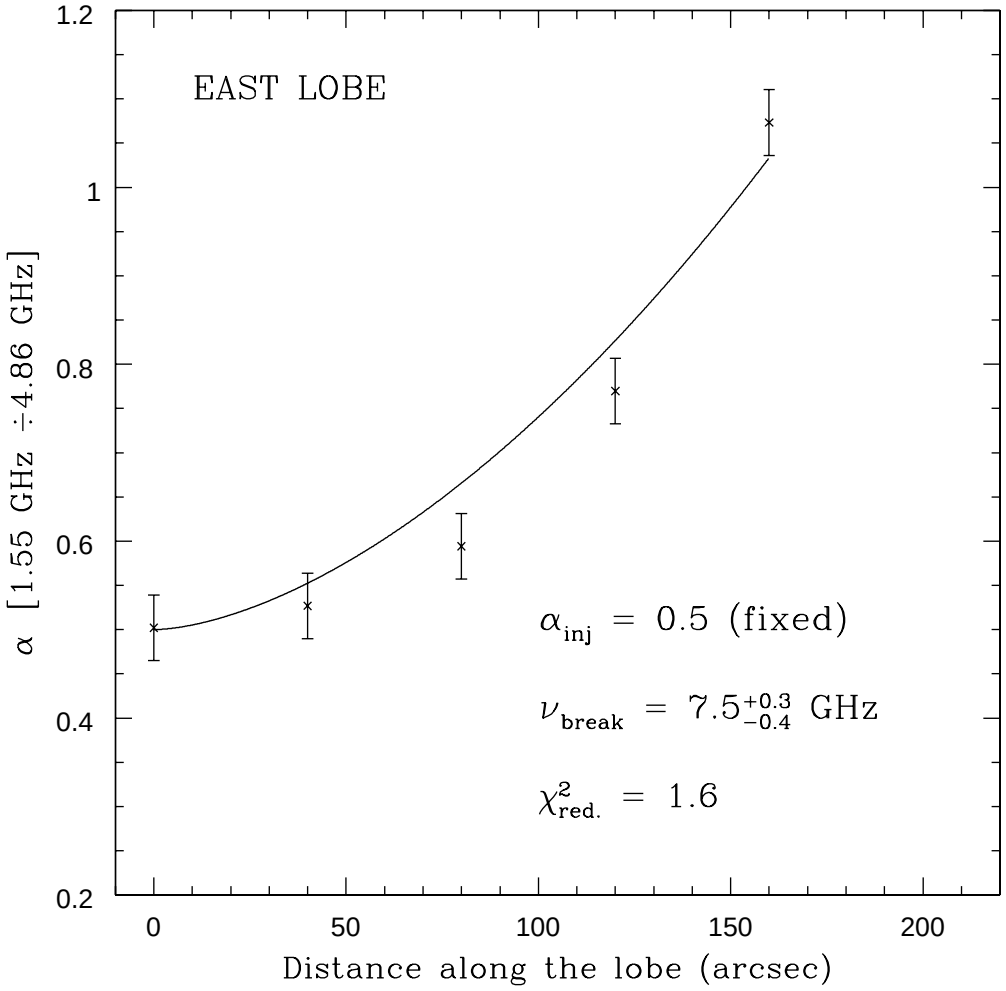

Figure 3.9 Same as Figure 3.8 but for the east lobe with the model fit performed by co-author Dr. Simona Giacintucci

where υ_A is the Alfven speed expressed in m s^{-1}, B_{eq} is the equipartition magnetic field in Tesla, μ_o the permeability of the vacuum and ρ the total mass density of the charged particles in g cm^{-3}.

3.7 Discussion

3.7.1 The age of the source

Before considering the implications of our radiative age measurements, we first discuss potential sources of error in our approach. We have performed a relatively simple modelling of the 1.55−4.86 GHz spectral index trend in the lobes, and our model rests on a number of assumptions. These include constant source expansion velocity, constant magnetic field, our choice of spectral model, and that reacceleration, adiabatic expansion and mixing are not important processes in the lobes. As mentioned in Section 3.6.1, the fact that our model provides a reasonable description of the spectral index trend suggests that the assumption of a constant expansion velocity is at least reasonable; we see no evidence that velocity changes are required, though of course other factors could disguise deviations from the trend. As a further test, we refitted the spectral index profiles, adding one additional region closer to the AGN. In both lobes, the fits were poorer, primarily because of the differences in the extent of the emission seen in the lobes close to the nucleus (back of the lobes) at 1.55 and 4.8 GHz, which lead to divergence from the smooth trend in spectral index. For example, in the west lobe, the added region is close to the edge of the lobe at 4.8 GHz, leading to a steeper than expected spectral index and a reduced χ^2=8.7. Both fits find lower break frequencies ∼4-5 GHz, suggesting radiative ages ∼45 Myr, older than our best estimate, but not by a large factor.

Our use of the JP model may be over-simple, but we are limited in this by the available data. Harwood et al. (2013) compare the utility of several spectral models to describe spectral ageing in FR-II galaxies and conclude that the Tribble (1993) model provides the best combination of fit quality and physical realism; Harwood et al. consider the JP model at least as physically accurate, but it provides a poorer fit. However, they find that to differentiate between models requires data at 7-9 frequencies, whereas we have only 3 available. Further observations are therefore needed to determine whether a different model might provide a better description (and age estimate) for 3C 270.

Losses caused by adiabatic expansion would affect our age estimate, lowering the break frequency and therefore the estimated age. However, adiabatic losses decrease the luminosity of the plasma, and are more effective in doing so than they are in reducing ν_{break}. We might expect losses in the jets as they flare from the narrowly collimated structures seen in the X-ray to the broad jets we observe in the radio, but the fact that the lobes have high surface brightnesses and smooth surface brightness distributions suggests that adiabatic losses within the lobes are probably not important. Variation in the magnetic field within the lobes could affect our results, but on large scales we only measure a relatively small ($\sim$20%) change in field strength across the lobes (see Table 3.7), perhaps as little as 8% in the radius range used to estimate age. This is insufficient to balance the observed spectral index trend, and we therefore consider our assumption of a constant field to be a reasonable approximation. Small-scale field variations cannot be ruled out, but would again require improved spectral modelling and additional observations.

Moving on to the results, our spectral-index profile modelling (Figures 3.8 and 3.9), implies ages of $t_{\rm rad} \sim 29$ and 37 Myr for the west and east lobes respectively (Table 3.6). These ages are younger than the <75 Myr upper limit on age estimated by O'Sullivan et

al. (2011) from the IGM sound speed, by a factor of 2. Discrepancies of this type are common. Eilek (1996) first noted that the synchrotron ages for FRI and FRII radio sources derived from the spectra differed from the dynamical ages as much as a factor of 10. By this standard the factor of 2 discrepancy we observe is relatively mild. Several studies suggest plausible explanations for the age difference between spectral and dynamical ages (Blundell & Rawlings, 2000), including in situ acceleration of particles (e.g., Carilli et al., 1991; Eilek, 1996) and magnetic fields that vary with position in the lobes (e.g., Eilek & Arendt, 1996; Katz-Stone et al., 1993). Studies for sources whose age is less than 10 Myr have shown that the spectral and dynamical age estimates are in quite good agreement (Kaiser et al., 1997; Matthews & Scheuer, 1990) but for most sources the cause is still unknown. We will discuss three possible explanations for the age discrepancy in 3C 270: i) a period of highly supersonic expansion early in the AGN outburst; ii) multiple outbursts or large changes in jet power; iii) a backflow capable of mixing younger electrons from the jets into the old plasma at the back of the lobes.

In scenario (i), the expansion of the lobes was much faster in the past, so that the assumption of a constant near-sonic expansion velocity by O'Sullivan et al. (2011) leads to an overestimate of the age of the source. For the larger eastern lobe, the radiative age (37 Myr) implies that the lobes should be driving into the IGM at Mach$\sim$2, if they have expanded at constant velocity. Shocks in the IGM, driven by this expansion, would be detectable in the available X-ray observations as increases in temperature and surface brightness, and are ruled out by the measurements described in O'Sullivan et al. (2011). However, there is also the possibility of that a period of supersonic expansion occurred early in the life of the source, followed by a period of slower expansion which we are now observing. In this case, the shocks would have detached from the lobe tips as the expansion speed dropped,

and moved outwards, potentially passing out of the field of view of the *XMM-Newton* observation. Assuming that the shock front is just outside the *XMM* field of view ($\sim$14$'$ or $\sim$130 kpc) we can calculate the duration of the supersonic phase. The minimum Mach number of such a shock would be $\mathscr{M}_{\rm min}$ $\sim$6 ($\sim$3500 km s^{-1}). The corresponding maximum period of supersonic expansion would be $\sim$7.5 Myr, during which time the lobes would expand to $\sim$28.5 kpc along the jet axis. After this, expansion would continue at the sound speed for the remaining 3/4 of the lifetime of the radio source.

A Mach$\sim$6 shock in the IGM would cause an increase in X-ray surface brightness of a factor $\sim$13.5 and a temperature increase of a factor $\sim$12. Even if the efficiency of energy deposition is low, such a shock would have strongly heated the IGM, and the observed temperature would be the result of this heating. For a 10% heating efficiency, we would expect the shock to have deposited $\sim$10^{58} erg in the central 10 kpc alone, and the current rate of radiative energy loss, $\sim$10^{41} erg s^{-1} would only have removed $\sim$1% of this energy. This implies a pre-shock core temperature as low as 0.1 keV, lower than is observed in any group or cluster, and more comparable with the temperature of the interstellar gas in our own Galaxy than that expected in a giant elliptical. Since NGC 4261 appears to be fairly typical of the population of group and cluster-central FR-I radio galaxies, we might also expect to see a population of such sources driving shocks of similar strength, with evidence of strong shock heating. No such population has been identified. The scenario of a single, highly supersonic outburst therefore seems unlikely.

In scenario (ii) the AGN would have undergone more than one outburst, or the jet power may have varied significantly over time. In this case our estimated age could correspond only to the newest outburst or period of high jet power. A restarted jet, or period of more powerful outflow, could drive shocks into the lobes, causing in situ reacceleration in the

old plasma while producing new expansion at the lobe tips. Worrall et al. (2010) note structure that could be caused by variations on $\sim 10^4$ yr timescales in the X-ray jet, while the changes in radio brightness along the western jet suggest variation on longer timescales. This scenario is plausible, and difficult to rule out with current data.

In scenario (iii) a backflow would transport young, energetic electrons back towards the nucleus, reducing the mean age of the plasma. Numerical simulations (e.g., Perucho & Marti, 2007) support the possibility of mildly relativistic backflows in a sheath surrounding light FRI jets. Modelling of the base of the jets in 3C 270 does not reveal any evidence of such a backflow (Laing & Bridle, 2014), but it cannot be ruled out on larger scales. However, if backflows are limited to a sheath around the jets (Laing & Bridle, 2012), the question of how electrons are mixed outward into the larger lobe remains. A bulk backflow, with transport of and mixing of plasma throughout the lobe would be required, but seems less plausible given the lobe morphology.

Considering the merits of these three possibilities, we favour scenario (ii), and suggest a model for the expansion history of the source in which, 75 Myr ago, an outburst swept its way through the X-ray gas, beginning the excavation of the cavities. These cavities grew in stages as the jet power varied over time, with the lobe plasma being refreshed by each new outburst or period of high jet power, the most recent of which is only $\sim$30 Myr old. The overall lobe/cavity inflation time would thus be similar to the X-ray estimate, but the plasma we see in the lobes is a mixture of old and new particles injected by a period of stronger jet activity over the last $\sim$30-40 Myr.

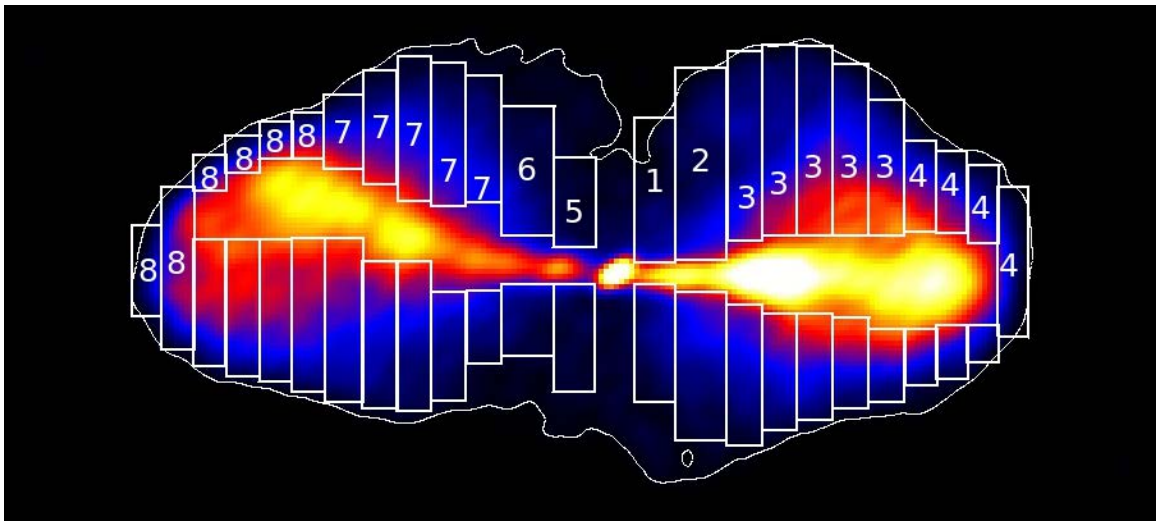

Figure 3.10 Regions used for the estimation of the volume and the other physical parameters described in Table 3.7. The 3.2 μJy (4σ) contour is shown to indicate the limit of the detected lobe emission.

3.7.2 Pressure balance and particle content

The non-thermal energy density in the lobes of an extended radio source cannot be determined by the radio data alone. Only a minimum value can be estimated when we assume the contribution from the magnetic field and the relativistic particles equal (Burbidge, 1958). The additional information needed to constrain the internal energy density can be obtained either from measurement of the inverse-Compton emission caused by the up-scattering of photons off the relativistic electrons in the lobes, or by assuming pressure equilibrium between the lobes and their environment and measuring the IGM pressure using X-ray data (Longair et al., 1973).

We first test our ability to detect inverse-Compton emission from the lobes. Assuming equipartition, O'Sullivan et al. (2011) estimated an expected X-ray flux density from up-scattered cosmic microwave background (CMB) photons to be $\sim$2 nJy from each lobe at 1 keV. Using our improved constraints on the properties of the lobe plasma, we repeat this calculation, and find that we expect a flux of $\sim 6.5\times10^{-14}$ erg s^{-1} in the 0.5-7 keV band

($\sim$4.1 nJy at 1 keV) from each lobe. We then reprocessed the longest *XMM-Newton* dataset available (ObsID 0502120101, $\sim$70 ks after cleaning) using the latest calibration and most recent version of the *XMM* Science Analysis System (SAS 13.5). Following the techniques described in O'Sullivan et al., we find no detection of inverse-Compton flux from the lobes, but are able to place 3σ upper limits on the 0.5-7 keV flux of $<6\times10^{-14}$ erg cm^{-2} s^{-1} ($<$3.8 nJy) for the west lobe, and $<6.2\times10^{-14}$ erg cm^{-2} s^{-1} ($<$4.0 nJy) for the east lobe. These limits are marginally below the predicted flux, and so may suggest that the lobe plasma is out of equipartition, with more energy in the magnetic field than in the particle population. However, the uncertainties in the radio fluxes, *XMM* calibration (see, e.g. Nevalainen et al., 2010, Tsujimoto et al. 2011) and the choice of X-ray spectral model only weakly constrain departures from equipartition in the sense of domination by the electron (and positron) energy density. Deeper X-ray data are needed to provide a lower flux limit and determine whether the lobes are truly in equipartition.

We also estimated the likely optical flux in the inner part of the lobes from up-scattering of infra-red photons emitted by the stellar population. Unfortunately, the expected signal is low, a factor $\sim10^{-3}$ below the optical luminosity of the stellar population in the same region. We are therefore unable to constrain the properties of the lobe emission from its inverse-Compton emission, at least with the currently available data.

As inverse-Compton emission does not provide a definitive constraint, we compare the apparent lobe pressure with that of the surrounding IGM. Using the values of B_{eq} and P_{radio} that were calculated by the best fit modelling in § 3.6.2 for the lobe regions (Table 3.7) making the usual minimum energy conditions assumptions, we can estimate the minimum

pressure of the relativistic plasma, P_{radio}, which is given by

$$P_{radio} = \frac{B_{eq}^2}{2\mu_0\varepsilon} + \frac{(1+k)E_e}{3V\phi} \tag{3.3}$$

where E_e is the energy of the electron population, V is the volume of each region in the lobe shown in Figure 3.10, μ_0 is the permeability of free space (4π in cgs units or $4\pi \times 10^{-7}$ in SI), ϕ is the filling factor of the lobes (assumed to be 1) and k is the energy ratio of the non-radiating particles to the radiating relativistic electrons (assumed to be 1). The factor ε illustrates the ordering of the magnetic field and the value of $\varepsilon = 3$ indicating a tangled magnetic field was adopted here as in O'Sullivan et al. (2011).

Figure 3.11 shows the pressure profiles of the thermal gas (P_{Xray}) along with the profile of the radio pressure derived in this study, as a function of the distance from the source's centre. The X-ray pressure profile is drawn from the XMM-Newton analysis of O'Sullivan et al. (2011). As can be seen from Fig. 3.11 the X-ray pressure profile declines with radius as expected, while the pressure profile derived from the radio lobes rises with radius. The radio lobes appear to be underpressured with respect to the surrounding environment in all regions and in both lobes by a factor ranging from $\sim$2 to $\sim$30. We note that the O'Sullivan et al. (2011) IGM pressure profile is in excellent agreement with the earlier measurements of Croston et al. (2008), but that Croston et al. (2008) found a mean internal pressure for the radio lobes ($\sim 9\times10^{-13}$ erg cm^{-3}) slightly lower than the pressures we measure in the lobes.

A similar pressure imbalance has been found in previous lobe studies of other FR I radio sources, where P_{gas}/P_{radio} is usually >1, reaching values up to 100, assuming the standard equipartition arguments (e.g. Bîrzan et al., 2008; Croston et al., 2008; Dunn et al., 2005, 2010; Feretti et al., 1992). This can only suggest two possible situations for the radio

lobes in the case of 3C 270: 1) Deviation from minimun energy condition within the radio lobes with a higher magnetic field energy density or higher relativistic particle content than calculated, 2) the equipartition argument is still valid but either the radio lobes contain a significant amount of non-radiating particles that contribute to the internal pressure or the filling factor ϕ of the plasma is less than unity. Since we believe that jets entrain material in FR I galaxies and in this specific galaxy we have reason to think the filling factor might be ≤ 1 at the back of the lobes (volume overestimation including part of the brighter X-ray emitting gas near the cool core), we examine the implications of the lack of pressure balance in the case where equipartition stands.

Assuming that the radio lobes of 3C 270 are in approximate pressure equilibrium with the intergalactic medium (IGM), we have the ability to constrain the particle content of the lobes from the comparison of the apparent pressures of the relativistic plasma of the radio lobes and that of the thermal plasma of the IGM (e.g. Hardcastle & Worrall, 2000, Bîrzan et al. 2008).

In Table 3.8, the results shown for $(1+k)/\phi$ estimation were calculated by forcing P_{radio} to equal P_{gas} (note that in Table 3.6 we adopted a fixed $(1+k)/\phi = 2$). The regions of the radio pressure in this study were chosen so as to match the X-ray annuli used by O'Sullivan et al. (2011). Both lobes show the same trend with the $(1+k)/\phi$ factor rising as we move from the end of the jets (regions 4 and 8) to the back of the lobes near the core (regions 1 and 5). The size of the bins were not exactly equal so the increase of $(1+k)/\phi$ is not linear.

Assuming that the filling factor $\phi = 1$, the additional pressure required by the rise of $(1+k)/\phi$ in regions 2-4 and 6-8, as the plasma flows back through the lobes, can be given by the presence of non-radiative particles in the relativistic plasma of the lobes. The dominating non-radiating particles probably need to be introduced in the relativistic plasma via the

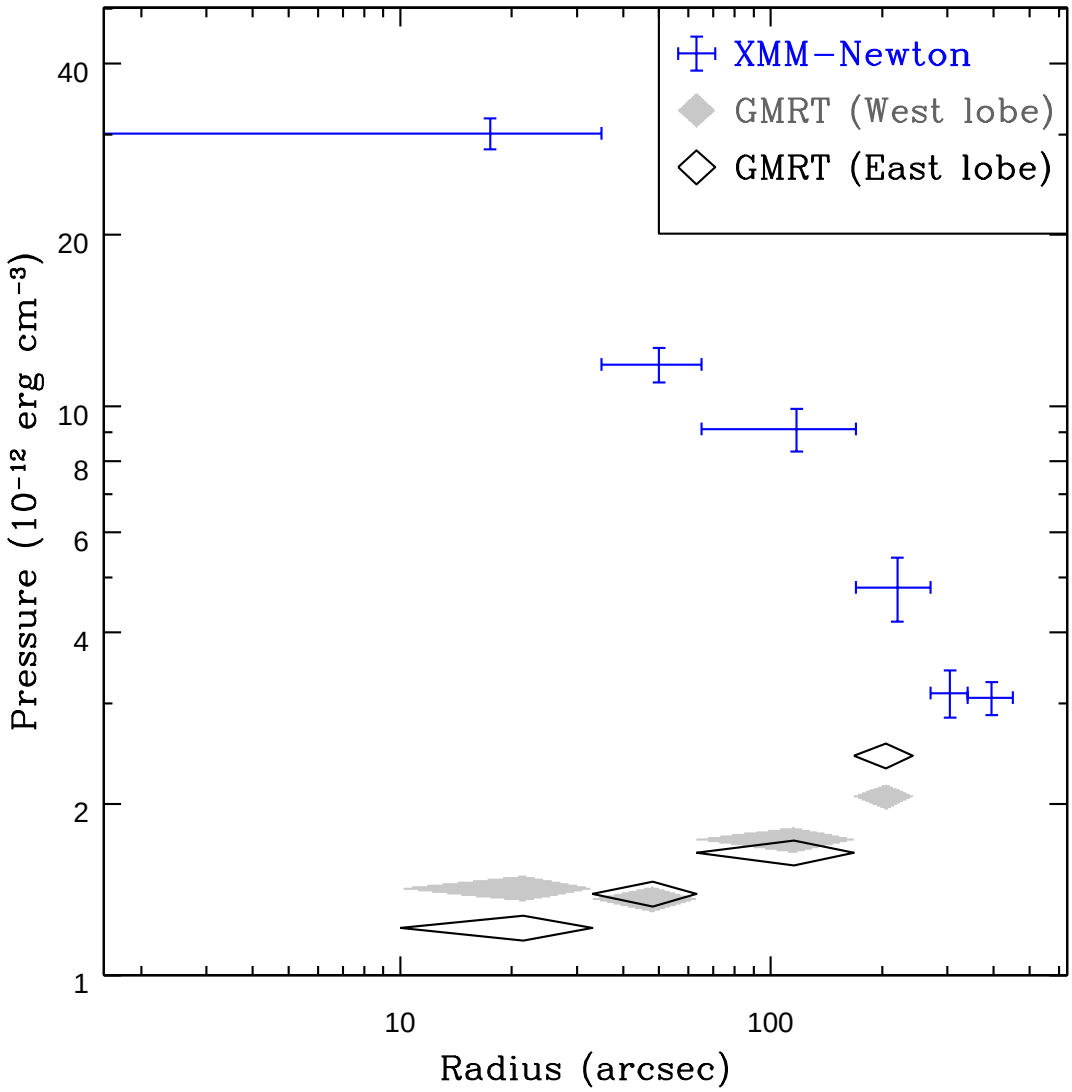

Figure 3.11 Deprojected pressure profile of X-ray thermal pressure and radio pressure with radius from the center of the source. This X-ray pressure profile was performed by co-author Dr. Ewan O'Sullivan

Table 3.8 In this Table is shown for each region the electron energy, the pressure in X-rays, the volume, the $(1+k)/\phi$ factor and the total energy

Region	E_e (10^{56} erg)	P_{Xray} (10^{-12}dyn cm^{-2})	V_{tot} (10^{67} cm^3)	$(1+k)/\phi$	Total energy (10^{56} erg)
West Lobe					
1	1.1	30.2	5.1	42.5	14.6
2	2.3	11.8	11.3	17.4	11.9
3	9.2	9.1	35.5	10.5	26.2
4	2.3	4.8	7.5	4.7	2.1
East Lobe					
5	0.6	30.2	3.1	49.8	9
6	1	11.8	4.8	17	5.1
7	7.1	9.1	28.7	11.1	21.4
8	5	4.8	13.7	3.9	3.3

entrainment and heating of thermal plasma by the radio jets. A probable source of entrained material for the radio jets, as has been suggested in Hardcastle et al. (2003) and Hardcastle et al. (2007) for the inner jets of Centaurus A, is the stellar mass-loss from stars within the jets. In O'Sullivan et al. (2011) the rate of stellar mass-loss from AGB stars into each jet was estimated to be $1.67 \times 10^{-3}\, M_{\odot}\, yr^{-1}$. By assuming a 36 Myr timescale for the AGN outburst, we expect a minimum of $\sim$60000 $M_{\odot}$ of stellar material to be entrained by each jet.

If the material entrained is in the form of thermal plasma mixed with the relativistic one in the radio lobes, we can use region 4 to estimate the minimum temperature required to balance the pressure of the surrounding IGM. The argument that the amount of material entrained is likely to have been picked up from stars, is applicable in region 4 and invalid for the other regions, since they almost certainly have additional entrained gas from the IGM. The minimum temperature is calculated by $k_B T = P_{Xray}/2n$ where P_{Xray} is the X-ray pressure in that region (Table 3.7) and n is the number density of the entrained material particles. The very low density of a plasma component like this ($n \sim 1.4 \times 10^{-7}$ cm^{-3})

means that no significant thermal or non-thermal emission is expected from it. $\mathbf{k_B T}$ is calculated to be 11 MeV which corresponds to a plasma of electrons with a Lorentz factor $\gamma \sim$20. Electrons of $\gamma \sim$20 are expected to radiate in the minimum-energy magnetic field at $\sim$1 kHz, making them invisible in the observable radio band. By summing up then $(P_{Xray} - P_{radio})V$ from each region, where V is the volume of each region, we estimate that the total energy (Table 3.7) required to heat up all the entrained material in the lobe to 11 MeV is $\sim 10^{58}$ erg.

On the other hand, the balance from the additional pressure could also be produced by a filling factor $<$1. This could occur in several ways: i) it is possible that a variation in the density of the relativistic particles and the magnetic field may exist; ii) there could be gas that has been entrained by the radio jets to the lobes and contributes as a radio-quiet plasma component (implying also $k > 1$) or iii) the volume of the lobe could be just overestimated so that it contains filaments of IGM plasma.

In regions 1 and 5, the large increase in the value of $(1+k)/\phi$ compared to other regions represents a more complicated situation. Since those parts of the lobes overlap with the brighter X-ray emission north and south of the cool core, a mixing of radio and X-ray emitting plasmas is possible, so part of that increase may be due to a decrease in the filling factor ϕ. In other words, the volume for the radio emitting plasma is likely to be overestimated in those regions and the values of k do not correspond to reality. We estimate the value of k based on the rate at which k increases as the plasma flows back from the lobe tips toward regions 1 and 5. We find that $k \sim$24 for region 1 and $k \sim$23 for region 5 which yields that $\phi \sim$0.59 for region 1 and $\phi \sim$0.48 for region 5.

In O'Sullivan et al. (2011) the total enthalpy, 4PV - the energy required to expand the lobe to its current size against the pressure of the IGM, plus the energy stored in the mag-

netic field and particles in the lobe - was estimated to be $\sim 2.4 \times 10^{58}$ erg. Our energy estimate of $\sim 10^{58}$ erg is about a third of the enthalpy estimated in O'Sullivan et al. (2011). This estimate changes little if the somewhat-lower filling factors in regions 1 and 5 are adopted. The difference of a factor 3 between the O'Sullivan et al. (2011) and our current energy estimate suggests that a fraction of the volume adopted by O'Sullivan et al. (2011) is occupied by thermal plasma, perhaps in the form of low density entrained material so the filling factor is probably less than unity (i.e. $\phi < 1$).

Guidetti et al. (2011) find a mean rotation measure (RM) across the source of 3C 270 of 14 rad m^{-2}. From a close examination of our 1.55−4.8 GHz spectral index map, the steep spectrum observed in regions 1 and 5, very close to the core, coincides with the area described in Guidetti et al. (2011). The steep spectrum of the emission from the lobe plasma observed, is assumed to be remnant from past nuclear activity, that was transported by the jets and flowed all the way back in to the galaxy core. Based on the mean RM value from Guidetti et al. (2011), we performed a calculation in order to see whether the internal RM produced by swept-up material is contributing to the Faraday depolarization. Following Feretti et al. (1999) we calculate the expected rotation measure from:

$$RM = 812 \int_0^L \mathrm{n_e B_z}\, \mathrm{dz} \tag{3.4}$$

where RM is the rotation measure in rad m^{-2}, $\mathrm{n_e}$ is the electron number density in cm^{-3}, $\mathrm{B_z}$ is the magnetic field along the line-of-sight in μG and L is the integration path (depth of the lobe along the line-of-sight) in kpc. Using the value of RM = 14 rad m^{-2} we find that an electron gas density of $\sim 2 \times 10^{-4}$ cm^{-3} would be required to produce the measured internal RM in Guidetti et al. (2011). The electron density of the thermal plasma that was entrained in the lobes ($\sim 1.4 \times 10^{-7}$ cm^{-3}) is therefore very low compared to the density required for

RM = 14 rad m^{-2} and it would have a minor contribution to the Faraday depolarization, with some RM structure across the source caused by magnetic and/or density substructure in the external thermal medium near the lobes.

We can also test whether regions 1 and 5, which we earlier suggested have filling factors less than unity, could contain a mix of thermal and relativistic plasmas, or whether it is more like that our adopted geometry leads us to overestimate their volume. If mixing has occurred, we expect to see depolarization. Using equation 4 and the IGM electron density derived from the X-rays in O'Sullivan et al. (2011) we find that we expect an internal RM of $\sim$ 500 rad m^{-2} for both regions, a value excluded by the polariation data, of Guidetti et al. (2011). This indicates that little 'mixing' between the thermal plasma and the relativistic one has occurred.

In summary, we have examined the constraints which can be placed on the particle populations in the radio lobes from the available radio and X-ray measurements. We find that only a relatively small mass of entrained gas is needed to bring the lobes into pressure equilibrium with their surroundings, and this is probably consistent with entrainment of stellar material lost from stars within the jets, and would not have detectable effects on the polarization.

3.8 Conclusions

In this paper, we have presented a detailed spectral analysis of the FR I radio source 3C 270, emanating from the nearby group-central elliptical galaxy NGC 4261. We have analysed 240 MHz and 610 MHz data from the GMRT, and data from the VLA at 1.55 GHz and 4.8 GHz.

Combining the analysed GMRT and VLA data with data from the literature at various

other frequencies (see Table 3.5) we derived the broadband radio spectrum of 3C 270 and found between 22 MHz and 33 GHz by the best fit Jaffe & Perola (JP) model (Fig. 3.4) an asymptotic low-frequency index of $\alpha_{inj} = 0.53^{+0.01}_{-0.02}$ and a steepening starting from ∼85 GHz. From the GMRT 240 MHz and VLA 1.55 GHz and 4.8 GHz, we calculated the spectral-index distribution at discrete intervals along the jets. The spectral-index maps we produced reveal a spectral index of α ∼0.16 for the unresolved core of the radio source, a constant spectral index along the jets of α ∼0.5 (Fig. 3.5) and a gradual steepening from the tip of the jets through the back of the lobes of α ∼0.8−1.2.

Assuming equipartition of energy between the magnetic field and the relativistic particles, and adopting a minimum Lorentz factor of $\gamma_{\rm min}$=100 for the radiating electrons, we estimate the radiative age of 3C 270. We performed a fit of the observed spectral index trend only along the region of the lobes (see Fig 3.7) for the 1.55 GHz - 4.8 GHz frequency range fitting a Jaffe & Perola (JP) model in each lobe (Fig. 3.8 & 3.9). We find a radiative age of $t_{\rm rad} \sim 29$ Myr for the west lobe and $t_{rad} \sim 36$ Myr for the eastern one (Table 3.6). The radiative ages derived from the best fit JP model suggests an age for the radio source of 29 − 36 Myr.

The radiative age is a factor of 2 younger than the dynamical age of 75 Myr found previously using X-ray data (O'Sullivan et al., 2011). We considered three possible scenarios for this discrepancy. The least likely scenario is that the lobe had a supersonic phase in the early life of the source and expanded into the IGM propagating a powerful shock of Mach 6 (3500 km s^{-1}), which is now beyond the field of view of the *XMM-Newton* telescope. While the constant flat spectral index in the jets may indicate that they are fast and that the radio estimates of the age are the true age of the radio lobes, the spectral index of the jets could be kept flat by reacceleration, caused by internal shocks in the jets or changes in the

jet power over time. In addition, the fact that the jets appear wide in the radio suggests they are not tightly confined, and the fact that we see no evidence of a strong shock in the X-ray, argues against a fast jet and a powerful shock.

In the second scenario we suggest that the radiative age indicates that we have a multiple AGN outburst or just large change in the jet power, where the radiative age corresponds to the newest outburst thus underestimating the true age of the source. Worrall et al. (2010) did see structure that could be caused by variations on about 10^4 yr timescales in the X-ray jet, while the effect of 'in situ acceleration' taking place near the jet in the lobes could also contribute in the underestimation of the age of the source.

In the third scenario a fast backflow that could transport young electrons to the back of the lobes relatively quickly, is considered to be the reason of the age underestimation. As most of the plasma in the lobe at any position will be old, in this scenario the injection of younger electrons is allowed, thus biasing the age young. So the radio ages that we find are probably not corresponding to the true age of the source but most likely trace the 'active age' of the radio emission in a mixed population of older and younger radio plasma.

Assuming that the pressure between the radio lobe and the hot X-ray emitting plasma surrounding the radio lobe is equal we calculate that the ratio of non-radiating to radiating particles, k, ranges from $\sim 4-24$ from the tip of the jets to the back of the lobes (Table 3.8, Fig. 3.10). This indicates that gas entrainment seems to occur throughout the jets and as the plasma flows back through the lobes. We assume a probable source of entrained material for the radio jets to be the stellar mass-loss from stars within the jets. We estimate the minimum temperature for the entrained material to balance the pressure of the surrounding IGM to be 11 MeV which corresponds to a total energy of $\sim 10^{58}$ erg (Table 3.8) that is required to heat up all the entrained material in the lobe to 11 MeV. This energy estimation is $\sim$39%

of the enthalpy estimated in O'Sullivan et al. (2011). Since the reduction of the lobe energy compared to O'Sullivan et al. (2011) by ∼65% is unlikely, we argue that the filling factor in regions 1 and 5 of the lobes is less than unity (i.e. $\phi < 1$) possibly occupied by thermal plasma, perhaps in the form of low density entrained material.

The number density of particles n from the estimate of entrained gas and the 1+k calculations is found, and then compared to the internal RM this would produce to Guidetti et al. (2011) measurements. The density of $\sim 1.4 \times 10^{-7}$ cm^{-3} indicates that the contribution of the entrained material to the Faraday depolarization is minor, most likely undetectable. In regions 1 and 5 where the thermal X-ray emitting plasma co-exists with the relativistic plasma, we would expect a RM of ~ 500 rad m^{-2} for both regions if mixing had taken place. The rotation measure calculated is much greater than observed by Guidetti et al. (2011) implying that little 'mixing' between the thermal and relativistic plasmas has occurred.

We conclude that the spectral ageing argument is relatively close to the sound travel time argument in setting the dynamical age of the source with the radiative age monitoring its 'active age'. If we consider that 3C 270 is typical of a population of young FRIs as a whole, we expect to see a population of such sources driving very strong shocks for maybe as long as 5 Myr, alongside with a population of groups and clusters with evidence of strong shock heating. No such populations have yet been identified, thus favoring the scenario that the jet appearance should go through many periods of change during the lifetime of a source.

Chapter 4

CLoGS : Properties of the groups and its central galaxies

4.1 CLoGS (Complete Local-Volume Group Sample)

In Chapter 1, we noted the importance of the study of galaxy evolution in groups of galaxies, since much of this evolution takes place while a galaxy is in the group environment. One of the main aspects of galaxy evolution which requires elucidation is the connection between galaxy evolution and the intergalactic medium (IGM) of a group or cluster, in the context of energy transfer to the IGM (often called "feedback") through a mechanism related to AGN or cycles of star formation. Observationally, to find the factors and processes that are important, one requires a sample of groups (or clusters) selected in a well-defined way so that the relevant parameters can be identified and estimated without any unknown biases. However, the choice of a statistically representative sample of groups of galaxies is a difficult task, as the results drawn from existing samples are open to various biases arising from the mechanism of identifying these systems.

Samples selected from optical catalogues detect a small number of group member galaxies at low mass systems, making them unreliable. For instance, the optically selected SDSS-based compact group catalogue of McConnachie et al. (2009) is complete to a magnitude limit, but no X-ray information is available for it. In this catalogue, the nearest groups are mostly made up of dwarfs, so they are probably of low mass and X-ray faint. Also, the focus of this sample is on compact groups, which are probably not representative of the total population of groups. Another example is the X-ray or optical group samples from the COSMOS survey field (e.g., Capak et al., 2007; Salvato et al., 2009) are both complete and relatively representative, but their groups are so distant that it is difficult to perform a detailed X-ray analysis to probe how AGN and galaxies interact with the IGM.

We discuss these biases in §1.6, and justify our choice of the sample used in this dissertation, the Complete Local-Volume Groups Sample (CLoGS) consisting of 53 groups within 80 Mpc. It is intended to be the first statistically complete sample of groups in the local Universe with X-ray, radio and optical coverage. At present, we have full coverage for only the richer half, consisting of 26 groups, which is our sample used in this Chapter and the next.

4.1.1 Sample selection

As discussed in §1.6, the sample of CLoGS groups was drawn from the shallow, all-sky Lyon Galaxy Group catalogue sample (LGG; Garcia 1993). The galaxies for this catalogue, were picked up using a friends-of-friends (FoF) analysis. The original catalogue from which the LGG sample is created is the Lyon-Meudon Extragalactic Database (LEDA) galaxy catalogue (Durand et al., 1994), complete to $m_B = 14$ and $v_r = 5500$ km/s (a distance $<$80 Mpc). Optical data were used to examine whether the groups are false, with the final sample

of galaxies containing only systems that were identified by both methods. The systems within the sample that we eventually selected, have a minimum of 4 members and at least one luminous early-type galaxy ($L_B > 3\times10^{10}$ $L_\odot$), all with a Declination $>30^\circ$.

Although Ponman et al. (1996) found that some spiral-rich groups do in fact contain X-ray emission, the detection of spiral-only groups in X-rays is impossible. This could be explained by the lower gas density that we see in spiral groups compared to other groups and the much lower temperature of the gas in spiral-only groups (Mulchaey et al., 2003). The main reason for selecting groups that have at least one early-type galaxy is that the presence of early-type galaxies in the group environment ensures a higher X-ray luminosity. This increases the probability that the group is collapsed with a detectable intragroup medium and that it has hosted in the past galaxy transformation processes (e.g. merging) (Mulchaey, 2000; Mulchaey et al., 2003), meaning that the group is at an evolutionary stage that it has already formed. The purpose of having a Declination greater than 30° is to make galaxies easily observable by both GMRT and VLA radio telescopes.

We then used the catalogue HyperLEDA (Paturel et al., 2003), which contains measured m_B within a velocity dispersion of 10.000 km/s, to extend and check the group membership by choosing galaxies which are within 1 Mpc and 2000 km/s of the brightest group-member early-type (BGE) galaxy. The mean group velocity and velocity dispersion is then estimated by using the gapper algorithm, from Beers et al. (1990). As group members then, we consider the galaxies that lie within 3σ of the mean velocity (see Figure 4.1 below). In our sample selection cluster subgroups and groups that had no obvious central galaxy density peak, along with cases where the position of the brightest group elliptical was misidentified, were re-evaluated. We finally end up with approximately 20 member galaxies for each group in our sample.

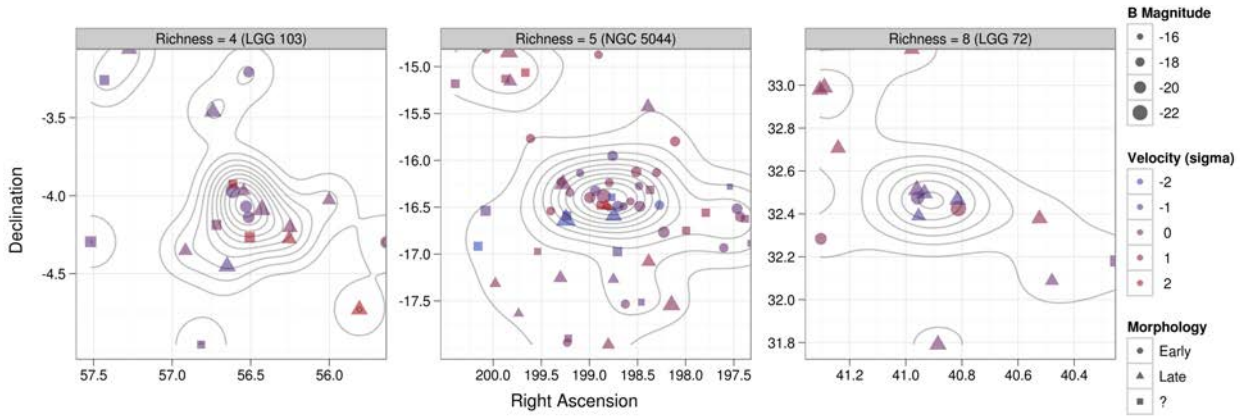

Figure 4.1 The spatial distribution of the CLoGS group member galaxies on isopleth maps (*http* : *//www.sr.bham.ac.uk/ ejos/CLoGS_Sample.html*).

4.1.2 Finding the centres of the groups

If we were aware of the location of the centre of the mass in any system, then we could easily define the centre of a group or a cluster. The dark matter halo of systems is not directly seen but only its weak gravitational lensing effect (Yang et al., 2006), a task quite difficult for groups of galaxies compared to clusters. The second best method to define the center of a group/cluster is by X-ray observations. The detection of the diffuse X-ray emission that confirms whether a group/cluster is gravitationally bound or not gives the center of the group as well. Unfortunately the problem with this method is that unlike clusters, most of the groups do not have diffuse X-ray emission (see §4.3.2).

For the purposes of this Thesis we therefore assume that the centre of mass of each of our groups coincides with the location of the BGE. In order though to evaluate the robustness of our group centre selection, we use a separate way to define the centre of our CLoGS groups.

In the absence of weak lensing estimates and diffuse X-ray emission for most of our groups, we test the method used in clusters from Pearson et al. 2014. This method uses the distribution of the galaxies. In more detail, the centres follow an iterative algorithm such that at each step a mean centroid is calculated, weighting each galaxy by its luminosity and

the inverse of its distance from a mean velocity. The galaxy that is furthest from this centre is discarded. This is repeated until only two galaxies remain, and a central galaxy is defined as the brightest of these two.

M_{500} for our CLoGS groups was estimated then by

$$log\Big(\frac{M_{500}}{10^{14}}\Big) = 0.0423 + log\Big(\frac{\sigma^3}{10^{8.3009}}\Big) \tag{4.1}$$

where σ is the velocity dispersion of each group in km/s. Using these values of calculated M_{500} we then estimate r_{500} adopting the formula of Pearson et al. 2014 assuming $v = cz$:Mulchaey0

$$R_{500} = \Big(\frac{M_{500}}{4/3\,\pi\,500\,\rho_{crit(z)}}\Big)^{1/3} \tag{4.2}$$

where $\rho_{crit(z)} = \frac{3H^2}{8\pi G} = 9.3 \times 10^{-27}$ Kg m^{-3} is the critical density of the Universe.

In Table 4.1 are shown the group centres and the estimations for M_{500} and R_{500} derived from this algorithm. Comparing to the BGE column in Table 4.1, we see that the group centres have been moved out of the BGE in more than half of our systems. This method was applied for the first time in groups of galaxies. We note that the M_{500} values for some of our systems (e.g. 10^{12} for NGC 930 and NGC 1587 or 0.5×10^{12} for NGC 5813 and NGC 4169) are slightly lower than the typical M_{500} low limit values considered in other samples of galaxy groups, as e.g. $1.4\times10^{12.5}-10^{14}$ M_{500} in Sun (2012). This is probably due to the very low velocity dispersion that some of our groups exhibit, which in some cases is almost comparable to the galaxy rotation speed as is known from Mulchaey (2000). A possible explanation for this is that some processes take place that are much more prevalent in groups than in clusters such as dynamical friction, tidal interactions and projection effects which reduce the velocity dispersion values of the galaxy groups (Vajgel et al., 2014). Therefore

Table 4.1 Properties of the Rich Sub-Sample Galaxy Groups

LGG Group Name	Central galaxy	M_{500} 10^{12} $M_{\odot}$	r_{500} kpc	σ km/s	BGE
LGG 018	NGC 403	33	479	393	NGC 410
LGG 345	NGC 5084	168	829	680	NGC 5084
LGG 027	NGC 584	2	197	160	NGC 584
LGG 061	NGC 930	1	156	126	NGC 924
LGG 031	NGC 677	9	306	249	NGC 677
LGG 363	NGC 5371	8	295	240	NGC 5353
LGG 351	NGC 5153	9	308	251	NGC 5153
LGG 402	NGC 5985	6.7	283	230	NGC 5982
LGG 310	ESO507-025	93	680	557	ESO507-025
LGG 421	NGC 6658	8	296	241	NGC 6658
LGG 276	NGC 4169	0.5	115	93	NGC 4169
LGG 262	NGC 4017	7	283	230	NGC 4008
LGG 158	NGC 2560	30	463	379	NGC 2563
LGG 042	NGC 777	14	357	291	NGC 777
LGG 058	NGC 940	7	281	229	NGC 940
LGG 185	IC2537	550	1231	1014	NGC 3078
LGG 066	NGC 969	5	257	209	NGC 978
LGG 072	NGC 1066	66	605	496	NGC 1060
LGG 103	NGC 1441	83	655	537	NGC 1453
LGG 393	NGC 5813	196	873	717	NGC 5846
LGG 080	NGC 1167	0.5	117	94	NGC 1167
LGG 117	NGC 1587	1	156	126	NGC 1587
LGG 009	NGC 194	64	601	493	NGC 193
LGG 473	NGC 7619	55	570	466	NGC 7619
LGG 338	NGC 5044	21	412	336	NGC 5044
LGG 278	NGC 4273	218	904	743	NGC 4261

these values in some of our groups could be considered as a sign of a mutual interaction that has 'slowed down' the galaxies in some of our systems due to their proximity. For example NGC 4169 (called 'The Box', see § 4.3.11), a system with the lowest velocity dispersion in our sample is in a very tight grouping with another two galaxies.

We present the results and the radial profiles from this method, applying also our initial group centre estimation to compare with the radial profiles that are discussed in Chapter 5.

4.2 Radio emission from group central galaxies

4.2.1 Overview

In this chapter we present for the first time the new low-frequency GMRT images at 235 and 610 MHz for the 21 groups of the CLoGS sample that we have analysed, along with 5 groups that were previously analysed by Dr. Simona Giacintucci in Giacintucci et al. (2011): NGC 193, NGC 7619, NGC 1587, NGC 5044 and NGC 5846. The mean sensitivity (rms) of the analysis is $\sim$0.08 mJy at 610 MHz and $\sim$0.6 mJy at 235 MHz. The theoritical values of noise calculated for our observations are 29 μJy for 610 MHz and 80 μJy for 235 MHz. The mean sensitivity achieved for 610 MHz is comparable to the theoritical noise while at 235 MHz the mean sensitivity is much higher than the theoritical one. The limiting luminosities over the redshift range of our sample are 5×10^{18} W Hz^{-1} – 5.8×10^{19} W Hz^{-1} at 610 MHz and 3.8×10^{19} W Hz^{-1} – 4.4×10^{20} W Hz^{-1}. All groups are listed in Table 4.2.

The radio images presented in this section are overlaid as contours on the red-band optical images from the Digitized Sky Survey (DSS) and on the X-ray images from *Chandra* or *XMM-Newton* observations. The conversion factor from angular to linear scale is mentioned in the caption of each figure and also, at the last column of Table 4.2. The X-ray images described in this chapter are drawn from the analysis of O'Sullivan et al., 2014 in prep.

In Table 4.7, the total flux densities at 235 MHz and 610 MHz are provided along with the spectral index α between these two frequencies for each radio source of the brightest group ellipticals. The flux densities were measured after the images were corrected for the primary beam attenuation with similar resolution at both frequencies. The error used associated with the flux density measurements, is the typical uncertainty in the residual amplitude calibration errors. That is 5% at 610 MHz and 8% at 235MHz.

The equatorial location (RA and DEC), the distance from our galaxy and the angular scale of the central group galaxies analysed, is shown in Table 4.2. For both frequencies the bandwidth used from the observations was 32 MHz except from the archival data for NGC 4261 where the bandwidth was 16 MHz at 235 MHz. A summary of the rms noise, resolution and position angle of the resulting radio images along with the details of the GMRT observations can be seen in Table 4.3.

We examine here the radio properties of the central only galaxies of each group: the number of central galaxies that host radio emission, the morphology of the radio emission and how these results compare to what is seen in clusters of galaxies or field galaxies to date. Then for all group members, the fraction of the radio to non-radio detected galaxies is examined, their connection to the morphology (which type of galaxies are the most probable to exhibit radio emission) and their distance from the centre of their group (radial profiles) using two different ways for the group centre definition.

Furthermore, a qualitative comparison between the GMRT radio images and the X-ray images from *Chandra* and *XMM-Newton* is performed, to examine any possible associations between the observed radio structures and the surrounding environment e.g. the amount of hot gas and the way its interaction with the source of the radio emission distributes it. The transportation of energy between the AGN and the IGM is yet not understood and requires the combination of multi-frequency radio data and high-quality X-ray observations to 'unlock' the processes involved. In general, detection of X-ray structures such as cavities (the detection of radio emmision where X-rays are not detected) and shocks, usually correlated with radio jets and lobes in many groups and clusters gives evidence of AGN heating (http://www.sr.bham.ac.uk/ ejos/CLoGS.html). So from the X-ray image we are able to trace the physical properties of the intra-group gas of galaxies (temperature, density,

Table 4.2 List of the Rich Sub-Sample Galaxy Groups

Group Name	BGE	Right Ascension (h m s)	Declination$_{(J2000)}$ $^\circ,',''$	Redshift (z)	Scale (kpc/$''$)
LGG 018	NGC 410	01 10 58.9	+33 09 07	0.017659	0.373
LGG 345	NGC 5084	13 20 16.9	-21 49 39	0.005741	0.112
LGG 027	NGC 584	01 31 20.7	-06 52 05	0.006011	0.121
LGG 061	NGC 924	02 26 46.8	+20 29 51	0.014880	0.310
LGG 031	NGC 677	01 49 14.0	+13 03 19	0.017012	0.378
LGG 363	NGC 5353	13 53 26.7	+40 16 59	0.007755	0.170
LGG 351	NGC 5153	13 27 54.3	-29 37 05	0.014413	0.291
LGG 402	NGC 5982	15 38 39.8	+59 21 21	0.010064	0.213
LGG 310	ESO 507-25	12 51 31.8	-26 27 07	0.010788	0.218
LGG 421	NGC 6658	18 33 55.6	+22 53 18	0.014243	0.305
LGG 276	NGC 4169	12 12 18.8	+29 10 46	0.012622	0.218
LGG 262	NGC 4008	11 58 17.0	+28 11 33	0.012075	0.262
LGG 158	NGC 2563	08 20 35.7	+21 04 04	0.014944	0.315
LGG 042	NGC 777	02 00 14.9	+31 25 46	0.016728	0.354
LGG 058	NGC 940	02 29 27.5	+31 38 27	0.017075	0.359
LGG 185	NGC 3078	09 58 24.6	-26 55 36	0.008606	0.165
LGG 066	NGC 978	02 34 47.6	+32 50 37	0.015794	0.334
LGG 072	NGC 1060	02 43 15.0	+32 25 30	0.017312	0.368
LGG 103	NGC 1453	03 46 27.2	-03 58 08	0.012962	0.305
LGG 393	NGC 5846	15 06 29.3	+01 36 20	0.005717	0.126
LGG 080	NGC 1167	03 01 42.4	+35 12 21	0.016495	0.349
LGG 117	NGC 1587	04 30 39.9	+00 39 43	0.0123	0.252
LGG 009	NGC 193	00 39 18.6	+03 19 52	0.014723	0.359
LGG 473	NGC 7619	23 20 14.5	+08 12 22	0.012549	0.262
LGG 338	NGC 5044	13 15 24.0	-16 23 08	0.009280	0.184
LGG 278	NGC 4261	12 19 23.2	+05 49 31	0.007465	0.155

entropy, etc.) that is surrounding each group.

Lastly, we examine the distribution of radio AGN within the member galaxies of our sample and the relative contribution that AGN feedback has in the group environment.

Table 4.3 Details of the GMRT Observations analysed in this Thesis

BGE	Observation Date	Frequency (MHz)	On source Time (minutes)	Beam, P.A. (Full array, $''\times''$, $^\circ$)	rms mJy beam^{-1}
NGC410	2011 Jul	610	218	6.97×4.09, 71.48	0.05
	2011 Jul	235	218	17.87×10.95, 50.40	0.40
NGC5084	2011 Jul	610	150	5.91×5.06, 29.68	0.05
	2011 Jul	235	150	15.71×12.62, -4.35	0.50
NGC584	2011 Jul	610	200	6.82×3.22, 59.80	0.20
	2011 Jul	235	200	17.87×10.95, 50.40	1.20
NGC924	2011 Jul	610	125	5.52×3.74, 56.25	0.05
	2011 Jul	235	125	12.40×10.43, 59.19	0.30
NGC677	2013 Oct	610	200	5.26×4.34, 68.59	0.04
	2013 Oct	235	200	12.94×10.76, 66.90	1.20
NGC5353	2011 Apr	610	207	5.92×4.44, -76.02	0.08
	2011 Apr	235	207	16.91×12.00, -79.87	0.30
NGC5153	2011 Apr	610	167	7.63×4.81, 26.32	0.06
	2011 Apr	235	167	16.01×11.25, 13.68	0.60
NGC5982	2011 Apr	610	237	7.99×6.47, -81.04	0.09
	2011 Apr	235	237	19.42×14.43, -63.66	0.40
ESO 507-25	2011 Apr	610	167	9.40×8.43, 2.59	0.10
	2011 Apr	235	167	15.59×12.22, 7.69	0.50
NGC 6658	2011 Apr	610	236	5.03×4.35, 55.03	0.05
	2011 Apr	235	236	12.82×10.30, 69.71	0.60
NGC 4169	2011 Apr	610	168	5.47×4.43, 61.96	0.08
	2011 Apr	235	168	13.94×10.78, 72.62	1.20
NGC 4008	2011 Apr	610	168	5.76×4.52, 78.93	0.05
	2011 Apr	235	168	14.38×11.78, 89.31	1.30
NGC 2563	2010 Dec	610	344	5.10×4.60, -57.85	0.07
	2010 Dec	235	344	11.88×9.93, 53.00	0.30
NGC 777	2010 Dec	610	338	5.71×4.76, -70.53	0.15
	2010 Dec	235	338	12.96×19.94, 65.78	0.40
NGC 940	2010 Dec	610	360	5.81×4.76, -75.11	0.06
	2010 Dec	235	360	13.27×11.16, 66.88	0.30
NGC 3078	2010 Dec	610	369	6.61×4.71, 2.38	0.20
	2010 Dec	235	369	16.02×10.99, 20.72	0.50
NGC 978	2010 Dec	610	341	5.81×4.65, -81.63	0.06
	2010 Dec	235	341	14.13×11.69, 76.74	0.40
NGC 1060	2010 Dec	610	286	3.97×3.54, -86.98	0.09
	2010 Dec	235	286	13.97×11.87, 81.36	0.50
NGC 1453	2011 Nov	610	187	7.99×4.60, 48.98	0.06
	2013 Oct	235	258	16.06×11.34, 58.47	0.60
NGC 5846	2012 Mar	235	145	14.02×11.27, 85.70	0.50
NGC 1167	2011 Jul	610	139	7.41×4.04, 68.27	3.95
	2011 Jul	235	139	16.08×10.40, 66.80	5.00
NGC 4261	2009 Feb	610	270	7.32×4.77, 76.62	1.00
	2009 Feb	235	270	15.30×11.00, 67.17	1.60

Table 4.4 Information on radio data analysed from previous work

Source	Frequency (MHz)	Beam, P.A. (Full array, $''\times''$, $^\circ$)	rms mJy beam^{-1}
NGC 5846	610	6.0×5.5, -84	0.06
NGC 1587	610	5.7×4.7, 67	0.05
	235	17.2×11.0, 46	1.00
NGC 193	610	7.0×6.0, 0	0.08
	235	13.5×12.9, -55	0.80
NGC 7619	610	6.1×4.6, 39	0.10
	235	34.6×11.3, -41.4	1.20
NGC 5044	610	6.2×4.4, 41.9	0.1
	235	15.9×11.3, -4.6	0.80

4.3 Radio and X-ray images

4.3.1 NGC 410

NGC 410 is the dominant elliptical of LGG 18 group. The NRAO VLA Sky Survey (NVSS) has detected a 6.3 mJy source Condon et al. (1998). The very high resolution X-band ($\sim2''$ at 8.4 GHz) system of the VLA has detected a 1.7 mJy unresolved core, coincident with the optical nucleus of the galaxy (Filho et al., 2002). The galaxy is characterized as Low-Ionization Emission Region (LINER) and exhibits Fe emission lines in the X-ray band (González-Martín et al., 2009). In the study of González-Martín et al. (2009) is revealed that the combination of X-rays, the lack of UV variability, broad Hα emission line and radio classifications at 2cm, in NGC 410 shows no evidence of any type of AGN.

We observed the radio galaxy with the GMRT at 235 MHz and 610 MHz. Figure 4.2 shows on the left the 610 MHz contours overlaid on the optical image while on the right the X-ray emission from the group with the 235 MHz contours overlaid. The radio emission detects a compact radio core, slightly elongated at both frequencies, with a small extension of $\sim$2kpc towards the east. At 610 MHz the flux density is 13.6 mJy while at 235 MHz is

28.5 mJy, with a steep spectral index of ∼0.78 indicative of past radio emission. As it is unlikely that this radio emission to be from star-formation due to the lack of UV variability examined earlier by González-Martín et al. (2009) we conclude from our radio observation that NGC 410 hosts a radio AGN.

In the X-ray image of the smoothed 0.3-2.0 KeV of *XMM-Newton*, a group scale gaseous halo is detected with the X-ray emission of the group traced to 75 kpc. A characteristic temperature of ∼1 keV is found, typical of a moderate mass group.

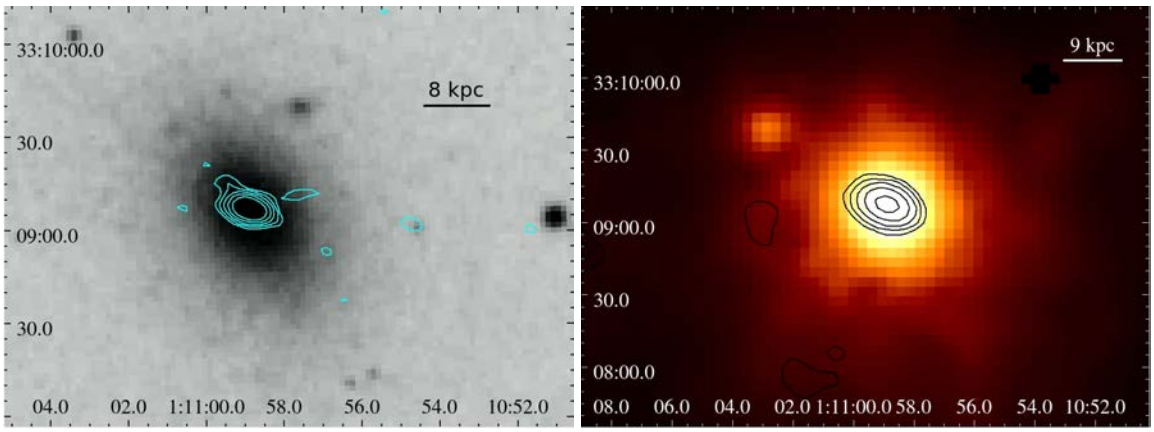

Figure 4.2 NGC 410. GMRT 610 MHz contours (1σ = 50 μJy beam^{-1}), overlaid on the optical SAO/DSS image (left). Contours start from 150 μJys (3 x r.m.s.) and increase by a factor of 2. On the right, GMRT 235 MHz contours (1σ = 400 μJy beam^{-1}) are overlaid on smoothed, 0.3-2.0 KeV *XMM-Newton* image. Contours start from 3σ and increase by a factor of 2. For this source the scale is 0.373 kpc arcsec^{-1}

4.3.2 NGC 5084

NGC 5084 is a massive central disk galaxy in a group orbited by several dwarf satellite galaxies Zeilinger et al. (1990). Zeilinger et al. (1990) first proposed that NGC 5084's massive structure might be explained by accretions of mass from its environment, with the galaxy now believed to be recovering from a recent merger event, probably with what was once a dwarf companion. More evidence is given by the distorted nature of its inner

regions (Carignan et al., 1997) and from its total HI mass which yields a very high $M_{(H)}/L_{(B)}$ $\sim$0.35 for a galaxy of this type, indicative of fresh gas accreted during a merger (vanDriel et al., 1991). On the radio side, the galaxy shows radio emission on earlier NVSS 1.4 GHz (Condon et al., 1998) (Table 4.7).

Our GMRT images are shown in Figure 4.3. On the left, the 610 MHz are overlaid in the optical SDSS image, while on the right, the X-ray emission of the group is shown with the 235 MHz contours overlaid. As can be seen, there isn't any radio detection in both of the GMRT frequencies for NGC 5084. The same applies for its dwarf companion ESO 576-031.

The X-ray image of the smoothed 0.3-2.0 KeV of *Chandra* reveals a central source dominated (probably an absorbed AGN) X-ray emission extending to $\sim$11 kpc.

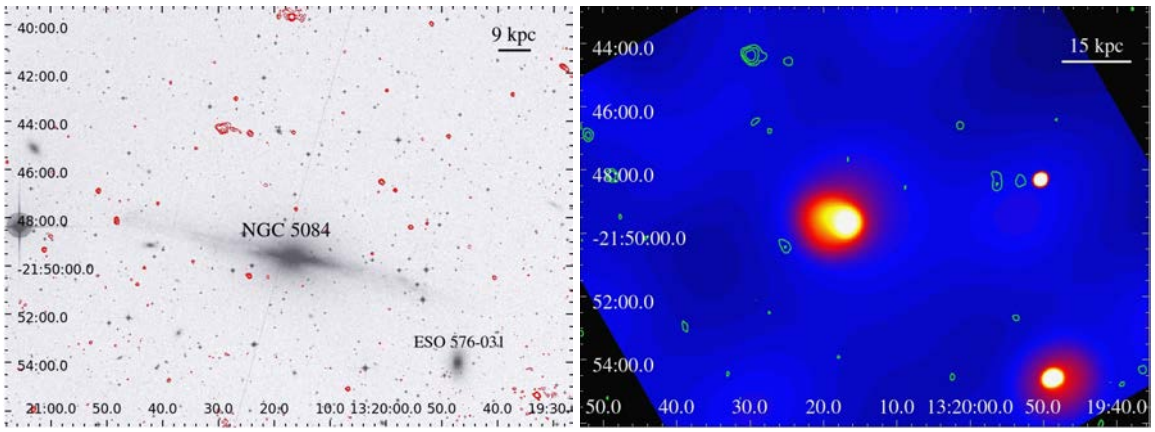

Figure 4.3 NGC 5084. GMRT 610 MHz contours (1σ = 50 μJy beam^{-1}), overlaid on the optical SAO/DSS image (left). Contours start from 150 μJys (3 x r.m.s.) and increase by a factor of 2. On the right, GMRT 235 MHz contours (1σ = 500 μJy beam^{-1}) are overlaid on smoothed, 0.3-2.0 KeV *Chandra* image. Contours start from 3σ and increase by a factor of 2. For this source the scale is 0.112 kpc arcsec^{-1}

4.3.3 NGC 584

NGC 584 is the dominant member of a small group of galaxies, where the measured radial velocities that include all of its members, suggest that NGC 584 is not the center of the

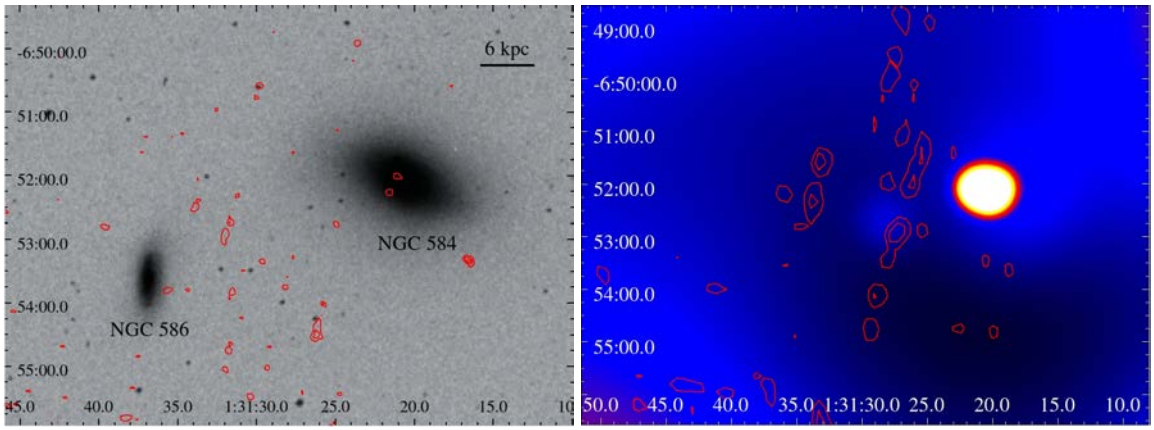

Figure 4.4 NGC 584. GMRT 610 MHz contours (1σ = 50 μJy beam^{-1}), overlaid on the optical SAO/DSS image (left). Contours start from 150 μJys (3 x r.m.s.) and increase by a factor of 2. On the right, GMRT 235 MHz contours (1σ = 500 μJy beam^{-1}) are overlaid on smoothed, 0.3-2.0 KeV *Chandra* image. Contours start from 3σ and increase by a factor of 2. For this source the scale is 0.121 kpc arcsec^{-1}

groups gravitanional potential (Madore et al., 2004). It is a lenticular galaxy that is suspected to be a merger remnant (Trager et al., 2000) and also an excellent candidate for the study of recent star formation in merger systems (Schweizer et al., 2000). Its companion galaxy, NGC 586, lies $\sim$30 kpc from NGC 584 in the plane of the sky. NGC 584 has a very low power radio emission at 1.4 GHz (Condon et al., 1998) as can be seen from Table 4.7.

The 610 and 235 MHz GMRT images show no radio detections at these frequencies as can be seen from Figure 4.4. The contours that coincide with the core of optical component of NGC 584 at both frequencies, are from the high residual noise of the map. The increased noise level at both GMRT images is because of two very strong background radio sources, $\sim$5 and $\sim$7 Jy at 235 MHz, very close to NGC 584. We set the upper limit for the radio detection of this galaxy at 5σ, as shown in Table 4.7, which is 1 mJy for 610 MHz and 6 mJy for 235 MHz.

The X-ray image of the smoothed 0.3-2.0 KeV of *Chandra* reveals a central source dominated X-ray emission with a total size of $\sim$5 kpc.

4.3.4 NGC 924

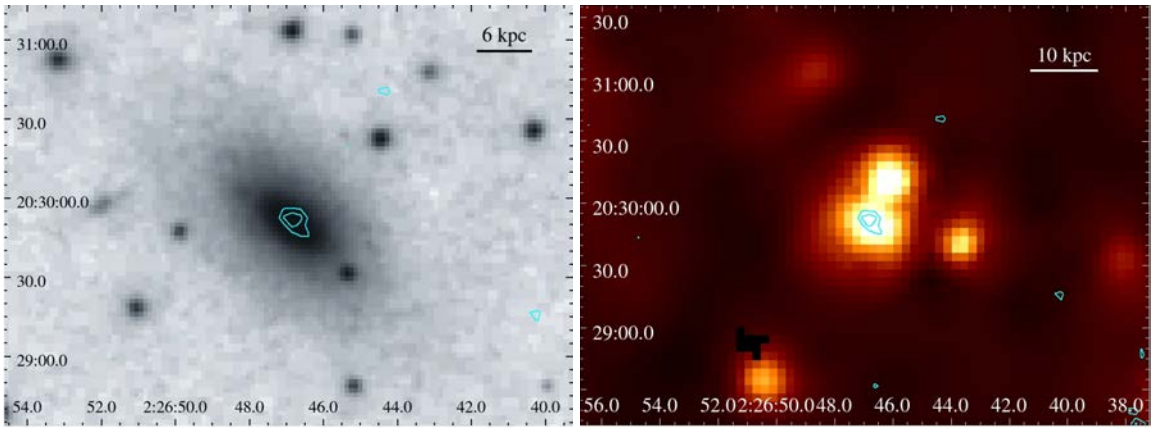

Figure 4.5 NGC 924. GMRT 610 MHz contours (1σ = 50 μJy beam^{-1}), overlaid on the optical SAO/DSS image (left). Contours start from 150 μJys (3 x r.m.s.) and increase by a factor of 2. On the right, GMRT 610 MHz contours are overlaid on smoothed, 0.3-2.0 KeV *XMM-Newton* image. For this source the scale is 0.310 kpc arcsec^{-1}

NGC 924 is a late type galaxy in a small group with a few companions. There is no previous study for that system in the radio wavelengths. Our GMRT 610 MHz image is presented in Figure 4.5 (left) as contours overlaid on the optical image. A weak point source which is associated with NGC 924 is detected. On the other hand at 235 MHz no radio emission is detected. The upper limit set for that frequency is 1.5 mJy, at 5σ level of significance (Table 4.7). On the right panel of Figure 4.5 the 610 MHz image is shown as contours overlaid on the smooth 0.3-2 KeV XMM-Newton.

The group in the smoothed 0.3-2.0 KeV of *XMM-Newton* appears to be point source dominated in the X-rays with the emission traced out to $\sim$9 kpc.

4.3.5 NGC 677

The elliptical (E0) galaxy NGC 677 lies at the center of a relaxed group with several neighbouring disk galaxies, exhibiting strong emission lines, classified as a LINER AGN from

the analysis of its emission line spectrum (Zhao et al., 2006). Previous 1.4 GHz from NVSS detects a radio source of 20.6 mJy (Condon et al., 1998).

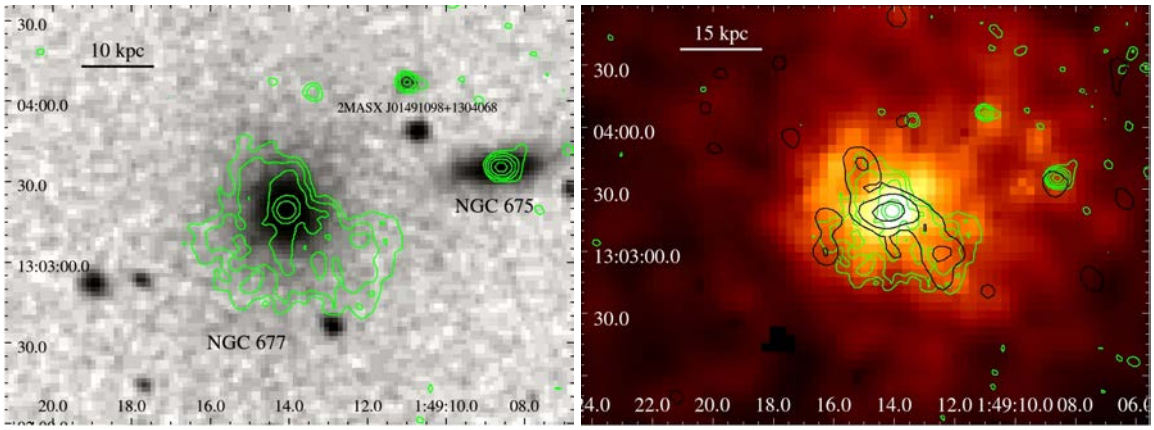

Figure 4.6 NGC 677. GMRT 610 MHz contours (1σ = 40 μJy beam^{-1}), overlaid on the optical SAO/DSS image (left). Contours start from 120 μJys (3 x r.m.s.) and increase by a factor of 2. On the right, GMRT 235 MHz contours in black (1σ = 1.2 mJy beam^{-1}) are overlaid on smoothed, 0.3-2.0 KeV *XMM-Newton* image. Contours start from 3σ and increase by a factor of 2. The contours in green on the right panel correspond to the 610 MHz emission. For this source the scale is 0.378 kpc arcsec^{-1}

Our GMRT images are presented in Figure 4.6. On the left, the 610 MHz emission is shown overlaid on the optical image. The right panel presents the 235 MHz contours overlaid on the 0.2-3 KeV XMM-Newton image. The morphology of NGC 677 at 610 MHz, is characterised by a very diffuse component mostly extending south of the galaxy. This blob of diffuse emission which is spherical-like, covers a scale of $\sim$30 kpc in width. On the other hand this is not what is seen at 235 MHz. The radio source has an assymetric twin-jet structure, that bends towards the west to the south and towards the east to the north. The total size of this structure at 235 MHz is $\sim$30 kpc with its main component being south of the galaxy. Furthermore, a separated component of $\sim$10 kpc, detached from the jet emission, is seen southeast of NGC 677. At 610 MHz the flux density for this galaxy is 45.6 mJy while at 235 MHz is 99.2 mJy, having a steep spectral index of $\sim$0.81. The emission appears as if an irregular halo surrounds the central component, having also an indication of

a jet connecting the point source and the extended emission at 610 MHz.

From its irregular spiral companions NGC 675 and 2MASX J01491098+1304068, GMRT detects a compact bright radio emission for each at both frequencies. In NGC 675 the flux density at 610 MHz is 4.3 mJys and 6.7 mJy at 235 MHz while in 2MASX J01491098+1304068 the flux density at 610 MHz is only 1.2 mJys without detection at 235 MHz. The radio emission from the two disk galaxies coincides in both galaxies with the disk of the optical component.

The X-ray emission from the smoothed 0.3-2.0 KeV image of *XMM-Newton*, reveals a group-scale gaseous halo with the X-ray emission of the group traced to 130 kpc. A characteristic temperature of $\sim$0.8 keV is found for this system.

4.3.6 NGC 5353

NGC 5353 is an edge-on spiral galaxy (S0) placed in the intermediate mass (2.1×10^{13} $M_{\odot}$) NGC 5353/4 Group and is the second brightest galaxy in that group among with 55 other galaxies, most of which either spiral or of unknown morphology (Hickson, 1982). It is considered as a group and not as a cluster despite its many members because of its low X-ray temperature. The five large galaxies near the group center are known as the sub-component Hickson Compact Group (HCG) 68 (Hickson, 1982). The most luminous galaxy in the group is the Sb system NGC 5371 but the dynamical center is coincident with the second, -and third- brightest galaxies, the S0 pair NGC 5353 and NGC 5354 (Tully et al., 2008). This is the dominant pair, with their projected separation being only 9 kpc and is suspected to be in the process of merging (Tully et al., 2008). The combined luminosity of the resultant galaxy from their imminent merging will make it the dominant in the group (Tully et al., 2008). Previous NVSS at 1.4 GHz detects point radio sources with flux density

of 41 mJy in NGC 5353 and of 8.4 mJy in NGC 5354 Condon et al. (1998).

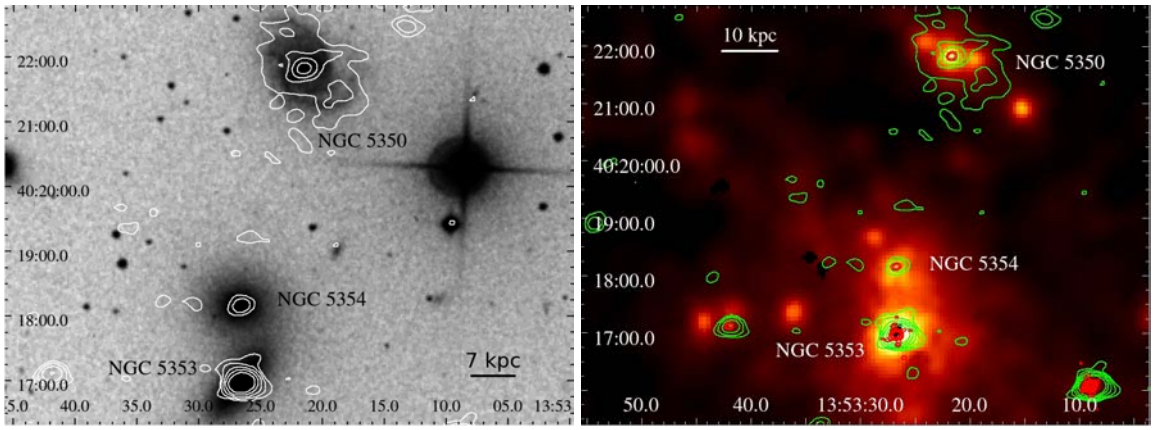

Figure 4.7 NGC 5353. GMRT 235 MHz contours (1σ = 600 μJy beam^{-1}) overlaid on the optical SAO/DSS image (left). Contours start from 3σ and increase by a factor of 2. On the right, GMRT 610 MHz contours (1σ = 60 μJy beam^{-1}), are overlaid on smoothed, 0.3-2.0 KeV *XMM-Newton* image (red). Contours start at 4σ and increase by a factor of 2. The contours in green on the right panel correspond to the 235 MHz emission from the left. For this source the scale is 0.170 kpc arcsec^{-1}

In Figure 4.7 the left panel shows the 235 MHz contours overlaid on the optical image and the right one the 610 MHz radio emission overlaid on the *XMM-Newton* image. The radio analysis performed at 610 MHz clearly detects a compact radio point source that coincides with the central regions of the optical components of NGC 5353 and NGC 5354 while extended diffuse emission is detected in NGC 5350. There is a hint of diffuse emission to the north direction in NGC 5353. The rms noise level at this frequency was assumed to be 200 μJy/beam for the central area of the group where the three detected galaxies reside, due to a very strong background radio source nearby. This causes a lot of structure in the noise, producing false structures symmetrically distributed in the eastwest direction of NGC 5353, possibly due to bad calibration. For that reason the contour levels at 610 MHz started at 4σ level of significance in order to avoid that issue.

On the other hand at 235 MHz in NGC 5353 a compact bright component is detected, but a bit more extended than the 610 MHz, covering all the galaxy and not only the central

region. The very flat spectral index of 0.38 indicates that the radio emission from the central point source is possibly due to a young AGN. In the face-on spiral, NGC 5350, the GMRT 235 MHz reveals a compact central point source and a faint diffuse radio structure which corresponds to the disk of the galaxy indicating that the radio emission comes from star formation.

The X-ray emission from the smoothed 0.3-2.0 KeV image of *XMM-Newton*, reveals a group-scale gaseous halo with the X-ray emission of the group traced to 100 kpc. Also a characteristic temperature of $\sim$0.8 keV is found for this system.

4.3.7 NGC 5153

NGC 5153 is an E_1 type[1] elliptical galaxy and is part of a close interaction with the Sb spiral NGC 5152 (Weilbacher et al., 2000). There is no previous radio measurement for this system.

Our GMRT image at 610 MHz is presented in Figure 4.8 as contours overlaid on the optical image. No emission is detected in radio from NGC 5153. We detect point sources associated with the centers of NGC 5152 and the 2MASX nomenclature spiral. In addition to these, in NGC 5150 there is a slightly extended emission associated with the disk of the spiral in the north-south direction and a similar emission from the 2MASX spiral towards the one side of the disk. At 235 MHz no detection was found at any galaxy. The interaction of NGC 5153 with NGC 5152 seems to be very 'relaxed' as no radio AGN activity has been triggered yet on NGC 5153 possibly implying that there is no significant gas supply from the spiral NGC 5152.

On the X-ray side, the smoothed 0.3-2.0 KeV image of *Chandra* reveals a central source

[1]Hubble type classification by NASA/IPAC Extragalactic Database (NED, http://ned.ipac.caltech.edu)

dominated X-ray emission with a total size of $\sim 6 - 15$ kpc. A characteristic temperature of $\sim$0.6 keV is found for this system.

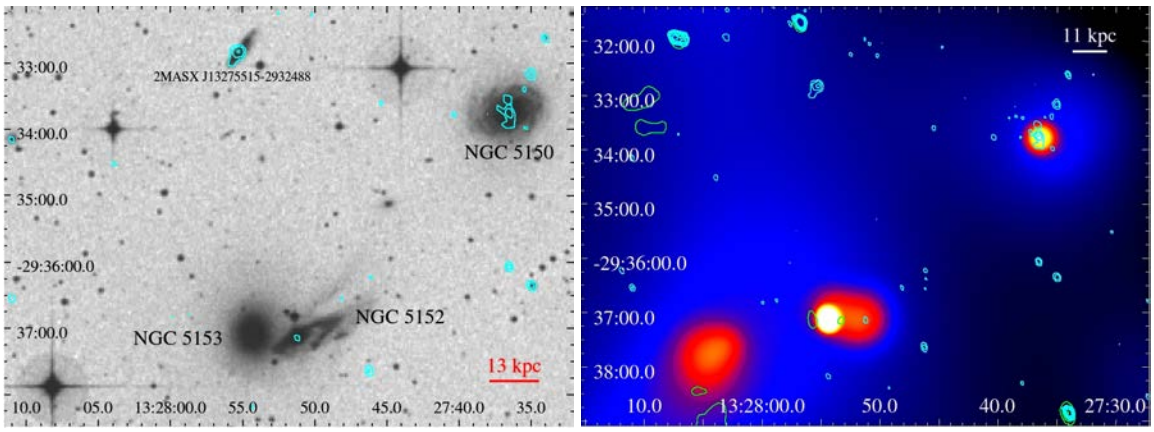

Figure 4.8 NGC 5153. GMRT 610 MHz contours (1σ = 60 μJy beam^{-1}), overlaid on the optical SAO/DSS image (left). Contours start at 3σ and increase by a factor of 2. On the right, GMRT 235 MHz contours (1σ = 0.3 μJy beam^{-1}) are overlaid on smoothed, 0.3-2.0 KeV *Chandra* image (green). Contours start from 3σ and increase by a factor of 2. The contours in cyan on the right panel correspond to the 610 MHz emission. For this source the scale is 0.291 kpc arcsec^{-1}

4.3.8 NGC 5982

LGG 402 is a relatively poor, nearby group (D=44 Mpc) (Garcia, 1993) dominated by the face-on elliptical NGC 5982 and two large spiral galaxies: the edge-on barred spiral galaxy NGC 5981 and the face-on barred spiral galaxy (Seyfert) NGC 5985. The group is also known as 'Draco Trio'. GMRT 610 and 235 MHz observations (Figure 4.9) detect weak, point-like AGN in all three galaxies with the addition of star-formation from the two disk galaxies. The emission from the two spirals, suggests that the diffuse emission from the disks (star formation) was developed independently from the central source. In the center of the main elliptical, NGC 5982, which is suggested to be a product of a minor merger (Del Burgo, Carter, & Sikkema, 2008), there is a clear indication of an AGN radio point source but with no evidence of jets or lobes. The rms noise level at 610 MHz is $\sim$90 μJy/beam and

the radio flux densities of the visible galaxies here are: 2.5 mJy for NGC 5982, 44 mJy for NGC 5985 and 6.4 mJy for NGC 5981. The spectral index of $\alpha_{240}^{610} = 1$ is an indication of an old, low power AGN.

In Brown et al. (2011) it is noted that radio emission from the central regions of massive galaxies (AGN) does not necessarily lead to a control of star formation, as there are cases (e.g., Baldi & Capetti, 2009) where the AGN has a small effect on the ionised gas that surrounds the central source. On the other hand, massive galaxies that do not present any radio emission, might exhibit short periods of AGN activity that are adequate to quench star formation (Hopkins et al., 2006).

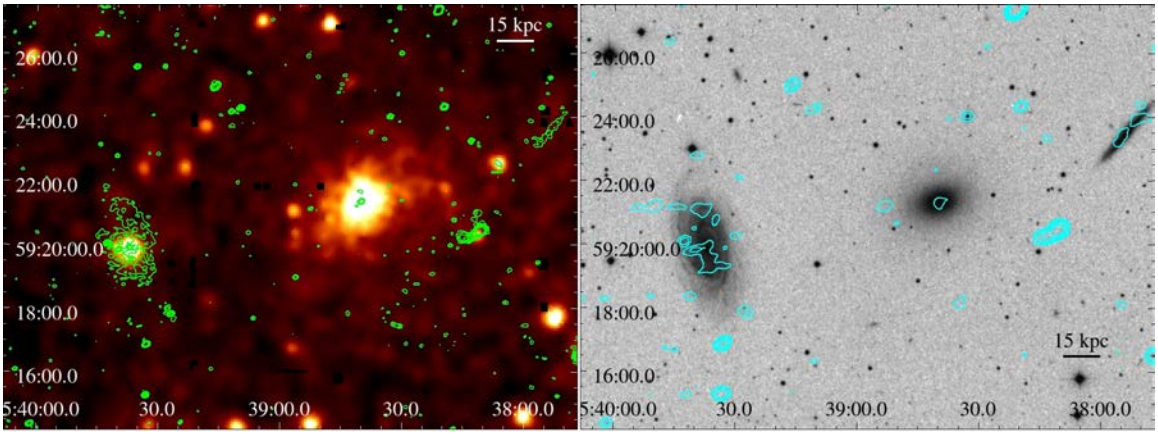

Figure 4.9 NGC 5982. GMRT 610 MHz contours (1σ = 90 μJy beam^{-1}), overlaid on smoothed, 0.3-2.0 KeV *XMM-Newton* image (green) (left). Contours start at 3σ and increase by a factor of 2. On the right, GMRT 235 MHz contours (1σ = 0.4 μJy beam^{-1}) are overlaid on the optical SAO/DSS image. Contours start from 3σ and increase by a factor of 2. For this source the scale is 0.213 kpc arcsec^{-1}

A short XMM pointing reveals a $\sim$0.5 keV IGM centred on the elliptical and detected out to 85 kpc, approximately the projected distance to the neighbouring spirals. The IGM appears relaxed with no obvious substructure suggesting that heating or disruption of a cool core by a merger or AGN outburst is unlikely.

4.3.9 ESO 507-25

ESO 507-25 is an elliptical galaxy in a nearby group (D=25 Mpc) with an indication of dense cold gas in its inner regions from the presence of weak broad CO emission line (Knapp et al., 1996). Previous NVSS data at 1.4 GHz detect a weak 24 mJy point source Brown et al. (2011).

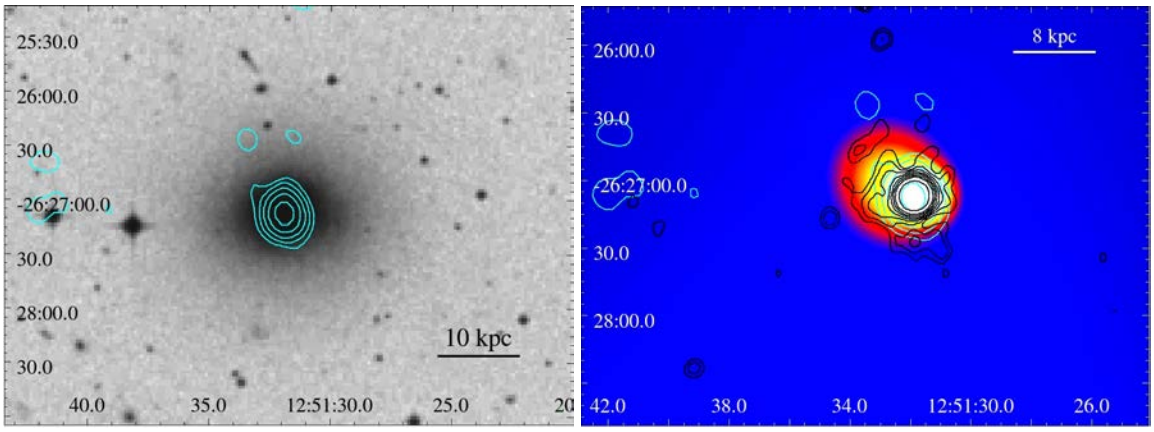

Figure 4.10 ESO 507-25. GMRT 235 MHz contours (1σ = 500 μJy beam^{-1}), overlaid on the optical SAO/DSS image (left). Contours start at 3σ and increase by a factor of 2. On the right, GMRT 610 MHz contours (1σ = 100 μJy beam^{-1}) are overlaid on smoothed, 0.3-2.0 KeV *Chandra* image. Contours start from 3σ and increase by a factor of 2. The contours in cyan on the right panel correspond to the 235 MHz emission. For this source the scale is 0.218 kpc arcsec^{-1}

In Figure 4.10 the 235 MHz is presented (left) as contours overlaid on the optical image. The 610 MHz contours are overlaid on the XMM-Newton image (right). The morphology of ESO 507-25 at the higher frequency is characterized by a point source surrounded by an assymetric diffuse component but with separated blobs of emission north and south of the central region of the galaxy. The 235 MHz does not detect a diffuse component but only a compact central radio point source coincident with the central region of the optical galaxy with a hint of extension to the north-east direction. No jets connecting the point source with the diffuse emission are detected in our images at 610 MHz. The very flat spectral index (α=0.18) that may indicate a young age for the outburst, is a possible explanation of why

the diffuse emission is only visible in the higher frequency. On the other hand, this could just be a resolution issue.

In the X-rays, the image of the smoothed 0.3-2.0 KeV of *Chandra* reveals a central source dominated (galaxy scale) X-ray emission with a total size of $\sim$6 kpc.

4.3.10 NGC 6658

NGC 6658 is an edge-on SO type galaxy in a poor group of galaxies with a few only members (Garcia, 1993). The galaxy was not observed before in radio and our GMRT observations find no radio detection at any frequency (Figure 4.11). The flux density upper limit set for this galaxy at 5σ level of significance is 0.3 mJy for 610 MHz and 3 mJy for 235 MHz (Table 4.7). Figure 4.11 shows only a point source detected in the spiral companion NGC 6660.

In the X-rays, the smoothed 0.3-2.0 KeV of *XMM-Newton* reveals that the group is point source dominated with the emission traced to $<$9 kpc. A characteristic temperature of $\sim$0.3 keV is found for this system.

4.3.11 NGC 4169

NGC 4169 is the brightest member in Hickson 61 group (Hickson, 1982). It is a lenticular S0 type galaxy[1] in a very tight grouping with another three galaxies (NGC 4173, NGC 4174, NGC 4175) that form a nearly perfect rectangle, sometimes called "The Box". The group has an interesting feature with the two highly elongated galaxies (NGC 4173, NGC 4175) being in a straight line. Previous 1.4 GHz from NVSS detects for NGC 4169 a very weak point radio source of $\sim$1 mJy (Table 4.7).

[1] NED

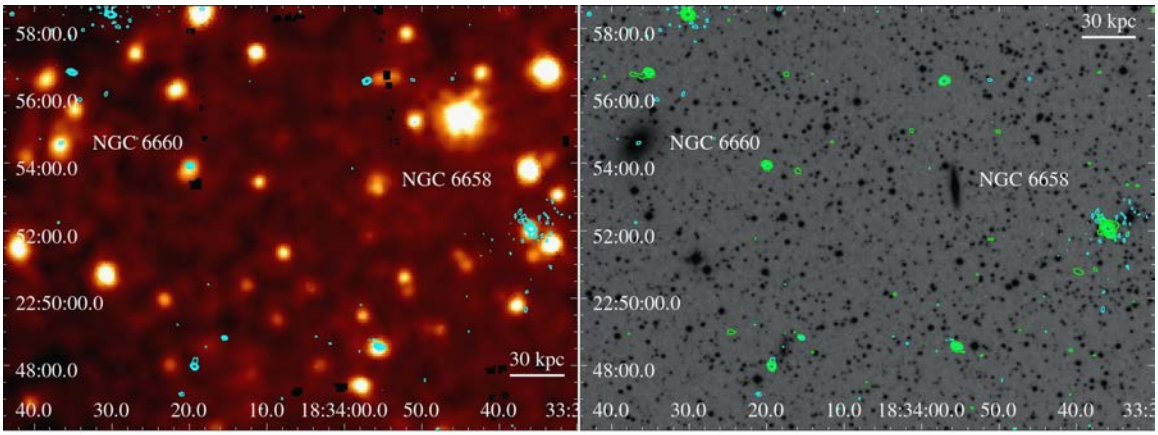

Figure 4.11 NGC 6658. GMRT 610 MHz (1σ = 50 μJy beam^{-1}), overlaid on the adaptively smoothed, 0.3-2.0 KeV of *XMM-Newton* image (left) and GMRT 235 MHz contours (1σ = 0.6 mJy beam^{-1}), overlaid on the optical SAO/DSS image. In both panels the radio contours are spaced by a factor of two, start from 3σ. The contours in cyan on the right panel correspond to the 610 MHz emission. For this source the scale is 0.305 kpc arcsec^{-1}

The characteristics of its close companions are as follows. NGC 4174 is the smallest apparent galaxy in the local group, with a NED classification of SO. This small galaxy is similar in structure and brightness to the NGC 4169 galaxy, only at a much smaller size. NGC 4175 is an edge-on barred (Sbc) spiral galaxy that exhibits clumps of gas and dust. Lastly, NGC 4173 is the faintest of all galaxies classified by NED as a barred spiral (SBd) galaxy (Herald-Bobroff Astroatlas, 2000). In Mendes (1995) is indicated by the recessional velocities that NGC 4173 is a foreground object not physically associated with the group despite the coincidental evidence of interaction.

The GMRT full resolution at 610 MHz is presented in Figure 4.12 (left) as contours on the *XMM-Newton* image. In the right panel is shown the overlay of the 235 MHz contours on the optical image. We detect a radio point source coincident with the center of NGC 4169 galaxy with a flux density of 3 mJy at 610 MHz while no detection is seen at 235 MHz. The upper limit placed for the 235 MHz is placed at 5σ level of significance at 6 mJy. On the other hand the spiral NGC 4175 is detected at both frequencies. At 610 MHz the source

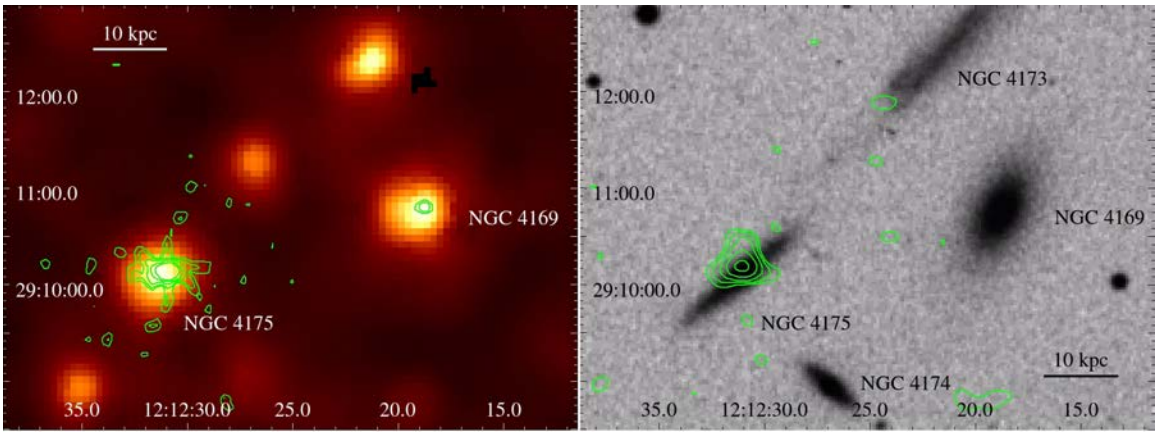

Figure 4.12 NGC 4169. GMRT 610 MHz (1σ = 80 μJy beam^{-1}), overlaid on the adaptively smoothed, 0.3-2.0 KeV of *XMM-Newton* image (left) and GMRT 235 MHz contours (1σ = 1.2 mJy beam^{-1}), overlaid on the optical SAO/DSS image. In both panels the radio contours are spaced by a factor of two, start from 3σ. For this source the scale is 0.218 kpc arcsec^{-1}

exhibits a small diffuse morphology in the east-west direction and at 235 MHz an obvious north extension beyond the optical galaxy. The spectral index of the spiral galaxy is α=0.47.

The smoothed 0.3-2.0 KeV of *XMM-Newton* shows that the group is point source dominated in the X-rays, with the emission traced to <6 kpc. A characteristic temperature of $\sim$0.7 keV is found for this system.

4.3.12 NGC 4008

NGC 4008 is an SO type[1] galaxy in a group of galaxies with a few members (Garcia, 1993). The galaxy was classified as HI rich and active in the sample work of Eskridge et al. (1991) from the comparison of the relative 60 μm/100μm FIR fluxes. NVSS at 1.4 GHz detects a weak point radio source of $\sim$11 mJy for NGC 4008 (Table 4.7).

Our GMRT images are presented in Figure 4.13. On the left we show the 610 MHz emission overlaid on the *XMM-Newton* image. The right panel presents the 235 MHz contours overlaid on the optical image. The emission at 610 MHz presents an elongated radio

[1]NED

source what may possibly be a small scale jet in the east-west direction with a flux density of 16.4 mJy. At 235 MHz, the emission seems to have a much wider and elongated component in the north-south direction. It seems like the orientation of the emission is different at 235 MHz and that it does not coincide with the optical center of the galaxy. The spectral index of $\alpha \sim 0.4$ indicates possibly a young radio emission from a low power outburst.

The X-ray emission from the adaptively smoothed, 0.3-2.0 KeV of *XMM-Newton* shows a central source dominated group, with the emission traced to $\sim$24 kpc. A characteristic temperature of $\sim$0.4 keV is found for this system.

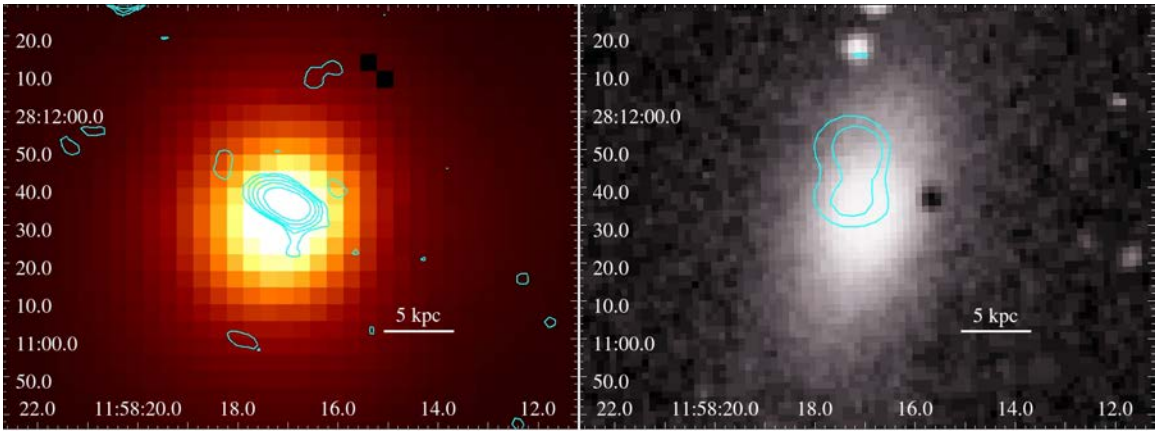

Figure 4.13 NGC 4008. GMRT 610 MHz (1σ = 50 μJy beam^{-1}), overlaid on the adaptively smoothed, 0.3-2.0 KeV of *XMM-Newton* image (left) and GMRT 235 MHz contours (1σ = 1.3 mJy beam^{-1}), overlaid on the optical SAO/DSS image. In both panels the radio contours are spaced by a factor of two, start from 3σ. For this source the scale is 0.262 kpc arcsec^{-1}

4.3.13 NGC 2563

NGC 2563 is the largest elliptical galaxy in the X-ray bright NGC 2563 group that consists of about 64 members, most of which star-forming spirals (Garcia, 1993). The galaxy is coincident with the group center as defined by the peak of the diffuse group *Chandra* X-ray emission. Results from Rasmussen et al. (2012) for this group indicate that the group members suffered hot and cold gas loss via a combination of ram pressure stripping and tidal

interactions. In addition, HI results suggest a reasonable HI mass reduction from the group members compared to similar field galaxies, with 16 of the 20 HI detections occurring on one side of the group, unveiling an unusual morphological division whose origin remains unclear. In the radio, previous results from Brown et al. (2011) at 1.4 GHz detected a very weak radio point source of 0.3 mJy, the weakest in our sample.

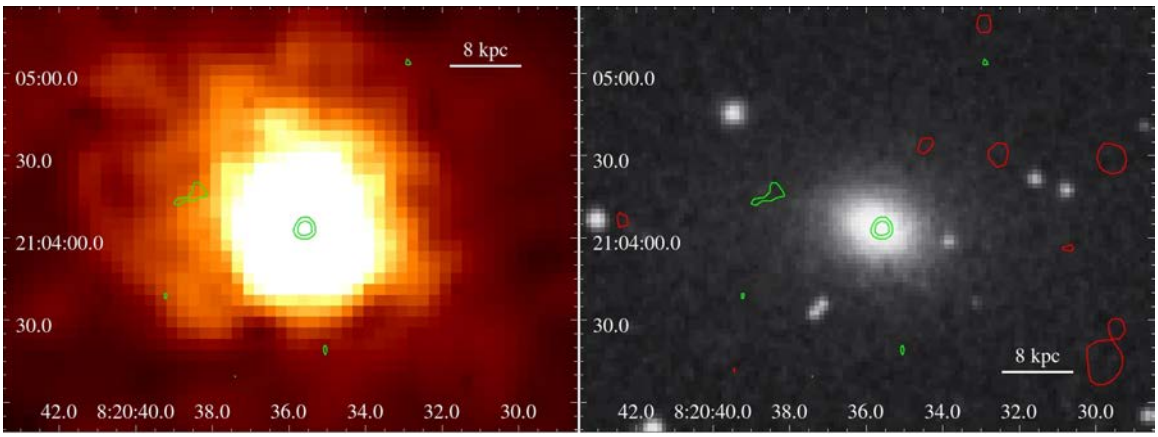

Figure 4.14 NGC 2563. GMRT 610 MHz (1σ = 70 μJy beam^{-1}), overlaid on the adaptively smoothed, 0.3-2.0 KeV of *XMM-Newton* image (left) and GMRT 235 MHz contours in red (1σ = 1.3 mJy beam^{-1}), overlaid on the optical SAO/DSS image along with the 610 MHz emission in green (right). In both panels the radio contours are spaced by a factor of two, starting from 3σ. For this source the scale is 0.315 kpc arcsec^{-1}

In Figure 4.14 (left), we present the 610 MHz contours (1σ = 70 μJy beam^{-1}) on the *XMM-Newton* image. We detect only a weak point radio source of 1.3 mJy flux density at this frequency. On the right panel the 235 MHz emission (red) along with the 610 MHz (green) is superposed on the optical image. As it is clear, we have no detection associated with NGC 2563 at 235 MHz.

X-ray results from the previous work of Rasmussen et al. (2012) indicate that NGC 2563 group is bright, presenting ram pressure stripping of the hot gas, but with no X-ray emission in the rear end being obvious. The X-ray emission from the adaptively smoothed, 0.3-2.0 KeV of *XMM-Newton* reveals a group-scale gaseous halo with the X-ray emission of the

group traced to ∼300 kpc with a characteristic temperature of ∼1.6 keV. and a luminosity of $L_X \sim 1.2 \times 10^{42}$ erg s^{-1}.

4.3.14 NGC 777

NGC 777 is a slow rotating Seyfert 2 galaxy (Ho et al., 1997) in a group of a few members. NGC 777 appears to be a dust free, bulge dominated elliptical galaxy with a population of very old stars (Jarrett et al., 2013). Compact nuclear radio source has been detected earlier by Ho & Ulvestad (2001). The flux density at 1.4 GHz measured from Brown et al. (2011) is 7 mJy (Table 4.7).

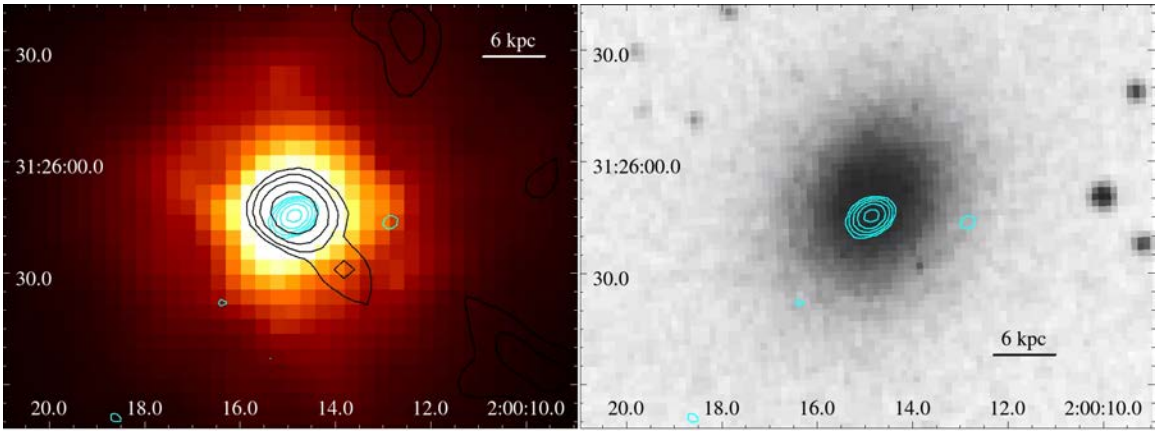

Figure 4.15 NGC 777. GMRT 235 MHz (1σ = 0.4 mJy $beam^{-1}$) contours in black overlaid on the adaptively smoothed, 0.3-2.0 KeV of *XMM-Newton* image (left) and GMRT 610 MHz contours in cyan (1σ = 150 μJy $beam^{-1}$), overlaid on the optical SAO/DSS image (right). In both panels the radio contours are spaced by a factor of two, starting from 3σ. The cyan contours in the left panel correspond to the 610 MHz emission. For this source the scale is 0.354 kpc $arcsec^{-1}$

Our GMRT high-resolution images at 610 MHz and 235 MHz are presented in Figure 4.15. On the left panel the 235 MHz radio emission is overlaid (in black) on the adaptively smoothed, 0.3-2.0 KeV of *XMM-Newton* along with the 610 MHz emission (in cyan). On the right panel the 610 MHz contours are overlaid on the optical image. The radio source appears to have only at 235 MHz an assymetric structure of ∼6 kpc extension south-west

from the central radio peak. At 610 MHz we detect a compact central radio source. The spectral index of $\alpha \sim 0.8$ indicates that the extended radio emission possibly comes from a relatively old, low power outburst.

The X-ray emission from the adaptively smoothed, 0.3-2.0 KeV of *XMM-Newton* shows a group-scale gaseous halo with the X-ray emission of the group traced to ∼275 kpc with a characteristic temperature of ∼0.9 keV.

4.3.15 NGC 940

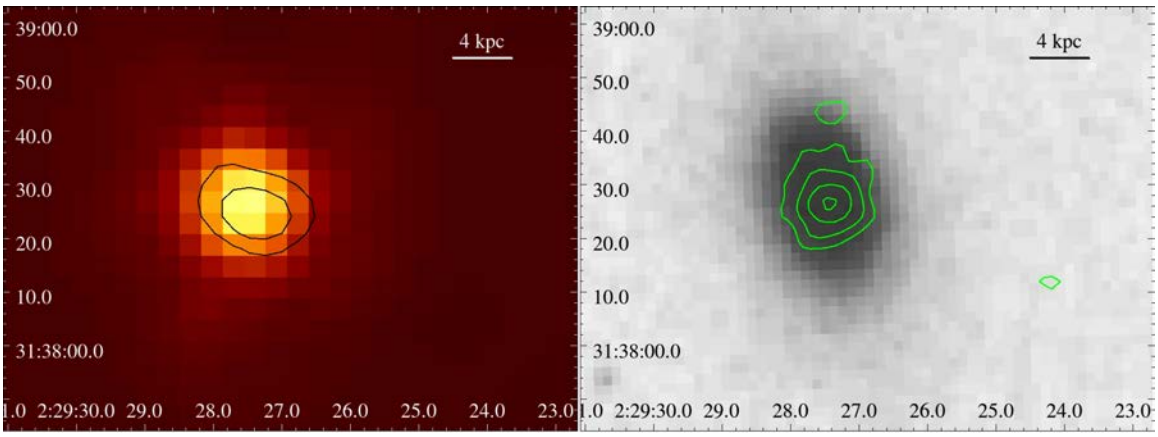

Figure 4.16 NGC 940. GMRT 235 MHz (1σ = 0.3 mJy beam^{-1}) contours in black overlaid on the adaptively smoothed, 0.3-2.0 KeV of *XMM-Newton* image (left) and GMRT 610 MHz contours in green (1σ = 150 μJy beam^{-1}), overlaid on the optical SAO/DSS image (right). In both panels the radio contours are spaced by a factor of two, starting from 3σ. The cyan contours in the left panel correspond to the 610 MHz emission. For this source the scale is 0.354 kpc arcsec^{-1}

NGC 940 is a lenticular SO type[1] galaxy in a group of galaxies with a few members (Garcia, 1993). No previous high resolution measurements exist for that galaxy. In Figure 4.16 we present the GMRT 235 MHz emission overlaid on the *XMM-Newton* image (left) and the 610 MHz emission overlaid on the optical image (right). We detect a slightly elongated radio point source at 235 MHz and a hint of an extended emission at 610 MHz

[1]NED

with an inverted spectral index α of $\sim$-0.3. The inverted spectral index could be due to a restarted activity but this is not so clear from the 610 MHz.

In the X-rays, the smoothed 0.3-2.0 KeV of *XMM-Newton* reveals that the group is point source dominated with the emission traced to $<$10 kpc. A characteristic temperature of $\sim$0.4 keV is found at the same band. and a luminosity of $L_X \sim 1.4 \times 10^{40}$ erg s^{-1}.

4.3.16 NGC 3078

NGC 3078 is the brightest elliptical galaxy (E2)[1] placed in the loose NGC 3078 group along with 22 other galaxies, most of which, spiral and is part of the Antila-Hydra region (Garcia, 1993). NGC 3078 exhibits a nuclear dust disk with a diameter of 1.4$''$ (Rest et al., 2001). The dust absorption combined with the presence of a strong AGN supports the fact that NGC 3078 is a core galaxy (Rest et al., 2001). Previous radio observations with VLA at 1.4 GHz detect a 310 mJy source (Table 4.7).

In Figure 4.17 (left), we present the 235 MHz contours on the smoothed 0.3-2.0 KeV of *Chandra* image. The radio source has a symmetric twin-jet-like structure along the E-W axis, with a total size of $\sim$25 kpc at 235 MHz. The eastern structure appears broader with respect to the western one. The 610 MHz image (cyan) is shown on the right panel of Figure 4.17, overlaid on the optical image. The emission here appears to have the same morphology as in 235 MHz but less extended, with a total size of $\sim$9 kpc. The flux density measured at 235 MHz is 583 mJy while at 610 MHz 385 mJy, indicating a flat spectral index ($\sim$0.5), possibly an ongoing radio activity from an AGN, and of low power as there is no clear morphological distinction between jets and lobes.

The X-ray image of the smoothed 0.3-2.0 KeV of *Chandra* reveals a central source

[1]Hubble type classification by NASA/IPAC Extragalactic Database (NED, http://ned.ipac.caltech.edu)

dominated X-ray emission (galaxy scale) with a total size of ∼16 kpc and a characteristic temperature of ∼0.8 keV.

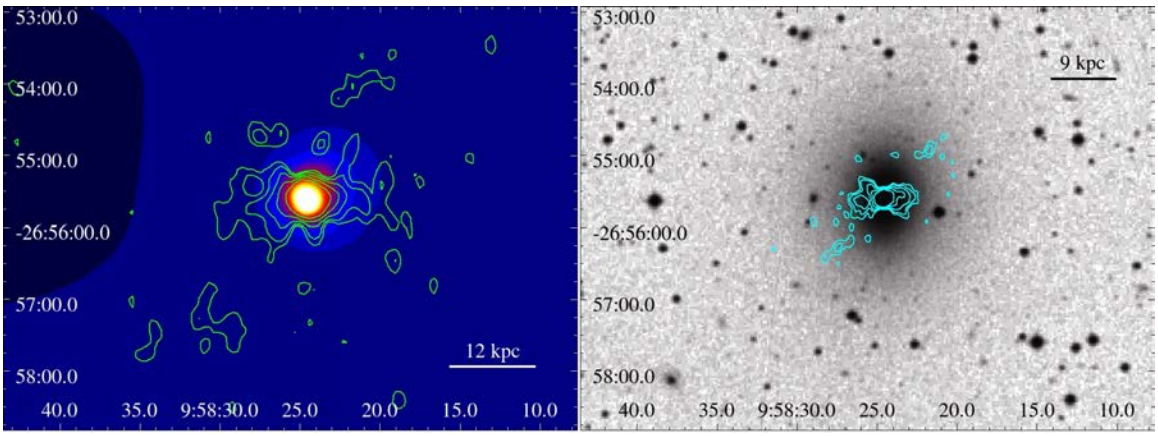

Figure 4.17 NGC 3078. GMRT 235 MHz (1σ = 0.5 mJy beam^{-1}) contours in green overlaid on the adaptively smoothed, 0.3-2.0 KeV of *Chandra* image (left) and GMRT 610 MHz contours in cyan (1σ = 200 μJy beam^{-1}), overlaid on the optical SAO/DSS image (right). In both panels the radio contours are spaced by a factor of two, starting from 3σ. For this source the scale is 0.165 kpc arcsec^{-1}

4.3.17 NGC 978

This is an SO type elliptical galaxy placed in the NGC 973 group along with several other galaxies, part of the Perseus-Pisces Supercluster, most of which spiral (Garcia, 1993). NGC 978 is the Brightest Group Elliptical (BGE) and is a pair galaxy that shows no signs of interaction or distortion in optical (Karachentsev, 1972). No previous radio observation exists for this galaxy.

In Figure 4.18 we present the 610 MHz contours overlaid on the smoothed *XMM-Newton* image (left) and on the optical image (right). No radio emission was detected at 235 MHz from NGC 978. At the full resolution image of 610 MHz we detect a weak radio point source that coincides with the center of the optical galaxy having a flux density of just 1.3 mJy.

In the X-ray image of the smoothed, 0.3-2.0 KeV of *XMM-Newton* we see a central source dominated X-ray emission (galaxy scale) with a total size of ∼50 kpc. A characteristic temperature of ∼0.7 keV is found for this system.

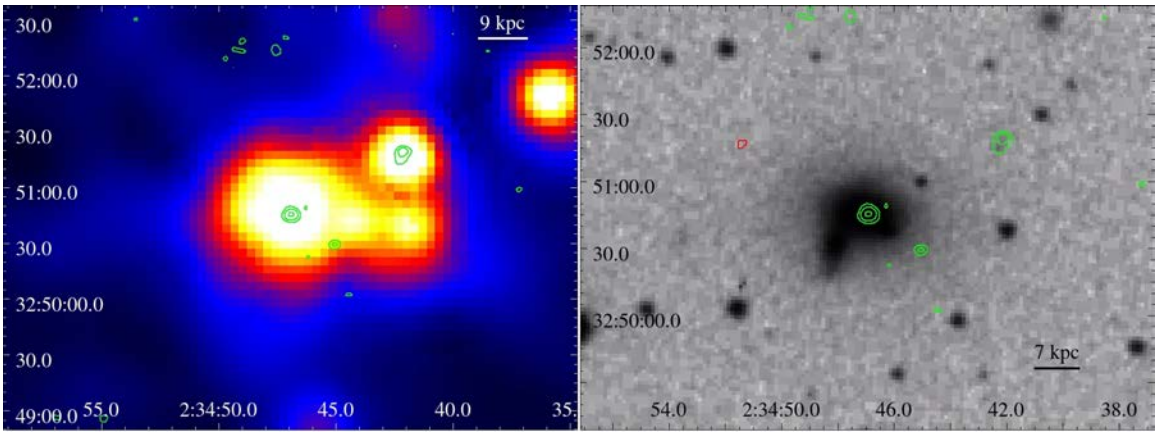

Figure 4.18 NGC 978. GMRT 610 MHz (1σ = 60 μJy beam^{-1}) contours in green overlaid on the adaptively smoothed, 0.3-2.0 KeV of *XMM-Newton* image (left) and on the optical SAO/DSS image (right). In both panels the radio contours are spaced by a factor of two, starting from 3σ. No radio emission detected at 235 MHz for this galaxy. For this source the scale is 0.334 kpc arcsec^{-1}

4.3.18 NGC 1060

LGG 72, is a strongly interacting, possibly merging system with the brightest group elliptical (BGE) galaxy of this group being NGC 1060 accompanied by 14 other galaxies, the majority of which are spiral (Garcia, 1993). The main characteristic of this group is that its galaxies exhibit velocity differences that are quite significant (Values taken from NED): NGC 1060 is at 5190 km/s, whereas NGC 1060 is at 4346 km/s, and the two big spirals to its northwest, NGC 1067 and UGC 2201 are at 4533 and 4130. According to these numbers, there is a subgroup around those three galaxies, moving at roughly 850 km/s relative to the group-dominant elliptical, NGC 1060. The group velocity dispersion is ∼500 km/s. Despite the many group members, NGC 1060 is assumed to be a group according to its mean group X-ray temperature of the gas which is ∼1 keV. NGC 1060 was previously observed with

VLA and the flux density recorded at 1.4 GHz was 9.2 mJy (Table 4.7).

In Figure we present the 235 MHz contours in green, on the smoothed 0.3-2.0 KeV of *XMM-Newton* image (left) and the 610 MHz contours in cyan, on the optical image (right). The radio analysis at 610 MHz for NGC 1060 reveals the detection of a small scale jet with a total size of $\sim$7 kpc, indicative of an AGN. At 235 MHz the emission resembles to a compact and slightly elongated component to the east-west direction. The spectral index of $\sim$0.9 indicates past AGN activity remnant of an old, low power outburst. The system appears to be undergoing a group-group merger, which may have triggered the nuclear activity in NGC 1060.

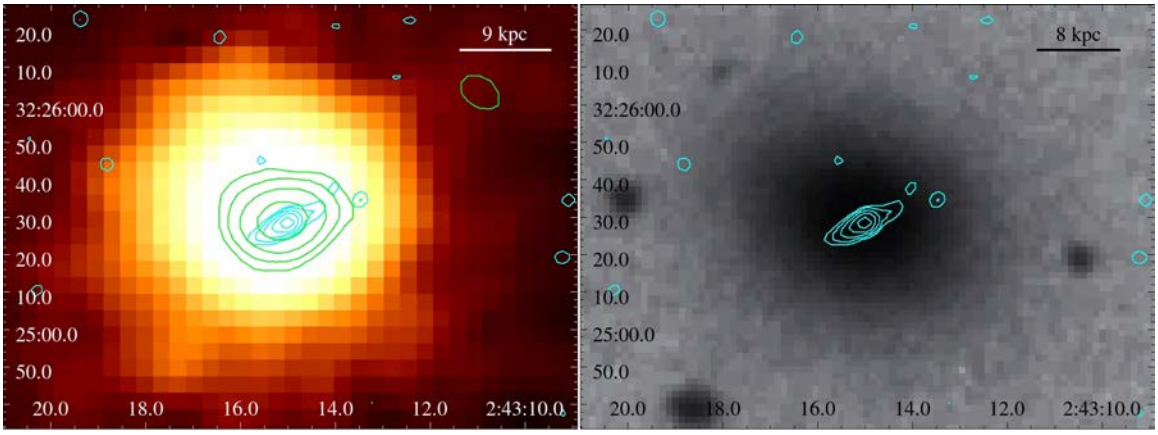

Figure 4.19 NGC 1060. GMRT 235 MHz (1σ = 0.5 mJy beam^{-1}) contours in green overlaid on the adaptively smoothed, 0.3-2.0 KeV of *XMM-Newton* image (left) and GMRT 610 MHz contours in cyan (1σ = 90 μJy beam^{-1}), overlaid on the optical SAO/DSS image (right). In both panels the radio contours are spaced by a factor of two, starting from 3σ. The cyan contours on the left panel correspond to the 610 MHz emission. For this source the scale is 0.368 kpc arcsec^{-1}

In Figure radio detections from other member galaxies can be seen. Star formation is detected in three spiral galaxies: from the disk of UGC 2201, with a spectral index of 1, from the disk of NGC 1061 with a spectral index of 0.9 and from the disk of UGC 2201 with a spectral index of 0.8. Radio point sources are also detected at the spirals NGC 1057 and NGC 1067 that coincide with the center of the optical galaxy.

In the X-ray image of the smoothed 0.3-2.0 KeV of *XMM-Newton*, a long arc-like path connecting 1066 and 1060 is seen, which suggests that both subgroups have X-ray halos, which have been strongly disturbed by the encounter. The group was not detected by the *ROSAT all-sky survey*, probably because it has a very disturbed cool core, that lacks the presence of a central surface brightness peak. A new *XMM-Newton* pointing for the group detects AGN in several of the galaxies, and reveals a previously unknown extended gaseous halo in the group. We find a characteristic temperature of $\sim$1 keV and luminosity $L_X \sim 2.6 \times 10^{42} ergs^{-1}$, typical of a moderate mass group. The X-ray emission of the group is traced to the edge of the XMM field of view, 14', equivalent to 310 kpc. The luminosity in that radius is $\sim 1.25 \times 10^{42} ergs^{-1}$ making it a bright system.

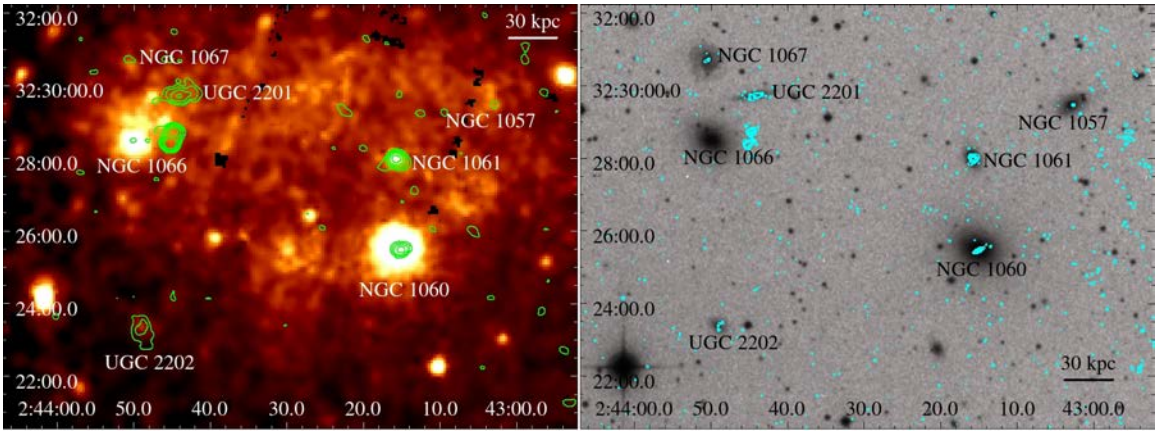

Figure 4.20 NGC 1060 Field. GMRT 235 MHz (1σ = 0.5 mJy beam^{-1}) contours in green overlaid on the adaptively smoothed, 0.3-2.0 KeV of *XMM-Newton* image (left) and GMRT 610 MHz contours in cyan (1σ = 90 μJy beam^{-1}), overlaid on the optical SAO/DSS image (right). In both panels the radio contours are spaced by a factor of two, starting from 3σ. For this source the scale is 0.368 kpc arcsec^{-1}

4.3.19 NGC 4261 (3C 270)

NGC 4261 hosts 3C 270, an FR-I radio galaxy and the strongest radio source in our sample (19 Jy at 1.4 GHz, Kuhr et al. 1981) whose twin jets lie close to plane of the sky (Piner et

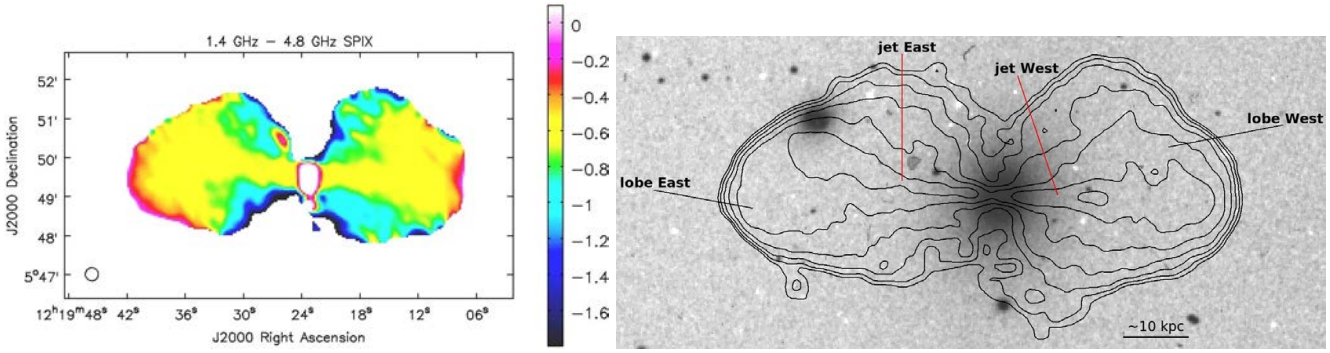

Figure 4.21 1.5 GHz - 4.8 GHz spectral index distribution over 3C 270 (*left*) produced from images with a restoring beam of $20'' \times 20''$. GMRT 240 MHz radio contours of 3C 270, overlaid on the r band optical image from the SDSS (*right*) with contour levels (black) which start at 4σ and rise by factor of 2.

al., 2001). We analysed archival VLA and GMRT observations of the source and produced spectral index maps. In Figure 4.21 the constant spectral index ($\sim$0.6) of the jets suggests that the internal plasma flows are still fast, with the plasma ageing very little over its travel time along the jets. The steeper values at the back of the lobes indicate that the plasma close to the core is actually older than that in the hotspots, suggesting that it was transported out to the hotspots by the jets and has then flowed all the way back in to the galaxy core.

From a point-to-point spectral index distribution analysis (Kolokythas et al. 2015, MNRAS submitted) the age of the outburst was estimated. The radio age that we find from our best fit JP model analysis is $\sim$29 Myr for the west lobe and $\sim$36 Myr for the east one. This is lower than the 75 Myr expected from the X-ray analysis in O'Sullivan et al. (2011), implying that either the source expansion must have been supersonic over a larger fraction of its lifetime, with stronger shock heating of the IGM, or multiple outbursts occured or a fast backflow transporting young electrons to the back of the lobes relatively quick (For more details on the properties and the analysis of this source, see Chapter 3).

4.3.20 NGC 1453

NGC 1453 is an elliptical galaxy with previous radio observations at 1.4 GHz detecting a radio source of 28 mJy (Table 4.7).

Our GMRT images at 610 MHz and 235 MHz are presented in Figure 4.22. On the left panel the 235 MHz radio emission is overlaid (in green) on the adaptively smoothed, 0.3-2.0 KeV of *XMM-Newton*. On the right panel the 610 MHz contours (in cyan) are overlaid on the optical image. We detect a compact radio point source that coincides with the central region of the optical galaxy. The spectral index of $\alpha \sim 0.2$ indicates that the radio emission possibly comes from a new AGN outburst.

In the X-ray image of the smoothed 0.3-2.0 KeV of *XMM-Newton*, possibly a group-scale gaseous halo is detected, with the X-ray emission of the group traced to 61 kpc. A characteristic temperature of $\sim$0.8 keV is found for this system.

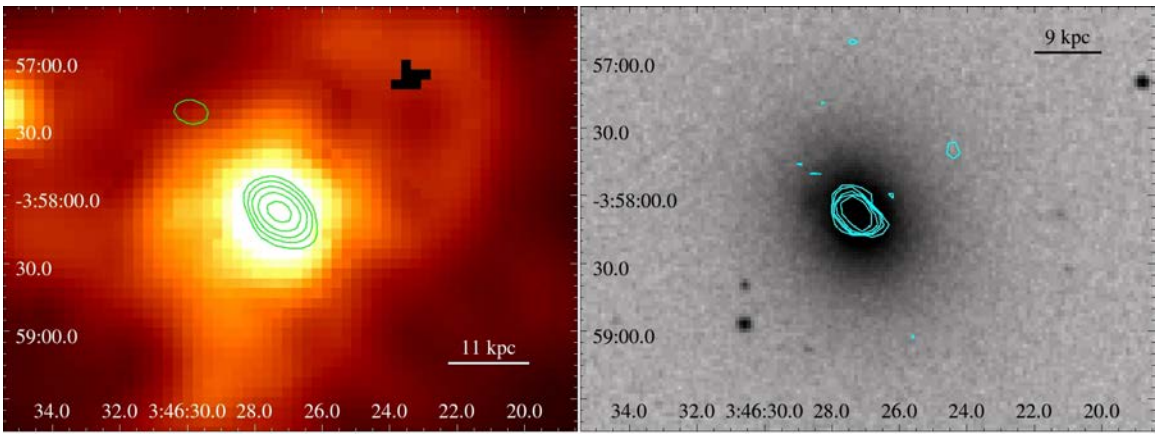

Figure 4.22 NGC 1453. GMRT 235 MHz (1σ = 600 μJy beam^{-1}) contours in green overlaid on the adaptively smoothed, 0.3-2.0 KeV of *XMM-Newton* image (left) and GMRT 610 MHz (1σ = 60 μJy beam^{-1}) contours in cyan overlaid the optical SAO/DSS image (right). In both panels the radio contours are spaced by a factor of two, starting from 3σ. For this source the scale is 0.305 kpc arcsec^{-1}

4.3.21 NGC 5846

NGC 5846 is the dominant elliptical galaxy of a huge group of galaxies with ∼250 possible members, and only ∼80 of them confirmed spectroscopically (Mahdavi et al., 2005). Previous radio observations detect a weak radio source of 21 mJy at 1.4 GHz (Table 4.7).

We analysed that galaxy only at 235 MHz as the 610 MHz were analysed and presented in the survey sample of Giacintucci et al. (2011). On the left panel of Figure 4.23 the 235 MHz radio emission is overlaid (in green) on the adaptively smoothed, 0.3-2.0 KeV of *XMM-Newton* and on the right panel on the optical image. We detect a compact radio point source that coincides with the central region of the optical galaxy. The point source at 235 MHz shows hints of extended emission toward the east-west direction. The resolution limit based on the beam size at 235 MHz is ∼3 kpc.

The X-ray emission from the adaptively smoothed, 0.3-2.0 KeV of *XMM-Newton* reveals a group-scale gaseous halo, with the X-ray emission of the group traced to 107 kpc with a characteristic temperature of ∼1.3 keV.

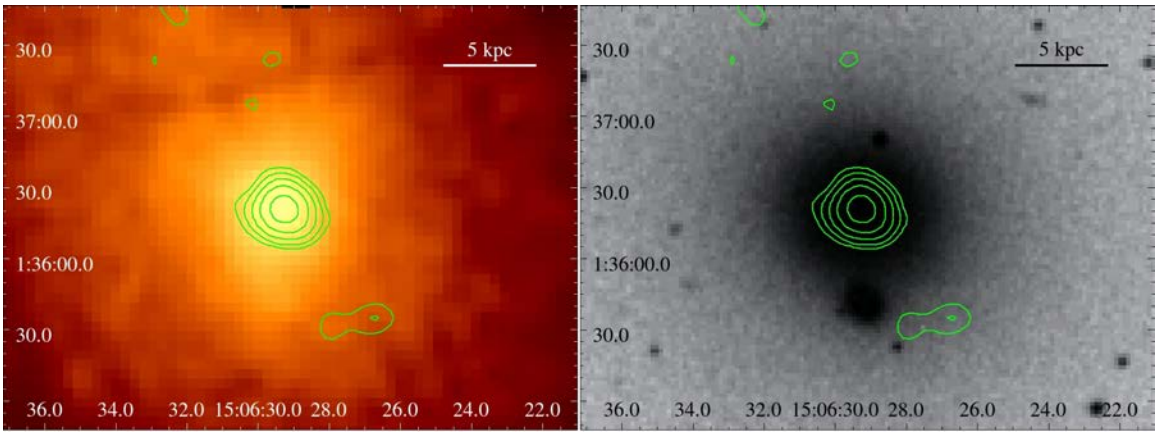

Figure 4.23 NGC 5846. GMRT 235 MHz (1σ = 500 μJy beam^{-1}) contours in green overlaid on the adaptively smoothed, 0.3-2.0 KeV of *XMM-Newton* image (left) and on the optical DSS image (right). The radio contours are spaced by a factor of two, starting from 3σ. For this source the scale is 0.126 kpc arcsec^{-1}.

4.3.22 NGC 1167

NGC 1167 is an HI-rich early type galaxy that hosts the radio source B2 0258+35 which is characterized as a young compact steep spectrum (CSS) source (Sanghera et al., 1995), despite the fact that its spectrum is not so steep $\alpha^{22}_{0.08}$=0.54. The radio source exhibits a jet-like structure with plume-like lobes that shows no evidence of hotspots (Giroletti et al., 2005). In VLA 22 GHz image there is a parsec scale core at the base of the south-east jet-like feature, while in the 8 GHz VLA image the core co-exists with a bright jet component (Giroletti et al., 2005). In the VLBI image at 1.6 GHz the faint compact core (7.6 mJy), is included in a bright diffuse region coincident with the peak of the VLA images (Giroletti et al., 2005). The surrounding diffuse emission appears to be steep with a spectral index of $\alpha^{22}_{0.08} \sim$1.0 – 1.5, while the spectrum is still flat in the central region and gradually steepens to become almost constant (0.6) in the inner bright region (Giroletti et al., 2005). The structure is suggested to represent a remnant from previous activity of an active galactic nucleus (AGN) where the fuel of the AGN is considered to be the cooling of gas from the hot X-ray halo (Shulevski et al., 2012). Previous radio observations of the radio source calculated a flux density of 1.7 Jy at 1.4 GHz (Table 4.7).

Our GMRT images at 610 MHz and 235 MHz are presented in Figure 4.24. On the left panel the 235 MHz radio emission is overlaid (in green) on the adaptively smoothed, 0.3-2.0 KeV of *XMM-Newton*. On the right panel the 610 MHz contours (in cyan) are overlaid on the optical image. We detect a compact radio point source at 610 MHz that coincides with the central region of the optical galaxy. The central component seems slightly elongated to the east west direction with a total size of $\sim$7 kpc at 610 MHz. At 235 MHz we also detect a bright point source radio component, and a small extension of $\sim$7 kpc toward the east. The resolution limit based on the beam size at 235 MHz is $\sim$3 kpc. There are also hints of much

fainter extended emission visible on the opposite direction with only one contour level at 4σ level of significance. The total size at 235 MHz of the radio source is $\sim$32 kpc and the spectral index of α $\sim$0.2 indicates that the radio emission possibly comes from a possibly reccurent AGN outburst as suggested in the study of Shulevski et al. (2012).

The group in the smoothed 0.3-2.0 KeV of *XMM-Newton* appears to be point-source dominated in the X-rays with the emission traced to $\sim$9 kpc.

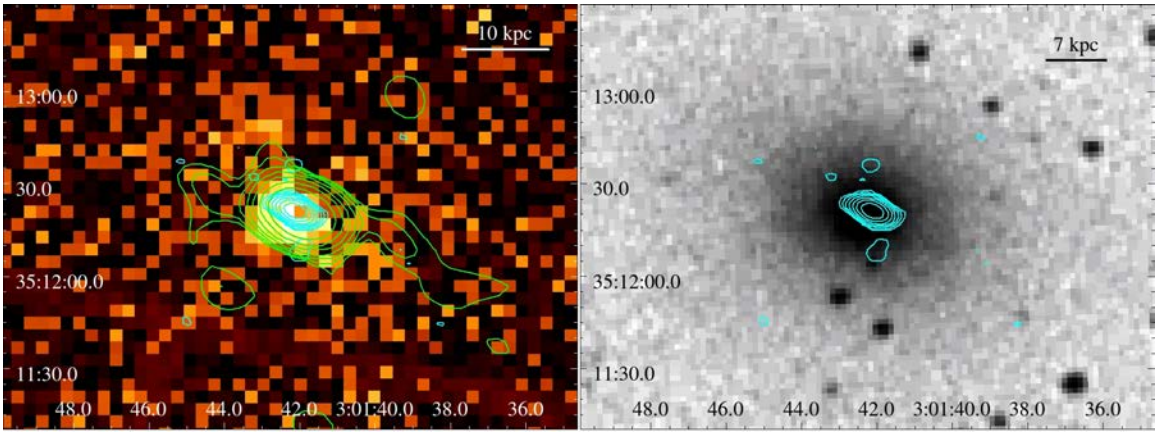

Figure 4.24 NGC 1167. GMRT 235 MHz (1σ = 600 μJy beam^{-1}) contours in green overlaid on the adaptively smoothed, 0.3-2.0 KeV of *XMM-Newton* image (left) and GMRT 610 MHz (1σ = 60 μJy beam^{-1}) contours in cyan overlaid on the optical SAO/DSS image (right). In both panels the radio contours are spaced by a factor of two, starting from 3σ. For this source the scale is 0.349 kpc arcsec^{-1}

4.3.23 NGC 1587

NGC 1587 is an elliptical galaxy that resides along with its companion NGC 1588, in a poor group with a characteristically low velocity dispersion (100 km s^{-1}; Mulchaey et al. 2003; Osmond & Ponman 2004). Previous radio observations for NGC 1587 detect a radio source of 131$\pm$5 [1] mJy at 1.4 GHz (Table 4.7).

The GMRT image at 610 MHz is presented in Figure 4.25. On the left panel the full

[1]Brown et al. (2011)

resolution radio emission is overlaid on the adaptively smoothed, 0.3-2.0 KeV of *Chandra*. On the right panel the 610 MHz contours that have a slightly lower resolution are overlaid on the optical POSS-2 image. A compact radio source that coincides with the central region of the optical galaxy is detected. The total size of the radio component is ∼5 kpc with a faint diffuse emission reaching ∼10 kpc further in the north-west direction. The analysis at 235 MHz revealed only the central compact source (Giacintucci et al., 2011).

The X-ray emission from the adaptively smoothed, 0.3-2.0 KeV of *Chandra* reveals a group-scale gaseous halo. The X-ray emission of the group is traced to ∼137 kpc with a characteristic temperature of ∼0.4 keV.

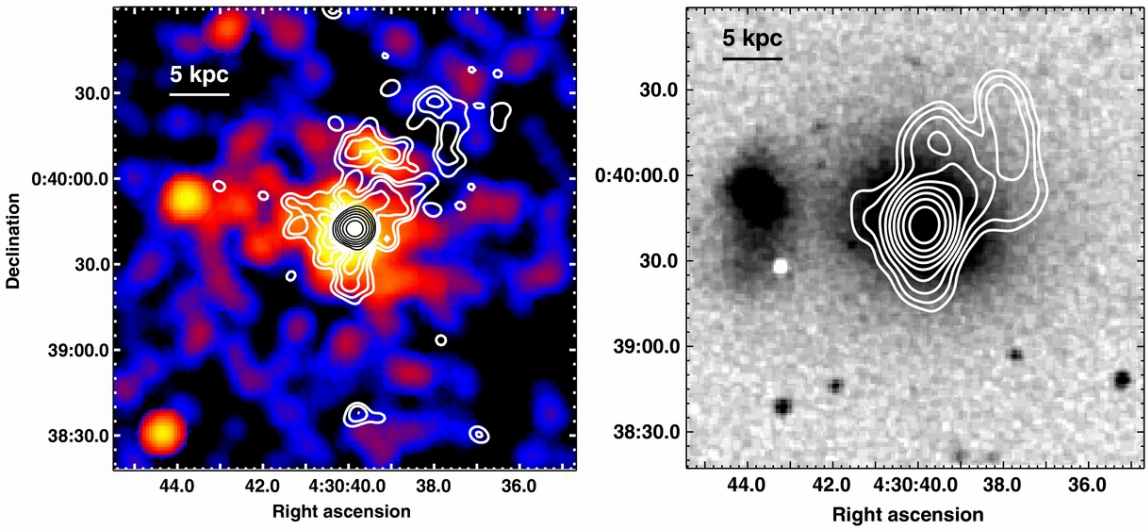

Figure 4.25 NGC 1587. GMRT 610 MHz (1σ = 50 μJy beam^{-1}; FWHM = $5.7'' \times 4.7''$) contours overlaid on the adaptively smoothed, 0.3-2.0 KeV of *Chandra* image (left) and GMRT 610 MHz (1σ = 120 μJy beam^{-1}; FWHM = $12.0'' \times 10.0''$) low-resolution contours overlaid on the POSS-2 red optical image (right). In both panels the radio contours are spaced by a factor of two, starting from 3σ. For this source the scale is 0.252 kpc arcsec^{-1} (Giacintucci et al., 2011)

4.3.24 NGC 193

NGC 193 (also known as UGC 408) is a central dominant SAB-type galaxy (lenticular; de Vaucouleurs et al. 1991) in a poor group of galaxies. It hosts the Fanaroff-Riley type I (FR I;

Fanaroff & Riley 1974) radio source 4C +03.01 with previous radio observations detecting a radio source of 983.1±31[1] mJy at 1.4 GHz (Table 4.8).

The GMRT images at 610 MHz and 235 MHz presented in Figure 4.26, are from the analysis of Giacintucci et al. (2011). On the left panel the 235 MHz radio emission is overlaid (in cyan) on the adaptively smoothed, 0.3-2.0 KeV of *Chandra*. On the right panel the 610 MHz contours (in green) are overlaid on the optical image. A twin jet radio source of a total size of ∼100 kpc is detected at both frequencies. The lobes of the radio source seem to surround the jets and the spectral index of α ∼0.5 indicates that the radio emission possibly comes from a new AGN outburst typical of an ongoing jet emission (Giacintucci et al., 2011).

The X-ray emission from the adaptively smoothed, 0.3-2.0 KeV of *Chandra* reveals a group-scale gaseous halo and a highly disturbed gas component owing to probable AGN-driven shock. The X-ray emission of the group is traced to ∼135 kpc with a characteristic temperature of ∼0.7 keV.

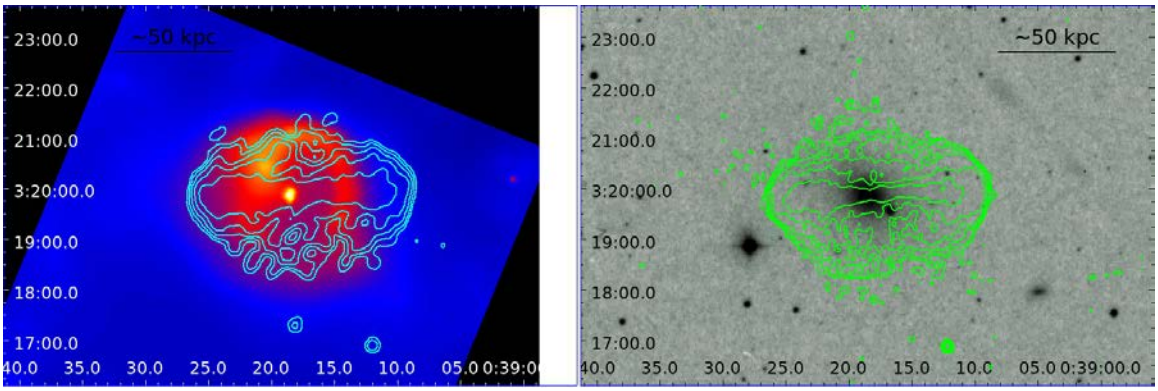

Figure 4.26 NGC 193. GMRT 235 MHz (1σ = 800 μJy beam^{-1}) contours in cyan overlaid on the adaptively smoothed, 0.3-2.0 KeV of *Chandra* image (left) and GMRT 610 MHz (1σ = 80 μJy beam^{-1}) contours in green overlaid the optical SAO/DSS image (right). In both panels the radio contours are spaced by a factor of two, starting from 3σ. For this source the scale is 0.359 kpc arcsec^{-1} (Giacintucci et al., 2011)

[1]Condon et al. (1998)

4.3.25 NGC 7619

NGC 7619 is the dominant elliptical of the NGC 7619/7626 pair in the Pegasus galaxy group. Previous radio observations detect a radio point source of 20 ± 1 [1] mJy at 1.4 GHz (Table 4.7) in NGC 7619, while NGC 7626 exhibits a huge radio source with symmetric jets of a total size of $\sim$180 kpc (Birkinshaw & Davies, 1985; Jenkins, 1982).

The GMRT images at 610 MHz and 235 MHz presented in Figure 4.27, are from the analysis of Giacintucci et al. (2011). The images are seen as contours on the POSS-2 and Chandra images. The images reveal the luminous radio core, the internal jets of NGC 7626 and a compact radio source in NGC 7619.

The X-ray emission from the adaptively smoothed, 0.3-2.0 KeV of *Chandra* reveals a group-scale gaseous halo and an asymmetric X-ray emission associated with NGC 7619. As NGC 7619 falls into the group its motion has removed gas causing this assymetry (Trinchieri et al., 1997), with latest Chandra study by Randall et al. (2009) revealing an X-ray brightness for every galaxy that is cut abruptly, which is interpreted as a proof of a merger event between the NGC 7626 and NGC 7619 subgroups.

4.3.26 NGC 5044

NGC 5044 is the central elliptical galaxy of a rich group, with previous radio observations detecting a radio source of 35 ± 1 [2] mJy at 1.4 GHz (Table 4.7).

The GMRT images at 235 MHz and 610 MHz have initially been presented in David et al. (2009) with the images presented here in Figure 4.28 being from the study of Giacintucci et al. (2011). The images have the 610 and 235 contours overlaid on the optical (left) and Chandra (right) images. Apart from the central region, an obviously extended radio lobe of

[1] Brown et al. (2011)
[2] Brown et al. (2011)

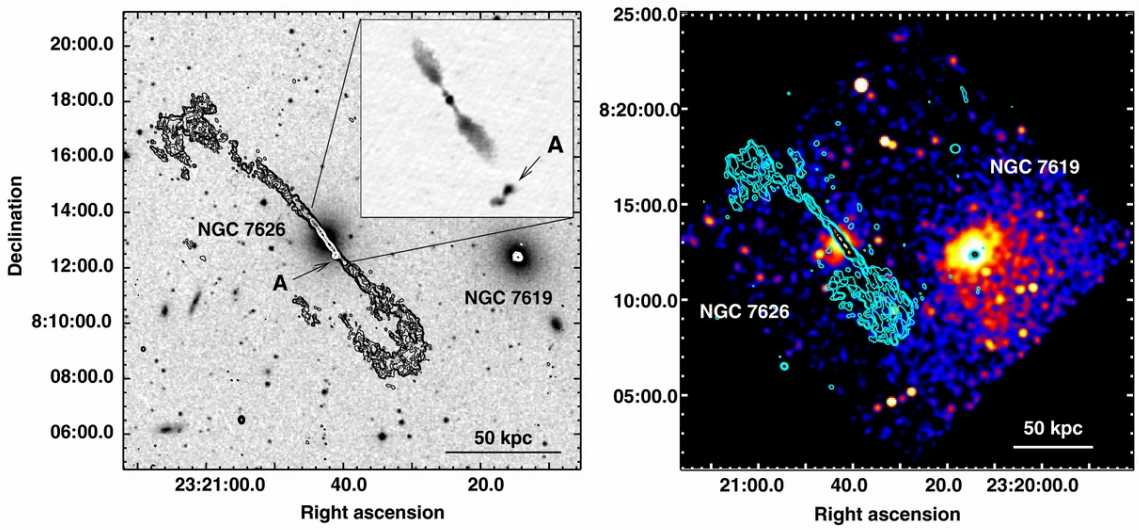

Figure 4.27 NGC 7626/NGC 7619. GMRT 610 MHz full-resolution contours ($1\sigma = 50\ \mu$Jy beam^{-1}; FWHM = $6.2'' \times 4.9''$) overlaid on the POSS-2 red optical image (left) and GMRT 235 MHz contours (1σ = 800 μJy beam^{-1}; FWHM = $14.2'' \times 12.0''$) overlaid on the adaptively smoothed, 0.3-2.0 KeV of *Chandra* image (right). In both panels the radio contours are spaced by a factor of two, starting from 3σ. The inset shows the VLA 1.4 GHz image of the central region of NGC 7626, with the resolution of $1.2''$. For this source the scale is 0.233 kpc arcsec^{-1} (Giacintucci et al., 2011)

$\sim$12 kpc is detected at 610 MHz while at 235 MHz a much larger and bright jet of different orientation with respect to the 610 MHz lobe is detected. Also an extra detached radio lobe at 235 MHz is detected. The emission appears to be steep with a spectral index of $\alpha > 1.6$, with the morphological structure of this system possibly interpreted by multiple radio-AGN outbursts, each one of a different age (Giacintucci et al., 2011).

Recent *Chandra* study of NGC 5044 by David et al. (2009) showed that the interaction of the central radio source coincides with interesting features observed in the group gas. For example, it is noted that a cool gas filament that co-exists with the 610 MHz lobe, is interpreted as an active AGN outburst in NGC 5044. In addition, a large cavity south of the center of the source is observed that is completely filled with the 235 MHz jet emission, while the detached radio emission that is observed, probably comes from past activity of the central AGN (David et al., 2011, 2009).

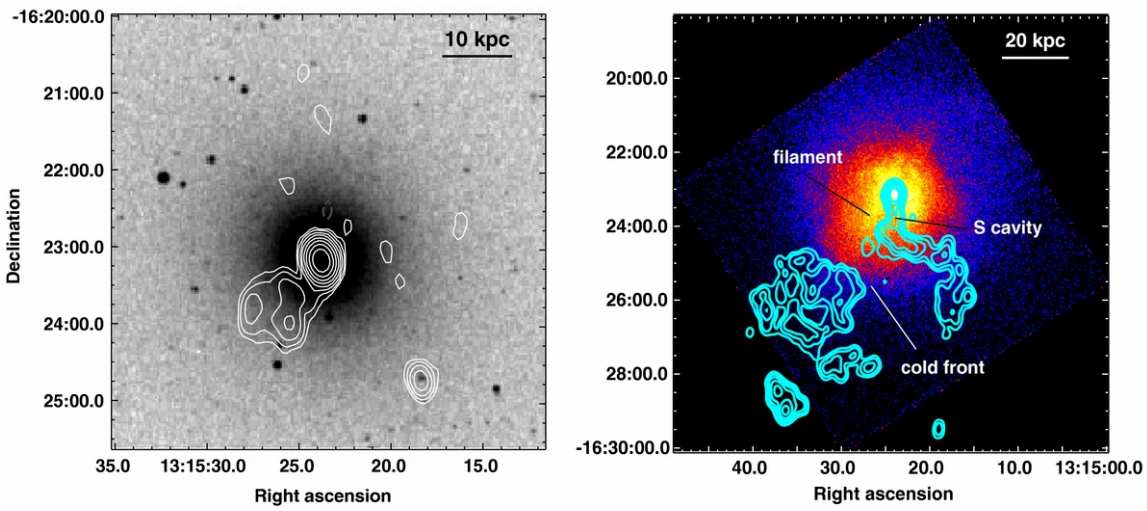

Figure 4.28 NGC 5044.GMRT 610 MHz low-resolution contours (1σ = 75 μJy beam^{-1}; HPBW = $18.3'' \times 12.7''$) overlaid on the POSS-2 red optical image (left) and GMRT 235 MHz low-resolution contours (1σ = 250 μJy beam^{-1}; HPBW = $22.0'' \times 16.0''$) overlaid on the adaptively smoothed, 0.3-2.0 KeV of *Chandra* image (right). In both panels the radio contours are spaced by a factor of two, starting from 3σ. For this source the scale is 0.185 kpc arcsec^{-1} (Giacintucci et al., 2011)

4.4 Radio and X-ray emission in CLoGS brightest group ellipticals (BGEs)

Our CLoGS sample exhibits a variety of cases both in the radio and X-ray bands. From the analysis of the 26 central group galaxies of the CLoGS high richness sub-sample, 22 out of the 26 dominant early-types are detected at 235 and/or 610 MHz. From the 4 group central galaxies that are not detected with GMRT, 2 present 1.4 GHz radio emission from previous studies. The first one is NGC 584 that has a very faint emission of just 0.6$\pm$0.5 mJy detected (Brown et al., 2011). The non detection of radio emission from this galaxy at both GMRT frequencies is realistic, as the GMRT sensitivity for both frequencies is high enough to detect such faint radio emission ($\sim$0.2 mJy beam^{-1} at 610 MHz and $\sim$1.2 mJy beam^{-1} at 235 MHz). The second one, is NGC 5084 where a detection of 46.6$\pm$1.8 mJy is noted from NVSS (Condon et al., 1998). As no radio source is detected at lower GMRT

frequencies this probably indicates that the emission originates from a very young source that hasn't aged yet.

The 22 detected central radio sources differ dramatically in size, radio power and morphology. Their physical scale ranges from a few kpc (point sources; galactic scale) to several tens of kpc (large jets; group/cluster scales), with their radio power at 610 MHz ranging from very low power (10^{20} W Hz^{-1}) point sources and small-scale jets, to that of powerful FR I radio galaxies (10^{24} W Hz^{-1}). The radio structures observed in central galaxies consist of the normal double-lobed radio galaxies, small-scale jets, point sources and irregular-diffuse structures with no preferable orientation.

4.4.1 Morphology of radio emission

Owing to the morphological variety of the radio emission that our galaxies exhibit, we classify the radio sources in 5 categories: i) No radio source detected, ii) Pointlike - radio extent smaller than beam at 235 MHz, iii) Extended but no jets - 'diffuse' emission with no preference in orientation (blob), bigger than the beam but without an obvious jet axis, iv) Small-scale jets - smaller than the mean D_{25} radius of the host galaxy, (e.g. NGC 1060), v) Large-scale jets - NGC 4261, 7626, 193, 5044, etc, full-sized radio galaxies.

In Table 4.5 we summarise these properties. For a radio source to be designated as pointlike as indicated above, its size needs to be smaller than the beam at 235 MHz. This corresponds to $\sim 13''$ and at a distance of 74 Mpc, which is the distance of our furthest pointlike source this is $\sim$5 kpc.

In more detail, based on our radio morphological classification the results are the following.

i) Four galaxies have no radio emission detected. NGC 5084, NGC 584, NGC 5153

Table 4.5 Radio properties of the brightest elliptical galaxies in the rich sub-sample groups

BGE	LLS[a] (kpc)	Radio morphology	P_{235} (10^{24} W Hz^{-1})	Energy output (10^{42} erg s^{-1})
NGC 410	11	Small scale jet	0.02	1.1
NGC 5084	-	No radio source detection	-	-
NGC 584	-	No radio source detection	-	-
NGC 924	5	Pointlike	-	-
NGC 677	30	Extended but no jets - 'diffuse' emission	0.06	2.6
NGC 5353	9	Extended but no jets - 'diffuse' emission	0.01	0.7
NGC 5153	-	No radio source detection	-	-
NGC 5982	3	Pointlike	0.001	0.14
ESO 507-25	11	Extended but no jets - 'diffuse' emission	0.01	0.8
NGC 6658	-	No radio source detection	-	-
NGC 4169	3	Pointlike	-	-
NGC 4008	7	Small scale jet	0.009	0.6
NGC 2563	3	Pointlike	-	-
NGC 777	15	Small scale jet	0.01	0.9
NGC 940	5	Pointlike	0.002	0.2
NGC 3078	25	Extended but no jets - 'diffuse' emission	0.08	3
NGC 978	4	Pointlike	-	-
NGC 1060	13	Small scale jet	0.02	1.1
NGC 1453	14	Small scale jet	0.02	1.2
NGC 5846	5	Pointlike	0.005	0.4
NGC 1167	32	Small scale jet	2.3	33.3
NGC 1587	12	Extended but no jets - 'diffuse' emission	0.1	3.5
NGC 193	100	Large scale jet	2.5	35.3
NGC 7619	4	Pointlike	0.02	1.1
NGC 5044	28	Large scale jet	0.04	1.8
NGC 4261	80	Large scale jet	5.8	63.7

[a]LLS is the Largest Linear Size calculated from the radio images. The definition for pointlike sources is given in § 4.1. The calculation of the energy output is from equation 4.4 (P_{cav}=energy output) explained in § 4.4.5

and NGC 6658 are the central galaxies that no radio emission is seen at neither 610 nor 235 MHz. The sensitivity of the GMRT observations was $\sim$60 μJy beam^{-1} at 610 MHz and $\sim$500 μJy beam^{-1} at 235 MHz, apart from NGC 584 where the analysis gave a worse sensitivity of $\sim$0.2 mJy beam^{-1} at 610 MHz and $\sim$1.2 mJy beam^{-1} at 235 MHz. We placed upper limits on the radio detection of these galaxies on the 5σ level of significance and we have: $\leq$0.3 mJy at 610 and $\leq$2.5 mJy at 235 for NGC 5084, $\leq$1 mJy at 610 and $\leq$6 mJy at 235 for NGC 584, $\leq$0.3 mJy at 610 and $\leq$3 mJy at 235 for NGC 5153 and $\leq$0.3 mJy at 610 and $\leq$3 mJy at 235 for NGC 6658.

ii) Eight galaxies present radio point sources, with their radio fluxes ranging from about $1-40$ mJy at 610 MHz and $4-50$ mJy at 235 MHz. The environment that these point sources are detected is very unique and different but some groups share some common characteristics: NGC 5982, NGC 2563 and NGC 4169 are placed in groups where most of the companions are spiral galaxies. NGC 5982 is accompanied by the edge-on barred spiral galaxy NGC 5981 and the face-on barred spiral galaxy (Seyfert) NGC 5985 that both show radio emission from their disks (star formation). NGC 4169 is in a very tight grouping, with another two galaxies, NGC 4174 and NGC 4175, both spiral. As NGC 4169 is also tidally interacting with two neighbouring galaxies with only one presenting radio emission, NGC 978 is on a similar situation, as is on a merging process with a neighbouring galaxy but with no radio emission detected from its companion. For the remaining radio point source galaxies we note that in NGC 5846 there is a tiny hint of extension ($\sim$3 kpc) at 610 MHz (Giacintucci et al., 2011), while NGC 7619 lies in the center of a group where its closest companion, NGC 7626, hosts a powerful jet radio source.

iii) Five galaxies exhibit 'diffuse'/amorphous emission surrounding the nuclear component. Groups NGC 1587, NGC 677 and NGC 3078 present this typical structure of a radio

emission that originates from the nucleus of the central galaxy and is surrounded by a diffuse structure with no apparent jets or lobes. Their sizes are typically small, between for example, ∼12 kpc for NGC 1587 and ∼30 kpc for NGC 677. In ESO 507-25 the diffuse emission is obvious at 610 MHz while in NGC 5353 it is confined very close around the central source. This morphology is, in a much smaller scale, alike to the radio mini-halos seen in cool core clusters (e.g., Mazzotta & Giacintucci, 2008), although the origin of the radio sources in the groups is unlikely to be the same as that of mini-halos in clusters. In clusters, radio mini-halos are thought to be produced by reacceleration caused by turbulence in the intracluster medium, possibly due to minor mergers (Ferrari et al., 2008), but the turbulence in groups does not have enough energy to produce the same effect.

iv) Six galaxies exhibit small scale jets, smaller than the mean D25 radius of the host galaxy. Their physical size ranges from a few kpc (e.g. NGC 4008 at 7 kpc) to a few tens of kpc (e.g. NGC 1167 at 32 kpc). In this class, the radio sources are very weak AGN outbursts that their power was not sufficient to trigger a large scale radio jet. NGC 1167 and NGC 777 exhibit one sided assymetric extensions, NGC 410 exhibits a hint of extension (∼2 kpc) at the frequency of 610 MHz, while NGC 1060 is a typical of low power AGN outburst.

v) Three galaxies host large radio sources with jet/lobe structure. NGC 5044, exhibits a nuclear component along with an extended structure that resembles to a weak radio lobe detected at 610 MHz. At 235 MHz, a deformed jet is detected with a different orientation than the lobe-like emission at 610 MHz. This radio jet appears to be relatively small (∼28 kpc) and confined to the core of the group (Giacintucci et al., 2011).

On the other hand NGC 193 and NGC 4261, both host a spectacular Fanaroff-Riley type I (FR I; Fanaroff & Riley 1974) radio source with their jet/lobe components extending many kpc away. NGC 193 hosts the symmetric double radio source 4C +03.01 which has a total

size of $\sim$100 kpc and NGC 4261 hosts the also symmetric double radio source 3C 270 which has a size of $\sim$80 kpc. They both present similar morphology with the lobes surrounding the very bright and straight jets. Bogdan et al. (2014) show that the expansion of the radio source at NGC 193 is expanding supersonically and is a great example of a reccurent AGN activity on top of the last one. In the study of Kolokythas et al. (2015), the radiative age of $\sim$29 Myr calculated for the 3C 270 radio source, suggests that either an early supersonic phase of about Mach 6 (3500 km s^{-1}) has occured, or that the source underwent multiple AGN outbursts with possible large changes in jet power. In the same study is also noted that in 3C 270, a significant gas entrainment has occured from the tip of the jets to the back of the lobes (Chapter 3).

We note that some of these systems can morphologically be placed in more than one of the classes described earlier. For example some of the 'pointlike' and small scale jet characterized radio sources exhibit some tiny extensions (e.g., NGC 410, NGC 5846) that could class them between small-scale jets and 'pointlike'. In addition, the classification depends on the radio frequency observed: for example in NGC 1167 the group seems to host a small-scale jet at 610 MHz, while, at 235 MHz the morphology of this source is 'pointlike' or NGC 677 presents diffuse emission at 610 MHz, but a clear lobe morphology at 235 MHz which could be characterized as a product of a small-scale jet. Therefore this division is done for informative reasons, as blending of various morphologies in different classes is unavoidable.

To summarise, there are only three systems with high-power AGN jets currently active (NGC 4261, NGC 193/UGC 408 and NGC 7626) though a couple of others have evidence of old AGN outbursts (NGC 5044, NGC 1167). Most other central galaxies are detected in the radio, but are either point sources or have small-scale jets. Lastly, as NGC 7626 is

not the central elliptical of its group we just note that a powerful, extended radio source is detected in this galaxy with bent lobes and a total size of $\sim$180 kpc.

4.4.2 The statistics of radio detections in BGEs

The consensus to date is that the detection of radio emission in group central galaxies is more common than in brightest cluster ellipticals (Feretti & Giovannini, 2008). There are several studies that confirm this. In the statistical study of Lin & Mohr (2007), that included 342 nearby clusters selected in the X-rays from *ROSAT All-Sky Survey* (RASS) with identified BCGs within a distance of z$\leq$0.2, the fraction of radio active BCGs was found to be 36%, and dependent on the mass of the cluster; for galaxies that are more luminous than the K-band magnitude, $M_K = -24$, the BCGs that reside in high-mass clusters exhibit more radio activity than their counterparts in low-mass clusters.

A more recent study from Huang & Chen (2010) identified BCGs from the maxBCG cluster catalogue, which were matched with the FIRST radio catalogue, at a redshift between 0.1 to 0.3. It was found that 43% (552 out of 13000) of the clusters had BCGs associated with double-lobe radio sources. Another similar literature collection from Andernach & Ramos-Ceja (2009) used the flux densities of the brightest cluster members (BCMs) in 1169 Abell clusters and found that 41% of these BCMs exhibited radio emission.

Overall, all these studies seem to be in good agreement with the fractional results of radio active BCGs that were found in earlier studies (e.g., Ball et al., 1993; Burns, 1990). Therefore we can claim that the fraction of the BCGs that exhibit radio activity associated with the central galaxy is $\sim$ 40%.

Group samples should be compared to cluster ones with great caution, as they have different scaling properties (X-ray, radio, optical etc). In order to perform a fair comparison

between a cluster sample and the observations of our central group galaxies, we must take into consideration the selection criteria of each cluster sample and apply similar criteria to our sample. For this reason, we carry out two comparisons for our group central galaxies, using our sample in two different ways, in order to perform a comparison that better matches with the corresponding cluster sample.

At first, our sample is compared with the sample of Andernach & Ramos-Ceja (2009), where no particular selection criteria were used for the brightest cluster galaxies of 1169 Abell clusters, as their only target was to study the radio morphology. It is reported that 578 (41%) were detected at either 1.4 GHz (NVSS or FIRST) or 843 MHz (SUMSS). The 1423 galaxies of this sample is in 1221 redshift components, which means that the clusters are along the line of sight. In our group sub-sample, we detect radio emission in a large fraction of the central group galaxies (85%) (even if it is 'pointlike') at either 610 or 235 MHz. For this comparison we use the 1.4 GHz values from the literature, for our central galaxies, and take into account the limiting fluxes of NVSS (2.5 mJy/beam, Condon et al. 1998), FIRST (1 mJy/beam, Becker et al. 2003) and SUMSS (1 mJy/beam, Mauch et al. 2003). We apply these thresholds in our sample and exclude any group central galaxy that its flux is not above the limiting flux. These were also used for the detection of the BCGS in radio in Andernach & Ramos-Ceja (2009), but we note that our sample is local and not along the line of sight as in Andernach & Ramos-Ceja (2009). We find that 69% (18 out of 26) of the central group galaxies were detected in the radio, matching the detection criteria of the sample of Andernach & Ramos-Ceja (2009). The fractional detection of our central group galaxies is higher than the one observed in cluster BCGs along the line of sight.

For the second comparison we try to match our sample with the detection criteria used in radio for the BCGs in Lin & Mohr (2007). Lin & Mohr (2007) detected 122 BCGs in

342 clusters that have a radio component with flux greater than 10 mJy at 1.4 GHz. The highest redshift of Lin & Mohr (2007) NVSS sample is 0.0647. This means that it is $\sim$300 Mpc, while our furthest BGE is $\sim$3.7 times closer ($\sim$80 Mpc). For that reason, in order to perform a fair comparison with the cluster sample of Lin & Mohr (2007), we consider as radio detected only our groups that have an NVSS 1.4 GHz flux $>$130 mJy as the flux is proportional to d^2. By applying this threshold to our sample, we exclude 17 central group galaxies whose flux is below this limit at this frequency. Taking into account that further 5 BGEs were not detected at 1.4 GHz, we end up with 4/26 BGEs being detected with this criterion in our sample. The fractional detection of our central group galaxies that matches the study of Lin & Mohr (2007) is 16%. The radio fractional detection rate of BGEs in our sample is lower than the rate of 36% observed in the study of BCGs in Lin & Mohr (2007), but with the results from this comparison being closer to the detection rate observed in BCGs.

4.4.3 X-ray detection statistics in CLoGS groups

On the X-ray side of things, as noted in O' Sullivan et al. (2014), 13/26 systems in our sample (50%) exhibit extended X-ray emission, detected at a distance larger than 65 kpc (group-scale X-ray halos), with their temperatures being typical of galaxy groups (0.5-1.5 keV). Furthermore, 7/26 systems (27%) present small-scale halos of X-ray emitting gas (galaxy scale), linked with the dominant early-type galaxy in each system (O' Sullivan et al., 2014). In addition, 5/26 groups show only point-like X-ray emission (19%) and 1 galaxy (NGC 1453) exhibits a possible group scale halo extending out to 61 kpc. We therefore consider that about half of the groups of this sub-sample are X-ray confirmed groups, while in the cluster environment, X-ray emitting thermal gas is almost always present (Ferrari et

al., 2008).

4.4.4 Radio/Xray Comparison

A variety of X-ray properties is observed in the 26-group high-richness subsample of CLoGS. Our sample is considered to be dynamically active, with distortions in the X-ray emission caused either by the central radio source (e.g., NGC 193) or by interactions between the central galaxy and its neighbours (e.g., the case of NGC 7626). This means that our sample contains systems that are in an advanced stage of formation (post-collapse) but not yet in virial equilibrium. These systems present radio emission that comes not only from passive lobes or past activity but also from currently acting mechanisms that can cause such emission and potentially heat the IGM. This applies to 6/26 systems of our sample.

In particular, we cite the case of NGC 5044, which is a group where the existence of cavities around the centre is evidence of AGN/IGM interaction. The fact that some of these cavities are filled with radio emission, while some others are not detected at radio wavelengths, can be interpreted in terms of differing cavity buoyancy timescales (David et al., 2011, 2009). In more detail, David et al. (2009) suggests that the small cavities that are (even at low frequencies) radio quiet, are no longer powered by the central AGN but mainly driven by buoyancy. Their isotropic distribution could then be attributed to the group 'weather', the origin of which could be from previous AGN outbursts or the sloshing of NGC 5044 with respect to the center of the group potential.

Overall, our sample includes three cavity systems which are the same as the ones that exhibit large radio lobes (jet systems; NGC 5044, NGC 193 and NGC 4261), two group-group mergers (NGC 1060 and NGC 7619) and two recently disturbed 'sloshing' systems (NGC 5846 and NGC 5044, Gastaldello et al. 2013).

We classify the systems that have a central decline in their X-ray temperature profile greater than 3σ significance as cool core. From previous studies (e.g., Cavagnolo et al. 2008) it is known that cool cores are connected to the presence of H_α emission and to the nuclear activity in cluster central galaxies, indicating the ability of gas to cool from the X-ray phase to fuel the central AGN.

In three systems (NGC 5044, NGC 193 and NGC 4261), direct proof of interactions between the central radio galaxy and the IGM can be seen. Here, an obvious correlation between the radio and X-ray structures exists (e.g., radio-filled X-ray cavities), but, in the remaining systems, the radio/X-ray associations were either less obvious or not clearly detected. Groups with amorphous/diffuse radio sources do not show X-ray cavities and the fact that no radio jets/lobes are present seems to naturally explain this lack of cavities. In general, the groups which possess significant substructure in the X-ray band (mostly cavity systems) constitute a minority in our sample.

As far as the temperature structure of the groups is concerned, we find that about a third (5/14) of the X-ray confirmed groups are non-cool-core, while the remaining two thirds (9/14) have a cool core. 3/5 of these confirmed non-cool-core groups present extended diffuse radio emission (NGC 677, NGC 1587 and NGC 5353) with the remaining 2 having a small scale jet (NGC 777 and NGC 1453). In cool core groups, 4/9 present radio point sources (NGC 5982, NGC 2563, NGC 5846, NGC 7619), 3/9 have large scale jets and 2/9 presents a small-scale jet (NGC 1060, NGC 410). Of those cool core systems, three are cavity systems, while in the rest of the systems, cavities are not detected, at least at the spatial resolutions achievable with the available X-ray data.

In our sample, we find that every group which has large-scale jets and an X-ray luminous IGM, has a cool core. This is in agreement with the study of Sun (2009), which also found

Table 4.6 X-ray Classification of CLoGS groups

LGG	BGE	$r_{detected}$ (kpc)	Radio morphology	Type of X-ray emission
			X-ray Bright (Class I)	
9	NGC 193	135	Large scale jet	Group
18	NGC 410	75	Small scale jet	Group
31	NGC 677	130	Extended but no jets - 'diffuse' emission	Group
42	NGC 777	275	Small scale jet	Group
72	NGC 1060	310	Small scale jet	Group
117	NGC 1587	137	Extended but no jets - 'diffuse' emission	Group
158	NGC 2563	300	Pointlike	Group
278	NGC 4261	85	Large scale jet	Group
338	NGC 5044	157	Large scale jet	Group
393	NGC 5846	107	Pointlike	Group
363	NGC 5353	100	Extended but no jets - 'diffuse' emission	Group
402	NGC 5982	85	Pointlike	Group
473	NGC 7619	223	Pointlike	Group
			X-ray Faint (Class II)	
27	NGC 584	5	No radio source detection	Galaxy
58	NGC 940	<9	Pointlike	Point
61	NGC 924	<9	Pointlike	Point
66	NGC 978	50	Pointlike	Galaxy
80	NGC 1167	<10	Small scale jet	Point
103	NGC 1453	61	Small scale jet	Group?
185	NGC 3078	16	Extended but no jets - 'diffuse' emission	Galaxy
262	NGC 4008	24	Small scale jet	Galaxy
276	NGC 4169	<6.5	Pointlike	Point
310	ESO 507-25	6.5	Extended but no jets - 'diffuse' emission	Galaxy
345	NGC 5084	11	No radio source detection	Galaxy
351	NGC 5153	6	No radio source detection	Galaxy
421	NGC 6658	<9	No radio source detection	Point

that group and cluster dominant galaxies with strong radio AGNs reside in a cool core. The physical scale of the cool cores varies between groups, with some of our systems having small-scale cool cores or galactic coronae. We note that these occur for galaxies that are confirmed X-ray groups. As is also suggested from the sample work of Giacintucci et al. (2011), all of our groups that exhibit cavities, host a relatively small, low-power, double radio source, with a potential bias owing to the difficulty of a cavity detection in extended, large-scale radio systems. This might suggest that cavities mostly occur in systems where low-power double radio sources exists.

The common radio morphologies that FR I radio galaxies present in the dense environment of the central regions of galaxy clusters (e.g., Giacintucci et al. 2007; Owen et al. 1992, 1993), are distorted and have asymmetric radio morphologies, unlike what we see for group-central radio galaxies in our sample. On the other hand, the majority of the non-cool-core groups show diffuse radio emission, where it seems most likely that the surrounding, thermal gas is important in deforming the components of radio sources in groups.

Furthermore, in order to examine the range of corresponding radio and X-ray structures, that reveal the interactions between the central radio galaxy and the IGM, we further divide our groups into two classes according to their X-ray properties: In Class I we include the galaxies where the X-ray emission is detected within a distance $>$65 kpc (X-ray bright) from their cores. In Class II, we put the remaining galaxies, which are X-ray faint.

Our brightness classification divides the sample in such a way that both Class I and Class II include 13/26 groups (see Table 4.6). In Class I, which contains groups with group-scale X-ray emission, we find that 6/13 groups ($\sim$46%) present in radio either a small scale jet emission or a large scale jet, another 4/13 ($\sim$32%) present point source radio emission while the remaining 3/13 ($\sim$22%) host diffuse/amorphous radio emission. We note that all

the sources that present radio jet emission are found in this Class, as X-ray bright groups or clusters are the most preferable environment that radio jets appear (e.g., Magliocchetti & Brüggen, 2007; McNamara & Nulsen, 2007).

On the other hand, in Class II, the majority of groups (4/13 $\sim$32%) present either a radio point source, or are not detected (4/13, $\sim$32%) in radio, with 3/13 ($\sim$23%) hosting a small scale jet and the remaining 2/13 ($\sim$15%) presenting diffuse/amorphous radio emission. We note here that all galaxies that lacked radio emission appear in this Clas, with the number of pointlike sources being the same in both Classes.

We can summarise the results from our X-ray/radio comparison as:

i) the largest radio sources in BGEs which are currently active, or have been in the recent past so that their resultant radio emission can be still detected, either lie in X-ray bright cool-core groups (NGC 193, NGC 5044, NGC 4261, and even NGC 7626) or have large amounts of cold gas (NGC 1167),

ii) lower power radio AGN are common in both X-ray bright and faint groups, and,

iii) the radio non-detections are in X-ray faint systems.

The fact that huge radio jets in BGEs appear only in X-ray bright groups could be attributed to the supply of gas that fuels the central AGN that comes from the X-ray cooling phase. Since X-ray bright groups are the ones that have the greatest amount of gas this means that they are also the most probable environment in order to feed the jet of the central engine enough to grow large. Since the selection of our groups requires the presence of a central elliptical this requirement in a way covers the fact that the groups are collapsing for the first time at the moment. Thus, the X-ray faint groups of our sample either have a very shallow gravitanional potential, unable to heat the gas (quite unlikely due to the sensitivity of our X-ray data and the velocity dispersions that our groups have) or there is no intra-

group gas at all to be heated and detected in the X-rays as is suggested for the X-ray faint XI groups in Rasmussen et al. (2006).

4.4.5 Radio spectral index distribution of group central galaxies

As the radio morphology of a galaxy depends on the environment in which it is embedded, its radio spectral distribution might have a similar dependence. To examine this, we compare the results of the spectral properties from the CLoGS groups with what is known for clusters and field galaxies.

In dense environments, such as the centres of clusters, radio galaxies usually present a steep synchrotron spectral slope compared to galaxies that reside in the field (e.g., Bornancini et al., 2010; Govoni et al., 2001).

The typical spectral index values of radio sources that are asscociated with a radio galaxy at the centre of cooling core clusters range from $\alpha > 1$ to $\alpha \sim 2$ (Giacintucci et al., 2011). The simplest interpretation for such steep radio spectra is most probably the restriction of the relativistic radio plasma in the central regions of the cluster by the high pressure and dense external medium that stops the radio source's expansion further out. In some cases, there is an absence of new particle injection (if jet activity has ceased), which is also a factor that prevents radio source expansion. The evolution of the radio plasma then is controlled only by synchrotron and inverse Compton energy losses, resulting in a steepening of the radio spectrum, since the confinement of the relativistic plasma could sustain the radio emission longer than expected and prevent its fading through adiabatic expansion (e.g., Ferrari et al. 2008; Giacintucci et al. 2011; Murgia et al. 2011). If the relativistic radio plasma was not confined, then adiabatic expansion of the radio lobes would cause the shifting of the spectral break to lower frequencies much faster and the source would quickly fade out.

In our sample, there is spectral index information for 18/26 galaxies, as 4 were not detected in radio and a further 4 were detected only at one frequency. The spectral indices of these 18 radio sources, measured between 235 MHz and 610 MHz, can be seen in Tables 4.7 and 4.8. Only 2 of 18 sources have steep radio spectra with $\alpha > 1$ (ultra-steep for NGC 5044). All the remaining sources have radio spectra with $\alpha < 1$ ranging from very flat values $\sim$0.3 to typical radio synchrotron spectra of $\sim$0.9. As a result 16/18 sources in our sample have a radio spectrum with $\alpha_{235}^{610} < 1$.

We have found that the mean spectral index value for the 16/18 radio sources that reside in the central galaxies of our groups sample (leaving the extreme outliers out) is $\alpha_{235}^{610} = 0.58 \pm 0.1$. The study of Lin & Mohr (2007) showed that the brightest cluster galaxies (BCGs) AGN that were detected by NVSS at 1.4 GHz and where combined with GB6 and PMN catalogues at 4.8 GHz have a mean spectral index value of α_{1400}^{4800}=0.74$\pm$0.05. The values from our sample indicate a flatter radio spectra but this could be attributed to the different frequency range at which our spectral indices are calculated, as younger radio emission is detected at higher frequencies that faints fastest. A plausible explanation could possibly be the fact that the nature of AGN in central group galaxies and clusters is actually different, with optical AGN being most likely present in BGEs and X-ray luminous AGN being mostly found in clusters (Shen et al., 2007; von der Linden et al., 2007).

The simple scenario analysed in Shen et al. (2007) yields that the majority of AGNs in groups are in the high-accretion optically dominant phase, while the AGN population in rich clusters is mostly in the low-accretion X-ray-dominant phase. There is an evolutionary connection between the two types of AGN. AGNs are optically dominant in the beginning and as time passes they progressively evolve into X-ray dominant AGNs. The properties that AGNs exhibit is therefore a natural consequence of accretion evolution: X-ray AGN prefer-

entially exhibit in evolved systems (cluster of galaxies) where merging processes have occured a long time ago and fast accretion onto the supermassive black hole has now stopped. On the other hand, optical AGNs are found in younger systems (groups of galaxies) where the merger events have more recently occured and are at the start of their evolution. This scenario could explain why group AGN radio sources have less steep spectrum (as they are younger) than the evolved steep spectrum observed in clusters.

In the study of Giacintucci et al. (2011) it is found that 9/15 groups observed with GMRT also, have a steep spectral index of $\alpha_{235}^{610} > 1$ which is the opposite of what we see in our CLoGS sample. However, in this study, all groups were X-ray bright and were chosen according to their X-ray structure or radio morphology in order to provide a census of the variety of forms of AGN/IGM interaction taking place in groups. As is also emphasized in this study this is a non-statistical sample, with the selection of systems being biased toward systems that currently possess features possibly associated with AGN feedback. Therefore it is not comparable with our CLoGS groups results.

The mean value of spectral index that we have calculated for our groups is $\alpha_{235}^{610} = 0.58 \pm 0.1$. The non-BCG values calculated in Lin & Mohr (2007), but in a different frequency range is α_{1400}^{4800}=0.47$\pm$0.15. In addition, since the population of field galaxies consists mainly of blue, starforming galaxies (Balogh et al., 1997; Goto et al., 2003), these values are comparable with the spectral indices of galaxies that emit in the radio and reside in the field.

We observe that the radio spectral index α_{235}^{610}, of the sources that reside in X-ray bright groups is systematically steeper (except of some cases, e.g., X-ray faint group NGC 1167 with $\alpha_{235}^{610} = 0.59 \pm 0.1$) than the spectral index observed in the X-ray faint groups. This could probably mean that in general X-ray bright groups are already evolved systems with

Table 4.7 Radio Source Data analysed in this Thesis. All upper limits shown here are 5 × r.m.s.

Source	S_{610MHz} ±5% (mJy)	S_{235MHz} ±8% (mJy)	α_{235MHz}^{610MHz} (±0.10)	$S_{1.4GHz}$ (mJy)	References 1.4 GHz	$\alpha_{235MHz}^{1400MHz}$ (±0.10)
NGC 410	13.6	28.5	0.78	6.3±0.6	Condon et al. (1998)	0.86
NGC 5084	≤0.3	≤2.5		46.6±1.8	Condon et al. (1998)	-
NGC 584	≤1	≤6		0.6±0.5	Brown et al. (2011)	-
NGC 924	1.7	≤1.5		-	-	-
NGC 677	45.6	99.2	0.81	20.6±1.6	Condon et al. (1998)	0.89
NGC 5353	45.8	65.8	0.38	41.0±1.3	Condon et al. (1998)	0.27
NGC 5153	≤0.3	≤3		-	-	-
NGC 5982	1.9	4.5	0.92	0.5±0.5	Brown et al. (2011)	1.25
ESO 507-25	46.6	55.2	0.18	24±2	Brown et al. (2011)	0.47
NGC 6658	≤0.3	≤3		-	-	-
NGC 4169	3	≤6		1.07±0.15	Becker et al. (1995)	-
NGC 4008	16.4	24.8	0.43	10.9±0.5	Brown et al. (2011)	0.47
NGC 2563	1.3	≤1.5		0.3±0.5	Brown et al. (2011)	-
NGC 777	10.2	20.9	0.75	7±0.5	Brown et al. (2011)	0.62
NGC 940	4.3	3.3	0.29	-	-	-
NGC 3078	384.5	582.8	0.44	310±10	Brown et al. (2011)	0.36
NGC 978	1.3	≤2		-	-	-
NGC 1060	12.4	28.5	0.87	9.2±0.5	Brown et al. (2011)	0.64
NGC 1453	40.4	47.1	0.16	28±1	Brown et al. (2011)	0.29
NGC 5846		58.5	0.52	21±1	Brown et al. (2011)	0.58
NGC 1167	2295.3	4018.4	0.59	1700±100	Brown et al. (2011)	0.50
NGC 4261	29600	48500	0.53	19000±800	Kuhr et al. (1981)	0.53

gas accretion and AGN triggering processes have taken place longer ago than the ones which occured in X-ray faint groups (older radio emission is observed in X-ray bright systems).

For the galaxies for which radio continuum 1.4 GHz information was available, the spectral index between 235 and 1400 MHz was also calculated with no substantial difference in most cases. In only four galaxies, α_{235}^{1400} was a lot different than α_{235}^{610}. In NGC 5982, the value of α_{235}^{1400} revealed a much steeper spectrum of 1.25, confirming the faint and most probably old nature of this point source AGN, while in NGC 1060 the value of α_{235}^{1400} showed a flatter spectrum of 0.65. In NGC 193, the spectral index α_{235}^{1400} of the FR I radio source appears to be much steeper than in the 235-610 MHz regime, while in the ultra steep spec-

Table 4.8 Radio source data analysed from previous work

Source	S_{610MHz} $\pm$5% (mJy)	S_{235MHz} $\pm$8% (mJy)	α_{235MHz}^{610MHz} ($\pm$0.10)	$S_{1.4GHz}$ (mJy)	References 1.4 GHz	$\alpha_{235MHz}^{1400MHz}$ ($\pm$0.10)
NGC 5846	36[1]		0.52	21$\pm$1	Brown et al. (2011)	0.58
NGC 1587	222[2]	655[3]	$>$1.13	131$\pm$5	Brown et al. (2011)	0.91
NGC 193	3154	5199	0.54	1710$\pm$102	Condon et al. (2002)	0.63
NGC 7619	32.3	56.3	0.60	20$\pm$1	Brown et al. (2011)	0.58
NGC 5044	38 [4]	229[5]	1.88	35$\pm$1	Brown et al. (2011)	1.05

trum of NGC 5044, the spectral index appears to be flatter as probably more components of this radio source were resolved at the higher frequency compared to the high resolution 610 MHz image.

The remarkable ultra-steep spectrum of NGC 5044 can be explained by the huge morphological difference detected at 610 and 235 MHz. Since the radio source covers a much larger area at 235 MHz than at 610 MHz, it implies that radio emission from different outbursts co-exists between the 2 frequencies, with the older emission prevailing at 235 MHz (Giacintucci et al., 2011). The opposite is seen in NGC 677 where its spectral index of $\sim$0.8 comes from a co-existence of a diffuse emission at 610 MHz, larger in area than the bending lobe/jet morphology at 235 MHz.

There were also two cases in our sample where a flat spectral index was observed. In NGC 1453 the spectral index between 235 and 610 MHz is 0.16, while the calculation of the spectral index between 235 and 1400 MHz yields also a relatively flat value of 0.29. As the morphology of the radio emission at both frequencies is the same with no dramatic difference, the very flat index can probably be explained by the emission from a very young AGN. On the other hand, the flat spectral index of 0.18 observed in ESO 507-25 possibly has a different explanation. The spectral index of the radio source between 235 and 1400 MHz is 0.48 which along with the different morphologies observed at 235 and 610, suggests that the diffuse emission of ESO 507-25 observed only at the high resolution image at 610

Figure 4.29 Spectral distribution of CLoGS central galaxies over 235, 610 and 1400 MHz

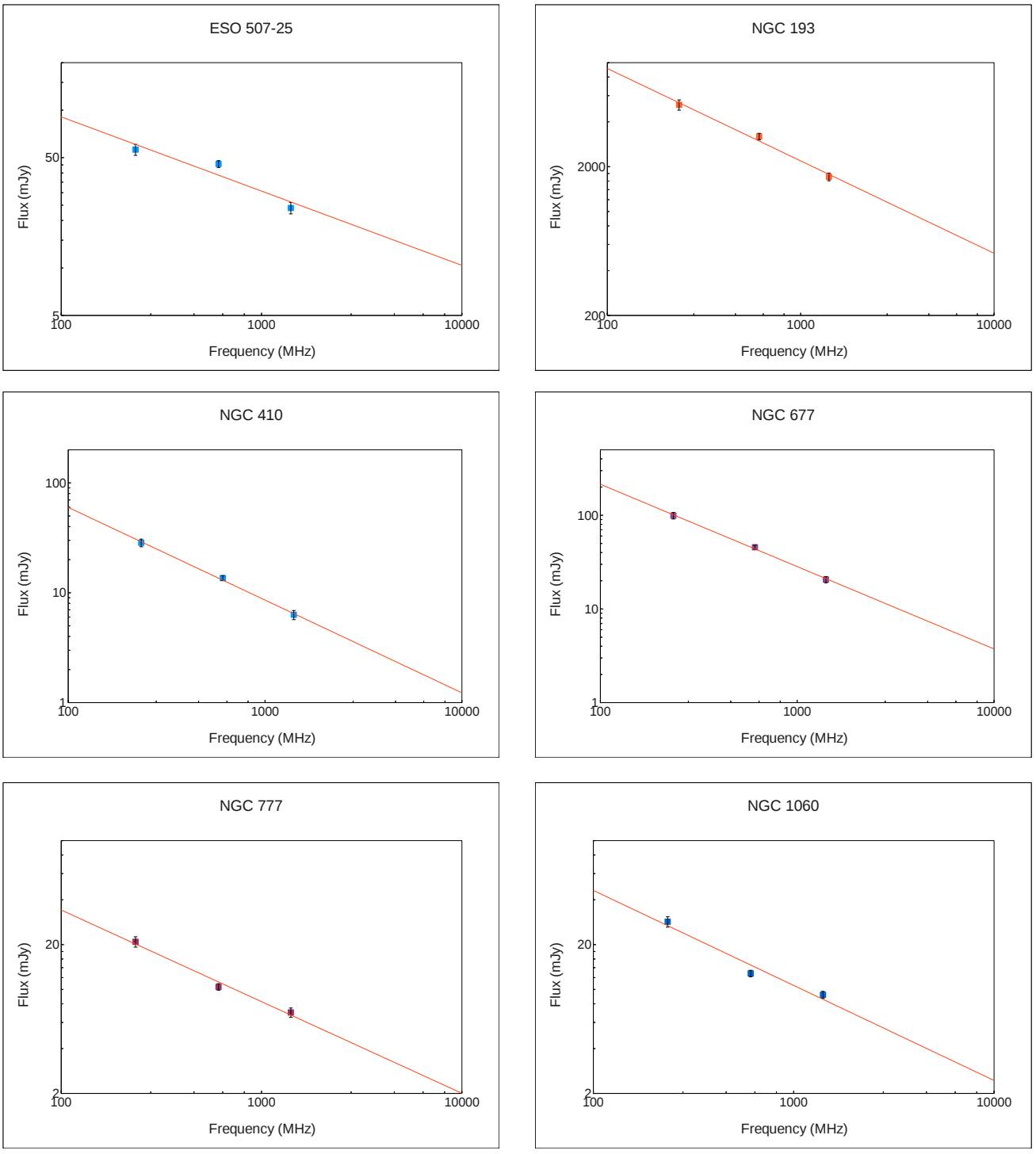

Figure 4.30 Continued

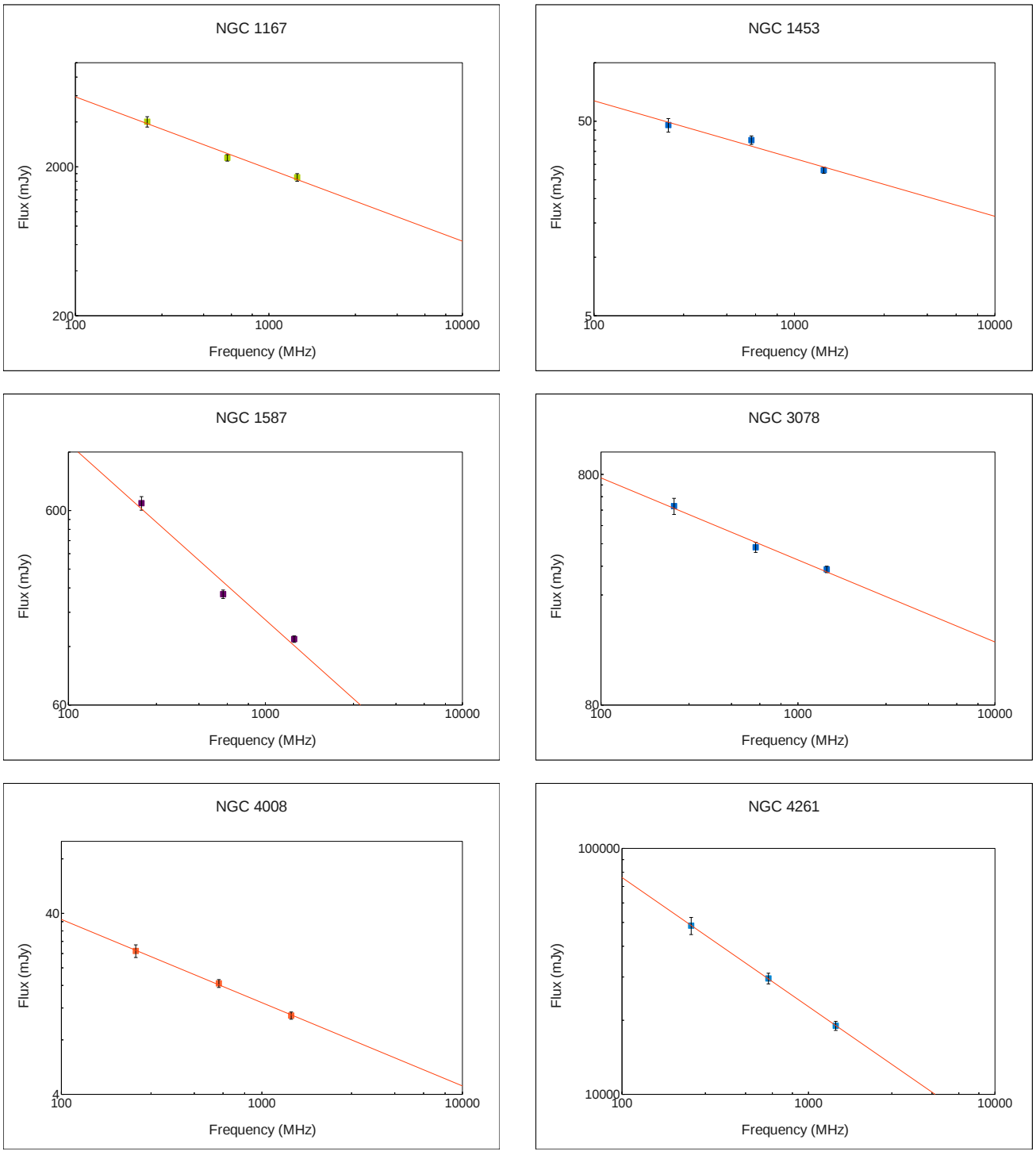

Figure 4.31 Continued from Figure 4.29

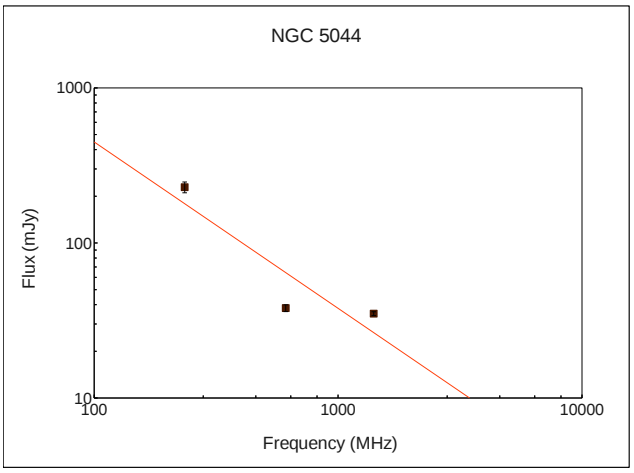

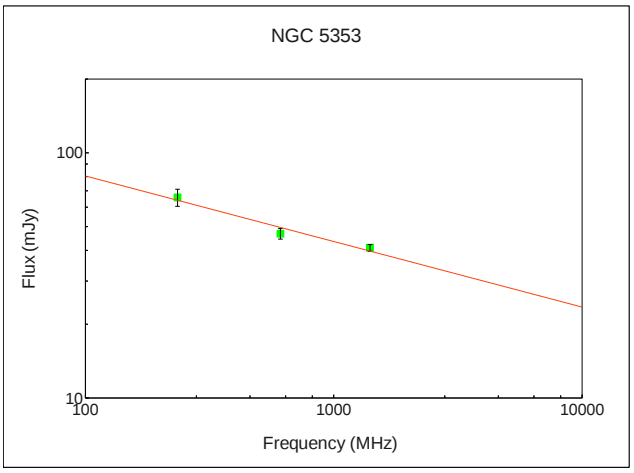

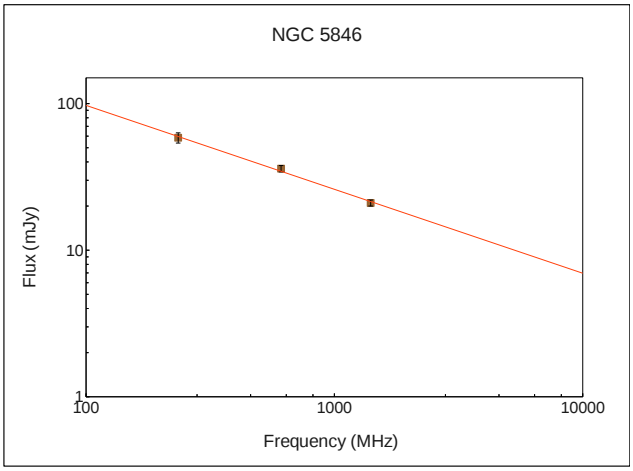

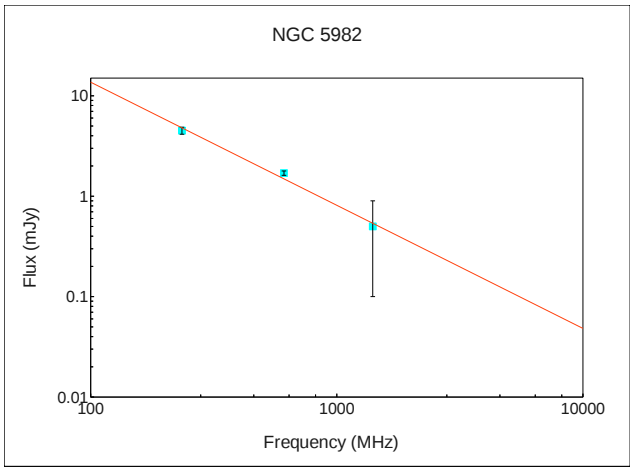

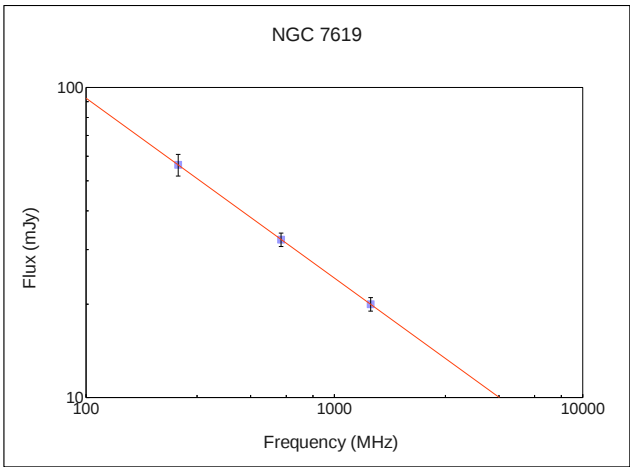

MHz has affected the spectral index value for this galaxy.

In order to map the spectral behaviour of our BGEs, we constructed for each BGE a spectrum, using the systems where we have flux information in three frequencies: 235 MHz, 610 MHz and 1.4 GHz. In most cases, as is seen in Figures 4.29, 4.30 and 4.31, the literature flux density at 1.4 GHz follows a powerlaw along with our GMRT observations, as is common in radio emission. In 5 systems (ESO 507-25, NGC 1060, NGC 1453, NGC 1587 and NGC 5044) we observe a deviation from the powerlaw. This could be attributed to a difference in the morphology between all three frequencies, thus the flux that is calculated from every frequency corresponds on a different area. For these systems the calculation of radio luminosity should be performed with caution.

4.4.6 AGN energy output in CLoGS

The impact of radio AGN feedback in our sample of groups can be calculated by the work done from the jets and lobes of the AGN in moving a volume of gas V and pressure P in their surrounding environment (PV). The energy that is required to create the X-ray cavities is equivalent to the energy output that is applied to the hot X-ray emitting gas from the feedback mechanism. This energy inside the cavity is $PV/(\gamma-1)$ and correlates with the total cavity energy of $E_{cav} = [\gamma/(\gamma-1)]PV = 4PV$, where is often assumed that $\gamma = 4/3$, owing to the synchrotron emission from relativistic electrons that the cavities are filled with (e.g., McNamara & Nulsen, 2007).

Radio emission can provide such estimation of the energy available, E_{mech}, via its relation with the mechanical power (P_{mech} = P_{cav}) (e.g., Best et al., 2007). This was firstly presented in Bîrzan et al. (2004) by the relation between cavity power (P_{cav}) and 1.4 GHz radio power, using a sample consisting mainly of cluster galaxies.

However, as synchrotron electrons of higher frequencies lose their energy fastest, the problem was that many cavities remained undetected at 1.4 GHz. Bîrzan et al. (2008) measured the mechanical power using the lower frequency of 327 MHz at the VLA (these observations were of variable quality) and the estimate of the integrated 10 MHz−10 GHz radio luminosity. An estimate of the integrated radio luminosity ought to give a more reliable relation with related physical parameters, as it covers the total energy output of the AGN.

The radio powers for each frequency were calculated from Condon (1992) by:

$$P_\nu = 4\pi L_D^2 (1+\mathrm{z})^{(-\alpha+1)} \mathrm{S}_\nu. \tag{4.3}$$

where L_D is the luminosity distance to the source, α is the spectral index, z the redshift and S_ν is the flux density of the source a frequency ν. In case where no spectral index is known for the source, α is by default set to -0.8, which is the typical value for extragalactic radio sources.

In Figures 4.32 and 4.33, the fractions of the 235 MHz and 610 MHz radio luminosities of the central CLoGS group galaxies are shown respectively. The number of galaxies in each bin is shown on the y-axis while x-axis corresponds to the luminosity bins for each frequency. The galaxies at 235 MHz are binned at $1\times10^{21}-1\times10^{22}$, $1\times10^{22}-1\times10^{23}$, $1\times10^{23}-1\times10^{24}$ and $1\times10^{24}-1\times10^{25}$ W Hz^{-1}, while at 610 MHz the bins are equally spaced but start from 1×10^{20}. The majority of the galaxies, as seen in both frequencies, typically have a very low radio luminosity in the range of $10^{22} - 10^{23}$ W Hz^{-1}. The lowest radio luminosities noted in the literature (e.g. $\mathrm{L}_{1.4GHz} \sim 10^{23}$ W Hz^{-1}; Best et al. 2005) have a value of $\mathrm{L}_{610} \sim 2\times10^{23}$ W Hz^{-1}. From Figs 4.32 and 4.33 we clearly see the lack of galaxies in the luminosity range $1\times10^{23}-1\times10^{24}$ W Hz^{-1} followed by the detection of three galaxies with luminosities $>10^{24}$ W Hz^{-1}. These are NGC 4261, NGC 193 and

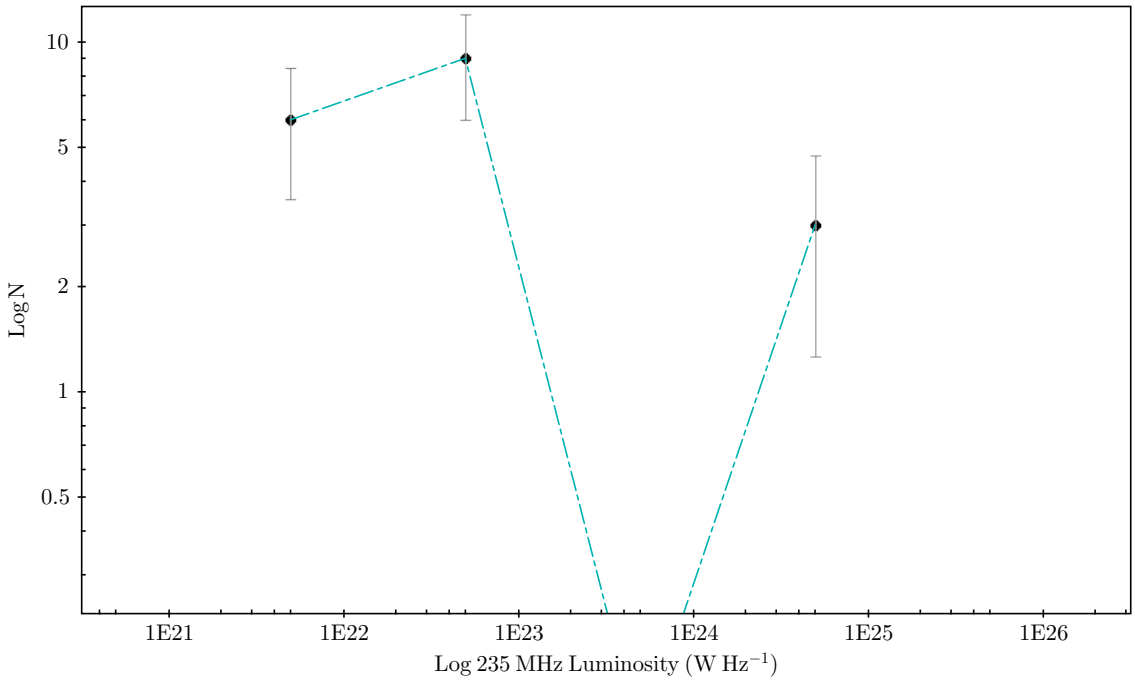

Figure 4.32 Radio luminosity of the detected at 235 MHz CLoGS group central galaxies. The data points are placed in the middle of each bin.

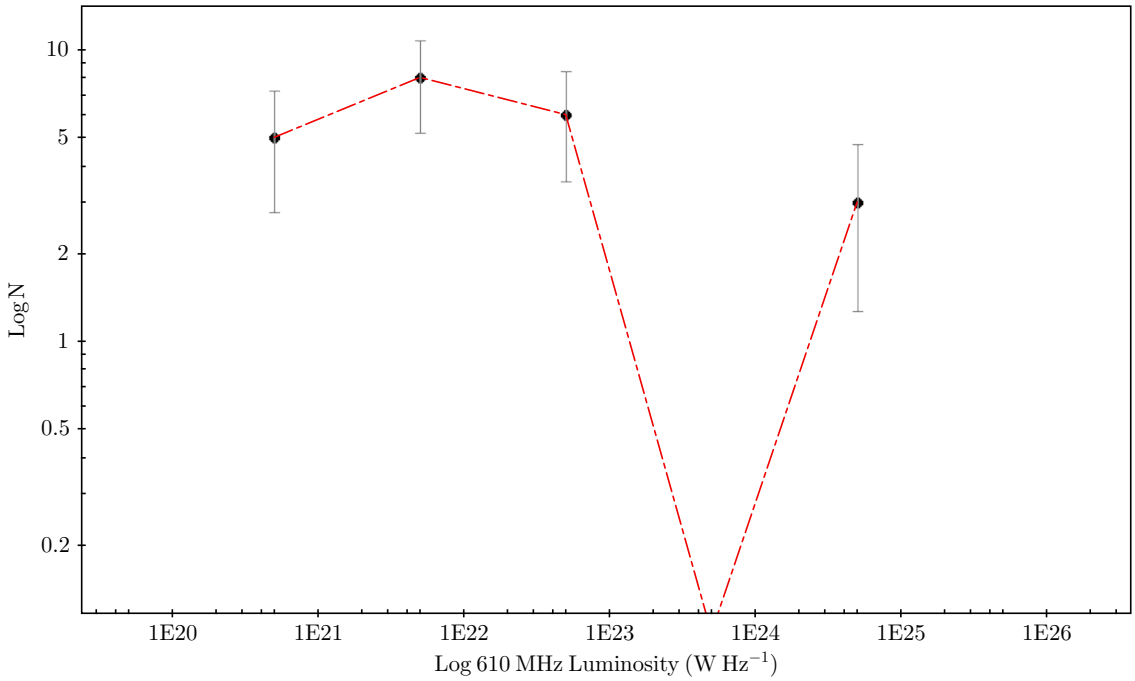

Figure 4.33 Radio luminosity of the detected at 235 MHz CLoGS group central galaxies. The data points are placed in the middle of each bin.

NGC 5044 which are the exceptional cases of galaxies that don't fit into our groups radio luminosity function. These are bright FR I radio galaxies that host jet systems, unlike any galaxy that we have detected in our groups.

The mechanical power of the group central AGNs is measured then from the two scaling relations given by O'Sullivan et al. (2011). In the first one,

$$\log \mathrm{P_{cav}} = 0.71\,(\pm 0.11)\log \mathrm{P_{235}} + 1.26\,(\pm 0.12) \tag{4.4}$$

where $\mathrm{P_{cav}}$ is in units of 10^{42} erg $\mathrm{s^{-1}}$ (to be compatible with literature values) and $\mathrm{P_{235}}$ in units of 10^{24} W $\mathrm{Hz^{-1}}$, the mechanical power is correlated with the single 235 MHz-frequency power. The reason that 235 MHz was used is that lower frequencies are believed to provide a better estimate of the true radio power because they are the least affected by ageing. The results from this relation are shown in Table 4.5 named as energy output. In the second scaling relation the mechanical power is now correlated to the integrated radio luminosity ($\mathrm{L_{radio}}$) in the 10 MHz $-$ 10 GHz band by:

$$\log \mathrm{P_{cav}} = 0.71\,(\pm 0.11)\log \mathrm{L_{radio}} + 2.54\,(\pm 0.21) \tag{4.5}$$

where $\mathrm{P_{cav}}$ and $\mathrm{L_{radio}}$ are both in units of 10^{42} erg $\mathrm{s^{-1}}$, with $\mathrm{L_{radio}}$ calculated from the integration in the frequency range 10 MHz $-$ 10 GHz by

$$L_{\mathrm{radio}} = \int S(\nu)d\nu = \int \kappa \nu^{\alpha} d\nu \tag{4.6}$$

These scaling relations are empirical, drawn from observations of the radio luminosity of the source and X-ray calculations of the cavities that they inflate. The radio integrated

luminosity shows a more accurate estimate of the power output compared to the results from the P_{235} relation. In addition, if any central AGN lacked radio emission at 235 MHz (possibly due to a break in the spectrum), they would be excluded from our energy calculations. For these reasons the values calculated from L_{radio} were used for the estimation of the total E_{mech}.

X-ray observations have revealed that AGN outbursts at the centers of clusters and groups of galaxies are sufficiently energetic to prevent the existing hot gas from cooling, a mechanism that is also consistent with models of 'radio mode' AGN feedback that moderates cooling and star formation (e.g., Bîrzan et al. 2004; Dunn & Fabian 2006; McNamara & Nulsen 2007; Rafferty et al. 2006). The long timescales of AGN outbursts ($>10^6$yr) allows us only to have a single snapshot of them, while non presence of outbursts in some clusters with short central cooling times (e.g., Wise et al. 2004) and mildly strong shocks (e.g.,Machacek et al. 2006; McNamara et al. 2005) support intermittent AGN outburst activity. However, the prevalence and duty cycle of AGN outbursts in clusters of galaxies that produce bubbles of X-ray gas and balance cooling flows with the ICM is still not well understood, thus the study of the cycles of intermittent AGN outbursts, is still required as there many different cases.

In order to calculate the mechanical energy that the central engine is outputing in the group environment, an appropriate timescale has to be assumed. The outburst timescale estimation is based on the amount of time the observed X-ray cavities take to rise ($t_{buoyancy}$, Churazov et al. 2001), or sometimes from the estimation of the sonic timescale (i.e., the travel time between the AGN core and the tip of the cavity at the sound speed, O'Sullivan et al. 2011). This timescale can be considered as a lower limit for the total energy, as the contribution of the energy dissipated in shocks is disregarded along with other possibly

important parameters (Gitti et al., 2012). Similar proof of AGN feedback exists in galaxy groups and isolated elliptical galaxies (Nulsen et al., 2009).

As the timescale of an AGN outburst varies from cluster to cluster and from group to group, there are multiple timescales that are considered in the literature. In the study of Miller et al. (2003) it is shown that the duty cycle of AGNs in clusters of galaxies should be $\sim 2 \times 10^8$ yr since the fraction of optical AGN was similar at higher redshifts to the one observed at lower redshifts, whereas in the study of Abell 262 atimescale of $\sim 3 \times 10^7$ yr has been assumed for the visible separate radio AGN outbursts (Clarke et al., 2007). As in Bîrzan et al. (2004), in the study of Fulai & Peng (2009) is also assumed that each AGN-heating episode lasts for 10^8 yr. Therefore the most commonly assumed timescale outburst for AGNs in clusters of galaxies is $\sim 10^8$ yr (Bîrzan et al., 2012).

On the other hand, in the case of two isolated non BCG elliptical galaxies in the Virgo cluster, NGC 4636 (Jones et al., 2002) and NGC 4552 (Machacek et al., 2006), much shorter outburst timescales are assumed at the order of $\sim 3 \times 10^6$ yr and $\sim 2 \times 10^6$ yr respectively. Studies of outburst timescales in central brightest galaxy group ellipticals (BGEs) indicate that the time between recent AGN outbursts is typically less than $\sim 10^8$ yr (e.g., David et al. 2011; Randall et al. 2011). In Randall et al. (2011) results from new Chandra, GMRT, and SOAR observations of NGC 5813 revealed three pairs of collinear cavities at 1 kpc, 8 kpc, and 20 kpc from the central source, that were assumed to be from three different outbursts of the central AGN, with a timescale of $\sim 3 \times 10^6$, $\sim 2 \times 10^7$ yr, and $\sim 9 \times 10^7$ yr for each one. In David et al. (2011) a deep Chandra observation of the X-ray bright-rich group, NGC 5044, showed that the core of this group has been repeatedly disturbed by AGN outbursts, with the presence of a multiphase gas indicating that the most recent occured in less than $\sim 10^8$ yr.

The output of the mechanical energy can then be estimated by assuming a timescale for the AGN outburst by $E_{mech} = P_{mech} \times \tau$, where we assume that the most representative timescale for our galaxy groups would be $\tau \sim 2 \times 10^7$ yr.

Lastly, in Figure 4.34 is shown the histogram from the calculation of P_{mech} for our BGEs using the scaling relation 4.5. The typical energies for our group sample vary from $10^{56} - 10^{58}$ erg, having a spread of 2 orders of magnitude. These values are indicative of the energies that are met in a group environment (e.g., for NGC 4325 group $E_{mech} = 2 \times 10^{59}$ erg, Fulai & Peng 2009).

These values are lower than the estimates of the work needed to inflate observed cavities in rich clusters (10^{60} erg; Bîrzan et al. 2004; McNamara et al. 2005), rising by $1-2$ orders of magnitude for the most extreme cases such as Hydra A (Nulsen et al., 2005) and MS 0735+7421 (McNamara et al., 2005). Such energies are observable in clusters of galaxies, as the role of feedback in the regulation of galaxy formation is examined from the aspect of systems with the greatest 'reservoir' of hot gas in the Universe (Gitti et al., 2012).

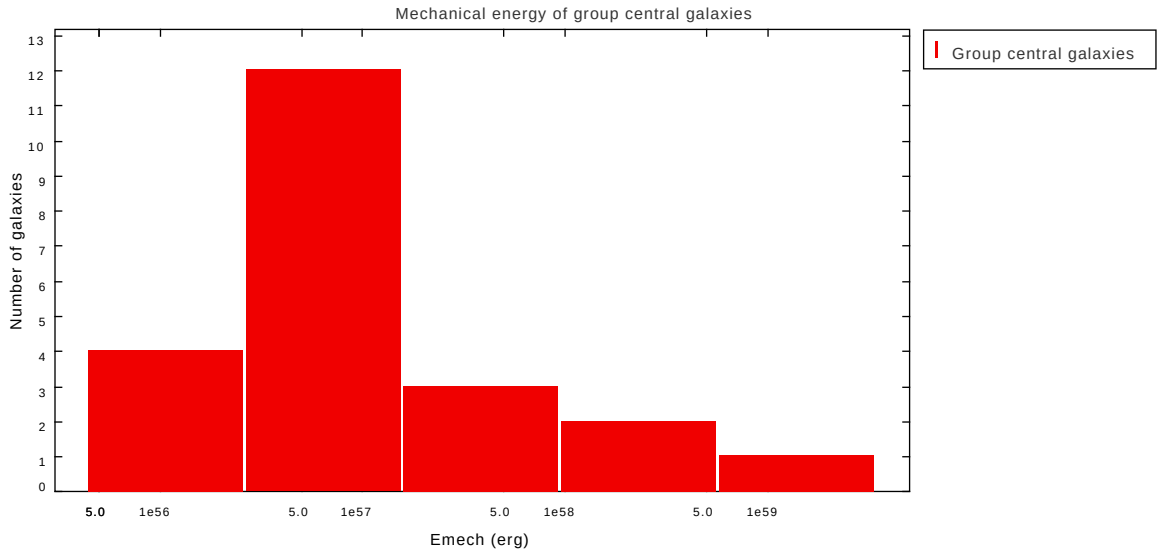

Figure 4.34 Histogram of the mechanical energy output of CLoGS group central galaxies calculated from total radio luminosity

4.5 Conclusions

In this Chapter we have presented, for the first time, low frequency GMRT radio images of the brightest group early-type galaxies (BGE) from the high richness CLoGS sub-sample at 235 and 610 MHz. We find that 22 out of the 26 BGEs are detected at either radio frequency, with the majority of the BGEs exhibiting a 'pointlike' radio morphology.

The comparison of our sample with both cluster samples of Andernach & Ramos-Ceja (2009) and Lin & Mohr (2007), does not yield a clear result that radio emission in BGEs is more common than in brightest cluster ellipticals (BCEs). For each comparison, we have adopted the same radio detection limits of each sample excluding some of our detected BGEs in order to have a fair method of comparison. In the first comparison with the cluster sample of Andernach & Ramos-Ceja (2009), the fractional detection of BCGs that shows radio emission is 41% compared to 69% of our BGEs, while in the second comparison with the sample of Lin & Mohr (2007) 36% of BCGs exhibits radio emission compared to 16% in our sample adopting an equivalent threshold due to the distance difference between the samples.

In the X-rays we see that 13/26 systems (50%) have a group scale X-ray emission that reaches beyond 65 kpc (X-ray bright). Of these 13 X-ray bright systems, we observe an equal fraction of systems (39%) that presents either a small or large scale jet radio emission (5/13) or a 'pointlike' one (5/13), with the remaining 3/13 (22%) hosting diffuse radio emission with no particular orientation. We find that the largest radio sources that are either currently active, or have been active in the recent past such that they are still observable in the radio, lie in X-ray bright cool-core groups with the systems that were not detected in radio appearing in X-ray faint systems. The common population of X-ray bright and faint groups seem to be the lower power radio AGN.

We find the spectral index distribution for the 18/26 galaxies for which we have spectral information at 235 and 610 MHz, with only 2/18 having a spectral index steeper than 1. The mean spectral index is calculated to be 0.58 ± 0.1, leaving out of this calculation the 2 systems that had a spectral index much steeper than 1. The mean value indicates that the radio spectral index in BGEs is flatter than the one observed in BCGs.

Finally, we find that the radio luminosity of our BGEs sample at both 235 and 610 MHz ranges between $10^{22} - 10^{24}$ W Hz^{-1}, with the total energy that a radio BGE can provide, assuming a timescale of $\tau\sim2\times10^{7}$ yr, ranging between 10^{56} to 10^{58} erg.

Chapter 5

Star formation and AGN in galaxies in the CloGS groups: A multiwavelength analysis

Although our understanding of the fine details of galaxy evolution and the processes involved is limited, significant revelations from multi-wavelength observations have shed light on many of these mechanisms in the past few decades. Following this approach, we begin our analysis of CLoGS galaxies by identifying our radio-detected sources with counterparts in other catalogues. This involved the following surveys:

- the Infrared Astronomical Satellite (IRAS) mission (Neugebauer et al., 1984) that provided shallow but useful data sets from the J band up to 100 μm,
- the Two Micron All-Sky Survey (2MASS; Skrutskie et al. 2006) in J, H and K infrared wavebands,
- the Wide-field Infrared Survey Explorer (WISE; Wright et al. 2010) in the mid-

infrared,

- the 1.4 GHz NRAO VLA Sky Survey (NVSS) (Condon et al., 1998) in the radio,
- the ultraviolet (UV) from the Galaxy evolution explorer (GALEX; Martin et al. 2005; Morrissey et al. 2005), and
- the Sloan Digital Sky Survey (SDSS; York et al. 2000) that has gathered a great amount of data in the optical regime.

In order to fully understand the observable properties of star-forming galaxies in the nearby Universe, various star formation rate (SFR) indicators need to be quantified and compared. We aim to use information from the different parts of the electromagnetic spectrum from the above surveys to obtain a more complete picture of global star formation in galaxies in the local Universe. The combination of the catalogue of CLoGs sources, with observations from a broad range of frequencies, gives the opportunity to estimate physical parameters for our group members and the SFR that comes out from different indicators available for our sample.

In general, while, matching catalogues, not all sources yield an ideal one to one correlation but often can end up in confusing an object in one catalogue with several objects in another catalogue. Often it is a matter of differing resolution, This could occur either because the corresponding objects are in reality not the same, or if they belong to the same system. This problem is more profound when catalogues with different resolutions are matched, which is the case with some of our matchings. However, as our sample galaxies are in the local Universe, we possess accurate optical positions and when multiple objects were matched within the search radius, our procedure was to select the one that is positioned nearest, excluding the rest of the matches.

The properties and the matching procedure followed for each survey is explained in detail in the following sections. Using emission lines from optical data, optical AGN are also identified and compared to the different kinds of AGN altogether. A separation between AGN and star forming galaxies is performed with the different star formation indicators from infrared, ultraviolet and radio being presented and compared. The fraction then of the star forming galaxies to the AGN is investigated.

Finally, we examine the statistics of the radio detected galaxies in our groups, and study the relation of the SFRs calculated from four different indicators (610 MHz radio, WISE W3 and W4, GALEX FUV) with distance from the centre of the groups.

5.1 Separating AGN and star forming galaxies with SDSS

One observable distinction between normal galaxies and AGN is the presence of, in AGN spectra, very strong optical and ultraviolet emission lines. In general, there are two categories of AGN (Hao et al., 2005): i) broad-line AGN that exhibit allowed broad emission lines of a few thousand km s^{-1} at Full Width at Half Maxima (FWHM) and ii) narrow-line AGN with both forbidden and allowed narrow emission lines of a few hundred km s^{-1} at FWHM. Despite the fact that the emission lines from narrow-line AGN are equivalent to the ones seen in normal star-forming galaxies, they are stronger and come from a larger ionized region (broad ionizing spectra, with a high energy component). That is the key feature that allows narrow-line AGN identification: their unique emission line ratios.

The study by Baldwin, Phillips & Terlevich (1981) was the first one to propose that AGN a priori exhibit higher [OIII]λ5007/H_β (flux ratio of [OIII]λ5007 to H_β) than other galaxies whose emission line processes are linked with star formation and therefore introduce the first line ratio diagram (known as BPT diagram). Later on, more combinations

of line ratios for the diagnostic diagrams were proposed by Veilleux & Osterbrock (1987): [OIII]λ5007/H$_\beta$, [NII]λ6587/H$_\alpha$, [OI]λ6300/H$_\alpha$ and [SII]λ6716,31/H$_\alpha$, who established a method to distinguish between AGN and starburst galaxies with the use of a semi-empirical line on the diagrams. The emission lines chosen had comparable wavelengths, in order to avoid spectroscopic and photometric uncertainties.

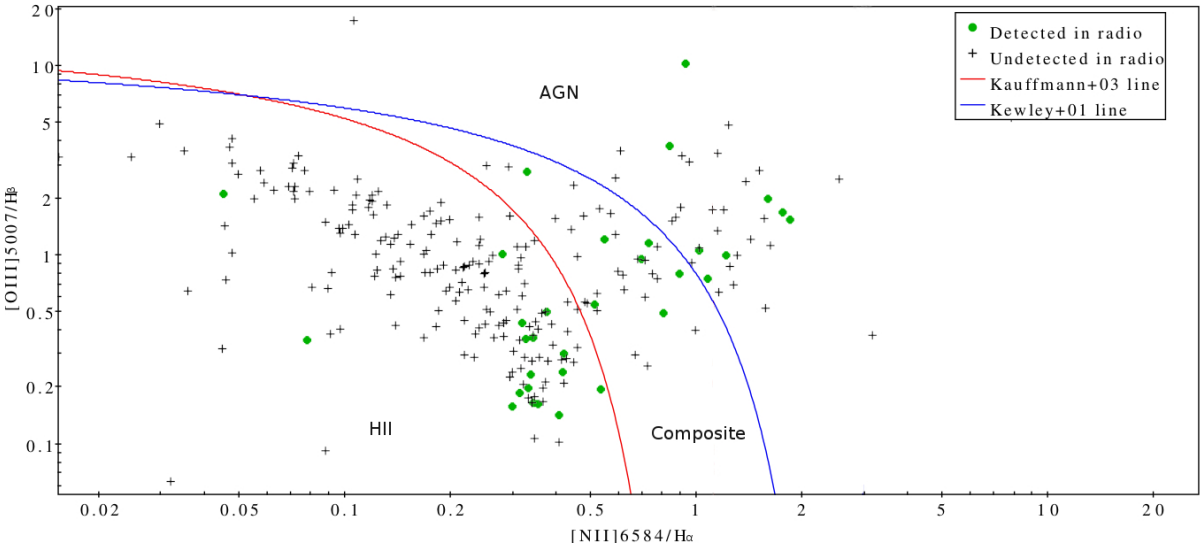

Figure 5.1 The diagnostic indices according to Baldwin, Phillips & Terlevich (1982) using [OIII]λ5007/H$_\beta$ and [NII]λ6587/H$_\alpha$ line ratios that separates the AGN by star-forming galaxies, plotted for all CLoGS galaxies of our sample for which the data were available in the SDSS catalogue. We indicate which of these galaxies are detected in our radio GMRT galaxies. Superposed on the graph are two theoritical lines corresponding on the models of Kewley et al. (2001) (blue) and Kauffmann et al. (2003) (red)

More recently, a realistic starburst model with a great range in metallicity and ionization parameters, was produced by Kewley et al. (2001). From the model, which yielded upper limits for star forming galaxies, a set of theoretical lines were extracted, separating the AGN from the star-forming galaxies on the diagnostic diagrams. These theoretical lines dividing

the AGN from star-forming galaxies have a semi-hyperbolic pattern:

$$
\begin{aligned}
log\left(\frac{[OIII]\lambda 5007}{H_\beta}\right) &= \frac{0.61}{log([NII]/H_\alpha)-0.47}+1.19 \\
log\left(\frac{[OIII]\lambda 5007}{H_\beta}\right) &= \frac{0.72}{log([SII]/H_\alpha)-0.32}+1.30 \\
log\left(\frac{[OIII]\lambda 5007}{H_\beta}\right) &= \frac{0.73}{log([OI]/H_\alpha)+0.59}+1.33.
\end{aligned}
\tag{5.1}
$$

In addition, Kauffmann et al. (2003), proposed another empirical and more conservative cut-off for AGN:

$$
log\left(\frac{[OIII]\lambda 5007}{H_\beta}\right) \geq \frac{0.61}{log([NII]/H_\alpha)-0.05}+1.3. \tag{5.2}
$$

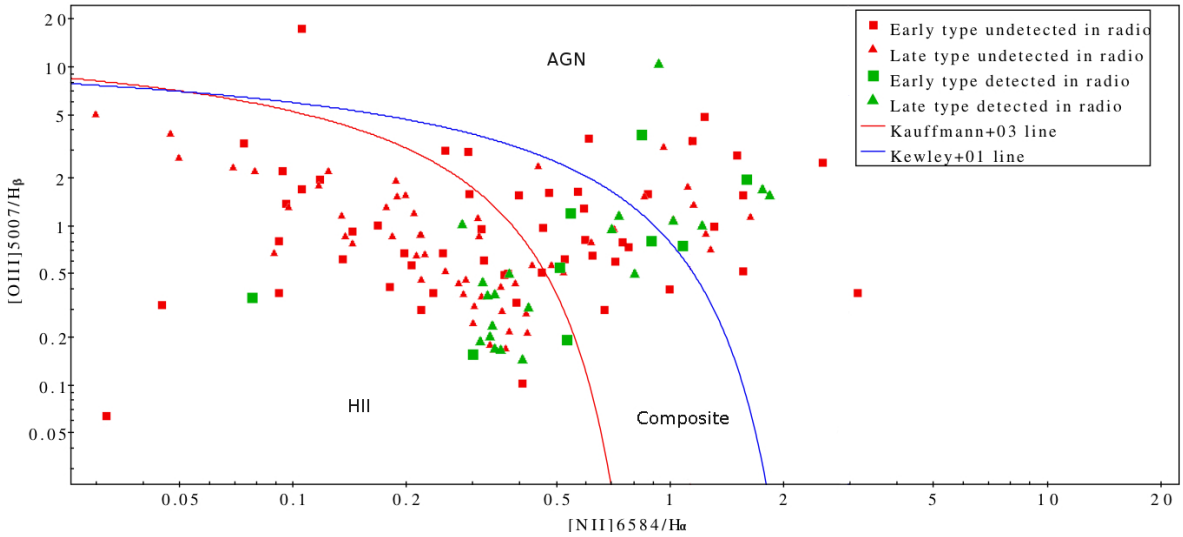

Figure 5.2 The diagnostic indices according to Baldwin, Phillips & Terlevich (1982) using [OIII]λ5007/H$_\beta$ and [NII]λ6587/H$_\alpha$ line ratios that separates the AGN by star-forming galaxies, plotted for all CLoGS galaxies of our sample for which the data were available in the SDSS catalogue. We indicate which of these galaxies are detected in our radio GMRT galaxies. Superposed on the graph are two theoritical lines corresponding on the models of Kewley et al. (2001) (blue) and Kauffmann et al. (2003) (red)

The position that each galaxy occupies in the BPT diagram according to these emission line flux ratios separates galaxies between: (i) star-forming galaxies, (ii) active galactic nu-

clei and (iii) composite systems that exhibit indicators from both previous types. We follow this BPT classification and create the BPT diagnostic diagrams to distinguish between the different types of galaxies in our sample. The emission lines are from the Sloan Digital Sky Survey (Stoughton et al., 2002; York et al., 2000), the spectroscopic survey that has mapped $\sim 25\%$ of the sky, providing photometry (ugriz band) and redshifts for over a million galaxies and quasars.

We created a catalogue that contained the information from our GMRT radio analysis of CLoGs galaxies, with our sample galaxy positions from the optical data extracted from the Garcia (1993) catalogue. We correlate the matched radio sources of our CLoGS catalogue, using the Sky algorithm in *Topcat* and a matching radius of $2'$ with the catalogue data from the Seventh Data Release (DR7, Abazajian et al. 2009) of the SDSS. The total number of galaxies that had spectroscopic data from SDSS DR7 using that selection criteria were 315 (Less than half of the total number of galaxies in our high richness sub-sample $\sim$46%). The galaxies with available fluxes for the emission lines needed to construct a BPT diagram were 250.

Using the fluxes of these emission lines (H_β, [O III], H_α, and [N II]), we constructed a BPT diagram in order to discriminate between the AGN and HII/star-forming galaxies. In Fig. 5.1 we can see a clear separation between the AGN and the star-forming galaxies. The details of the galaxies in the BPT diagram are seen in Table 5.1. The majority of the galaxies shown in Fig. 5.1 (179/250, $\sim$72%) falls below the Kauffmann et al. (2003) line indicating that they are star-forming. 17 of the 179 galaxies that are optically characterised as star-forming are detected in radio. In the AGN area above the Kewley et al. (2001) line, lie 37 optical AGN ($\sim$15%), 8 of which are detected in radio, and between the Kewley et al. (2001) and Kauffmann et al. (2003) line, we have 33 composite galaxies ($\sim$13%) with 7

detected in radio. From the radio detected galaxies in SDSS we see that ∼53% of them are star-forming, while ∼25% of the galaxies have AGN.

Using this optical identification, based on the galaxies detected with SDSS from our sample, we find that only 10% of the star-forming galaxies are detected with GMRT in radio, whereas the fraction of radio detected galaxies in AGNs is ∼22% and for composites ∼21%. We note that in these statistics the BGEs are included and the fractions mentioned above are only for the galaxies that exhibited optical lines from SDSS.

In Figure 5.2, we see the morphology of the radio detected galaxies in each region (AGN, Star-forming). As expected, in the star-forming regions we mostly find late-type galaxies (∼80% of the population in that area), but in the AGN region of the BPT plot (above the Kewley et al. 2001 line), the fraction between early-type and late-type galaxies is found to be almost even. The fraction of early-type AGN in our sample, independent of their radio detection, is found to be 16%.

We note that as the definition of the SDSS classification is based on the position of the masks, this plays a fundamental role in the characterisation of the galaxies. Since our galaxies are in the local Universe the position of the mask in the centre or in the outskirts of the galaxy may significantly affect the classification of some of our galaxies.

5.1.1 Sample comparison for the (BPT) optically selected AGN

The previous study from Miller et al. (2003), at redshifts $0.05 \leq z \leq 0.95$, found that the overall fraction of galaxies that have AGN signature in their optical spectra is at least 20%, with similar result of 17% found by Carter et al. (2001). These studies included every galaxy at that range of redshift in the local Universe, without any discrimination based on whether they reside in a group, a cluster or the field. We then perform a one on one comparison of

Table 5.1 Detection statistics from SDSS matches. In the first line of Column 1 is the total number of galaxies that matched with our catalogue and are contributing in the BPT diagram. The second line of Column 1 shows the number of galaxies detected in radio, with the third and fourth line in Column 1 showing respectively the total number of early type and late type galaxies. In Column 2,3 and 4 we note the number of galaxies that were Star-forming, Composite and AGN for each category of Column 1.

Total number of galaxies matched with SDSS	Star-forming	Composite	AGN
250	179 (72%)	33 (13%)	37 (15%)
Total number of galaxies detected in radio	Star-forming	Composite	AGN
32	17 (53%)	7 (22%)	8 (25%)
Total number of early type galaxies	Star-forming	Composite	AGN
61	29 (48%)	18 (30%)	14 (23%)
Total number of late type galaxies	Star-forming	Composite	AGN
72	52 (72%)	8 (11%)	12 (17%)

our groups sample, with a study of a cluster sample in optical AGN. The first statistically well-defined work for optical AGN in cluster and field galaxies was performed by Dressler et al. (1985). In this study, that included 1095 galaxies in rich clusters and 173 field galaxies, it was found that the fraction of optical AGN in clusters is 1%, in fact 5 times less than the equivalent fraction in field galaxies (5%). This study was supported later by several other studies (e.g., Grogin et al. 2005), but with the difference between the two environments being smaller for lower luminosity AGNs. The fraction of the optically selected AGN from plots 5.1 and 5.2 in our CLoGS groups is found to be $\sim$5% (37/690), a fraction which is exactly the same as the optical AGN fraction that is found in field galaxies in the study of Dressler et al. (1985). We note here that the environment we call "group" would have been included in the "field" category in Dressler et al. (1985). The optical AGN identification on the above studies was based on emission-line diagnostics using galaxies with SDSS spectroscopy (BPT technique) which is the same as we used for our analysis.

Our result suggests that the fraction of optical AGN in groups of galaxies is higher than that observed in clusters, as does the study of Shen et al. (2007) which implies that optical AGN are most probably found in a group environment, although the groups used in the Shen et al. (2007) sample were of low density, and thus vulnerable to biases. Furthermore, Arnold et al. (2009), adopting a limit for absolute magnitude M_R of -20 mag, found that the fraction of optical AGN in groups and clusters of galaxies is $\sim$7%. We also calculated the optical AGN fraction applying the same absolute magnitude limit for our BPT AGNs and found that the AGN fraction is the same as our previous estimation (5%) thus not dissimilar to the one calculated by Arnold et al. (2009).

The result we find here, that the AGN fraction is higher in galaxy groups than in clusters of galaxies, is similar to what many previous authors have found by studying the AGN population in groups at low and intermediate readshifts (e.g., Allevato et al. 2012; Georgakakis et al. 2008). This result supports the scenario that galaxies in groups contain a greater reservoir of cold gas to fuel AGN activity and can also trigger nuclear activity more easily than galaxies in rich clusters, as they are more probable to experience an interaction (Oh et al., 2014).

In addition to the optical emission line ratios for the identification of AGN, another way to identify an AGN is from the X-rays. X-ray AGN are identified mainly from their X-ray luminosity. In Arnold et al. (2009) the limit in order to characterize a galaxy as X-ray AGN was set to L_X=10^{41} erg s^{-1} and the corresponding fraction of X-ray AGN in groups was found to be $\sim$9%. Comparing our fraction of line emission AGN with the X-ray AGN fraction by Arnold et al. (2009), we find that the incidence of X-ray AGN is almost a factor of 2 higher in groups than optical AGN.

Arnold et al. (2009) notes that different results from different samples are most probably

due to different selection techniques, implying that there is no specific type of AGN in an environment, but both can be found in any, with BPT AGN and X-ray AGN being populations that are not necessarily connected. In the study of Hickox et al. (2009) the supported idea is also that AGN selection using different techniques represents separate populations that have differences in host galaxies, environments, and accretion modes. In the subset of groups and galaxies that have SDSS spectroscopy of Arnold et al. (2009), between the 14 BPT AGN and 6 X-ray AGN, only one is characterised as both BPT and X-ray AGN. This clearly shows how diffferent techniques of selecting AGN may identify different populations of AGN.

As X-ray emission in systems suggests that they are virialized, the presence of BPT AGN and X-ray AGN may depend on the different dominant accretion mode between unvirialized and virialized systems (Arnold et al., 2009). As BPT AGNs have line ratios that are found in AGN whose spectral energy distributions relate to thin disk models where the accretion rate is greater than 1% of the Eddington rate, in contrast, no emission lines (or weak), in combination with significant X-ray luminosities, suggest radiatively inefficient accretion with sub-Eddington accretion rates (Vasudevan & Fabian, 2007). A physical explanation then is that BPT and X-ray AGN come from different accretion modes. This is also supported by the fact that the host galaxies of these two AGN types are different in the sense that the X-ray AGN are more likely to be hosted by the more massive early-type galaxies that exhibit larger SMBHs. There is though an evolutionary connection between the two types of AGN. AGNs are optically dominant in the beginning and as time passes they progressively evolve into X-ray dominant AGNs. The properties that AGNs exhibit is therefore a natural consequence of accretion evolution: X-ray AGN preferentially exhibit in evolved systems where merging processes have occured a long time ago and fast accretion

onto the supermassive black hole has now stopped. On the other hand, optical AGNs are found in younger systems where the merger events have more recently occured and are at the start of their evolution. Within the context of this scenario, acknowledging that the understanding of the properties of X-ray and optical AGNs (i.e., luminosity functions, clustering properties) and many other factors (e.g., merger rate, AGN lifetimes) is yet required to be established, optically and X-ray selected AGN are in a different evolutionary epoch (Shen et al., 2007; von der Linden et al., 2007). Hickox et al. (2009) also notes that differences in the host galaxies between AGNs of different types suggest that accretion is related to the mass and age of the host galaxy with AGN accretion shifting from radiatively efficient (optical and IR-bright) to radiatively inefficient (optically faint, X-ray-bright) modes, above a dark matter halo mass of $\sim 10^{12} - 10^{13}$.

Lastly, for the galaxies of our sample that were optically classified, we illustrate the radial distribution of the AGN and star-forming galaxies with their distance *r* from the central galaxy, scaled by the 'virial radius' r_{500} estimates given in §4.1.2. In Fig. 5.3, we have selected 7 bins in order to track clearly the behaviour of star-forming and AGN galaxies within r_{500}. We see that the number of galaxies that are detected with SDSS decreases with the increase of radius (r/r_{500}) from the centre of the group. The fraction of the star-forming galaxies increases with the increase of radius within r_{500}, as is observed by other SDSS studies (e.g., Wetzel et al. 2012). This means that star-formation is the prevailing process observed in our groups with the fraction of AGN decreasing towards the edge of our groups until $\sim 1 r/r_{500}$ and then remaining constant. We observe that at a distance of $\sim 1 r/r_{500}$ the fraction of star-forming galaxies also has a small decrease which can be attributed to the presence of a significant number of composite galaxies at this distance. In particular, we find that the fraction of star-forming galaxies decreases by a factor of 2 closer to the centre

than $0.5r/r_{500}$ with a corresponding factor of 2 rise in AGN in the same bin. Further away (at distances $>1.5r/r_{500}$) we see that the fraction of both AGN and star-forming galaxies remains constant (flat distribution).

The small increase that the AGN fraction presents towards the group centre is not like the increase that is observed in clusters of galaxies (Best et al., 2005; Miller, 2009). The reason for this small increase compared to clusters is that many of our groups do not possess a dominant cD galaxy -that hosts strong AGN- as is the case in clusters.

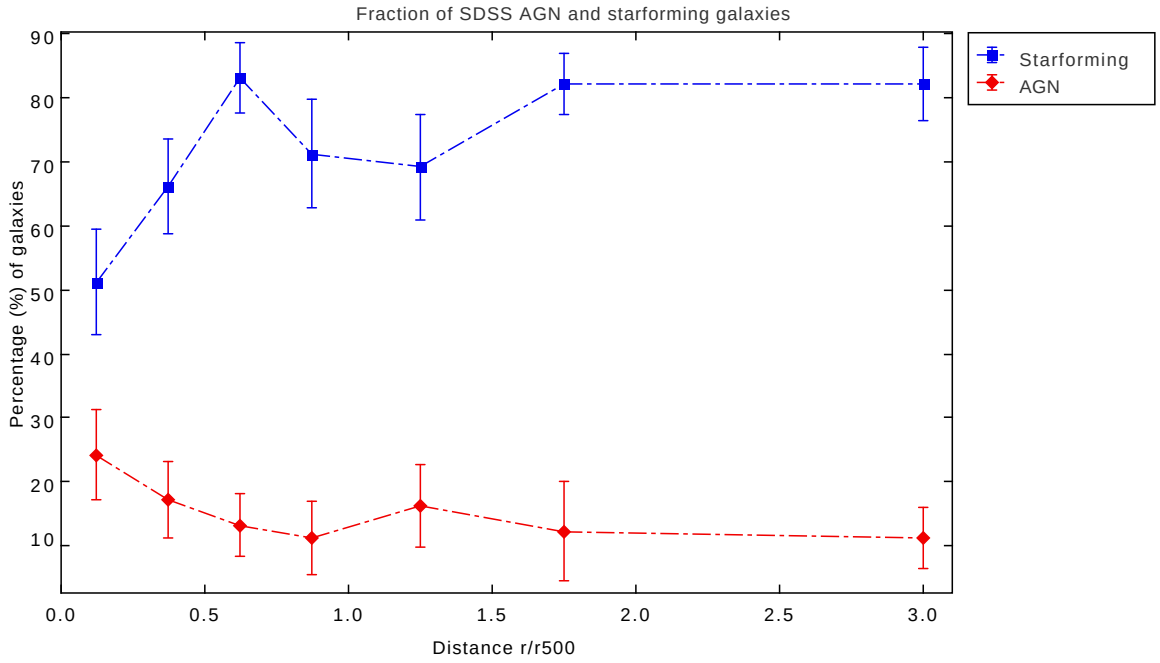

Figure 5.3 Radial distribution of the fraction (%) of AGN and star-forming galaxies with r/r_{500} for galaxies in our sample that have SDSS data. The galaxies are binned at $0-0.25$, $0.25-0.5$, $0.5-0.75$, $0.75-1$, $1-1.5$, $1.5-2$, $2-4$ r/r_{500} with the total number of galaxies at each bin being 37, 41, 47, 28, 32, 17 and 45 respectively.

In several earlier studies on the dependence of galaxy populations with distance from the cluster centre using emission-line strength, the consensus is that the fraction of star-forming galaxies decreases towards the cluster centre (e.g., Balogh et al. 2004; Christlein & Zabludoff 2005) with the star-formation quenching traced out to $2\text{-}4r_{200}$. If we scale things down to the group virial radius, this is equivalent to what we observe in our group sample.

The process that is most probably responsible for this radial trend is 'strangulation' (e.g., Weinmann et al. 2006). By strangulation is meant the loss of the diffuse gas reservoir that is surrounding the galaxy which takes place already from the cluster outskirts, stripping the gas of the galaxy within a few Gyr (Bekki et al., 2002). As there is no diffuse gas left to restore the cold gas from the disk, inevitably star-formation will cease. The termination of star-formation might even happen in a shorter timescale than a few Gyr if the cold gas from the disk is also stripped due to a dense intra-cluster environment (ram-pressure stripping; Gunn & Gott 1972; Quilis, Moore & Bower 2000).

Besides strangulation, which is the most probable process to occur in an infalling (spiral) galaxy in the group environment, the low velocity dispersion that galaxies have in groups, promotes tidal interactions that even if do not lead to mergers, they can still affect the galaxy properties by heating the stellar disk. This process is called harassment (Moore, Lake & Katz, 1998). While strangulation will cause a gradual decline in star-formation, tidal interactions will trigger bursts of star formation owing to the gas that is transported to the group centre (von der Linden et al., 2010). This is possibly the reason why we still see, although decreased, a greater fraction of star-formation towards the group centre compared to AGN.

5.2 Multi-wavelength catalogue matching

As mentioned earlier, the CLoGS catalogue that was observed and analysed in radio for the purposes of this thesis, is combined with various catalogues across the electromagnetic spectrum in order to examine the properties of star formation and AGN in the nearby Universe. The only caveat while matching catalogues is that it is not always a procedure that leads to a perfect one to one correlation but often might be a confusion by correlating an object in one catalogue with several objects in another catalogue (multiple matching). This

is most probably due to the very different resolution that the two matching catalogues may have, either because the corresponding objects are in reality not the same, or if they belong to the same system there are more than one sources that could correspond to the true one (double-counting). As the catalogues that we match and the CLoGS catalogue have different resolutions, this might be the case with some of our matchings. However, as our sample galaxies are in the local Universe, we possess accurate optical positions and when multiple objects were matched within the search radius, our procedure was to select the one that is positioned nearest, excluding the rest of the matches. Choice of the closest position source can avoid all the forementioned problems.

It is possible to predict the number of chance (false matches) coincidences from the position-based matching probability between each catalogue. For NVSS/FIRST catalogue McMahon et al. (2002) by matching nearly 383.000 radio sources with their optical catalogue (APM), estimates that using a $2''$ matching radius, 95% of the sources are physically connected with their optical catalogue (5% chance matches). In White et al. (1997) using the IRAS Faint Source Catalog it was found that within 2 σ error ellipse, for IRAS sources within the FIRST survey area, only 3.6% of them is attributed to chance matches. For the near-infrared 2MASS XSC catalogue Díaz-Giménez et al. (2012) found 26 misidentifications of galaxies over a total of 1158, giving a 97.8% catalogue reliability. Wang et al. (2014) calculated the chance matches significance between a randomized IRAS FSC and a WISE catalogue, by using the Sutherland & Saunders (1992) formula that estimates the overall probability as a normalisation of the likelihood ratio that each individual candidate is a match. It was found that the false identification rate was 4% . Finally, Ogle et al. (2015) using the new cross-matching algorithm called Match Expert (MatchEx), cross-matched the GALEX All Sky Survey Catalog (GASC) (containing nearly 40 million NUV-detected

sources), against a directory of 180 million objects in NED. Candidate matches were identified for each GASC source within a $7.5''$ radius and by position-based matching probability, a false chance estimation of 2.4% was found.

As the number of matched galaxies in our analysis was in most cases low and the fact that we possess accurate optical positions due to proximity of our galaxies the number of chance matches calculated by all previous studies can be considered as an upper limit as manual inspection was performed for all galaxies with the cases of double matching being rare. We separately discuss the probability of chance matches for each of the catalogue matching we perfomed below.

In Table 5.2 at the end of this section, we summarise the total number of matches between NVSS, FIR, WISE, 2MASS, GALEX and our catalogue, showing the way they break down by morphology, while in Table 5.3 we present the fraction of these galaxies that were detected in radio from our 610 and 235 MHz analysis. In more detail, the first line of Table 5.3 shows the total number of galaxies that are detected in radio (117) and each column represents the number of radio detected galaxies (out of 117 for each catalogue) that are matched with NVSS, FIR, WISE, 2MASS and GALEX respectively. Then the first column of line 2 shows the number of galaxies that were detected in radio and were of early type morphology in relation to the total number of galaxies (117). As in the first line now each column represents the number of early type radio detected galaxies (out of 42 for each catalogue) that are matched with NVSS, FIR, WISE, 2MASS and GALEX respectively. The same logic is followed for the third and fourth line of Table 5.3 which shows the number of late type radio detected galaxies (out of 62 for each catalogue) and unknown type radio detected galaxies of the sample (out of 13) that are matched with NVSS, FIR, WISE, 2MASS and GALEX respectively. The percentages represent in each category the number of radio

detected galaxies to the total matched number of galaxies in each catalogue (shown in line 1).

5.2.1 Radio observations from the literature

We started by producing a combined radio catalogue that contained objects from four radio catalogues with corresponding optical information from SDSS. The four radio surveys used to create this catalogue are FIRST (Faint Images of the Radio Sky at Twenty Centimeters), NVSS (NRAO-VLA Sky Survey, 20cm), GB6 (Green Bank Telescope, 6cm) and WENSS (Westerbork Northern Sky Survey, 92cm). All the objects from each survey were matched initially to the NVSS positions with the complete catalogue having around 3 million entries in the sky area north of -40° declination covered by the NVSS. We briefly describe each survey used for the creation of this multi-wavelength radio catalogue with more details to be found in Kimball & Ivezić (2008).

The FIRST (Becker et al., 1995) and NVSS (Condon et al., 1998) surveys were both performed at the Very Large Array (VLA) at 20cm (1.4 GHz). Their spatial resolution was quite different. With FIRST having a $\sim 5''$ beam and NVSS a $\sim 45''$ beam, small-scale structures with accurate positions could be better resolved by FIRST than NVSS. We find that NVSS is more accurate in calculating fluxes for extended sources compared to FIRST, since the latter underestimates the flux for some extended sources by resolving out some of the large-scale structure, and also sometimes breaking up extended sources into smaller sub-images. With a detection limit of 2.5 mJy, the NVSS survey contains more than 1.8 million sources while FIRST, with a detection limit of 1 mJy, over 800.000 sources.

The Green Bank survey (Gregory et al., 1996) at 6cm (4.85 GHz) with a resolution of $\sim 3.5'$ covers the $0° < \delta < 75°$ sky region. It is complete up to 25 mJy and contains

approximately 75,000 sources.

The WENSS survey (Rengelink et al., 1997) is observed at 92cm (325 MHz) and covers the sky north of 29° declination to a limiting flux of 18 mJy. Its beam size is 54 × 54 cosec(δ) and contains almost 220,000 sources.

We then matched the positions of the radio sources from the combined multi-radio catalogue with our CLoGS catalogue, using a matching radius of 20″. The total number of matches within this radius is 67 with NVSS and FIRST, 41 with WENSS and only 11 with GB6. Of the 67 galaxies detected in NVSS the majority is being of unknown morphology (Table 5.3). The number of chance matches for this catalogue was 1 (double matching) which yields a $<$1% chance probability match.

5.2.2 Mid and Far Infrared: IRAS

The Infrared Astronomical Satellite (IRAS) scanned 96% of the sky in four bands, at 12, 25, 60 and 100 μm. The objects extracted from this survey were released in the IRAS Point Source Catalog (PSC) which contains around 250.000 sources. The properties of the PSC, along with other aspects of the IRAS mission, are explained in detail in the Explanatory Supplement to the IRAS Catalogs and Atlases (Beichman et al., 1988). The spatial resolution of the IRAS survey ranges from a few to $\sim$5′.

The CLoGS catalogue was matched with the IRAS Point Source Catalog. If the source centres were within the matching distance used then we had a positional match between the optical galaxy and the corresponding infrared source. The distance used in this case was 30″ with a total number of 90 objects matched. Of those only 32 were detected in radio from our GMRT data analysis. The number of misidentifications (double matching) for this catalogue was found to be 2, whichs means that the catalogue is $\sim$98% reliable.

We then consider, for the matched objects, the IRAS 60 μm luminosity as a star formation tracer. We use the formula provided by Helou et al. (1988) in order to calculate the total FIR luminosity of galaxies as

$$L_{FIR} = 1.26 \times 10^{-14}(2.58 f_{60} + f_{100})(\text{Watts/m}^2), \tag{5.3}$$

where f_{60} and f_{100} are flux densities in the 60 and 100 μm IRAS bands in units of Jy.

5.2.3 Near-infrared: 2MASS

The Two Micron All Sky Survey (2MASS) project scanned the whole sky in the J (1.24 μm), H (1.66 μm) and Ks (2.16 μm) near-infrared bands with an angular resolution of $4''$. In this survey the signal-to-noise ratio (SNR) for the sources that had brightness greater than 1 mJy in each band, was higher than 10 (The Two Micron All Sky Survey (2MASS); Skrutskie et al. 2006). The 2MASS All-Sky Data Release includes data from images and catalogues corresponding to almost the entire sky (99.998%), combining all northern and southern survey observations. The All-Sky Release products contain a Point Source Catalog (PSC), with positions and photometry for half a billion objects (Cutri et al., 2003).

We combined the CLoGS catalogue with the 2MASS PSC using a matching radius of $30''$. As the light from the red optical wavebands, and in the near-infrared J, H, and K bands from 2MASS is overwhelmed by older stars, its origin is intimately connected with the total mass of the galaxy. The 2MASS Ks band is therefore used as an estimator for stellar mass. The total number of member galaxies that had Ks band information in the 240 GMRT field of view was 575. The number of misidentifications for this catalogue was 7, whichs means that the catalogue has a $\sim$1% chance match probability.

Following Bell et al. (2003), we calculated the mass to light ratio for the galaxies selected as radio-loud (see §5.4.1) using

$$log\left(\frac{M}{L_K}\right) = \alpha_K + (\beta_K \times (g-r)) \tag{5.4}$$

where M/L_K is the mass to light ratio in solar units, α_K and β_K are known coefficients presented in Bell et al. (2003) and g, r are SDSS magnitudes in their standard filters. We find that the mass to light ratio ranges between 0.62 to 0.67 which corresponds to a stellar mass of 10^{10}-10^{12} $M_\odot$ for those galaxies.

Of the 575 galaxies that were matched with 2MASS catalogue the ones that were radio detected from our analysis at 235 and 610 MHz are 85.

5.2.4 Mid-Infrared: WISE

The most recently generated catalogue at these wavelengths is the WISE all-sky survey catalogue from the Wide-field Infrared Survey Explorer (WISE; Wright et al. 2010), the successor of the IRAS survey. WISE has mapped the whole sky in four bands in the mid and far infrared at 3.4, 4.6, 12 and 22 μm (also known as W1, W2, W3 and W4) with a 3σ sensitivity of approximately 0.05, 0.07, 0.6 and 3.6 mJy respectively. The sensitivity of WISE is many times deeper than any other infrared survey, in fact a hundred times more sensitive than IRAS at 12 μm. It has an angular resolution of 6.1, 6.4, 6.5 and 12$''$ from 3 to 22 μm, containing information for over 563 million objects. For more details we refer to the WISE Preliminary Release Explanatory Supplement (Cutri et al., 2011).

Using our CLoGS catalogue once again, we identify the WISE objects associated with the CLoGS member galaxies in a matching tolerance of 20$''$. To avoid contamination from

nearby sources within the matching radius, in cases where there were potential multiple matches, we select the closest WISE match to the CLoGS member galaxy. We note that all of of our CLoGS galaxies were matched with a counterpart in the WISE catalogue (690), yielding a value for W3 and W4 magnitudes. The number of misidentifications (double matching) for this catalogue was found to be 21, whichs means that the catalogue used for our purposes is $\sim$97% reliable.

We concentrate on galaxies that exhibit WISE 12 and 22 μm detection in the spectroscopic sample. The reason for this is that at wavelengths longer than $\sim$8 μm, the dominant emission that traces star formation (SF) is warmed up dust by younger stars. Lee et al. (2013) found a strong correlation between the SFR from H_α and the WISE 12 and 22 μm monochromatic luminosities, suggesting that L_{W3} and L_{W4} can be very good SFR indicators. Following Lee et al. (2013), we estimate the SFR from L_{W3} and L_{W4} using

$$SFR_{W3}(M_\odot yr^{-1}) = (9.54 \pm 0.44) \times 10^{-10} L_{W3}^{1.03\pm0.01}(L_\odot); \tag{5.5}$$

$$SFR_{W4}(M_\odot yr^{-1}) = (4.25 \pm 0.20) \times 10^{-9} L_{W4}^{0.96\pm0.01}(L_\odot). \tag{5.6}$$

The advantage of WISE all-sky data for extragalactic sources lies in the diagnostic ability that mid-infrared colours have. Mid-infrared colours have the ability to identify the most heavily obscured, luminous AGN since the obscuring material is thermally heated by the AGN (Stern et al., 2012). This is supported by the fact that stellar systems, star-forming galaxies and QSO/AGN have distinctly different near-infrared SEDs yielding very different observed mid-infrared colours for different types of objects. Stern et al. (2005) showed that WISE colours alone can separate such source populations. This can be done by a simple

W1 - W2 colour cut that differentiates robustly AGN from stars and galaxies. Pure AGN have red W1 − W2 mid-infrared colours up to the redshift of 3. On the other hand, normal galaxies and Galactic sources are not probable to present such red W1 − W2 colours. Mid-infrared selection of AGN therefore relies on distinguishing the approximately power-law AGN spectrum from the black body stellar spectrum of galaxies which peaks at rest-frame 1.6μm. Several other studies have also noted the efficiency with which WISE identifies AGN (e.g., D'Abrusco et al. 2012; Edelson & Malkan 2012). In addition Stern et al. (2012) and Assef & Stern (2012) present detailed studies of WISE-selected AGN within the COSMOS and Bootes field, respectively, having also careful analyses of completeness and reliability of WISE AGN selection using W1 − W2 colour selection. The galaxy templates of Assef et al. (2010) are blue in this WISE color combination, with W1 − W2 $\leq$0.8 out to z$\sim$1.2. However, dilution by the host galaxy limits mid-infrared surveys from identifying low luminosity AGN (Stern et al., 2012).

In order to avoid AGN contibution in the WISE matched sample we employ the technique used by Stern et al. (2005) applying a colour cut of W1 - W2$\geq$0.8. Then these sources were cross matched with the optically selected star forming galaxies from the BPT diagram and any additional sources that were marked as AGN with the BPT technique were excluded.

5.2.5 Ultraviolet: GALEX

The Galaxy evolution explorer (GALEX; Martin et al. 2005) is a sky survey focusing on the UV continuum, the most frequently used star formation indicator (usually at λ >2000Å). It has a field of view of 1.25° functioning in either imaging or grism spectroscopic mode, generating at the same time a far-UV (FUV) and a near-UV (NUV) image. The two filters are broadband and have effective wavelengths of 1520Å in the far ultraviolet (FUV) and

Table 5.2 Detection statistics from our multiwavelength matches. In the first line we mention the total number of galaxies that matched with our catalogue. In the second and third line we note the number of the matched galaxies at each frequency that were early and late types respectively.

Total number of galaxies	Matched with NVSS	Matched with FIR	Matched with WISE	Matched with 2MASS	Matched with GALEX
690	67	90	690	575	531
Total number of early types	Matched with NVSS	Matched with FIR	Matched with WISE	Matched with 2MASS	Matched with GALEX
225	5	13	225	190	162
Total number of late types	Matched with NVSS	Matched with FIR	Matched with WISE	Matched with 2MASS	Matched with GALEX
220	16	69	220	183	181

2310Å in the near ultraviolet (NUV). The resolution of GALEX is $\sim$4.5$''$ in the FUV and $\sim$6.5$''$ in the NUV. More details on the technical side of GALEX telescope and data products can be found in Morrissey et al. (2005).

The data that we use are from GALEX's primary all sky survey (AIS) data release 5 (DR5; Bianchi et al. 2011) containing FUV and NUV magnitudes and fluxes. We search for a match between the CLoGS catalogue and the GALEX source catalogue DR5 (which already combines FUV and NUV detections) within a search radius of 20$''$. The member galaxies with a match in GALEX that also contain line information from the optical SDSS are found to be 531 with 97 being detected from the GMRT including the 240 MHz GMRT field of view detections. Of these 531 matches, 9 misidentifications (double matching) were found, whichs means that the catalogue is 98.3% reliable or a chance match probability of 1.7%.

Following Salim et al. (2007), we calculate the star formation rate from the FUV emission from:

$$SFR(M_{\odot}yr^{-1}) = 1.08 \times 10^{-28} L_{FUV}(erg^{-1}s^{-1}Hz^{-1}) \tag{5.7}$$

where L_{FUV} is the luminosity of FUV.

Table 5.3 Fractional detection statistics of radio detections from multiwavelength matches. The number (and fraction) of the matched galaxies at each catalogue that are detected in radio with GMRT at any frequency is shown based on their morphology. Line 1 shows the total number of galaxies that are detected in radio (117) and each column represents the number of radio detected galaxies (out of 117 for each catalogue) that are matched with NVSS, FIR, WISE, 2MASS and GALEX. The first column of line 2 shows the number of galaxies that are detected in radio and are of early type morphology in relation to the total number of galaxies (117). As in line 1, now each column represents the number of early type radio detected galaxies (out of 42 for each catalogue) that are matched with NVSS, FIR, WISE, 2MASS and GALEX. The same logic is followed for lines 3 and 4 which show the number of late type radio detected galaxies (out of 62 for each catalogue) and unknown type radio detected galaxies of the sample (out of 13) that are matched with NVSS, FIR, WISE, 2MASS and GALEX.

Total number of galaxies detected in radio	Matched with NVSS	Matched with FIR	Matched with WISE	Matched with 2MASS	Matched with GALEX
117	13	46	117	113	96
Number of radio detected early types	Matched with NVSS	Matched with FIR	Matched with WISE	Matched with 2MASS	Matched with GALEX
42	4 (31%)	5 (11%)	42 (36%)	42 (37%)	35 (37%)
Number of radio detected late types	Matched with NVSS	Matched with FIR	Matched with WISE	Matched with 2MASS	Matched with GALEX
62	7 (54%)	38 (83%)	62 (53%)	60 (53%)	52 (54%)
Number of radio detected unknown	Matched with NVSS	Matched with FIR	Matched with WISE	Matched with 2MASS	Matched with GALEX
13	2 (15%)	3 (6%)	13 (11%)	11 (10%)	13 (9%)

5.3 Matching Statistics of the radio detected galaxies

In the 26-group high richness sub-sample of CLoGS, which is the subject of this thesis, the total number of the member galaxies in all groups is found to be 373 within the GMRT 610 MHz field of view (FOV; $\sim$1°). Of those, we detect $\sim$23% (85 out of 373) at 610 MHz, $\sim$19% (70 out of 373) at 235 MHz and $\sim$17% (65 out of 373) at both 610 and 235 MHz.

The detection rate for our sample galaxies at any radio emission is observed to be almost the same ($\sim$47%) between spiral galaxies and early type galaxies ($\sim$42%), with the detected ones of unknown morphology being at $\sim$11%. At the 235 MHz GMRT FoV ($\sim$3°) the number of the member galaxies reach to 690 in total. We detect a further 27 galaxies at 235 MHz thus the fractional detection at 235 MHz becomes $\sim$14% (97 out of 690) at the 235 MHz FoV. As can be seen from Fig. 5.11 where the 610 MHz luminosity is plotted against the K band magnitude, there are only 6 galaxies classified as having unknown morphology and are detected at 610 MHz. 5 of them are being significantly fainter compared to the rest of the sample. It is not statistically possible to make a strong statement about a sample that has only 6 members but it is no surprise that these galaxies are faint.

We inspected every image of our radio sources by eye in optical surveys (SDSS/DSS). As far as the morphology is concerned, 20 of the further 27 galaxies that were detected at the 235 MHz FoV, are late type galaxies with only 4 being early types and 3 of unknown morphology. The radio detection rate at 235 MHz FoV seems to be slightly higher for late type (spiral) galaxies ($\sim$53%) than early types ($\sim$36%) with the ones detected of unknown morphology having the same detection rate $\sim$11%. The above statistical results include the central dominant ellipticals of each group.

If we ignore in our statistics the contribution from the central dominant early-type galaxies, whose natural position makes them more probable to host a radio AGN (Best et al.,

Table 5.4 Fractional detection statistics of radio detections in 610 MHz Field of View (FoV). We firstly note the total number of galaxies, the total number of Early types and the total number of Late types and then at Column 2,3,4 and 5 we note the number of galaxies detected in radio at 610 MHz, 235 MHz, 610 and 235 MHz and NVSS/FIRST.

Total number of galaxies	610 MHz	235 MHz	610 and 235 MHz	NVSS/FIRST
373	85 (18%)	70 (19%)	49 (13%)	67 (18%)
Total number of Early types	610 MHz	235 MHz	610 and 235 MHz	
141	37 (26%)	28 (20%)	27 (20%)	
Total number of Late types	610 MHz	235 MHz	610 and 235 MHz	
126	40 (32%)	35 (28%)	31 (25%)	

Best06; von der Linden et al., 2007), we get that ∼18% (63 out of 373) of the galaxies are detected in radio at 610 MHz in the 610 MHz FoV and ∼14% (52 out of 373) at 235 MHz. The detection rate for the radio emission is observed to be significantly higher (∼62%) for spiral galaxies compared to early type galaxies (∼23%), with the detected ones of unknown morphology being ∼15%. At the 235 MHz GMRT FoV the fractional detection at 235 MHz is ∼12% (79 out of 690) with the morphological radio detection rate being much higher for late type galaxies (∼65%) than early types (∼21%) with the detection rate for the unknown morphology being ∼14%.

Table 5.5 Fractional detection statistics of radio detections in 235 MHz Field of View (FoV). The same as previous Table at 610 MHz FoV.

Total number of galaxies	610 MHz	235 MHz	610 and 235 MHz	NVSS/FIRST
690	85 (12%)	97 (14%)	49 (7%)	67 (10%)
Total number of Early types	610 MHz	235 MHz	610 and 235 MHz	
225	37 (16%)	32 (14%)	27 (12%)	
Total number of Late types	610 MHz	235 MHz	610 and 235 MHz	
220	40 (18%)	56 (26%)	31 (14%)	

We then examine and compare the results of the radio detection in X-ray bright and X-

ray faint groups, that is the ones with and without group-scale X-ray-detected IGM (Table 4.6). As the detection or absence of an IGM might indicate changes in gas properties with group mass, we expect interaction with the IGM to affect star-formation and AGN properties in member galaxies via processes such as gas stripping, accretion, etc. In X-ray bright groups, we find that in the 235 MHz FoV, 66/494 (13%) are detected at either radio frequency, with 46 detected at 610 MHz only, while in X-ray faint groups 52/196 (27%) are detected at either frequency, with 39 detected at 610 MHz.

As we see the fraction of radio detected galaxies in X-ray faint groups is twice the one observed in X-ray bright ones. This is the opposite of what we observe with the radio detection of the brightest group ellipticals. While all of the BGEs, including those that host the large scale jets, are radio detected in the X-ray bright groups, almost 1/3 of the BGEs are not detected in radio in X-ray faint groups. This means that our CLoGS X-ray faint groups are either still in the process of dynamical relaxation or could be X-ray faint due to small amount of intragroup gas. In this case, the radio emission from these systems does not come from the central AGN as there is not enough fuel to feed the AGN -as we observe- but is relying on the emission from star-formation of individual galaxies. The number of such galaxies in X-ray faint groups is significant thus a greater fraction of radio detections is seen in these groups.

5.3.1 Radial distribution of radio detected galaxies and their morphological properties

Working from the R_{500}-temperature relation in Sun (2009), we get that the virial radius for most of our groups is between 0.3 and 0.6 Mpc. We note that R_{200} is $\sim$0.5 Mpc for an X-ray temperature of 1 keV. We therefore set a single threshold to divide our sample and

examine the galaxy properties above and below this limit. We assume that 500 kpc is a realistic approximation for the "virial radius" in all of our groups. We will use this value to scale distances from the centre of groups when stacking them. The errors on the fractions were calculated by using a statistical binomial distribution. For a fraction F=n/N then, the error on the fraction is given by:

$$\sigma F = \sqrt{\frac{n(N-n)}{N^3}} \tag{5.8}$$

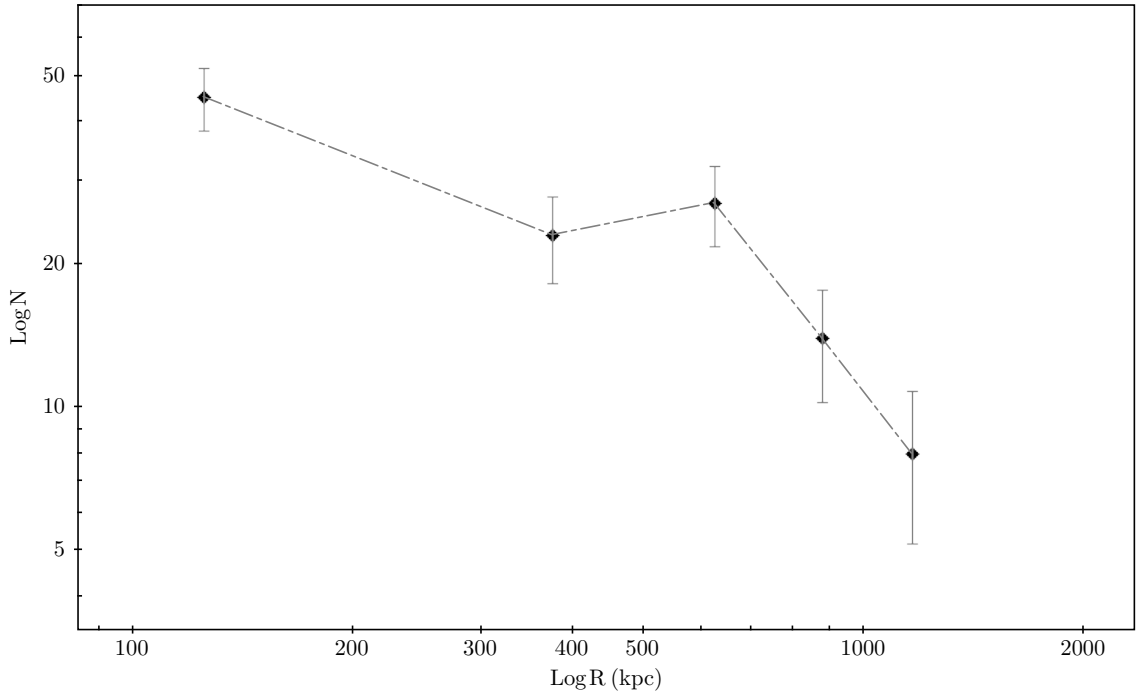

Figure 5.4 Number of the radio detected galaxies as a function of distance from the BGE in kpc.

In Figure 5.4, we see the logarithm of the total number of galaxies detected in radio, plotted as a function of distance from the BGE in kpc. It can be clearly seen that the total number of the radio detected galaxies is dropping with the rise of distance from BGEs.

We now start by examining the fraction of galaxies detected in radio above and below 500 kpc. From this analysis, we exclude the contribution of BGEs. The fraction of galaxies

that were detected in radio at a distance smaller than 500 kpc is $\sim$17$\pm$2%, while the fraction for the radio detected galaxies at a distance greater than 500 kpc is $\sim$11$\pm$2%. We find that a greater fraction of galaxies is detected in radio $<$500 kpc with the radio detected galaxies at a distance $>$500 kpc being $\sim$5% less.

By examining the fraction of late type galaxies (spirals) above and below 500 kpc we find that there is almost the same number of late type galaxies above and below 500 kpc (109 late types $<$500 kpc and 111 $>$500 kpc). The fraction of late type galaxies that are detected in radio $<$500 kpc is 33$\pm$5% (36 out of 109), while the fraction of late type galaxies detected in radio $>$500 kpc is 24$\pm$4% (27 out of 111). The drop of radio detected late type with distance follows the trend as the total number of galaxies.

Comparing though the total number of radio detected galaxies based on their morphology, we find an interesting result. At a distance $<$500 kpc the fraction of the radio detected galaxies that are late types is 58$\pm$6%, whereas at distances $>$500 kpc, nearly 80$\pm$7% of the radio detected galaxies are late types. This basically means that the galaxies that are detected in radio at distances greater than 500 kpc are mainly late types and could be indicative of galaxies where the radio emission is dominated by the effects of star-formation (see §5.4).

As a summary, the radial distribution results, applying a sample division of 500 kpc, yield that i) the fraction of galaxies detected in radio regardless of galaxy type is greater for distances $<$500 kpc and ii) at distances $>$500 kpc (large radii from BGE), the most probable type of galaxy to be detected in radio is the late type.

Using the values of R_{500} calculated from the equation 4.2, we then examine the fraction of galaxies that are detected in radio with distance r/r_{500} based on their morphology (Fig. 5.5). In Fig 5.5, we present the fraction of the radio detected galaxies in relation to their

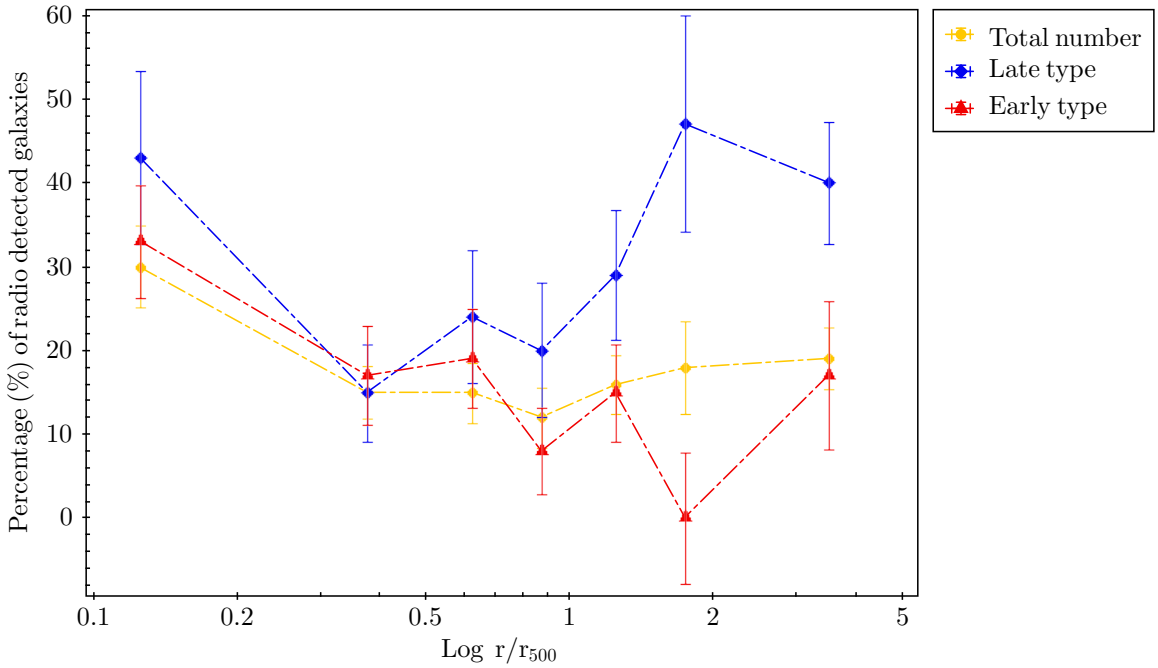

Figure 5.5 Fraction of radio detected galaxies based on morphology with r/r_{500}. In yellow is shown the total fraction of the radio detected galaxies over r/r_{500}, in blue the fraction of late type radio detected galaxies and in red the fraction of late type radio detected galaxies. The galaxies are binned at $0-0.25$, $0.25-0.5$, $0.5-0.75$, $0.75-1$, $1-1.5$, $1.5-2$, $2-5$ r/r_{500} with the total number of galaxies at each bin (in yellow) being 87, 123, 100, 83, 108, 49 and 114 respectively.

morphology and their fractional distance r/r_{500}, including the BGEs. From the total fraction (all morphology type galaxies; in yellow) we observe that the biggest fraction of galaxies are detected in radio very close to the centre of the groups ($\sim$30%) with the fraction of radio detected galaxies dropping as the distance from the centre increases. We find that late type galaxies have a greater fraction of radio detected galaxies close to the centre of the group compared to early type galaxies. The fraction of both late and early type radio detected galaxies drops until $1r/r_{500}$ and, while the fraction of the late type radio detected galaxies rises above $0.5r/r_{500}$, the fraction of the early types falls. Individually we see that the fraction of late type galaxies detected in radio is greater at the outskirts of the groups (distances $>1.5r/r_{500}$) than in the centre, while the opposite stands for the fraction of the early type radio detected galaxies (fraction of radio detected galaxies drops with distance

from the group centre). Overall, we see that the fraction of late type radio detected galaxies is systematically higher than that of the early types.

In Fig. 5.6 we see the radial distribution of the BPT radio detected galaxies regardless in which population they belong. We see that the radial trend of the optically (SDSS) selected galaxies is similar to the total number of radio detected galaxies. The statistics of the BPT selected star-forming and AGN galaxies was too small in order to perform a further investigation of the radial trend between detected in radio AGN and star-forming galaxies (only 1 or 2 galaxies per bin in most cases) that would lead us to unsafe conclusions. Thus it is not included in our analysis here.

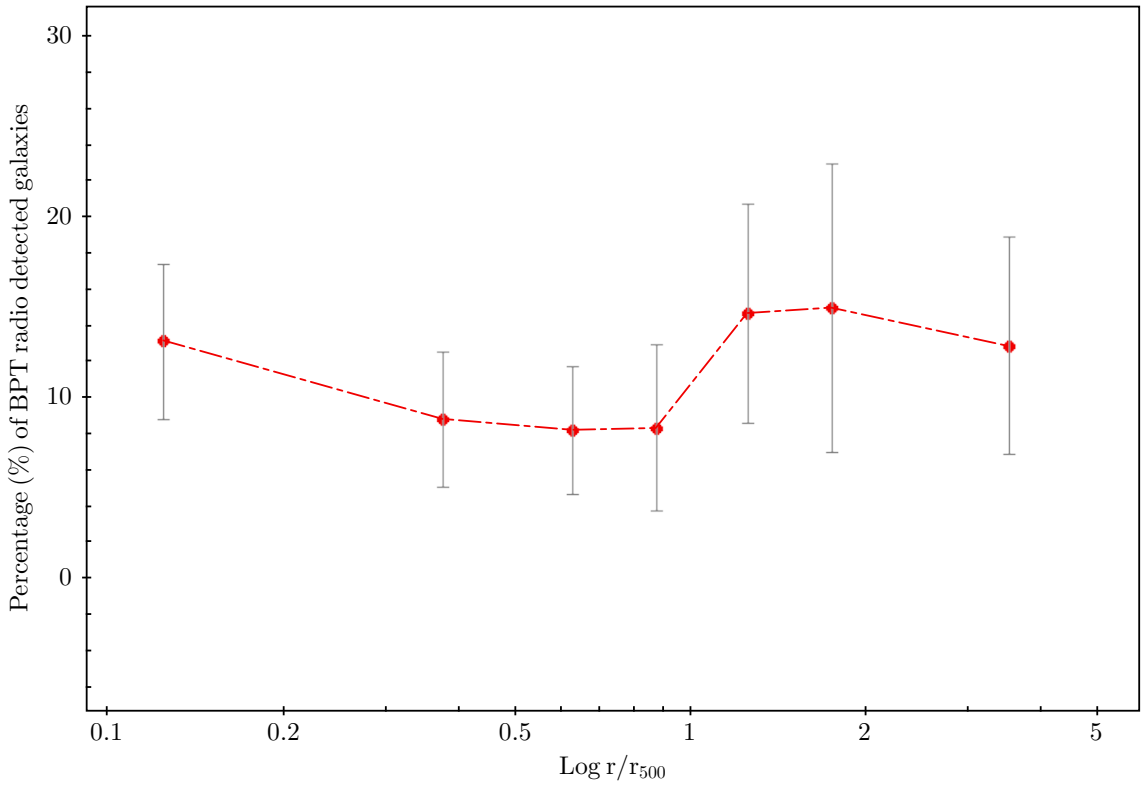

Figure 5.6 Fraction of BPT radio detected galaxies with r/r_{500}. The galaxies are binned at 0−0.25, 0.25−0.5, 0.5−0.75, 0.75−1, 1−1.5, 1.5−2, 2−5 r/r_{500} with the total number of galaxies at each bin being 61, 57, 61, 36, 34, 20 and 31 respectively.

In comparison to the BPT radial distribution results (Fig. 5.3) we see that in the centre

of the groups the radio detections could come either from star-formation (from late type galaxies) or AGN (from early type galaxies). As we move outwards from the group centre, to distances $0.5<r/r_{500}<1.5$ we see that the increase of radio detected late type galaxies correlates with the increase of star-forming galaxies from the BPT plot, while on the other hand the decrase of AGN at the same bin correlates with the decrease of early type radio detected galaxies.

We also examine here the number of the radio detected galaxies per morphology type. We find that the majority of the galaxies detected in radio within 1 r/r_{500} are early type galaxies and at larger radii the galaxies that mostly present radio emission are late types. This is now considered to be natural as Weinmann et al. (2006) using SDSS DR2 data had found that the early-type fraction increases with decreasing halocentric radius, increasing halo mass and increasing luminosity. We note that our results would be different and in agreement with the previous method if the central BGEs were not included as they insert a bias owing to their natural position.

5.3.2 Radio luminosity function of CloGS groups at 610 MHz

The radio luminosity function (RLF) is a tool that shows the path of the evolutionary history of galaxies. From previous studies it is known that the radio luminosity and number density of star-forming galaxies is greater at higher redshifts (Afonso et al., 2005), with the observed evolution of powerful radio AGN being the same. On the other hand, the evolution of low-luminosity radio AGN is less understood with some studies supporting no evolution of the RLF for low-luminosity radio AGN (Clewley et al., 2004) and others that low-luminosity AGN do evolve with redshift, but slower than the higher luminosity galaxies (McAlpine & Jarvis, 2011).

Using the luminosities at 610 MHz we constructed the radio luminosity function of our galaxies that are detected at 610 MHz for the whole redshift range of our sample ($0.005<z<0.02$). The results were corrected using the $1/V_{max}$ approach following the study of Mao et al. (2012). The luminosity bins were chosen as such in order to match the previous study of Mao et al. (2012): $5.66\times10^{1}9 - 1.79\times10^{2}0$, $1.79\times10^{2}0 - 5.66\times10^{2}0$, $5.66\times10^{2}0 - 1.79\times10^{2}1$, $1.79\times10^{2}1 - 5.66\times10^{2}1$ and are equally spaced until $5.66\times10^{2}4$. In Fig. 5.7 we see the results of the total radio luminosity function (RLF). We used the same bins as in the study of Mao et al. (2012) and overplotted the data from this study, where also the radio luminosity functions for both star-forming and radio AGN were calculated up to the redshift of 0.5 for star-forming and 0.8 for AGNs (median redshift $\sim$0.3). We see that the two functions are in good agreement apart from the first couple of bins. If we remove the first two bins of Fig. 5.7 that represent the faintest population of radio galaxies that are observed in our groups, a KS test indicates that the samples are similar.

Compared to our sample, in the sample of Mao et al. (2012) there are galaxies that are much further away (our sample is limited to the galaxy population of our local Universe) that also includes the brightest radio galaxies from clusters that do not exist in groups. For radio luminosities above 10^{25} W Hz^{-1} we note that there are 9 galaxies in the Mao et al. (2012) sample, whereas none of such luminosity exists in our groups. We then observe that in groups of galaxies the brightest radio ellipticals are absent, unlike other studies of clusters (e.g., Best et al. 2005; McNamara & Nulsen 2007) where the brightest radio ellipticals are clearly seen.

In Fig. 5.8 we see the radio luminosity function of 610 MHz between AGN and star-forming galaxies. We find that at the bright end, the slopes of both populations are the same but the AGN function is reaching to higher luminosities than the star-forming galaxies

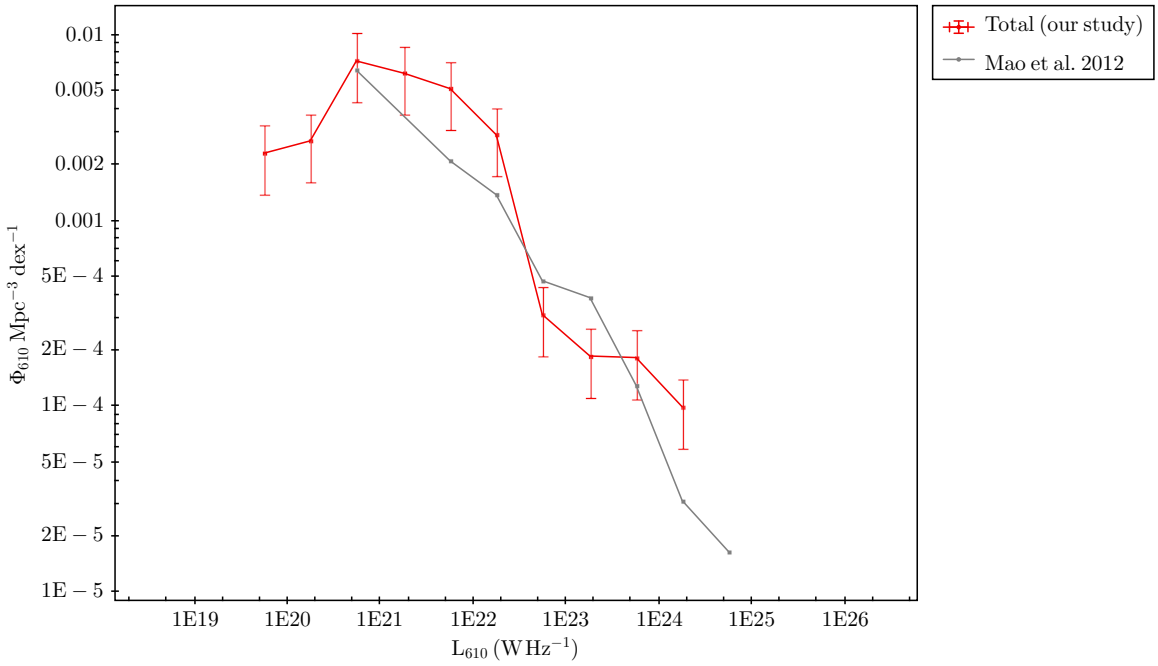

Figure 5.7 Total radio luminosity function (RLF) of 610 MHz using $1/V_{max}$ correction at 10 bins. The number of galaxies at each bin is 1, 8, 23, 17, 19, 9, 1, 1, 2 and 2 respectively. In grey are shown the equivalent values from Mao et al. 2012. We also convert the radio flux at 1.4 GHz (from Mao et al. (2012)) to luminosity at 610 MHz, assuming a spectral index $\alpha = 0.7$ (where flux density $\sim \nu^{-\alpha}$).

one. We see that the last two bins are only occupied by AGNs, and the reason for this is because the brightest radio galaxies will exist in the most massive elliptical galaxies that don't present star-formation (their star-formation will be quenched by the AGN activity) but will only have AGN in them. On the other hand, at the faint end we see that there are fewer AGN and more star-forming galaxies. This is possibly a mass effect due to the presence of star-forming dwarf galaxies in the local Universe that do not have massive AGN in them. The interaction of these dwarf galaxies with massive galaxies, is promoting the star-formation. In the middle we see that we have roughly equal numbers of star-forming and AGN galaxies in groups.

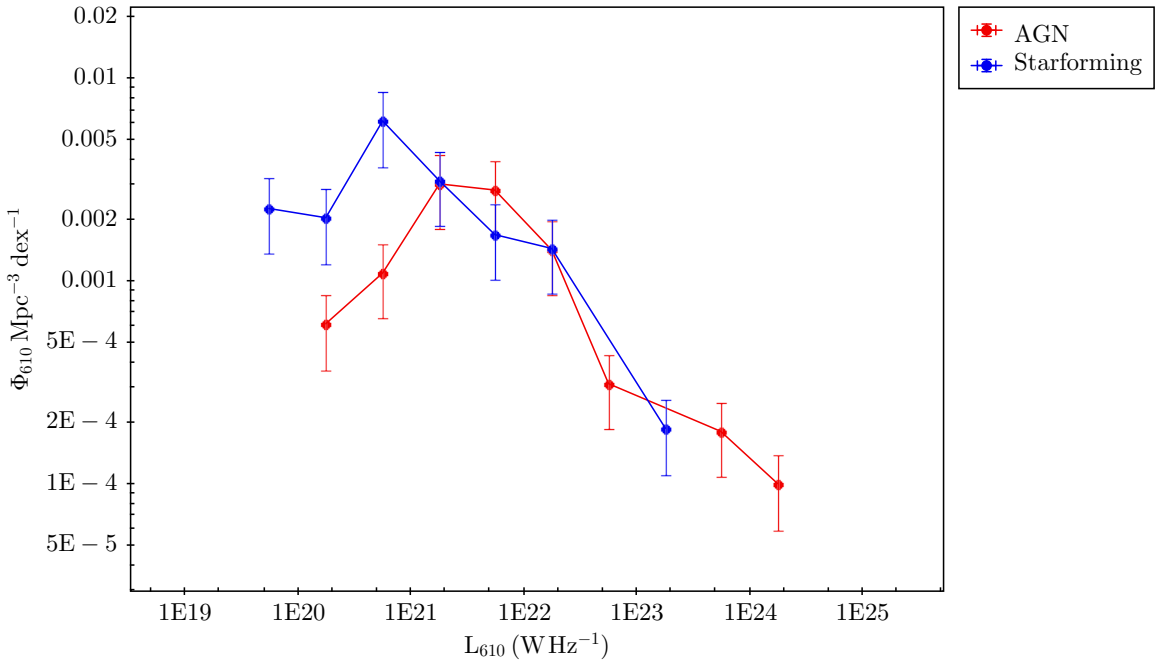

Figure 5.8 Radio luminosity function (RLF) of 610 MHz using $1/V_{max}$ correction at 10 bins for both AGN and star-forming galaxies. The number of galaxies at each bin for the AGN type galaxies is 0, 2, 6, 5, 8, 4, 1, 0, 2 and 1 and for the star-forming type galaxies 1, 6, 17, 12, 11, 5, 0, 1, 0 and 0 respectively.

5.4 Radio-loud AGN in CLoGS groups: comparison with those in clusters

Best et al. (2005) used a sample of galaxies selected from SDSS in order to study the properties of 2215 radio-loud AGN within our local Universe (0.03<z<0.1). In this study as radio-loud AGN were classified, all the radio galaxies that their radio luminosity at 1.4 GHz was above 10^{23} W Hz^{-1} and it was shown that the fraction of galaxies that host radio-loud sources depends highly on the stellar mass, rising with increase in stellar mass.

Where data were available, we calculated for the galaxies in our CLoGS sample the 1.4 GHz radio luminosity using the equation:

$$\log L_{1.4GHz} = 20.08 + 2\log D + \log S_{1.4GHz} \tag{5.9}$$

where $L_{1.4GHz}$ is the radio luminosity at 1.4 GHz in W Hz^{-1}, D the distance of the source in Mpc and $S_{1.4GHz}$ the flux density at 1.4 GHz in Jy.

The total number of galaxies with 1.4 GHz information available in our sample were 86 including the central BGEs. The calculated radio luminosities at 1.4 GHz were in the range of 10^{20} to 10^{24}W Hz^{-1}, which can in general characterise them as low luminosity radio sources. Adopting the same limit for the radio-loud cutoff as in Best et al. (2005), in order to perform a qualitative comparison, we find that the number of galaxies having luminosity greater than 10^{23} W Hz^{-1} are only 3 (see Table 5.6). We note that all of these galaxies were found in central groups ellipticals, in accordance with the result from Best et al. (2007) that BGEs or BCGs of any stellar mass are most probable to be radio–loud AGN hosts than other galaxies.

Table 5.6 This table shows the radio-loud AGN with $L_{1.4GHz} > 10^{23}$ W Hz^{-1}. In Column 1 is the name of the galaxy group is given, while in Columns 2-4 are shown the radio luminosities at 1.4 GHz, the stellar mass calculated by eq. 5.4 and the position of the galaxy in the group. Lastly, in Column 5 the K-band apparent magnitudes are shown.

Group (Name)	$L_{1.4GHz}$ (10^{23} W Hz^{-1})	Stellar mass 10^{12} $M_\odot$	Position	m_K (mag)
LGG80 (NGC 1167)	10.6±0.5	2.7	BGE	11.2
LGG278 (NGC 4261)	23.4±1.2	1.7	BGE	9.9
LGG09 (NGC 193)	11.3±0.6	2.1	BGE	11.5

Lin & Mohr (2007) also used the same threshold of radio-loudness, set by Best et al. (2005), and showed that while in high-mass clusters ∼36% of the BCGs presented $L_{1.4GHz} > 10^{23}$ W Hz^{-1}, this fraction drops to only ∼13% in low-mass clusters. By adopting the same criteria as in Lin & Mohr (2007), we characterise the BGEs as radio active if their radio luminosity at 1.4 GHz is greater than 10^{23} W Hz^{-1}. Then the radio active fraction (RAF) is the ratio between the number of active BGEs and all the BGEs in our CLoGS sample (26). We find that the radio active fraction in our groups sample is ∼12% (3/26)

which is similar to the RAF found for clusters of low mass in Lin & Mohr (2007).

But the available energy emitted in the AGN activity in galaxies at the centre of groups can be a few orders of magnitude lower than the corresponding energy in central galaxies in clusters. Since our GMRT observations go much deeper than NVSS, in order to obtain better statistics for the variation of radio-loud AGN fraction with stellar mass, we vary and re-set the threshold for the characterisation of a galaxy as radio-loud AGN at $L_{1.4GHz} = 10^{22}$ W Hz^{-1}. Using this limit, we find that 15 galaxies out of 86 are radio-loud in our groups sample which corresponds to a fraction of $\sim$17%. With this limit, we find that the number of radio-loud galaxies detected in non-BGEs is similar to those detected in central group ellipticals.

From equation 5.4 we calculated the stellar mass to luminosity ratio for 13/15 radio-loud galaxies that *K*-band absolute magnitude information was available from 2MASS catalogue. We find that the stellar masses range from 10^{10} to 10^{12} $M_\odot$ for these radio-loud galaxies. By setting the value of 5×10^{11} $M_\odot$ as a turning point (due to the low number of radio-loud detected AGN that we have in our sample) we calculate the fraction of radio-loud AGN above and below this mass threshold. We find that 3.5% (3/86) is the radio-loud AGN fraction in our sample for galaxies less massive than 5×10^{11} $M_\odot$ and 11.6% (10/86) for more massive than 5×10^{11} $M_\odot$, about a third of the radio-loud fraction in clusters. Looking at the radio-loud AGN population only, we see that 3/13 (23%) are below 5×10^{11} $M_\odot$ and 10/13 (77%) above.

We note a trend of a rising radio-loud AGN fraction above 5×10^{11} $M_\odot$ and that of the 10/13 radio-loud AGN detected above the mass limit, 7/10 are BGEs, a factor of two more than the non-BGE number.

In Best et al. (2005), it was shown that galaxies with stellar mass 3×10^{10} $M_\odot$ have

a radio-loud AGN fraction of 0.01% that becomes more than 30% for galaxies that are more massive than 5×10^{11} $M_{\odot}$, investigating radio–loud AGN fractions for a higher radio luminosity cut–off of $L_{1.4GHz} = 10^{23}$ W Hz^{-1}.

We note that the absolute fraction values that we have here cannot be compared with the results from Best et al. (2005), due to the different threshold values used for radio loud AGN and the very low number of radio-loud AGN in our group sample adopting the threshold of Best et al. (2005) (only 3 radio loud AGN).

5.5 Star formation indicators

After matching the CLoGS catalogue with the various multi-wavelength surveys that were mentioned earlier in §5.2, we constructed a series of colour magnitude diagrams (CMDs) in order to discover the best star formation indicator amongst the different wavebands that we have explored for our sample, so that we can infer which one is the most reliable to use for the calculation of star formation rates (SFRs). The colour magnitude diagrams are a good place to start.

We examine various magnitudes in relation to K-band magnitude, the latter being an indicator of the stellar mass of a galaxy. In Figure 5.9 we see the colour magnitude diagram between the WISE W3 magnitude minus K-band magnitude (from 2MASS) to K-band magnitude. The same diagram but replacing W3 with W4 magnitude is shown in Figure 5.10. In both Figures 5.9 and 5.10 we see that there is a separation between early type and late type galaxies with the detected ones in radio being shown in green for both types. Late type galaxies appear mostly concentrated to the top left of the graph with the ones detected in radio having higher K-band magnitude (lower stellar mass) compared to early types. On the other hand, the radio detected early type galaxies are on the bottom right of the graph

(smaller W3/W4-K value, thus lower SF) and appear to have lower K-band magnitude (more stellar mass) which probably indicates that their radio emission is triggered by an AGN.

In Figure 5.11 is shown the relationship between the 610 MHz luminosity (L_{610}) and the K magnitude value from 2MASS, with the galaxies detected from NVSS being noted as inverted triangles. We see that the most massive early type galaxies are the most luminous at 610 MHz radio (same as the result in §5.4) with the majority of late type galaxies appearing mostly above K-band value 12. Lastly, the systems detected by NVSS were preferentially the most massive ones.

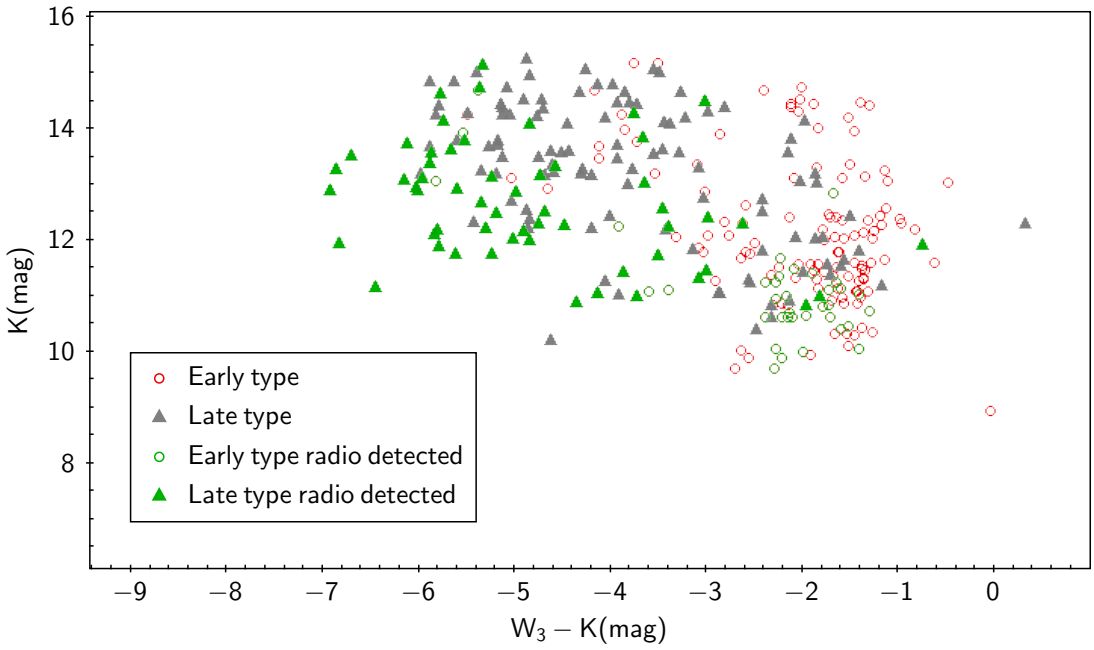

Figure 5.9 The colour magnitude diagram between the WISE W3 magnitude minus K magnitude from 2MASS to K magnitude

5.6 Star formation in galaxy groups

As most previous studies have focused on the investigation of star formation in rich environments (clusters of galaxies), detailed knowledge of the properties of star formation in

galaxy groups will reveal the key mechanisms that govern star formation and drive galaxy evolution in lower mass systems (e.g., McCarthy et al. 2008). This motivated us to look at indicators of star formation in the group enivronment within our sample.

We have calculated, for the CLoGS groups sample, the star formation properties from 5 different wavebands (§5.2 subsections). The first star formation indicator is from the radio (GMRT), where the star formation rate (SFR) is calculated from the radio luminosity at 610 MHz using equations 1.9 and 1.10. The second star formation indicator comes from the FIR (IRAS) 60μm and 100μm using the equation 1.8. The third and fourth ones come from the monochromatic W3 12μm and W4 22μm (WISE) using the equations 5.5 and 5.6 respectively. Lastly SFR is calculated from the FUV (GALEX) using Eq. 5.7, where a dust extinction correction was applied in the FUV magnitude.

While SFR from the radio can be calculated for every galaxy that we have detected in the radio, a distinction between AGN and star-forming galaxies is required in order to exclude

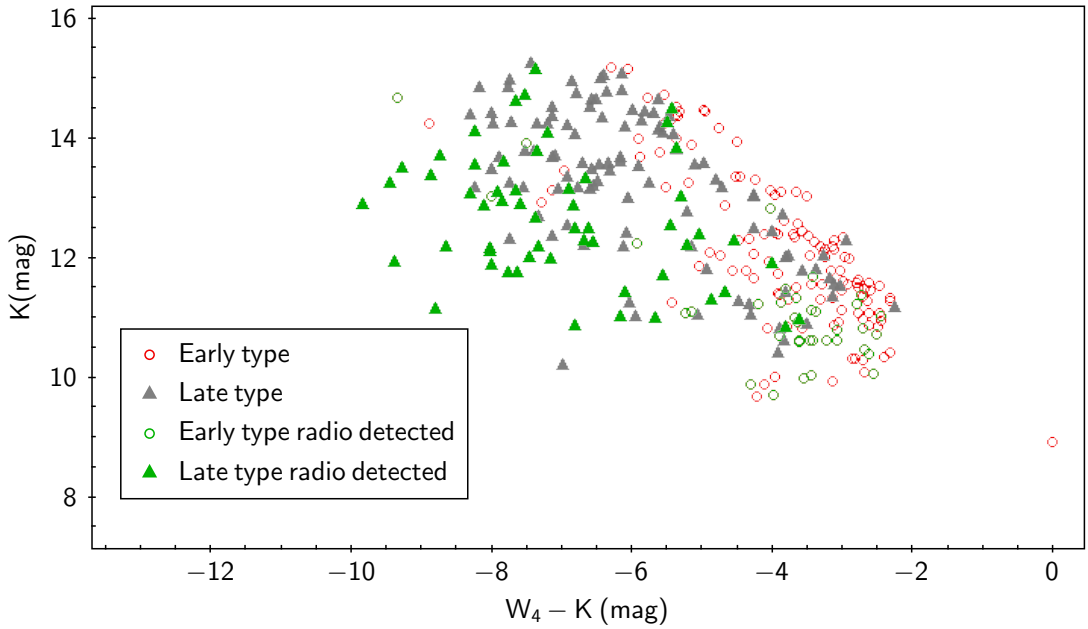

Figure 5.10 The colour magnitude diagram between the WISE W4 magnitude minus K magnitude from 2MASS to K magnitude

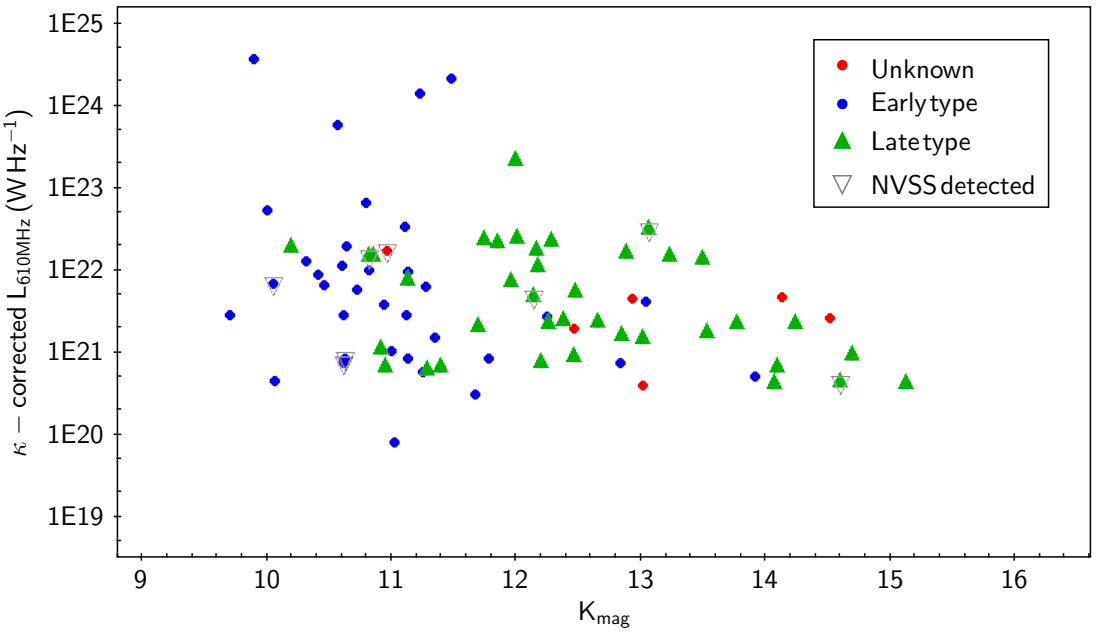

Figure 5.11 The relationship between the 610 MHz luminosity and K magnitude from 2MASS with galaxies detected from NVSS noted.

the AGN contribution from our calculations. For this reason we exclude the BGEs (which are the main AGN candidates) and every early type galaxy that has a radio luminosity at 610 MHz greater than 3×10^{22} W Hz^{-1} (which corresponds to $L_{1.4GHz} \sim 10^{22}$ W Hz^{-1}), as we assume that above this threshold the radio emission cannot be significantly attributed to star formation, as galaxies that present AGN activity are detected across the range of $10^{22} - 10^{28}$ W Hz^{-1} at 1.4 GHz (Jackson, 2004). In the end the galaxies were also cross checked with our BPT results for the star-forming candidates.

5.6.1 Comparison of Star formation rates

In this subsection we show, through a series of plots, the correlation between the star formation rate calculated from the radio 610 MHz and the star formation rates inferred from the rest of the wavebands that SFRs were calculated for.

For a better estimation of the correlation between the SFR_{610MHz} and the different SFR

wavebands we calculated the product moment correlation r. In Table 5.7 we show the coefficient r values of the correlation between the SFR_{610MHz} and SFR_{FUV}, SFR_{W3}, SFR_{W4} and SFR_{FIR} for the total number of galaxies, then for the early type galaxies and finally for the late type ones.

Figure 5.12 shows the relation between the star formation rate at radio 610 MHz and the star formation rate calculated from the GALEX FUV. The SFR from the 610 MHz luminosity was calculated for the galaxies that fullfilled the above criteria.

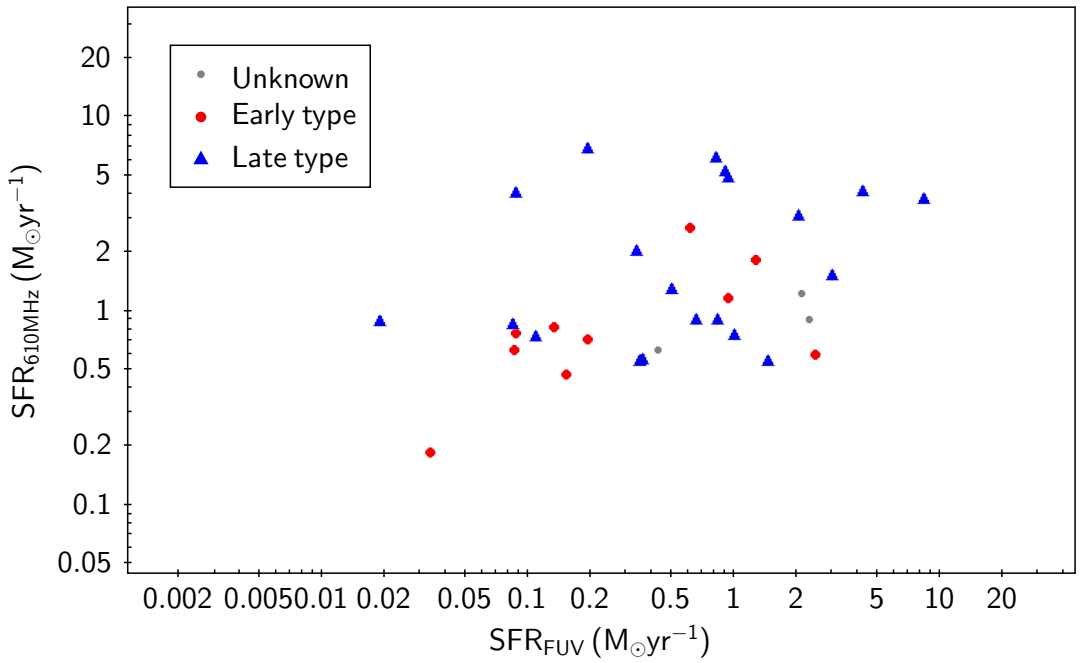

Figure 5.12 The relationship between the star formation rate at radio 610 MHz and the the star formation rate calculated from FUV GALEX.

The correlation between these two SFRs has a low positive correlation coefficient $r = 0.38$ (Table 5.7) indicating that they are only broadly correlated. We also see that r is greater for early type galaxies than late types meaning that there is a better correlation between SFR_{610MHz} and SFR_{FUV} for early type galaxies. In Figure 5.13 we see the correlation between the star formation rate at 610 MHz and the star formation rate from WISE W3 waveband. Although a few outliers are obvious in the plot, there is a good positive corre-

lation between the two indicators with $r = 0.56$, with the same approximately values found for for early and late type galaxies. A good positive correlation is also observed in Figure 5.14 where the SFR from 610 MHz is presented in relation to the SFR from WISE W4 waveband. The SFR from W4 is spanning to much higher values of SFR than W3. The correlation between these two indicators is even stronger with $r = 0.61$ and the correlation between late type galaxies being slightly better ($r = 0.59$) than the one in early types ($r = 0.51$). Lastly in Figure 5.15 a clear correlation is seen with the SFR from 610 MHz and SFR from FIR, apart from some points which seem to be having an excess of SFR in radio (above the main branch of FIR-radio correlated galaxies). Indeed the good positive correlation is supported by the value of $r = 0.64$ with an even stronger correlation between SFR_{610MHz} and SFR_{FIR} for late type galaxies ($r = 0.71$) and a very strong anti-correlation for early types ($r = -0.95$).

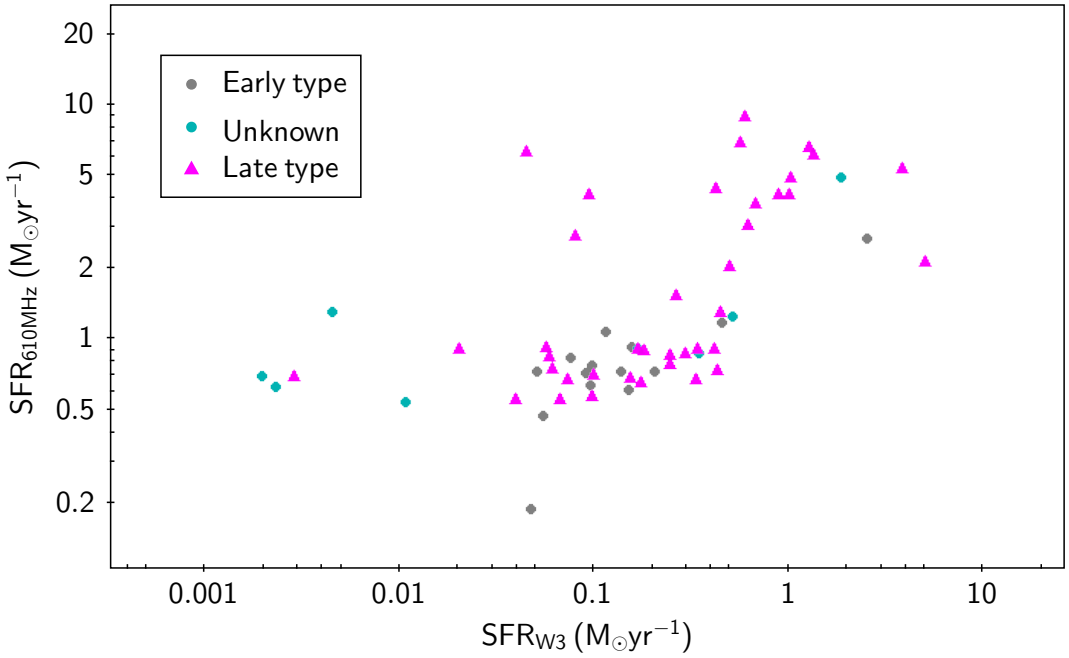

Figure 5.13 The relationship between the star formation rate at 610 MHz and the the star formation rate calculated from the monochromatic W3 WISE.

From Table 5.7 we see that the strongest correlation for the star formation indicator at

Table 5.7 Product moment correlation coefficient (r) for the multiple star formation correlation plots in the log space. In the first line we mention the correlation coefficient between SFR_{610MHz} and the SFRs from the different wavelengths for the total number of galaxies. In the second and third line we note the correlation coefficient between SFR_{610MHz} and the SFRs from the different wavelengths for the early and late type galaxies respectively.

r Coefficient for total	SFR_{FUV}	SFR_{W3}	SFR_{W4}	SFR_{FIR}
SFR_{610MHz}	0.38	0.56	0.61	0.64
r Coefficient for early type	SFR_{FUV}	SFR_{W3}	SFR_{W4}	SFR_{FIR}
SFR_{610MHz}	0.51	0.57	0.51	-0.95
r Coefficient for late type	SFR_{FUV}	SFR_{W3}	SFR_{W4}	SFR_{FIR}
SFR_{610MHz}	0.28	0.56	0.59	0.71

610 MHz is with the FIR waveband and especially for late type galaxies ($r = 0.71$). Despite the fact that the number of galaxies in this plot is the lowest (only 32 galaxies) of any other, the correlation is obviously the strongest. The reason for this (as explained earlier in 1.4.1) is the well known tight radio-FIR correlation (Condon, 1992), owing to the UV radiation of massive young stars that heats the interstellar dust which then re-radiates to FIR, with the radio emission originating from the supernova explosion of the same stars. The strong anti-correlation seen with early type galaxies can be attributed to the low number of early types that correlate with FIR emision in the plot, thus to the low number of late types that present star formation. This is very reasonable, as most of the gas and star-formation is known to be currently held in late type galaxies that have not depleted their gas reservoir yet.

In the study of Lee et al. (2013) it is noted that both monochromatic MIR WISE W3 and W4 luminosities are reliable SFR indicators with W3 tending to underestimate SF at

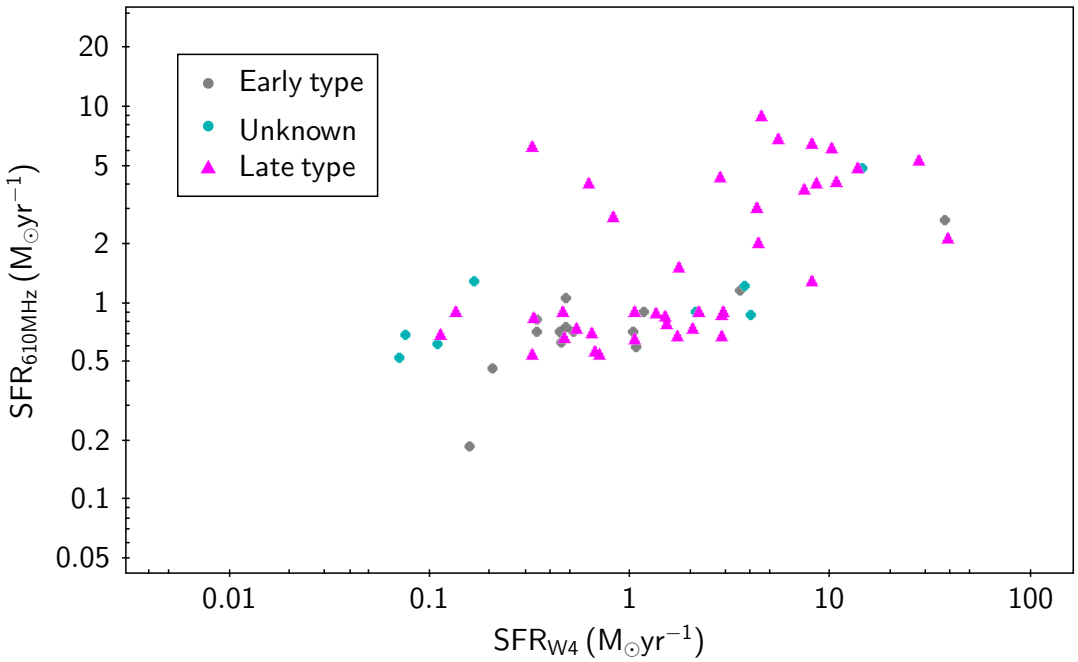

Figure 5.14 The relationship between the star formation rate at 610 MHz and the the star formation rate calculated from the monochromatic W4 WISE.

galaxies with SFR < 1 $M_\odot$ yr^-1. We confirm that both have a good positive correlation with SFR_{610MHz} with the correlation being better between the W4 waveband and individually for late type galaxies. The lowest correlation with SFR_{610MHz} is seen with SFR_{FUV}. The reason for this maybe that FUV detects the amount of obscured star formation. For this reason we present another one SFR indicator that consists of the FUV and FIR, that is $SFR_{FUV+FIR}$ in order to detect both obscured and unobscured star-formation in comparison to SFR_{610MHz}. The total matched number of galaxies that had both FUV and FIR is 16. From Fig. 5.16 we see that the correlation between SFR_{610MHz} and $SFR_{FUV+FIR}$ is lower than any other SFR indicator with $r = 0.23$. Probably the low number of galaxies involved in the statistics does not allow us to draw safe conclusions on the validity of this indicator.

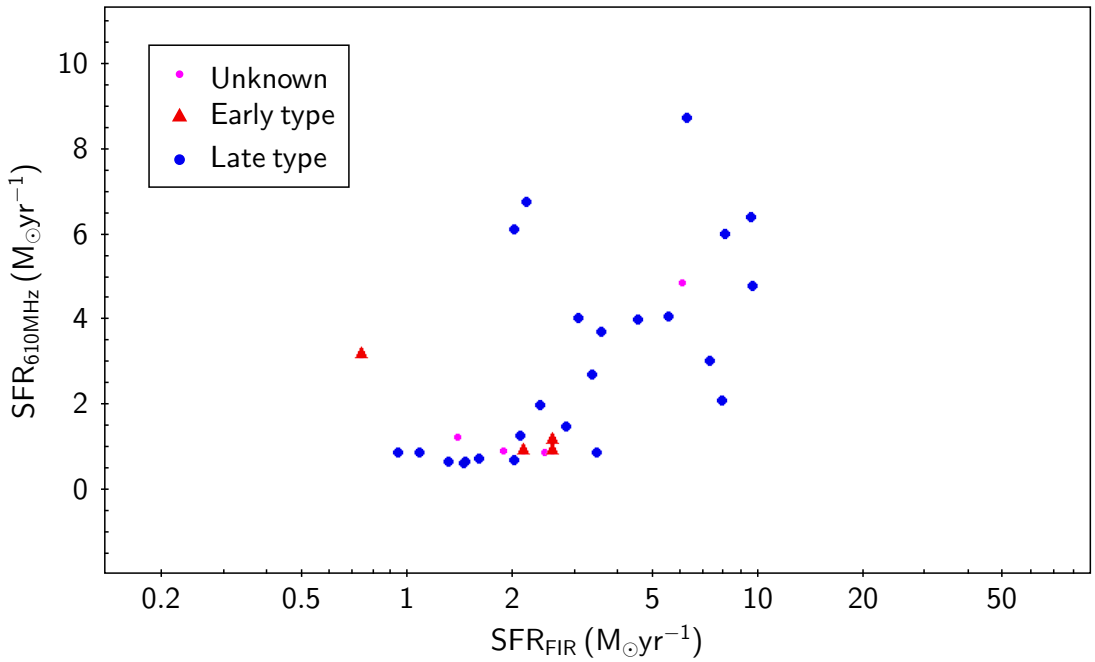

Figure 5.15 The relationship between the star formation rate at 610 MHz and the the star formation rate calculated from FIR.

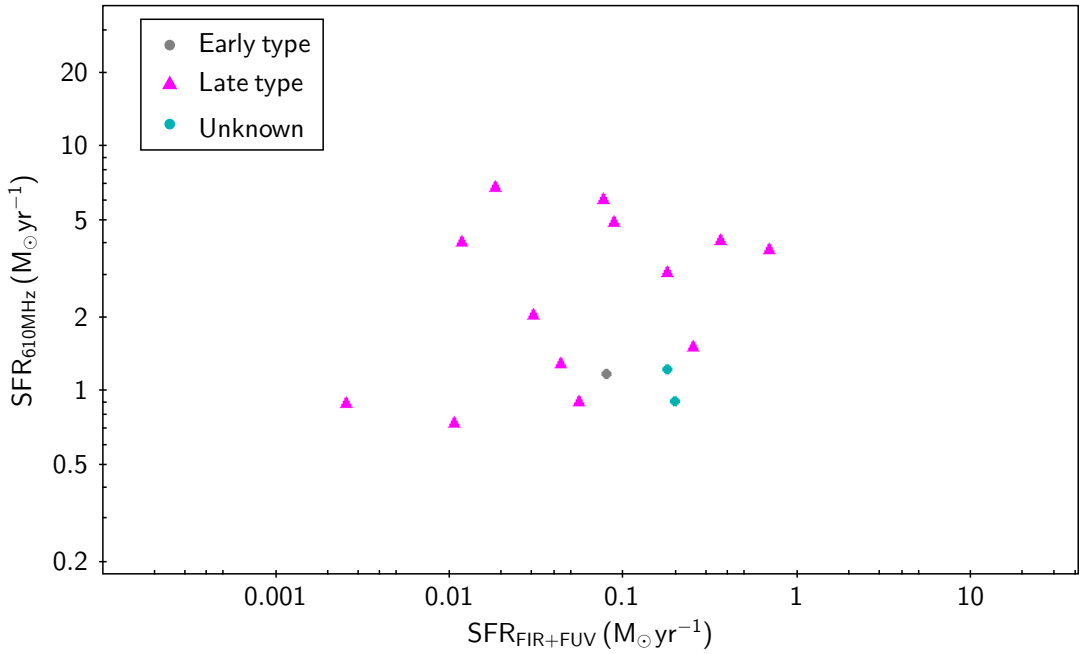

Figure 5.16 The relationship between the star formation rate at 610 MHz and the the star formation rate calculated from FIR+FUV.

5.6.2 Radial distribution of star formation in CLoGS groups

In this subsection we investigate the radial profiles of the star formation rates (SFRs) in CLoGS groups, by using four different SFR indicators (610 MHz radio, WISE W3, WISE W4 and GALEX FUV). The calculation of R_{500} is based on the algorithm used for our groups, explained in §4.1.2. The SFRs of galaxy groups in relation to the distance from the centre of the group, are very important for the study of galaxy evolution, with quite a few studies lately focusing on this aspect.

We studied the relation between the mean SFR and the distance from the centre of the group, binning the SFRs that we find from the different SF indicators, at distances 0.2, 0.5, 1, 2 and 4 R/R_{500} (Figures 5.17, 5.18, 5.19 and 5.20). On the top of Figure 5.17 is shown the radial distribution of SFR_{Radio} with R/R_{500}, with the same distribution shown in the bottom, but with the data binned at distances of 0.2, 0.5, 1, 2 and 4 R/R_{500} for each morphology type separately. We see that the SFR value from the 610 MHz radio is slightly higher for late type galaxies at all distances with no specific gradient being obvious from the centre to the outskirts of the groups for any galaxy morphology. The small drop in SF in the range between 0.5 - 1 R/R_{500} that is observed is probably due to the lower detection rate of galaxies in the radio at this range of distance.

The SFRs calculated from the W3 luminosity (Figure 5.18), show no clear presence of a gradient for early and late type galaxies with only a mild increase of the SFR with rise of the distance from the group centre for late type galaxies. The mean SFR value at each bin is slightly higher for late type galaxies. Figure 5.19 shows a steep increase of SFRs with distance for late type galaxies (blue line) and no trend for early types. In order to confirm the existence of a gradient we used all galaxies together (pink line) where small trend is still obvious with the increase of distance. In Figure 5.20 we note that the SFRs calculated for

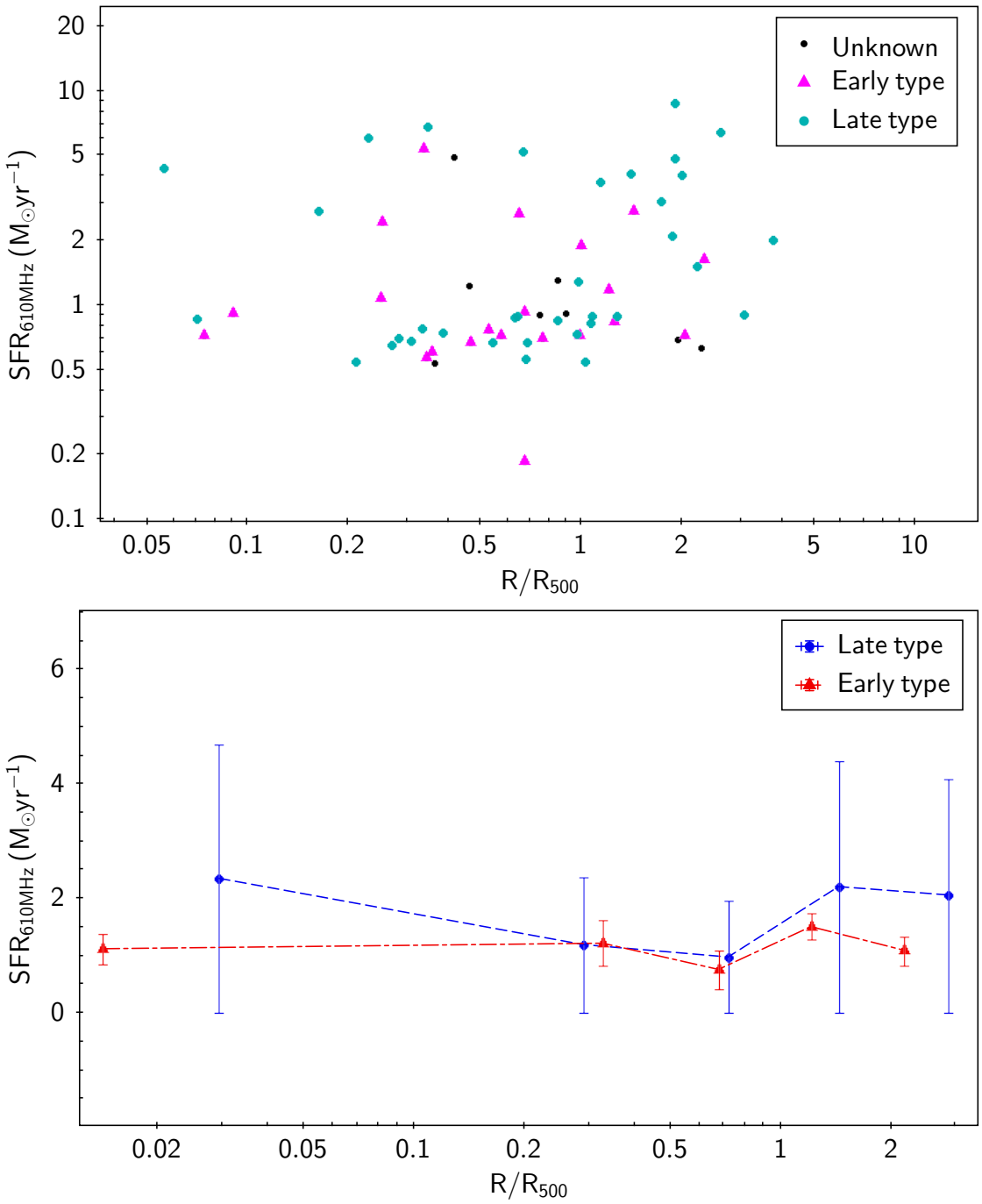

Figure 5.17 Top: Radial distribution of SFR_{Radio} with R/R_{500} with the different morphologies of the member galaxies visible. Bottom: Radial distribution of mean SFR_{Radio} with data binned at 0.2, 0.5, 1, 2 and 4 R/R_{500}. In red is shown the distribution for early type galaxies and in blue for late types. The mean SFR for the late type galaxies is calculated in each bin from 4,8,9,11 and 4 galaxies respectively and for the early types, from 2,6,7,4 and 2 galaxies in each bin respectively.

all galaxies from the FUV dust corrected magnitude (due to the small number of galaxies in individual morphologies), present a small rise with the rise of the group-centric distance. A K-S test statistic applied to the SFR_{Radio}, SFR_{W3}, SFR_{W4} and SFR_{FUV} sample of early and late type population, showing that the latter distribution of populations are probably drawn from the same sample.

Bai et al. (2010) using *Spitzer* MIPS observations in a sample of 9 optically-selected groups at a redshift of $0.06<z<0.1$, found no gradient in the mean SFR with group-centric distance. This is exactly the opposite of what is observed in clusters of galaxies, where the accretion of blue field galaxies produces a SFR gradient that declines as cluster-centric radius becomes smaller (Balogh et al., 2000). A rise of SF with distance from cluster centre is also found for a sample of nearby clusters in Chung et al. (2010) using WISE data. Rasmussen et al. (2012) using the same sample as Bai et al. (2010) but with ultraviolet (UV) data, focused on the low mass galaxies ($<10^{10}$ $M_{\odot}$) and found a SF gradient at a distance of $2R_{200}$, but with no such gradient observed for the higher-mass sample of galaxies.

The most recent study that investigates the properties of SFRs with group-centric distance is from Ziparo et al. (2013). In this study, the properties of star formation with distance from the halo centre is examined at various redsfhifts from Herschel PACS data. Using a sample of group galaxies that was divided in several redshift bins from 0 to $\sim$1.6, and applying a mass cut-off of $10^{10.3}$ $M_{\odot}$, it was shown that the mean SFRs in groups have no gradient with distance from the centre.

Although the use of several SFR indicators may introduce biases by the presence of an AGN (radio), we find by the SFRs calculated from 610 MHz radio and WISE W3 (12μm) monochromatic luminosity, as in Bai et al. (2010) and Ziparo et al. (2013), that there is no clear trend for the mean SFR with group-centric distance for both early and late type

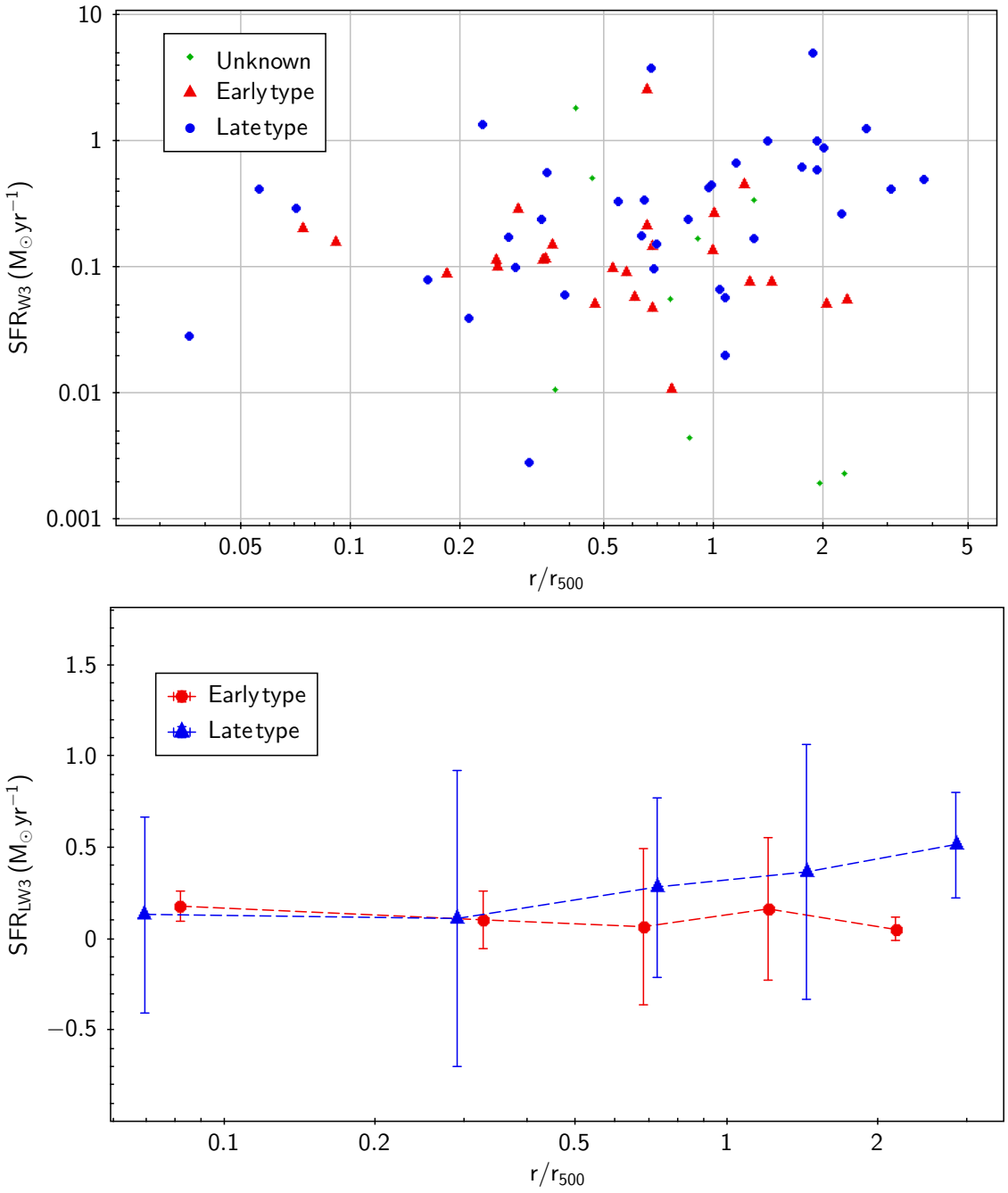

Figure 5.18 Top: Radial distribution of SFR_{W3} with R/R_{500} with the different morphologies of the member galaxies visible. Bottom: Radial distribution of mean SFR_{W3} with data binned at 0.2, 0.5, 1, 2 and 4 R/R_{500}. In red is shown the distribution for early type galaxies and in blue for late types. The mean SFR for the late type galaxies is calculated in each bin from 4,8,10,11 and 4 galaxies respectively and for the early types, from 2,6,6,4 and 2 galaxies in each bin respectively.

galaxies. On the other hand, a mild gradient with rise of group-centric distance is observed for the SFRs calculated by the GALEX FUV and WISE W4 (22μm) monochromatic luminosity. The small gradient that is observed for the SFRs from the GALEX FUV data could be attributed either to the poor statistics (low number of galaxies) in the last bins which may enhance the contribution of star forming galaxies with high SFRs, thus introducing bias towards high SFR, or to the inclusion of lower mass galaxies (lower than 10^{10} $M_{\odot}$) as we have not introduced any mass cut-off in our sample. The latter could also possibly lead to a mild gradient as Rasmussen et al. (2012) has found that a SF gradient exists for low mass galaxies. The different timescale of star formation from this indicator may also play a crucial role. For WISE W4 (22μm) monochromatic luminosity the small gradient observed including all galaxies can also be explained by the contribution of high star forming galaxies biasing the gradient to higher SFRs.

In addition, for the comparison of our results with previous studies we need to be cautious about two things. First, the radius of previous studies extends to slightly different radii (1.5 R_{200} in Ziparo et al. 2013 $-$ 5 R_{200} in Rasmussen et al. 2012) while our analysis for the CLoGS groups is out to 4 R_{500} ($\sim$2.5 R_{200}). This could possibly introduce some bias to the gradient result as at higher radii we approach to the region where galaxies start to enter the group and many studies have found high SF (e.g., Haines et al. 2010) while using lower radii the quenching of SF is probably missed (Wetzel et al., 2012). Secondly, we include all galaxies with SFR data from the different SFR indicators excluding BGEs but not applying a low mass cut-off as in previous studies. This probably means that we also include galaxies with mass lower than $10^{10.3}$ $M_{\odot}$ which is the average limit in most previous studies.

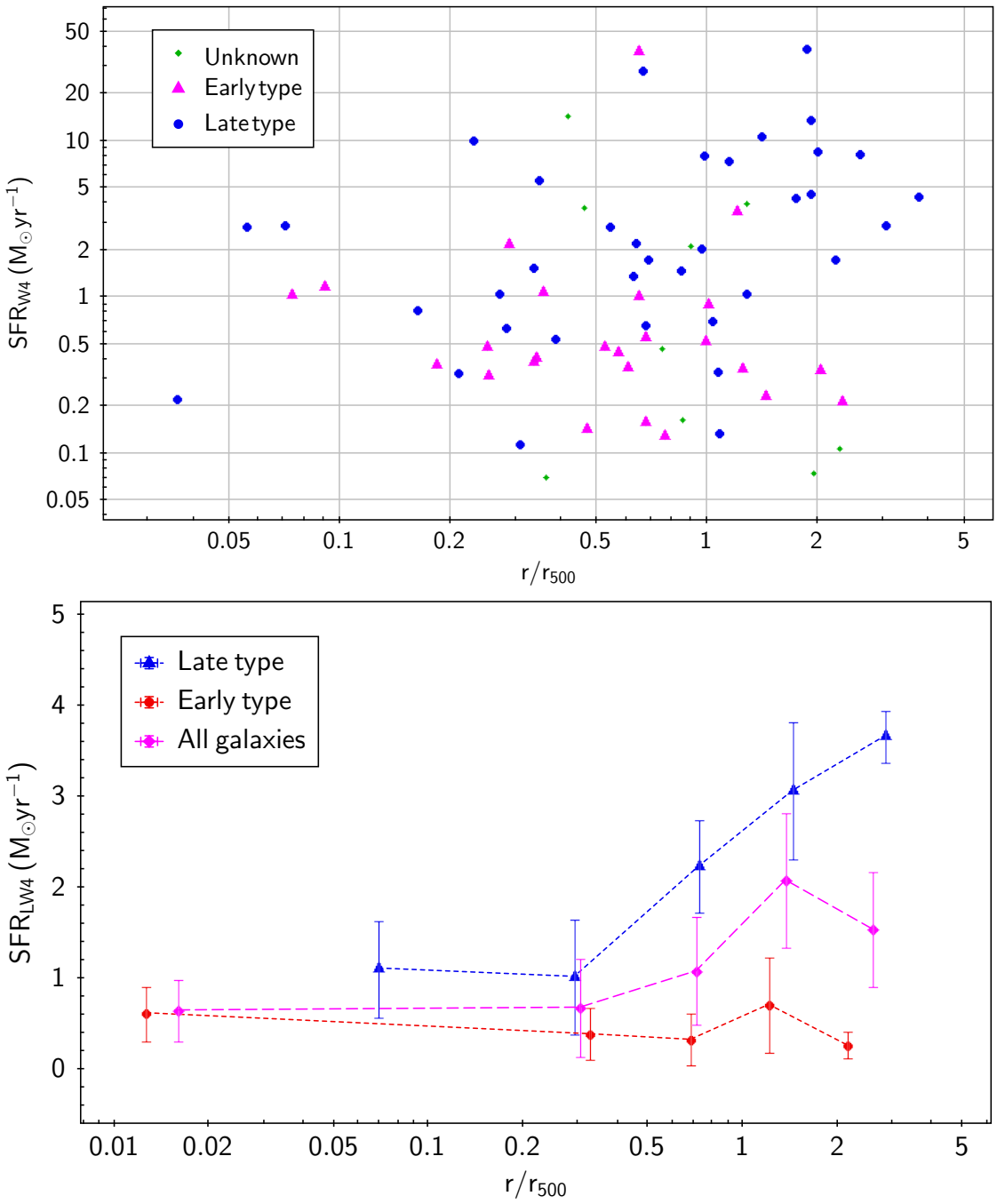

Figure 5.19 Top: Radial distribution of SFR_{W4} with R/R_{500} with the different morphologies of the member galaxies visible. Bottom: Radial distribution of mean SFR_{W4} with data binned at 0.2, 0.5, 1, 2 and 4 R/R_{500}. In red is shown the distribution for early type galaxies and in blue for late types. In pink is presented teh distribution for all galaxies. The mean SFR for the late type galaxies is calculated in each bin from 4,8,10,11 and 4 galaxies respectively and for the early types, from 2,6,6,4 and 2 galaxies in each bin respectively.

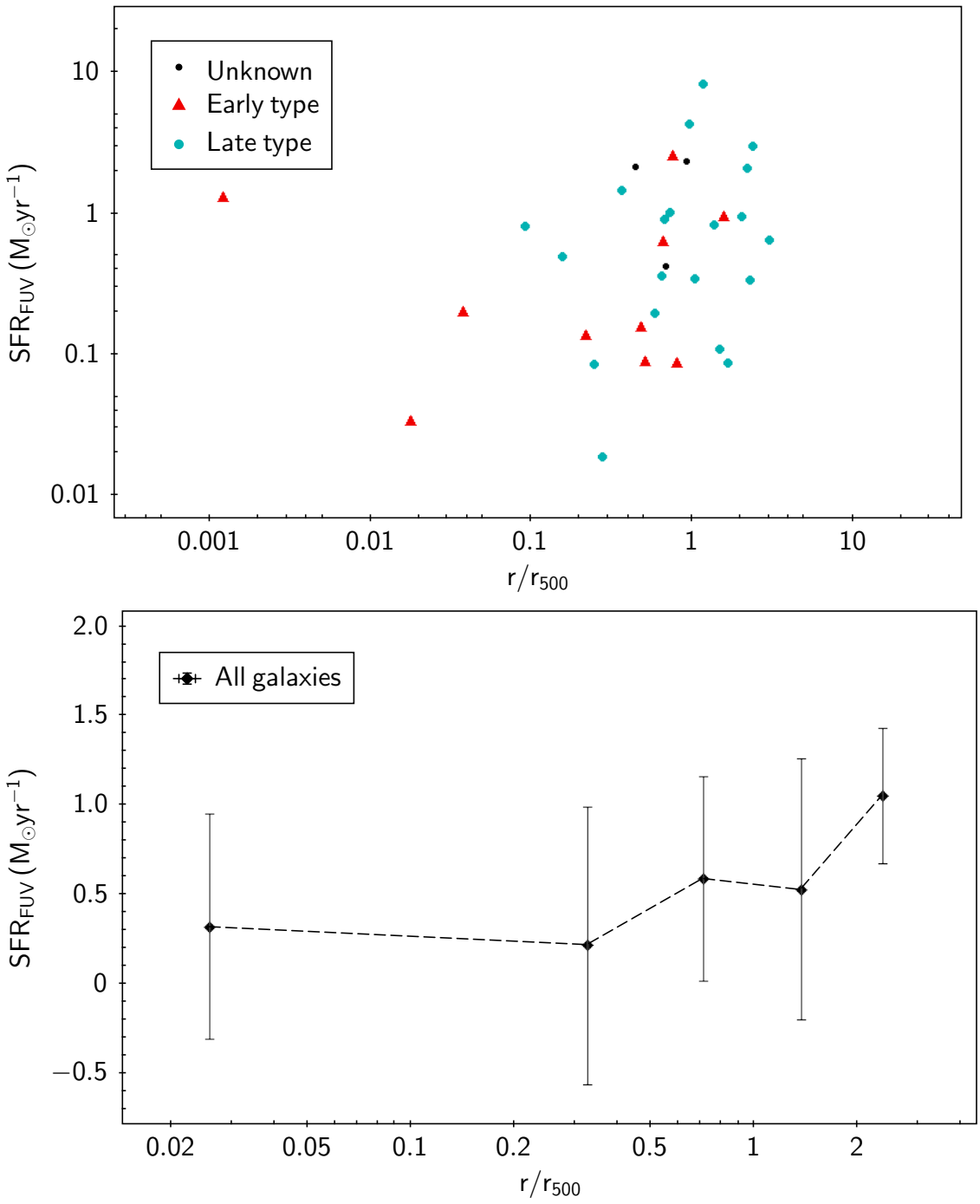

Figure 5.20 Top: Radial distribution of SFR_{FUV} with R/R_{500} with the different morphologies of the member galaxies visible. Bottom: Radial distribution of mean SFR_{FUV} with data binned at 0.2, 0.5, 1, 2 and 4 R/R_{500}. In black is shown the distribution of all types of galaxies together. The mean SFR is calculated in each bin from 5,6,11,6 and 5 galaxies respectively.

5.7 Discussion

In the previous Chapter (Chapter 4) we have focused on the properties of the group central brightest ellipticals. From the X-rays we see that 13/26 systems (50%) have a group scale X-ray emission that reaches beyond 65 kpc (X-ray bright). Of these 13 X-ray bright systems, we observe an equal fraction of systems (39%) that presents either a small or large scale jet radio emission (5/13) or a 'pointlike' one (5/13), with the remaining 3/13 (22%) hosting diffuse radio emission with no particular orientation. As far as the temperature structure of the groups is concerned, we find that about a third (5/14) of the X-ray confirmed groups are non-cool-core, while the remaining two thirds (9/14) have a cool core. We find that the largest radio sources that are either currently active, or have been active in the recent past, lie in X-ray bright cool-core groups.

We find that only 2/18 BGEs have a spectral index α_{235}^{610} steeper than 1. The mean spectral index is calculated to be 0.58 ± 0.1, leaving out of this calculation the 2 systems that had a spectral index much steeper than 1. The mean value from our sample indicates that the radio spectral index in BGEs is flatter than the ones observed in BCGs ($\alpha_{1400}^{4800}=0.74\pm0.05$), but this could be attributed to the different frequency range at which our spectral indices are calculated, as younger radio emission, detected at higher frequencies, gets fainter more rapidly than emission at lower frequencies, resulting in a steeper spectrum.

The radio luminosity of our BGEs sample at both 235 and 610 MHz is found to range between $10^{22} - 10^{24}$ W Hz^{-1}, with the total energy that a radio BGE can provide, assuming a timescale of $\tau \sim 2 \times 10^7$ yr, ranging between 10^{56} to 10^{58} erg.

In chapter 5 we widened our search and looked at all the galaxies in the CLoGS groups. We presented a multi-wavelength approach across the electromagnetic spectrum, examining the properties of star formation and AGN of CLoGS groups, starting from our radio

catalogue as the baseline. Using the line indices and established relations from the BPT criteria we have separated the AGN from star-forming galaxies amongst our CLOGS sample galaxies for which we have optical data. As a result, out of 250 galaxies we have 72% star-forming, 15% AGN and 13% composite galaxies. Out of that, only 10% of star-forming galaxies are detected in radio, while 22% of the AGN and 21% of the composite are detected in radio.

We find that the fraction of the optically selected AGN, using the BPT diagram, is 5%, in agreement with previous studies (Arnold et al., 2009; Dressler et al., 1985) confirming also that the fraction of optical AGN is higher in groups of galaxies than in clusters. Elsewhere, it has been seen to be true that the fraction of X-ray AGN is higher in rich clusters (see Shen et al. 2007; Sivakoff et al. 2008).

Within the GMRT 610 MHz field of view (FOV; $\sim 1^{\circ}$) in a total of 373 galaxies, we detect $\sim$23% (85 out of 373) at 610 MHz, $\sim$19% (70 out of 373) at 235 MHz and $\sim$17% (65 out of 373) at both 610 and 235 MHz. At any radio frequency we detect approximately the same late ($\sim$47%) and early type galaxies ($\sim$42%), with the detected of unknown morphology being $\sim$11%.

Within the much larger FOV at 235 MHz ($\sim 3^{\circ}$), the number of the member galaxies reach 690 in total, of which we detect $\sim$12% (85 out of 690) at 610 MHz, $\sim$14% (97 out of 690) at 235 MHz and $\sim$7% (49 out of 690) at both 610 and 235 MHz. The detection rate for our sample galaxies at any radio emission is observed to be slightly higher for late type (spiral) galaxies ($\sim$53%) than early types ($\sim$36%) with the ones detected of unknown morphology having a detection rate of $\sim$11%.

For the galaxies of our sample that were visually classified, we find from the radial distribution of the AGN and star-forming galaxies with their distance r from the central galaxy

scaled by the 'virial radius' r_{500} (Fig. 5.3), that the fraction of the star-forming galaxies increases with the increase of radius within r/r_{500} and that the AGN fraction increases slightly towards the group centre but not like the increase that is observed in clusters of galaxies. We find that there is a flat distribution between $0.5-3\,r/r_{500}$ for both AGN and star-forming galaxies, with star-forming galaxies decreasing by a factor of 2 closer to the centre than $0.5\,r/r_{500}$ with a corresponding factor of 2 rise in AGN in the same bin. The fact that many of our groups do not possess a dominant cD galaxy, which would host bright AGN as is the case in clusters, is a possible explanation for this shallow rise in AGN towards the centre. In addition, the low velocity dispersion that galaxies have in groups, promotes tidal interactions in galaxies, even before mergers become a possibility. This can trigger bursts of star formation as the gas in the disk is transported to the centres of the respective galaxies. This accounts for the higher fraction of star formating galaxies everywhere in the groups (compared to that in the field), except for the very cores ($< 0.5\,r_{500}$), where the effect of the AGN, in some cases, or the presence of ram-pressure-stripping hot gas, might quench the star formation.

The fraction of radio detected galaxies in X-ray faint groups is twice that observed in X-ray bright ones, meaning that our CLoGS X-ray faint groups are either still in the process of dynamical relaxation or have a small amount of hot (X-ray emitting, $> 10^6$K) intragroup gas. In this case, the radio emission from these systems does not come from the central AGN, both due to less massive black holes being involved as well as the lower supply of gas. In these systems, the radio emission is almost entirely due to emission from the effects of star formation.

By examining the fraction of galaxies that are detected in radio with distance r/r_{500}) based on their morphology we find that a significant fraction ($\sim$30%) of the galaxies that

are detected in the radio lie close to the centre of the groups, with the fraction of the radio detected galaxies dropping as the distance from the centre increases. We find that late type galaxies have a greater fraction of radio detected galaxies close to the centre of the group compared to early type ones. Compared to the radial distribution for each population of galaxies from the BPT, the radial distribution of the fraction of the radio detected late type galaxies correlates with star-forming galaxies, while the fraction of early types with the AGN ones. We see that the natural position of AGN is close to the group centre while star-forming galaxies (although can be found at all distances) are most probable to reside between $0.5-1\mathrm{r/r_{500}}$.

Adopting a threshold for the characterisation of an AGN as radio-loud for the galaxies detected with NVSS in our sample, at $\mathrm{L_{1.4GHz}} = 10^{22}$ W Hz^{-1}, we find that 15 galaxies out of 86 are radio-loud ($\sim$17%) with their stellar masses ranging from 10^{10} to 10^{12} $\mathrm{M_{\odot}}$. We also find a dependence of the radio loud AGN on stellar mass, with the fraction of radio-loud AGN above 5×10^{11} $\mathrm{M_{\odot}}$ being 77% (10/13).

From the radio luminosity function we constructed (Fig. 5.7) for our groups we show that this is very similar (almost identical) to the radio luminosity function of galaxies in the field (e.g., Mao et al. 2012). This is also very similar to the result of Best et al. (2005) that showed that the radio luminosity function of clusters of galaxies is the same as the one in the field, if one excludes the brightest cluster galaxies from the centre. The same result is also found for the luminosity function of groups in the optical (Miles et al., 2004). This means that group galaxies in their luminosity distribution are very much alike to those in the field.

Galaxies are known to form in small groups, which in turn slowly get assimilated into clusters. The very bright galaxies have AGN in them with the star-forming galaxies lacking that brightness. In the brightest galaxies, star-formation is progressively quenched, and the

galaxies found at this end (bright end) are predominantly hosts of AGN (Fig 5.8). As AGN become more active, they produce energy that heats the surrounding gas and quenches the star-formation. At the faint end, however, there are fewer AGN in the less massive galaxies, but the rate of minor and major mergers, and of tidal interaction between dwarf and giant galaxies is higher, and as a result star formation is triggered in the fainter systems. The faint end, thus, lacks AGN and is dominated by star forming galaxies (Fig. 5.8).

Once groups get assimilated into clusters, their luminosity function changes. The bright end of the group luminosity function turns brighter, developing into the BCG of the cluster, which also hosts a very bright radio source, while the faint end slope changes as well as the fainter galaxies undergo minor or major merger, and move towards the bright end. In the group environment, however, star formation takes places at almost all locations, with major-minor and minor-minor interaction between galaxies being more common. This is not happening in groups. Groups thus are the important environments to study the interaction between galaxies, and the transformation of the radio properties of galaxies, as far as both the star formation and evolution of the AGN are concerned.

In §5.5, we looked at various indicators of star formation in our quest to find an efficient way to differentiate between effects of star formation and AGN in radio-luminous galaxies. Taking the 610 MHz luminosity as a star formation indicator, and comparing with similar star-formation indices from GALEX FUV, WISE W3 and W4 and IRAS FIR, we find that the strongest correlation for the star formation indicator at 610 MHz is with the FIR wave-band and especially for late type galaxies ($r = 0.71$, Table 5.7). This is in confirmation of the well known tight radio-FIR correlation (Condon, 1992). A good positive correlation is also seen between the star formation rate at 610 MHz and the star formation rate from WISE W3 and W4 wavebands with $r = 0.56$ and $r = 0.61$ respectively.

We also find that the SFRs calculated from 610 MHz radio and WISE W3 (12μm) monochromatic luminosity, show no appreciable change for the mean SFR with group-centric distance for both early and late type galaxies, while SFRs calculated from the GALEX FUV and WISE W4 (22μm) monochromatic luminosity, present a mild gradient with rise with group-centric distance. Potential biases for this apparent trend possibly arise from the low number of galaxies in each bin, the inclusion of lower mass galaxies (lower than 10^{10} $M_{\odot}$) and the radius out to where SFR properties are estimated. We infer that the presence of this gradient is statistically insignificant.

We find that the central brightest group galaxies are qualitatively different from the central brightest galaxies in clusters. They are less massive, host fainter radio sources, and many show evidence of star-formation, along with the presence of low-luminosity AGN.

Finally, we see that our sample of 26 groups hosts a diverse population of galaxies, implying that we have groups at different stages of their evolutionary history. We observe an evolutionary sequence where we have groups that are just forming and are still early in the evolution (e.g., NGC 5153, NGC 924, NGC 5084), and groups that are 'middle aged' that have already formed, where their star-formation is being slowly quenched as their AGN population grows (NGC 677, NGC 1060). Finally, we have groups that are more advanced in the evolution to forming a cluster (NGC 4261, NGC 193, NGC 5044), having already formed a substantial elliptical galaxy at the centre of the system, with a well established AGN hosting large-scale jets with radio emission. In-depth multiwavelength studies of this sequence will provide crucial information about how galaxies and groups evolve to present-day systems.

Chapter 6

Conclusions

In this Thesis, we have presented new deep observations in the radio waveband, making use of the the Giant Metrewave Radio Telescope in order to study the radio properties of the brightest group galaxies in a complete well-defined sample of groups (CLoGS), along with the examination of the processes that drive galaxy evolution in groups (AGN, star formation).

In Chapter 3, we chose one of the most spectacular radio sources in our sample, the strong FR I radio source 3C 270 in the nearby group-central elliptical NGC 4261, and performed a detailed spectral analysis utilising 240 MHz and 610 MHz data from the GMRT, and VLA data at 1.55 GHz and 4.8 GHz.

We derived the broadband radio spectrum of this source between 22 MHz and 33 GHz, adding literature data to our observations. Applying the best fit Jaffe & Perola (JP) model, we found an asymptotic low-frequency index of $\alpha_{inj} = 0.53^{+0.01}_{-0.02}$. The spectral-index distribution was calculated in two different frequency ranges (240 MHz $-$ 1.55 GHz and 1.55 GHz $-$ 4.8 GHz) revealing a spectral index of $\alpha \sim$0.16 for the unresolved core of the radio source, a constant spectral index along the jets of $\alpha \sim$0.5 and a gradual steepening from the

tip of the jets through the back of the lobes of $\alpha \sim 0.8-1.2$.

From a Jaffe & Perola (JP) model fit in each lobe, we find a radiative age of $t_{\rm rad} \sim 29$ Myr for the west lobe and $t_{rad} \sim 37$ Myr for the eastern one, suggesting an age for the radio source of $29 - 37$ Myr. We calculated that the ratio of non-radiating to radiating particles k ranges from $\sim 4-24$ from the tip of the jets to the back of the lobes, which indicates gas entrainment throughout the jets to the back of the lobes. We also estimated the minimum temperature for the entrained material to balance the pressure of the surrounding IGM to be 11 MeV, which corresponds to a total energy of $\sim 10^{58}$ erg that is required to heat up all the entrained material to this temperature. This energy estimate amounts to $\sim$39% of the enthalpy estimated in O'Sullivan et al. (2011). Since the reduction of the lobe energy compared to O'Sullivan et al. (2011) by $\sim$65% is unlikely, we argue that the filling factor in regions 1 and 5 of the lobes is less than unity (i.e. $\phi < 1$), possibly occupied by thermal plasma, perhaps in the form of low density entrained material.

As the radiative age indicates that the age of the source is about half the dynamical age of 75 Myr found previously using X-ray data (O'Sullivan et al., 2011), we suggested three possible scenarios for this discrepancy:

1. The lobe had a supersonic phase in the early life of the source that produced a powerful shock of Mach 6 (3500 km s^{-1}), pushing it beyond the field of view of the *XMM-Newton* telescope. The fact that the jets appear wide in the radio, and the lack of evidence of a strong shock in the X-ray, argue against a fast jet and a powerful shock.

2. The radiative age indicates that we have a multiple AGN outburst or just large change in the jet power, where the radiative age corresponds to the newest outburst thus underestimating the true age of the source. Worrall et al. (2010) did see structure that could be caused by variations on about 10^4 yr timescales in the X-ray jet of this source,

while the effect of 'in situ acceleration' near the jets in the lobes could also contribute in the underestimation of the age of the source.

3. A fast backflow that could transport young electrons to the back of the lobes relatively fast, could possibly be the reason of the under-estimation of the age. As most of the plasma in the lobe at any position will be old, in this scenario the injection of younger electrons is allowed, thus biasing the age towards smaller values.

We therefore concluded that the radio ages that we find probably do not correspond to the true age of the source, but most likely trace the 'active age' of the radio emission in a mixed population of older and younger radio plasma. If we consider that the first scenario is the case, then 3C 270 should be typical of a population of young FRIs as a whole, and we should expect to see a population of such sources driving very strong shocks for maybe as long as 5 Myr, alongside with a population of groups and clusters with evidence of strong shock heating. No such populations have yet been identified, thus favouring the scenario that the jet appearance should go through many periods of change during the lifetime of a source.

In Chapter 4, we have presented for the first time the low-frequency GMRT radio images of the nearby central brightest group ellipticals from the high richness CLoGS sub-sample at 235 and 610 MHz. We performed a detailed description of the radio properties for each of the central group radio sources and combined the results with findings from X-ray emission. Overall we find that 22 out of the 26 BGEs are detected at any radio frequency, with the majority of the BGEs exhibiting a 'pointlike' radio morphology.

We see that 13/26 systems (50%) have a group scale X-ray emission that reaches beyond 65 kpc (X-ray bright) with 5/13 (39%) of these X-ray bright systems, presenting a small/large scale jet radio emission with another 5/13 (39%) being radio point sources. The

remaining 3/13 (22%) groups host diffuse radio emission with no particular orientation. We find that the largest radio sources that are currently active or were in the recent past, lie in X-ray bright cool-core groups with the systems that did not present radio emission at any frequency appearing in the X-ray faint systems. The common radio population of X-ray bright and faint groups from our study appear to be radio AGN of lower power.

From the comparison performed with the two cluster samples of Andernach & Ramos-Ceja (2009) and Lin & Mohr (2007), we see that radio emission in brightest group ellipticals does not yield a clear result that radio emission in BGEs is more common than in brightest cluster ellipticals (BCEs). In the first comparison with the cluster sample of Andernach & Ramos-Ceja (2009), the fractional detection of brightest cluster galaxies that shows radio emission is 41% compared to 69% that is seen for our brightest group ellipticals, while in the second comparison with the sample of Lin & Mohr (2007) 36% of brightest cluster galaxies exhibits radio emission compared to 16% that we observe in our groups, matching the criteria from this study.

We found that from the 18/26 galaxies that have spectral information at 235 and 610 MHz, only 2/18 have a spectral index distribution steeper than 1. The mean radio spectral index for all of our central group galaxies is calculated to be 0.58 ± 0.1, if we ignore the two systems that had a spectral index steeper than 1. The mean value from our sample indicates that the radio spectral index in BGEs is flatter than the ones observed in BCGs ($\alpha_{1400}^{4800}=0.74\pm0.05$), but this could be attributed to the different frequency range at which our spectral indices are calculated, as younger radio emission, detected at higher frequencies, gets fainter more rapidly than emission at lower frequencies, resulting in a steeper spectrum.

The radio luminosity of our BGEs sample at both 235 and 610 MHz is found to range between $10^{22} - 10^{24}$ W Hz^{-1}, with the total energy that a radio BGE can provide, assuming

a timescale of $\tau \sim 2 \times 10^7$ yr, ranging between 10^{56} to 10^{58} erg.

In Chapter 5, we presented a multiwavelength approach across the electromagnetic spectrum, examining the properties of star formation and AGN in the galaxies belonging to the CLoGs groups. For the galaxies in our sample which are also detected in the SDSS, we identified optical AGN and star-forming galaxies using the BPT line diagnostic diagram, and found that the fraction of the optically selected AGN compared to the whole sample is $\sim$5% (35/690). Only 7% of the star-forming galaxies are detected with GMRT in radio, whereas the fraction of radio detected galaxies for AGNs is $\sim$23%.

At the GMRT 235 MHz field of view (FOV; $\sim 1^\circ$) in a total of 690 galaxies we detect $\sim$12% (85 out of 690) at 610 MHz, $\sim$14% (97 out of 690) at 235 MHz and $\sim$7% (49 out of 690) at both 610 and 235 MHz. The detection rate for our sample galaxies at any radio emission is observed to be slightly higher for late type (spiral) galaxies ($\sim$53%) than early types ($\sim$36%) with the ones detected of unknown morphology having a detection rate of $\sim$11%.

For the galaxies of our sample that were visually classified, we find from the radial distribution of the AGN and star-forming galaxies with their distance r from the central galaxy scaled by the 'virial radius' r_{500}, that the fraction of the star-forming galaxies increases with the increase of radius within r/r_{500} and that the AGN fraction increases slightly towards the group centre but not like the increase that is observed in clusters of galaxies.

The fraction of radio detected galaxies in X-ray faint groups is twice that observed in X-ray bright ones, meaning that our CLoGS X-ray faint groups are either still in the process of dynamical relaxation or have a small amount of hot (X-ray emitting, $> 10^6$K) intragroup gas.

By examining the fraction of galaxies that are detected in radio with distance r/r_{500})

based on their morphology we find that a significant fraction ($\sim$30%) of the galaxies that are detected in the radio lie close to the centre of the groups, with the fraction of the radio detected galaxies dropping as the distance from the centre increases. We find that late type galaxies have a greater fraction of radio detected galaxies close to the centre of the group compared to early type ones.

From the radio detected galaxies in our sample, we found that only three had radio luminosity at 610 MHz above 10^{24} W Hz^{-1}. By characterising a radio AGN as radio-loud if exhibited radio luminosity at 1.4 GHz above $L_{1.4GHz}$ =10^{22} W Hz^{-1}, we found (for the NVSS detected galaxies in our sample) that 15 galaxies out of 86 are radio-loud ($\sim$17%) with their stellar masses ranging from 10^{10} to 10^{12} $M_{\odot}$. The equivalent fraction for clusters is 30-40% (Best et al., 2005) but using a different radio-loud threshold. Due to the low number of galaxies detected as radio-loud we did not perform a fraction of radio-loud versus stellar mass plot as in Best et al. (2005), but we show a dependence of the radio-loud AGN on stellar mass comparing the fraction of radio-loud AGN above and below 5×10^{11} $M_{\odot}$. We found that 77% (10/13) of the radio-loud galaxies were lying above this mass limit.

From the radio luminosity function we constructed for our groups we show that this is very similar to the radio luminosity function of galaxies in the field. This is also very similar to the result of Best et al. (2005) that showed that the radio luminosity function of clusters of galaxies is the same as the one in the field, if one excludes the brightest cluster galaxies from the centre. The same result is also found for the luminosity function of groups in the optical (Miles et al., 2004). This means that group galaxies in their luminosity distribution are very much alike to those in the field.

Various indicators of star formation were also examined. Taking the 610 MHz luminosity as a star formation indicator, and comparing with similar star-formation indices from

GALEX FUV, WISE W3 and W4 and IRAS FIR, we find that the strongest correlation for the star formation indicator at 610 MHz is with the FIR waveband and especially for late type galaxies ($r = 0.71$, Table 5.7). This is in confirmation of the well known tight radio-FIR correlation (Condon, 1992). A good positive correlation is also seen between the star formation rate at 610 MHz and the star formation rate from WISE W3 and W4 wavebands with $r = 0.56$ and $r = 0.61$ respectively.

Finally, we find that the star formation rates (SFRs) calculated from 610 MHz radio and WISE W3 (12μm) monochromatic luminosity, do not exhibit a gradient with group-centric distance for both early and late type galaxies, as is found in Bai et al. (2010) and Ziparo et al. (2013) for galaxy groups, while SFRs calculated from the GALEX FUV and WISE W4 (22μm) monochromatic luminosity, present a mild gradient with rise of group-centric distance. We suggest that this gradient is not to be trusted for WISE W4 (22μm) monochromatic luminosity, with a potential bias for this trend being the contribution of one or two highly star-forming galaxies or the different timescale of star formation. For the SFRs calculated from the GALEX FUV luminosity the inclusion of lower mass galaxies (lower than 10^{10} $M_{\odot}$) and the radius out to where SFR properties are estimated could reveal a gradient as shown in Rasmussen et al. (2012).

6.1 Future Work

There are a variety of things that can be done in future to extend the work done for this dissertation, using the existing data, in conjunction with extant observations elsewhere of the same systems. We would firstly like to study in more detail some of the individual group systems that show very interesting features in the radio, particularly in terms of group dynamics. The interesting features will vary from system to system, but the main target is the

comprehension of the interplay between star formation and the central AGN in galaxies. The paradigms are many, but as examples of extreme cases, we mention that we have NGC 1060 which resides in a newly confirmed group presenting a disturbed halo of X-ray emission and showing a hint of an extended radio emission attributed to a low power AGN, while in NGC 5982, we find a point source AGN, in a compact group with two spiral galaxies, both of which present radio emission from their disks indicative of star formation.

In the individual study of the NGC 4261 group, we had to reject the archival GMRT 610 MHz observation and use only one lower frequency in combination with the higher ones from the VLA radiotelescope (1.4 and 4.8 GHz). The GMRT proposal for the re-observation of NGC 4261 is approved, and the detailed analysis of this system, combined with future observations from LOFAR at lower frequencies, will enable us to set stronger constraints on the age modelling of this interesting source, which would tell us a lot about the validity of the models we use, and the various circumstances that one must consider while studying the interaction between jets and the interstellar/intergalactic medium.

Apart from the central radio sources we have performed the identification of all the radio sources in our fields. Follow-up spectroscopic studies of counterparts could confirm membership of groups, and extend our analysis of optical spectral features (star formation, AGN) of the complete sample.

Two systems, NGC 4472 and NGC 5903 are an ongoing work for future publications aside from the whole CLoGS project. For both systems I have analysed GMRT data at multiple frequencies and performed spectral index maps with NGC 5903 being part of the low-richness subsample and NGC 4472 being a very interesting cavity system in the Virgo cluster. The results mentioned here (More details in Appendix B and C) show just the beginning of the work which will be an interesting study combining X-rays and low frequency

radio observation for the first time for NGC 4472 and HI with X-rays for NGC 5903.

As we were unable to establish an accurate estimate for the virial radius of our groups, due to the low velocity dispersion that they appear, the proper estimation will be done after the X-ray data analysis is perfomed for each group by Dr. Ewan O'Sullivan. The calculated X-ray emission weighted temperatures will enable us to have a better idea of the hot gas reservoir in each group and derive a more accurate value for the virial radius in each of our groups.

The ultimate target of our future work is to extend the data analysis in the radio and X-rays for the CLoGS low-richness subsample, for which radio data already exist, with X-ray data also being acquired, and eventually include them in our results completing the survey. Extending CLoGS in volume will not only give us a bigger range of population of groups in order to stack values, but will provide us with a big diversity of groups and yield valuable results for the sample as a whole, in comparison with the results from the rich subsample dealt with in this work.

The AGN activity in all of these galaxies is currently being modelled using GMRT data down at 610 and 240 MHz along with VLA data at 1.4 and 5 GHz. There is evidence of low-frequency turn-over in several systems which leads us to believe that lower frequency observations will facilitate better radio modeling for both central and non-central group galaxies. LOFAR and GMRT 150 MHz from the TIFR GMRT Sky Survey (TGSS) which finishes in a couple of years will be useful here for much deeper observations. As in NGC 5044, which is in our current sample, observations at 150 and 240 MHz have shown the existence of plasma left over from earlier outbursts and thus has given a measure for the duty cycle in this system (David et al., 2011, 2009; O'Sullivan et al., 2013). Combining LOFAR observations with our extensive GMRT data will yield an excellent sample of galaxies with direct

evidence of multiple outbursts.

Finally, what can also be done as future work is the comparison of the properties of the CLoGS galaxies with a similar sample of groups at higher redshift ($>$0.2) in order to study the evolution of groups of galaxies and that of radio emission with time. Surveys such as COSMOS (Smolčić et al., 2014) or XXL (Pierre and XXL Consortium, 2014) could be crucial to this work.

Bibliography

Abazajian K. N., Adelman-McCarthy J. K., Agüeros M. A., Allam S. S. et al., 2009, ApJS, 182, 543

Afonso J., Georgakakis A., Almeida C., Hopkins A. M., Cram L. E. et al., 2005, ApJ, 624, 135

Allevato V., Finoguenov A., Hasinger G., Miyaji T., Cappelluti N. et al., 2012, ApJ, 758, 47

Andernach H. and Ramos-Ceja M. E., 2009, pra, confE, 57

Appleton P. N., Pedlar A. and Wilkinson A., 1990, ApJ, 357, 426

Arnold T. J., Martini P., Mulchaey J. S., Berti A. and Jeltema T. E., 2009, ApJ, 707, 1691

Artyukh V. S., Dagkesamanskii V. V., Vitkevich R. D., Kozhukhov V. N., 1969, SvA, 12, 567

Assef R. J., Kochanek C. S., Brodwin M., Cool R., Forman W., Gonzalez A. H., Hickox R. C., et al., 2010, ApJ, 713, 970

Assef R. and Stern D. K., 2012, AAS, 219, 42506
101

Bai L., Rasmussen J., Mulchaey J. S., Dariush A., Raychaudhury S. and Ponman T. J., 2010, ApJ, 713, 637

Balogh M. L., Wilman D., Henderson R. D. E., Bower R. G., Gilbank D., Whitaker R., Morris S. L., Hau G., Mulchaey J. S., Oemler A. and Carlberg R. G., 2007, MNRAS, 374, 1169

Balogh M. L., Navarro J. F. and Morris S. L., 2000, ApJ, 540, 113

Ball R., Burns J. O. and Loken C., 1993, AJ, 105, 53

Baars J. W. M., Genzel R., Pauliny-Toth I. I. K, Witzel A., 1977, A&A, 61, 99

Baring M. G., 1997, vhep,conf,97

Baldwin J. A., Phillips M. M. and Terlevich R., 1981, PASP, 93, 5

Baldi R. D. and Capetti A., 2009, A&A, 508, 603

Balogh M. L., Baldry I. K., Nichol R., Miller C., Bower R., Glazebrook K., 2004, ApJ, 615,

Balogh M. L., et al. 1997, ApJ, 488, L75

Bardelli S., Zucca E., Bolzonella M., Ciliegi P., Gregorini L., Zamorani G., Bondi M. et al., 2009, A&A, 495, 431

Bekki K., Couch W. J. and Shioya Y., 2002, ApJ, 577, 651

Bennett C. L., Hill R. S., Hinshaw G., Nolta M. R., Odegard N., Page L., Spergel D. N., Weiland J. L., Wright E. L., Halpern M., Jarosik N., Kogut A., Limon M., Meyer S. S., Tucker G. S. and Wollack E., 2003, ApJS, 148, 97

Beers T. C., Flynn K. and Gebhardt K., 1990, AJ, 100, 32

Becker R. H., White R. L. and Helfand D. J., 1995, ApJ, 450, 559

Beichman C. A., Neugebauer G., Habing H. J., Clegg P. E. and Chester T. J., 1988, iras, 1, B

Bekki K., Shioya Y. and Tanaka I., 1999, ApJ, 520, 99

Bell E. F., McIntosh D. H., Katz N. and Weinberg M. D., 2003, ApJS, 149, 289

Berlind A. A., Frieman J., Weinberg D. H., Blanton M. R., Warren M. S., Abazajian K. et al., 2006, ApJS, 167, 1

Best P. N., Röttgering H. J. A. and Longair M. S., 2000, MNRAS, 311, 23

Best P. N. and Heckman T. M., 2012, MNRAS, 421, 1569

Best P. N., Kauffmann G., Heckman T. M., Brinchmann J., Charlot S., Ivezić Ž and White S. D. M., 2005, MNRAS, 362, 25

Best P. N., von der Linden A., Kauffmann G., Heckman T. M. and Kaiser C. R., MNRAS, 379, 894

Birkinshaw M., Davies R. L., 1985, ApJ, 291, 32

Bîrzan L., McNamara B. R., Nulsen P. E. J., Carilli C. L. and Wise M. W., 2008, ApJ, 686, 859

Bîrzan L., Rafferty D. A., Nulsen P. E. J., McNamara B. R., Röttgering H. J. A., Wise M. W. and Mittal R., 2012, MNRAS, 427, 3468

Blanton M. R., Hogg D. W., Bahcall N. A., Baldry I. K., Brinkmann J., Csabai I., Eisenstein D. et al., 2003, ApJ, 594, 186

Blundell K. M. and Rawlings S., 2000, AJ, 119, 1111

Bonfini P., Zezas A., Birkinshaw M., Worrall D. M., Fabbiano G., O'Sullivan E., Trinchieri G., Wolter A., 2012, MNRAS, 421, 2872

Brough S., Forbes D. A., Kilborn V. A., Couch W., 2006, MNRAS, 370, 1223

Burbidge, 1958, ApJ, 127, 48

Boselli A., Gavazzi G., Donas J. and Scodeggio M., 2001, AJ, 121, 753

Bornancini C. G., O'Mill A. L., Gurovich S. and Lambas D. G., 2010, MNRAS, 406, 197

Bîrzan L., Rafferty D. A., McNamara B. R., Wise M. W. and Nulsen P. E. J., 2004, ApJ, 607, 800

Böhringer H., Schuecker P., Guzzo L., Collins C. A., Voges W., Cruddace R. G., Ortiz-Gil A. et al., 2004, A&A, 425, 367

Bianchi L., Efremova B., Herald J., Girardi L., Zabot A., Marigo P. and Martin C., 2011, yCat, 74112770

Bogdán Á., van Weeren R. J., Kraft R. P., Forman W. R., Randall S., Giacintucci S., 2014, ApJ, 782, 19

Brown M. J. I., Jannuzi B. T., Floyd D. J. E. and Mould J. R., 2011, ApJ, 731, 41

Bicknell G. V., 1995, ApJS, 101, 29

Benson A. J., Bower R. G., Frenk C. S., Lacey C. G., Baugh C. M., Cole S., 2003, ApJ, 599, 38

Burbidge G. 1956, ApJ 124, 4

Best P. N., 2004, MNRAS, 351, 70

Blanton M. R. and Moustakas J., 2009, ARA&A, 47, 159

Bell E. F., 2002, ApJ, 577, 150

Begelman M. C., Blandford R. D., Rees M. J., 1984. Rev. Mod. Phys. 56:255-351

Blanton M. R., Eisenstein D., Hogg D. W., Schlegel D. J., Brinkmann J., 2005, ApJ, 629, 143

Blandford R. D., Rees M. J., 1974. MNRAS 169:395

Burns J. O., 1990, AJ, 99, 14

Becker R. H., Helfand D. J., White R. L., Gregg M. D., Laurent-Muehleisen S. A., 2003, Cat, 8071, 0

Bower R. G., Benson A. J., Malbon R., Helly J. C., Frenk C. S., Baugh C. M., Cole S., Lacey C. G., 2006, MNRAS, 370, 645

Best P. N., Kaiser C. R., Heckman T. M., Kauffmann G., 2006, MNRAS, 368, 67

Booth C. M. and Schaye J., 2013, NatSR, 1738

Bykov A. M. and Treumann R. A., 2011, A&ARv, 19, 42

Bondi H. and Hoyle F., 1944, MNRAS, 104, 273

Bondi H., 1952, MNRAS, 112, 195

Bourne N., Dunne L., Ivison R. J., Maddox S. J., Dickinson M., Frayer D. T., 2011, MNRAS, 410, 1155

Buat V., Deharveng J. M. and Donas J., 1989, A&A, 223, 42

Buat V., 1992, A&A, 264, 444

Buat V. and Xu C., 1996, A&A, 306, 61

Calzetti D., Kennicutt Jr. R. C., Bianchi L., Thilker D. A., Dale D. A., Engelbracht C. W. et al., 2005, ApJ, 633, 871

Carignan C., Cote S., Freeman K. C. and Quinn P. J., 1997, AJ, 113, 1585

Carilli C. L., Perley R. A., Dreher J. W., Leahy J. P., 1991, ApJ, 383, 554

Capak P., Aussel H., Ajiki M., McCracken H. J., Mobasher B., Scoville N. and Shopbell P., 2007, ApJS, 172, 99

Carter B. J., Fabricant D. G., Geller M. J., Kurtz M. J. and McLean B., 2001, ApJ, 559, 606

Cattaneo A. and Best P. N., 2009, MNRAS, 395, 518

Cattaneo A., Faber S. M., Binney J., Dekel A., Kormendy J., Mushotzky R., Babul A. Best P. N. et al. 2009, Natur, 460, 213

Cavagnolo K. W., Donahue M., Voit G. M., Sun M., 2008, ApJ, 683, 107

Chi X. and Wolfendale A. W., 1990, MNRAS, 245, 101

Croft R. A. C., Matteo T. D., Khandai N., Springel V., Jana A. and Gardner J. P., 2012, MNRAS, 425, 2766

Cox T. J., Jonsson P., Primack J. R. and Somerville R. S., 2006, MNRAS, 373, 103

Cowie L. L., Songaila A. and Barger A. J., 1999, AJ, 118, 603

Cooper M. C., Tremonti C. A., Newman J. A., Zabludoff A. I., 2008, MNRAS, 390, 245

Condon J. J., 1992, ARA&A, 30, 575

Caplan J. and Deharveng L., 1986, A&A, 155, 297

Croton D. J., Springel V., White S. D. M., De Lucia G., Frenk C. S., Gao L. et al., 2006, MNRAS, 365, 11

Condon J. J., Anderson M. L., Helou G., 1991, ApJ, 376, 95

Condon J. J., Anderson M. L. and Helou G., 1991, ApJ, 376, 95

Côté P., McLaughlin D. E., Cohen J. G. and Blakeslee J. P., 2003, ApJ, 591, 850

Chung S. M., Gonzalez A. H., Clowe D., Markevitch M., Zaritsky D., 2010, ApJ, 725, 1536

Cutri R. M., Skrutskie M. F., van Dyk S., Beichman et al., 2003, yCat, 2246, 0

Cutri R. M., Wright E. L., Conrow T., Bauer J., Benford D. et al., 2011, wise, rept, 1

Chengalur J. N., Gupta Y. & Dwarakanath K. S., 2007, Low Frequency Radio Astronomy.book

Condon J. J. and Cotton W. D., 2002, AJ, 124, 675

Condon J. J., Cotton W. D., Greisen E. W., Yin Q. F., Perley R. A., Taylor G. B. and Broderick J. J., 1998, AJ, 115, 1693

Cappellari M., Emsellem E., Krajnović D., McDermid R. M., Scott N., Verdoes Kleijn G. A. et al., 2011, MNRAS, 413, 813

Carilli C., Perley R., Dreher J., Leahy J., 1991, ApJ, 383, 554

Chandra P., Ray A., Bhatnagar, 2004, ApJ, 612, 974

Chiaberge M., Gilli R., Macchetto F. D., Sparks W. B. and Capetti A., 2003, ApJ, 582, 645

Churazov E., Brüggen M., Kaiser C. R., Böhringer H. and Forman W., 2001, ApJ, 554, 261

Clarke T., Blanton E., Sarazin C. L., Kassim N., Anderson L., Schmitt H., Gopal-Krishna and Neumann D. M., 2007, hvcg, conf, 124

Clewley L. and Jarvis M. J., 2004, MNRAS, 352, 909

Christlein D. and Zabludoff A. I., 2005, ApJ, 621, 201

Croston J. H., Hardcastle M. J., Birkinshaw M., Worrall D. M. and Laing R. A., 2008, MNRAS, 386, 1709

Croston J. H., Kraft R. P., Hardcastle M. J., Birkinshaw M., Worrall D. M., Nulsen P. E. J., Penna R. F. et al., 2009, MNRAS, 395, 1999

D'Abrusco R., Fabbiano G., Strader J., Zezas A., Mineo S., Fragos T., Bonfini P., Luo B., Kim D. W. and King A., 2013, ApJ, 773, 87

D'Abrusco R., Massaro F., Ajello M., Grindlay J. E., Smith H. A. and Tosti G., 2012, ApJ, 748, 68

David L. P., O'Sullivan E., Jones C., Giacintucci S., Vrtilek J., Raychaudhury S., Nulsen P. E. J. Forman W., Sun M. and Donahue M., 2011, ApJ, 728, 162

Davies R. L., Birkinshaw M., 1986, ApJ, 303, L45

Davis D. S., Mushotzky R. F., Mulchaey J. S., Worrall D. M., Birkinshaw M., Burstein D., 1995, ApJ, 444, 582

David L. P., O'Sullivan E., Jones C., Forman W., Nulsen P., Vrtilek J., O'Sullivan E., Giacintucci S. and Raychaudhury S., 2009, ApJ, 705, 624

Dariush A. A., Raychaudhury S., Ponman T. J., Khosroshahi H. G., Benson A. J., Bower R. G., Pearce F., 2010, MNRAS, 405, 1873

De Lucia G., Weinmann S., Poggianti B. M., Aragón-Salamanca A. and Zaritsky D., 2012, MNRAS, 423, 1277

Díaz-Giménez E., Mamon G. A., Pacheco M., Mendes de Oliveira C. and Alonso M. V., 2012, MNRAS, 426, 296

de Jong T., Klein U., Wielebinski R. and Wunderlich E., 1985, A&A, 147, 6

Devereux N. A. and Eales S. A., 1989, ApJ, 340, 708

de Vaucouleurs G., de Vaucouleurs A., Corwin Jr. H. G., Buta R. J., Paturel G. and Fouqué P., 1991, rc3, book, D

Dressler A., 1980, ApJ, 236, 351

De Propris R., Colless M., Peacock J. A., Couch W. J., Driver S. P., Balogh M. L., Baldry I. K., 2004, MNRAS, 351, 125

Dong R., Rasmussen J. and Mulchaey J. S., 2010, ApJ, 712, 883

Durand N., Bottinelli L., Gouguenheim L., Paturel G., Garnier R., Marthinet M. C., Petit C., 1994, ASPC, 67, 281

Dressler A., Thompson I. B. and Shectman S. A., 1985, ApJ, 288, 481

De Young D. S., 2010, ApJ, 710, 743

De Young D. S., 2001. The Physics of Extragalactic Radio Sources. Chicago: Univ. Chicago Press. 569 pp.

Del Burgo C., Carter D., Sikkema G., 2008, A&A, 477, 105

Dunn R. J. H., Fabian A. C. and Taylor G. B., 2005, MNRAS, 364, 1343

Dunn R. J. H. and Fabian A. C., 2006, MNRAS, 373, 959

Dunn R. J. H., Allen S. W., Taylor G. B., Shurkin K. F., Gentile G., Fabian A. C. and Reynolds C. S., 2010, MNRAS, 404, 180

Ebeling H., Voges W., Boehringer H., 1994, ApJ, 436, 44

Eckert D., Molendi S. and Paltani S., 2011, A&A, 526, 79

Edelson R. and Malkan M., 2012, ApJ, 751, 52

Einasto J., Hütsi G., Einasto M., Saar E., Tucker D. L., Müller V., Heinämäki P. and Allam S. S., 2003, A&A, 405, 425

Einasto J., Tago E., Einasto M. and Saar E., 2005, ASPC, 329, 27

Eke V. R., Baugh C. M., Cole S., Frenk C. S., Norberg P., Peacock J. A., Baldry I. K., Bland-Hawthorn J., Bridges T., Cannon R., Colless M., Collins C., Couch W., Dalton G., de Propris R., Driver S. P., Efstathiou G. et al., 2004, MNRAS, 348, 866

Eke V. R., Baugh C. M., Cole S., Frenk C. S., King H. M. and Peacock J. A., 2005, MNRAS, 362, 1233

Eke V. R., et al., 2004, MNRAS, 355, 769

Eskridge P. B. and Pogge R. W., 1991, AJ, 101, 2056

Eilek J. A., 1996, ASPC, 100, 281

Eilek J., Arendt P., 1996, ApJ, 457, 150

Fabian A. C., Sanders J. S., Taylor G. B., Allen S. W., Crawford C. S., Johnstone R. M., Iwasawa K., 2006, MNRAS, 366, 417

Fabian A. C., 2012, ARA&A, 50, 455

Fabian A. C., 1999, MNRAS, 308, 39

Fanaroff B. L., Riley J. M., 1974, MNRAS, 167, 31P

Fanidakis N., Baugh C. M., Benson A. J., Bower R. G., Cole S., Done C. and Frenk C. S., 2011, MNRAS, 410, 53

Fermi E., 1949, PhRv, 75, 1169

Fraser-McKelvie A., Brown M. J. I., Pimbblet K. A., 2014, MNRAS, 444, 63

Forbes D. A., Ponman T., Pearce F., Osmond J., Kilborn V., Brough S., Raychaudhury S., Mundell C., Miles T. and Kern K., 2006, PASA, 23, 38

Fujita A., Martin C. L., Mac Low M.-M. and Abel T., 2003, ApJ, 599, 50

Fukugita M., Hogan C. J. and Peebles P. J. E., 1998, ApJ, 503, 518

Finoguenov A., Sarazin C. L., Nakazawa K., Wik D. R. and Clarke T. E., 2010, ApJ, 715, 1143

Fitt A. J., Alexander P. and Cox M. J., 1988, MNRAS, 233, 907

Ferrari C., Govoni F., Schindler S., Bykov A. M., Rephaeli Y., 2008, SSRv, 134, 93

Feretti L., Giovannini G., Govoni F. and Murgia M., 2012, A&A Rev., 20, 5

Feretti L. and Giovannini G., 2008, LNP, 740, 143

Filho M. E., Barthel P. D. and Ho L. C., 2002, ApJ, 142, 223

Feretti L., Perola G. C. and Fanti R., A&A, 265, 9

Feretti L., Dallacasa D., Govoni F., Giovannini G., Taylor G. B. and Klein U., A&A, 344, 472

Ferrarese L., Ford H. C., Jaffe W., 1996, ApJ, 470, 444

Forman W., Jones C., Churazov E., Markevitch M., Nulsen P., Vikhlinin A., Begelman M., Böhringer H., Eilek J., Heinz S., Kraft R., Owen F. and Pahre M., 2007, ApJ, 665, 1057

Guo F. and Oh S. P., 2009, MNRAS, 400, 1992

Garcia A. M., 1993, A&AS, 100, 47

Giacintucci S., Vrtilek J. M., Murgia M., Raychaudhury S., O'Sullivan E. J., Venturi T., David L. P., Mazzotta P., Clarke T. E. and Athreya R. M., 2008, ApJ, 682, 186

Giacintucci S., O'Sullivan E., Vrtilek J., David L. P., Raychaudhury S., Venturi T., Athreya R. M., Clarke T. E., Murgia M., Mazzotta P., Gitti M., Ponman T., Ishwara-Chandra C. H., Jones C. and Forman W. R., 2011, ApJ, 732, 95

Giacintucci S., O'Sullivan E., Clarke T. E., Murgia M., Vrtilek J. M., Venturi T., David L. P., Raychaudhury S. and Athreya R. M., 2012, ApJ, 755, 172

Gastaldello F., Di Gesu L., Ghizzardi S., Giacintucci S., Girardi M., Roediger E., 2013, ApJ, 770, 56

Gaspari M., Brighenti F., D'Ercole A., Melioli C., 2011, MNRAS, 415, 1549

Garn T., Green D. A., Riley J. M. and Alexander P., 2009, MNRAS, 397, 1101

Geller M. J. and Huchra J. P., 1983, ApJS, 52, 61

Gregory S. A. and Thompson L. A., 1978, ApJ, 222, 784

Giodini S., Pierini D., Finoguenov A., Pratt G. W., Boehringer H., Leauthaud A., Guzzo L., Aussel H., Bolzonella M., Capak P., Elvis M., Hasinger G. et al., 2009, ApJ, 703, 982

Goto T., Yagi M., Tanaka M., Okamura S., 2004, MNRAS, 348, 515

Guo Y., Giavalisco M., Cassata P., Ferguson H. C., Dickinson M., Renzini A., Koekemoer A. et al., 2011, ApJ, 735, 18

Gordon K. D., Clayton G. C., Witt A. N. and Misselt K. A., 2000, ApJ, 533, 236

Georgakakis A., Gerke B. F., Nandra K., Laird E. S., Coil A. L., Cooper M. C. and Newman J. A., 2008, MNRAS, 391, 183

Goto T. et al., 2003, PASJ, 55, 757

Giacintucci S., Venturi T., Murgia M., Dallacasa D., Athreya R., Bardelli S., Mazzotta P. and Saikia D. J., 2007, A&A, 476, 99

Govoni F., Enβlin T.A., Feretti L. and Giovannini G. 2001, A&A, 369, 441

Gitti M., Brighenti F. and McNamara B. R., 2012, AdAst, 2012, 6

Giacintucci S., O'Sullivan E., Vrtilek J., David L. P., Raychaudhury S., Venturi T., Athreya R. M., Clarke T. E., Murgia M., Mazzotta P., Gitti M., Ponman T. et al., 2011, ApJ, 732, 95

Giroletti M., Giovannini G. and Taylor G. B., 2005, AAP, 441, 89

Giovannini, G. & Feretti, L., 2002, in Astrophysics and Space Science Library, Vol. 272, 197, Merging Processes in Galaxy Clusters, ed. L. Feretti, I. M. Gioia, & G. Giovannini, (Kluwer Academic Publishers, Dordrecht, 2002)

Grogin N. A., Conselice C. J., Chatzichristou E., Alexander D. M., Bauer F. E., Hornschemeier A. E., Jogee S. et al., 2005, ApJ, 627, 97

Gregory P. C., Scott W. K., Douglas K. and Condon J. J., 1996, ApJS, 103, 427

Gopal-Krishna, Mhaskey M., Wiita P. J., Sirothia S. K., Kantharia N. G. and Ishwara-Chandra C. H., 2012, MNRAS, 423, 1053

Grandi S. A., Osterbrock D. E., 1978, ApJ, 220, 783

González-Martín O., Masegosa J., Márquez I., Guainazzi M. and Jiménez-Bailón E., 2009, AAP, 506, 1107

Giordano L., Cortese L., Trinchieri G., Wolter A., Colpi M., Gavazzi G. and Mayer L., 2005, ApJ, 634, 272

Gliozzi M., Sambruna R. M. and Brandt W. N., 2003, A&A, 408, 949

Goodger J. L., Hardcastle M. J., Croston J. H., Kraft R. P., Birkinshaw M., Evans D. A., Jordán A., Nulsen P. E. J., Sivakoff G. R., Worrall D. M., Brassington N. J., Forman W. R., Gilfanov M., Jones C., Murray S. S., Raychaudhury S., Sarazin C. L., Voss R. and Woodley K. A., 2010, ApJ, 708, 675

Guidetti D., Laing R. A., Bridle A. H., Parma P. and Gregorini L., 2011, MNRAS, 413, 2525

Gunn J. E. and Gott III, J. R., 1972, ApJ, 176, 1

Hardcastle M. J. and Worrall D. M., 2000, MNRAS, 319, 562

Hardcastle M. J., Worrall D. M., Kraft R. P., Forman W. R., Jones C. and Murray S. S., 2003, MNRAS, 593, 169

Hardcastle M. J., Kraft R. P., Sivakoff G. R., Goodger J. L., Croston J. H., Jordán A., Evans D. A., Worrall D. M., Birkinshaw M., Raychaudhury S., Brassington N. J., Forman W. R., Harris W. E., Jones C., Juett A. M., Murray S. S., Nulsen P. E. J., Sarazin C. L. and Woodley K. A., 2007, ApJ, 670, L81

Hao L., Strauss M. A., Fan X., Tremonti C. A., Schlegel D. J., Heckman T. M. et al., 2005, AJ, 129, 1795

Haines C. P., Smith G. P., Pereira M. J., Egami E., Moran S. M., Hardegree-Ullman E. et al., 2010, A&A, 518, 19

Hardcastle M. J., Evans D. A., Croston J. H., 2006, MNRAS, 370, 1893

Hardcastle M. J., 2009, ASPC, 407, 121

Hardcastle M. J., 2005, RSPTA, 363, 2711

Harwood, J. J., Hardcastle, M. J., Croston, J. H. and Goodger, J. J., 2013, MNRAS, 435, 3353

Harris D. E., Krawczynski H., 2006. Annu. Rev. Astron. Astrophys. 44:463-506

Haines C. P., Busarello G., Merluzzi P., Smith R. J., Raychaudhury S., Mercurio A. and Smith G. P., 2011, MNRAS, 412, 127

Haines C. P., Busarello G., Merluzzi P., Smith R. J., Raychaudhury S., Mercurio A. and Smith G. P., 2011, MNRAS, 412, 145

Hashimoto Y. and Oemler Jr. A., 2000, ApJ, 530, 652

Helou G., Khan I. R., Malek L. and Boehmer L., 1988, ApJS, 68, 151

Hine R. G. and Longair M. S., 1979, MNRAS, 118, 111

Ho L. C., 2008, ARA&A, 46, 475

Hunt R., 1971, MNRAS, 154, 141

Hickox R. C., Jones C., Forman W. R., Murray S. S., Kochanek C. S., Eisenstein D., Jannuzi B. T., Dey A., Brown M. J. I., Stern D., Eisenhardt P. R. et al., 2009, ApJ, 696, 891

Helou G., Soifer B. T. and Rowan-Robinson M., 1985, ApJ, 298, 7

Hou A., Parker L. C., Balogh M. L., McGee S. L., Wilman D. J., Connelly J. L., Harris W. E., Mok A., Mulchaey J. S., Bower R. G., Finoguenov A., 2013, MNRAS, 435, 1715

Hickson P., 1982, ApJ, 255, 382

Ho L. C. and Ulvestad J. S., 2001, ApJS, 133, 77

Ho L. C., Filippenko A. V. and Sargent W. L. W., 1997, ApJS, 112, 315

Heckman T. M. and Best P. N., 2014, ARA&A, 52, 589

Millennium Star Atlas Vol II Chart 655, Sky Atlas 2000 Chart 7, Uranometria 2000 Vol I Chart 107, Herald-Bobroff Astroatlas B-05 C-21

Hopkins P. F., Somerville R. S., Hernquist L., Cox T. J., Robertson B., Li Y., 2006, ApJ, 652, 864

Huang M.-L. and Chen L.-W., 2010, IAUS, 267, 110

Ho L. C., Filippenko A. V., Sargent W. L. W., 1997, ApJS, 112, 315

Humphrey P. J., Buote D. A., Brighenti F., Gebhardt K., Mathews W. G., 2009, ApJ, 703, 1257

Ivison R. J., Magnelli B., Ibar E., Andreani P., Elbaz D., Altieri B., Amblard A., Arumugam V., 2010, A&A, 518, 31

Jackson C. A., 2004, NewAR, 48, 1187

Jaffe W. J., Perola G. C., 1973, A&A, 26, 423

Jaffe W., Ford H. C., Ferrarese L., van den Bosch F., O' Connell R. W., 1993, Nat, 364, 213

Jarrett T. H., Masci F., Tsai C. W., Petty S., Cluver M. E., Assef R. J., Benford D., Blain A., Bridge C., Donoso E., Eisenhardt P., Koribalski B., Lake S., Neill J. D., Seibert M., Sheth K., Stanford S., Wright E., 2013, AJ, 145, 6

Jaffe W. J., Perola G. C., 1973, A&A, 26, 423

Jenkins C. R., 1982, MNRAS, 200, 705

Jõeveer M., Einasto J. and Tago E., 1978, MNRAS, 185, 357

Jones C., Forman W., Vikhlinin A., Markevitch M., David L., Warmflash A., Murray S. and Nulsen P. E. J., 2002, ApJ, 567, 115

Jones D. L. and Wehrle A. E., 1997, AAS, 191, 10403

Kaiser C. R. and Alexander P., 1997, MNRAS, 286, 215

Katz-Stone D., Rudnick L., Anderson M., 1993, ApJ, 407, 549

Karachentsev I. D., 1972, SoSAO, 7, 1

Kardashev N. S., 1962, SvA, 6, 317

Kauffmann G., Heckman T. M. and Best P. N., 2008, MNRAS, 384, 953

Kauffmann G., White S. D. M., Heckman T. M., Ménard B., Brinchmann J., Charlot S., Tremonti C., Brinkmann J., 2004, MNRAS, 353, 713

Kauffmann G., Heckman T. M., Tremonti C., Brinchmann J., Charlot S., White S. D. M., Ridgway S. E., Brinkmann J., Fukugita M. et al., 2003, MNRAS, 346, 1055

Kawata D. and Mulchaey J. S., 2008, ApJ, 672, 103

Klein U., Wielebinski R. and Thuan T. X., 1984, A&A, 141, 241

Klein U., Weiland H. and Brinks E., 1991, A&A, 246, 323

Knapp G. R. and Rupen M. P., 1996, ApJ, 460, 271

King A., 2003, ApJ, 596, 27

Kolokythas K., O'Sullivan E., Giacintucci S., Raychaudhury S., Ishwara-Chandra C.H., Worrall D. M. and Birkinshaw M., 2015, MNRAS, 14, 1422

Kovač K., Lilly S. J., Knobel C., Bolzonella M., Iovino A., Carollo C. M., Scarlata C., Sargent M. et al., 2010, ApJ, 718, 86

Kennicutt Jr., R. C., 1998, ARA&A, 36, 189

Kennicutt Jr., R. C., Hao C.-N., Calzetti D., Moustakas J., Dale D. A., Bendo G., Engelbracht C. W., Johnson B. D. and Lee J. C., 2009, ApJ, 703, 1672

Kimball A. E. and Ivezić Ž., 2008, AJ, 136, 684

Kewley L. J., Dopita M. A., Sutherland R. S., Heisler C. A. and Trevena J., 2001, ApJ, 556, 121

Kraft R. P., Forman W. R., Jones C., Nulsen P. E. J., Hardcastle M. J., Raychaudhury S. et al., 2011, ApJ, 727, 41

Kellermann K.I., Pauliny-Toth I.I.K. and Williams P. J. S., 1969, ApJ, 157, 1

Kellermann K.I., Pauliny-Toth I.I.K., 1973, AJ, 78, 828

Kraft R. P., Nulsen P. E. J., Birkinshaw M. Worrall D. M., Penna R. F., Forman W. R., Hardcastle M. J., Jones C. and Murray S. S., 2007, ApJ, 665, 1129

Kraft R. P., Vázquez S. E., Forman W. R., Jones C., Murray S. S., Hardcastle M. J., Worrall D. M., Churazov E., 2003, ApJ, 592, 129

Kraft R. P., Birkinshaw M., Nulsen P. E. J., Worrall D. M., Croston J. H., Forman W. R., Hardcastle M. J., Jones C. and Murray S. S., 2012, ApJ, 749, 19

Kuhr H., Witzel A., Pauliny-Toth I. I K. and Nauber U., 1981, A&AS, 45, 367

Laing R. A. and Bridle A. H., 2002, MNRAS, 336, 1161

Laing R. A. and Bridle A. H., 2012, MNRAS, 424, 1149

Laing R. A. and Bridle A. H., 2013, MNRAS, 432, 1114

Laing R. A. and Bridle A. H., 2014, MNRAS, 437, 3405

Lacki B. C. and Thompson T. A., 2010, ApJ, 717, 196

Lacki B. C., Thompson T. A. and Quataert E., 2010, ApJ, 717, 1

Laing R.A., Bridle A.H., 2002, MNRAS, 336, 328

Laganá T. F., Martinet N., Durret F., Lima Neto G. B., Maughan B., Zhang Y.-Y., 2013, A&A, 555, 66

Laganá T. F., Zhang Y.-Y., Reiprich T. H., Schneider P., 2011, ApJ, 743, 13

Ledlow M. J. and Owen F. N., 1996, AJ, 112, 9

Lewis I., Balogh M., De Propris R., Couch W., Bower R., Offer A., Bland-Hawthorn J., Baldry I. K., Baugh C., Bridges T., Cannon R., Cole S. et al., 2002, MNRAS, 334, 673

Li C., Jing Y. P., Mao S., Han J., Peng Q., Yang X., Mo H. J. and van den Bosch F., 2012, ApJ, 758, 50

Li Z., Mao C., Chen L. and Zhang Q., 2012, ApJ, 761, 22

Lonsdale Persson C. J. and Helou G., 1987, ApJ, 314, 513

Lin Y.-T. and Mohr J. J., 2007, ApJS, 170, 71

Lee J. C., Hwang H. S., Ko J., 2013, ApJ, 774, 62

Longair M. S., 1979, Rech, 10, 632

Ledlow M. J., Owen F. N., 1996, IAUS, 175, 238

Leahy J. P., 1990, Lessons from Large-Scale Radio Sources.conf, 174

Liu F. S., Mao S., Meng X. M., 2012, MNRAS, 423, 422

Léna P., Rouan D., Lebrun F., Mignard F. and Pelat D., 2012, obas, book, L

Lin H. W., McDonald M., Benson B. and Miller E., 2015, ApJ, 802, 34

Longair M. S., Ryle M., Scheuer P. A. G., 1973, MNRAS, 164, 243

Matthews A. P. and Scheuer P. A. G., 1990, MNRAS, 242, 616

Mahdavi A., Trentham N. and Tully R. B., 2005, AJ, 130, 1502

Madore B. F., Freedman W. L. and Bothun G. D., 2004, ApJ, 607, 810

Mannheim K. and Biermann P. L., 1989, A&A, 221, 211

Martin D. C. and GALEX Science Team, 2005, AAS, 207, 5201

Magliocchetti M. and Brüggen M., 2007, MNRAS, 379, 260

Ma C.-J., McNamara B. R., Nulsen P. E. J., Schaffer R. and Vikhlinin A., 2011, ApJ, 740, 51

Machacek M., Nulsen P. E. J., Jones C. and Forman W. R., 2006, ApJ, 648, 947

Mazzotta P. and Giacintucci S., 2008, ApJ, 675, 9

Mayya Y. D. and Rengarajan T. N., 1997, AJ, 114, 932

Markevitch M., 2006, ESASP, 604, 723

Macario G., Markevitch M., Giacintucci S., Brunetti G., Venturi T. and Murray S. S., 2011, ApJ, 728, 82

Mao M. Y., Sharp R., Norris R. P., Hopkins A. M. et al., 2012, MNRAS, 426, 3334

Mamon G. A., 2000, BAAS, ASPC, 197, 377

McGee S. L., Balogh M. L., Bower R. G., Font A. S., McCarthy I. G., 2009, MNRAS, 400, 937

Mulchaey J. S. and Zabludoff A. I., 1998, ApJ, 496, 73

Moss C. and Whittle M., 2000, MNRAS, 317, 667

Mulchaey J. S., 2000, ARA&A, 38, 289

Mulchaey J. S., Davis D. S., Mushotzky R. F., Burstein D., 1996, ApJ, 456, 80

McNamara B. R., Rohanizadegan M. and Nulsen P. E. J., 2011, ApJ, 727, 39

McNamara B. R., Wise M., Nulsen P. E. J., David L. P., Sarazin C. L., Bautz M., Markevitch M., Vikhlinin A. et al., 2000, ApJ, 534, 135

McNamara B. R., Nulsen P. E. J., Wise M. W., Rafferty D. A., Carilli C., Sarazin C. L. and Blanton E. L., 2005, Natur, 433, 45

McMahon R. G., White R. L., Helfand D. J. and Becker R. H., 2002, ApJS, 143, 1

McKee C. F. and Hollenbach D. J., 1980, ARA&A, 18, 219

Miniati F., Ryu D., Kang H., Jones T. W., Cen R., Ostriker J. P., 2000, ApJ, 542, 608

Miller N. A. and Owen F. N., 2001, AJ, 121, 1903

Meurer G. R., Heckman T. M. and Calzetti D., 1999, ApJ, 521, 64

Miles T. A., Raychaudhury S., Forbes D. A., Goudfrooij P., Ponman T. J. and Kozhurina-Platais V., 2004, MNRAS, 355, 785

McConnachie A. W., Patton D. R., Ellison S. L. and Simard L., 2009, MNRAS, 395, 255

Mauch T., Murphy T., Buttery H. J., Curran J., Hunstead R. W., Piestrzynski B., Robertson J. G. and Sadler E. M., 2003, MNRAS, 342, 1117

Miller C. J., Nichol R. C., Gómez P. L., Hopkins A. M. and Bernardi M., 2003, ApJ, 597, 142

McCarthy I. G., Babul A., Bower R. G. and Balogh M. L., 2008, MNRAS, 386, 1309

Morrissey P., Schiminovich D., Barlow T. A., Martin D. C., Blakkolb B. et al., 2005, ApJ, 619, 7

Myers S. T., Spangler S. R., 1985, ApJ, 291, 52

McCarthy I. G., Schaye J., Ponman T. J., Bower R. G., Booth C. M., Dalla Vecchia, et al., 2010, MNRAS, 406, 822

Meier D. L., 2003, NewAR, 47, 667

Meisenheimer K., 1989, RvMA, 2, 129

McNamara B. R., Nulsen P. E. J., 2007, ARA&A, 45, 117

Mendes de Oliveira C., 1995, MNRAS, 273, 139

McAlpine K. and Jarvis M. J., 2011, MNRAS, 413, 1054

McNamara B. R. and Nulsen P. E. J., 2007, ARA&A, 45, 117

Miller N. A., Hornschemeier A. E., Mobasher B. et al., 2009, AJ, 137, 4450

Moore B., Lake G. and Katz N., 1998, ApJ, 495, 139

Mulchaey J. S., Davis D. S., Mushotzky R. F. and Burstein D., 2003, ApJ, 145, 39

Murgia M., Fanti C., Fanti R., Gregorini L., Klein U., Mack K.-H. and Vigotti M., 1999, A&A, 345, 769

Murgia, 2000, Ph.D. thesis, Univ. Bologna

Murgia, 2003, PASA, 20, 19M

Murgia M., Parma P., Mack K.-H., de Ruiter H. R., Fanti R., Govoni F., Tarchi A., Giacintucci S. and Markevitch M., 2011, A&A, 526A, 148

Myers S. T. and Spangler S. R., 1985, ApJ, 291, 52

Narayan R. and Yi I., 1995, ApJ, 452, 710

Narayan R., 2005, Ap&SS, 300, 177

Nesvadba N. P. H., Lehnert M. D., De Breuck C., Gilbert A. M. and van Breugel W., 2008, A&A, 491, 407

Newton R. D. A. and Kay S. T., 2013, MNRAS, 434, 3606

Niklas S., 1997, A&A, 322, 29

Neugebauer G., Habing H. J., van Duinen R., Aumann H. H., Baud B., Beichman C. A. et al., 1984, ApJ, 278, 1

Nevalainen J., David L. and Guainazzi M., 2010, A&A, 523, 22

Nulsen P. E. J., McNamara B. R., Wise M. W., David L. P., 2005, ApJ, 628, 629

Nulsen P. E. J., Jones C., Forman W., Churazov E., McNamara B., David L. and Murray S., 2009, AIPC, 1201, 198

Oemler Jr. A., 1974, ApJ, 194, 1O

Ogle P. M., Mazzarella J., Ebert R., Fadda D., Lo T., Terek S., Schmitz M. and for the NED Team, 2015, arXiv150301184O

Osmond J. P. F. and Ponman T. J., 2004, MNRAS, 350, 1511

O'Sullivan E., Giacintucci S., Vrtilek J. M., Raychaudhury S., Athreya R., Venturi T. and David L. P., 2009, ASPC, 407, 250O

O'Sullivan E., Kolokythas K., Raychaudhury S., Vrtilek J. M., Kantharia N., 2014, arXiv1402, 4676O

Oh S., Mulchaey J. S., Woo J.-H., Finoguenov A., Tanaka M., Cooper M. C., Ziparo F. et al., 2014, ApJ, 790, 430

Owen F. N., Voges W., Burns J. O. and Ledlow M. J., 1992, AAS, 181, 1507O

Owen F. N., White R. A. and Ge J., 1993, ApJS, 87, 135O

O'Sullivan E., Giacintucci S., David L. P., Gitti M., Vrtilek J. M., Raychaudhury S., Ponman T. J., 2011, ApJ, 735, 11

O'Sullivan E., Giacintucci S., David L. P., Vrtilek J. M. and Raychaudhury S., 2011, MNRAS, 411, 1833

O'Sullivan E., Worrall D. M., Birkinshaw M., Trinchieri G., Wolter A., Zezas A., Giacintucci S., 2011, MNRAS, 416, 2916

O'Sullivan E., David L. P. and Vrtilek J. M., 2013, MNRAS, 437, 730O

Pacholczyk A. G., 1970, Series of Books in Astronomy and Astrophysics, Freeman & Co., San Francisco

Parma P., Murgia M., de Ruiter H. R. et al., 2007, A&A, 470, 875

Pauliny-Toth I. I. K., Wade C. M. and Heeschen D. S., 1966, ApJS, 13, 65

Pauliny-Toth I. I. K. and Kellermann K. I., 1968, AJ, 73, 953

Paturel G., Petit C., Prugniel P., Theureau G., Rousseau J., Brouty M., Dubois P. and Cambrésy L., 2003, A&A, 412, 45

Pacholczyk A. G., 1970, ranp.book

Petrosian V. and Bykov A. M., 2008, SSRv, 134, 207

Perley R. A. and Butler B. J., 2013, ApJS, 204, 19

Perucho M. and Martí J. M., 2012, MNRAS, 382, 526

Peterson J. R. and Fabian A. C., 2006, PhR, 427, 1

Pierre M. and XXL Consortium, 2014, xru, confE, 17P

Pipino A., Kaviraj S., Bildfell C., Babul A., Hoekstra H. and Silk J., 2009, MNRAS, 395, 462

Ponman T. J., Sanderson A. J. R. and Finoguenov A., 2003, MNRAS, 343, 331

Ponman T. J., Bourner P. D. J., Ebeling H., Böhringer H., 1996, MNRAS, 283, 690

Price R. and Duric N., 1992, ApJ, 401, 81

Porter S. C. and Raychaudhury S., 2005, MNRAS, 364, 1387

Piner B. G., Jones D. L., Wehrle A. E., 2001, AJ, 122, 2954

Quilis V., Moore B. and Bower R., 2000, Sci, 288, 1617

Randall S. W., Jones C., Kraft R., Forman W. R. and O'Sullivan E., 2009, ApJ, 696, 1431

Rafferty D. A., McNamara B. R., Nulsen P. E. J. and Wise M. W., 2006, ApJ, 652, 216

Randall S. W., Forman W. R., Giacintucci S., Nulsen P. E. J., Sun M., Jones C., Churazov E., et al., 2011, ApJ, 726, 86

Rasmussen J., Ponman T. J., Mulchaey J. S., Miles T. A. and Raychaudhury S., 2006, MNRAS, 373, 653

Rasmussen J., Bai X.-N., Mulchaey J. S., van Gorkom J. H., Jeltema T. E., Zabludoff A. I., Wilcots E., Martini P., Lee D., Roberts T. P., 2012, ApJ, 747, 31

Rasmussen J., Mulchaey J. S., Bai L., Ponman T. J., Raychaudhury S. and Dariush A., 2012, ApJ, 757, 122

Rasmussen J. and Ponman T. J., 2007, ggnu, conf, 325

Robertson B., Hernquist L., Cox T. J., Di Matteo T., Hopkins P. F., Martini P. and Springel V., 2006, ApJ, 641, 90

Roettiger K., Burns J. O. and Stone J. M., 1999, ApJ, 518, 603

Ruderman M. A. and Spiegel E. A., 1971, ApJ, 165, 1

Rieke G. H., Alonso-Herrero A., Weiner B. J., Pérez-González P. G., Blaylock M., Donley J. L., Marcillac D., 2009, ApJ, 692, 556

Rengarajan T. N., Karnik A. D. and Iyengar K. V. K., 1997, MNRAS, 290, 1

Roychowdhury S. and Chengalur J. N., 2012, MNRAS, 423, 127

Rengelink R. B., Tang Y., de Bruyn A. G., Miley G. K., Bremer M. N. et al., 1997, A&AS, 124, 259

Rees M. J., 1971, Natur, 229, 312

Rosswog S., Bruggen M., 2007, Introduction to High-Energy Astrophysics.book

Rest A., van den Bosch F. C., Jaffe W.,Tran H., Tsvetanov Z., Ford H. C., Davies J., Schafer J., 2001, AJ, 121, 2431

Roger R. S., Costain C. H. and Lacey J. D., 1969, AJ, 74, 366

Salim S., Rich R. M., Charlot S., Brinchmann J., Johnson B. D., Schiminovich D. et al., 2007, ApJS, 173, 267

Sanderson A. J. R., Ponman T. J., O'Sullivan E., 2006, MNRAS, 372, 1496

Sanderson A. J. R., Ponman T. J. and O'Sullivan E., 2006, MNRAS, 372, 1496

Sanghera H. S., Saikia D. J., Luedke E., Spencer R. E., Foulsham P. A., Akujor C. E. and Tzioumis A. K., 1995, AAP, 295, 629

Sanders D. B., Soifer B. T. and Scoville N. Z., 1988, Sci, 239, 625

Shabala S. S., Ash S., Alexander P. and Riley J. M., 2008, MNRAS, 388, 625

Shakura N. I. and Sunyaev R. A., 1973, A&A, 24, 337

Springel V., White S. D. M., Jenkins A., Frenk C. S., Yoshida N., Gao L., Navarro J. Thacker R. et al.,2005, Natur., 435, 629

Sijacki D., Springel V., Di Matteo T., Hernquist L., 2007, MNRAS, 380, 877

Sutherland W. and Saunders W., 1992, MNRAS, 259, 413

L. Spitzer, 1978, Physical Processes in the Interstellar Medium, Wiley, New York

Stern D., Eisenhardt P., Gorjian V., Kochanek C. S., Caldwell N., Eisenstein D., Brodwin M., Brown M. J. I., et al., 2005, ApJ, 631, 163

Stern D., Assef R. J., Benford D. J., Blain A., Cutri R., Dey A., Eisenhardt P., Griffith R. L., et al., 2012, ApJ, 753, 30

Sun M., 2009, AIPC, 1201, 210

Sun M., 2012, NJPh, 14d5004S

Salvato M., Hasinger G., Ilbert O., Zamorani G., Brusa M., Scoville N. Z., Rau A., Capak P., 2009, ApJ, 690, 1250

Shen Y., Mulchaey J. S., Raychaudhury S., Rasmussen J. and Ponman T. J., 2007, ApJ, 645, 115

Skrutskie M. F., Cutri R. M., Stiening R., Weinberg M. D., Schneider S. et al., 2006, AJ, 131, 1163

Stoughton C., Lupton R. H., Bernardi M., Blanton M. R et al., 2002, AJ, 123, 485

Scheuer P. A. G., 1974, MNRAS, 166, 513

Scheuer P. A. G., Williams P. J. S., 1968, ARA&A, 6, 321

Schweizer F. and Seitzer P., 1992, AJ, 104, 1039

Shulevski A., Morganti R., Oosterloo T. and Struve C., 2012, AAP, 545, 91

Sivakoff G. R., Martini P., Zabludoff A. I., Kelson D. D. and Mulchaey J. S., 2008, ApJ, 682, 803

Scaife A. M. M. and Heald G. H., 2012, MNRAS, 423, 30

Smolčić V., Ciliegi P., Jelić V., Bondi M., Schinnerer E. et al., 2014, MNRAS, 443, 2590

Tal T., van Dokkum P. G., Nelan J. and Bezanson R., 2009, AJ, 138, 1417

Tanaka M., Kodama T., Arimoto N., Okamura S., Umetsu K., Shimasaku K., Tanaka I. and Yamada T., 2005, MNRAS, 362, 268

Taylor J. E. and Babul A., 2005, MNRAS, 364, 515

Teyssier R., Chapon D. and Bournaud F., 2010, ApJ, 720, 149

Terlevich A. I. and Forbes D. A., 2002, MNRAS, 330, 547

Tully R. B., 1987, ApJ, 321, 280

Toomre A. and Toomre J., 1972, BAAS, 4, 214

Trinchieri G., Fabbiano G. and Kim D.-W., 1997, A&A, 318, 361

Tribble P. C., 1993, MNRAS, 261, 57

Trager S. C., Faber S. M., Worthey G. and González J. J., 2000, AJ, 119, 1645

Tully R. B. and Trentham N., 2008, AJ, 135, 1488

Tremblay G. R., Chiaberge M., Sparks W. B., Baum S. A., Allen M. G., Axon D. J. Capetti A. et al., 2009, ApJS, 183, 278

Tsujimoto M., Guainazzi M., Plucinsky P. P., Beardmore A. P., Ishida M., Natalucci L., Posson-Brown J. L. L., Read A. M., Saxton R. D., Shaposhnikov N. V., 2011, A&A, 525, 25

Vajgel B., Jones C., Lopes P. A. A., Forman W. R., Murray S. S., Goulding A., Andrade-Santos F., 2014, ApJ, 794, 88

van Driel W. and van Woerden H., 1991, AAP, 243, 71

Vasudevan R. V. and Fabian A. C., 2007, MNRAS, 381, 1235

Veilleux S. and Osterbrock D. E., 1987, ApJS, 63, 295

Vermeulen R. C., Ogle P. M., Tran H. D., Browne I. W. A., Cohen M. H., Readhead A. C. S., Taylor G. B., Goodrich R. W., 1995, ApJ, 452, L5

Voit G. M., Kay S. T. and Bryan G. L., 2005, MNRAS, 364, 909

Vikhlinin A., Markevitch M. and Murray S. S., 2001, ApJ, 551, 160

Vollmer B., Cayatte V., Balkowski C. and Duschl W. J., 2001, ApJ, 561, 708

von der Linden A., Best P. N., Kauffmann G. and White S. D. M., 2007, MNRAS, 379, 867

Vulcani B., Poggianti B. M., Fritz J., Fasano G., Moretti A., Calvi R., Paccagnella A., 2015, ApJ, 798, 52

Viner M. R., Erickson W. C., 1975, AJ, 80, 931

von der Linden A., Wild V., Kauffmann G., White S. D. M. and Weinmann S., 2010, MNRAS, 404, 1231

Wang L., Rowan-Robinson M., Norberg P., Heinis S. and Han J., 2014, MNRAS, 442, 2739

Weilbacher P. M., Duc P.-A., Fritze v. Alvensleben U., Martin P., Fricke K. J., 2000, AAP, 358, 819

Weinmann S. M., van den Bosch F. C., Yang X., Mo H. J., 2006, MNRAS, 366, 2

Wetzel A. R., Tinker J. L. and Conroy C., 2012, MNRAS, 424, 232

White R. L., Becker R. H., Helfand D. J. and Gregg M. D., 1997, ApJ, 475, 479

Wiita P. J., Gopal-Krishna, 1990, ApJ, 353, 476

Wise M. W., McNamara B. R. and Murray S. S., 2004, ApJ, 601, 184

Worrall D. M. and Birkinshaw M., 2006, LNP, 693, 39

Worrall D. M. and Birkinshaw M., 1994, ApJ, 427, 134

Worrall D. M., Birkinshaw M., O' Sullivan E., Zezas A., Wolter A., Trinchiery G., Fabbiano G., 2010, MNRAS, 408, 701

Worrall D. M., Birkinshaw M., Young A. J., Momtahan K., Fosbury R. A. E., Morganti R., Tadhunter C. N. and Verdoes Kleijn G., 2012, MNRAS, 424, 1346

Wright E. L., Eisenhardt P. R. M., Mainzer A. K., Ressler M. E., Cutri R. M. et al., 2010, AJ, 140, 1868

Wykes S., Croston J. H., Hardcastle M. J., Eilek J. A., Biermann P. L., Achterberg A., Bray J. D., Lazarian A., Haverkorn M., Protheroe R. J., Bromberg O., 2013, A&A, 558, 19

Xu C., Lisenfeld U., Volk H. J. and Wunderlich E., 1994, A&A, 282, 19

Xu C., Buat V., Boselli A. and Gavazzi G., 1997, A&A, 324, 32

Yang X., Mo H. J., van den Bosch F. C., Jing Y. P., Weinmann S. M., Meneghetti M., 2006, MNRAS, 373, 1159

York D. G., Adelman J., Anderson Jr., J. E., Anderson S. F., Annis J., Bahcall N. A. et al., 2000, AJ, 120, 1579

Young A., Rudnick L., Katz D., Delaney T., Kassim N.E., Makishima K., 2005, ApJ, 626, 748

Yun M. S., Reddy N. A. and Condon J. J., 2001, ApJ, 554, 803

Zeilinger W. W., Galletta G. and Madsen C., 1990, MNRAS, 246, 324

Zeldovich Y. B., 1982, SvAL, 8, 102

Zezas A., Birkinshaw M., Worrall D. M., Peters A., Fabbiano G., 2005, ApJ, 627, 711

Zhao Y.-H., Gu Q.-S., Peng Z.-X., Shi L., Luo X.-L., Peng Q.-H., 2006, ChJAA, 6, 15

Ziparo F., Popesso P., Biviano A., Finoguenov A., Wuyts S., Wilman D., Salvato M., Tanaka M. et al., 2013, MNRAS, 434, 3089

Appendix A

NGC 4261

A.1 610 MHz data

The analysis of NGC 4261 included also the frequency of GMRT 610 MHz. The analysis of the 610 MHz data was performed separately for each side band where we report a flux disposition that produced multiple ghost images of the source, offset to the north and south from the true jet, introducing false structure.

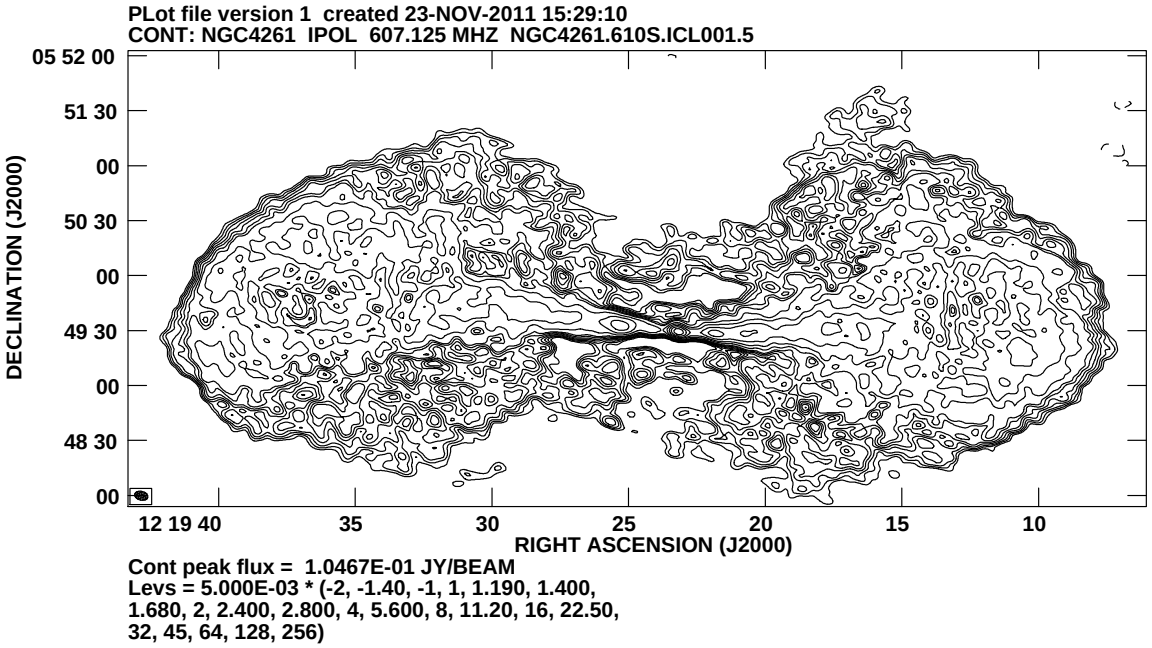

Figure A.1 GMRT 610 MHz contours starting from 5σ (1σ = 1 mJy beam^{-1}), rising by $\sqrt{2}$.

Here we present the GMRT 610 MHz image to reveal the morphological anomaly the

analysis for this frequency featured. In Figure A.1, it is clearly seen by the radio contours, that the emission north and south from the core of the galaxy resembles a repeating jet with 5σ contour level of significance. The maximum amplitude of these ghost images was found to be $\sim$10% of the true source flux ($\sim$3 Jy).

We considered the possibility that the ghost images are caused by residual amplitude and phase errors due to the brightness of the source with the deconvolution ('CLEAN' algorithm) not accounting for the spectral gradients. Amplitude errors show up if the delays can't be fitted and an amplitude self-calibration would be needed. We tested the effect of amplitude self-calibration with solution interval 1 but found no improvement. Several other tests with different methods were performed, i.e. imaging only one side band or performing one round of self calibration only. Eventually the optimum solution was to use the 610 MHz data only for the total source flux estimation for the integrated spectrum and it was decided to exclude it from our point-to-point spectral analysis of the radio source as the images could not be trusted for the creation of spectral-index maps.

Appendix B

Falling into the Virgo Cluster: NGC 4472

B.1 Introduction

M49 (NGC 4472) is a massive ($\sim 8 \times 10^{11}$ $M_{\odot}$, Côté et al. 2003) X-ray bright nearby early-type galaxy that is falling into the Virgo cluster (d=16.7 Mpc, $1''$=80 pc) along with the group in which NGC 4472 is the brightest group elliptical (BGE). In this system, when X-ray images from *Chandra* are combined with the radio, are seen cavities on several scales. However, X-rays also confirm the existence of a pair of elongated cavities on much larger scales ($>$ 2 arcmin), first seen in the XMM images we have, which have so far not been associated with any radio emission.

In Kraft et al. (2011), an upper limit of about 5 mJy on the radio emission from each cavity was placed from the not so deep NVSS data, and showed that if the cavities are in pressure balance, the plasma in the cavities then must be old and only radiate at low frequencies. For that reason low-frequency observations were performed using GMRT to detect this large-scale plasma or to put even stronger constraints on the physical conditions inside the ghost cavities. I performed the analysis of NGC 4472 at three frequencies: 240 MHz, 610 MHz and 1400 MHz. Then I combined each frequency in order to produce various spectral index maps. Multi-frequency detections or upper limits will allow us to make estimates of (relative) spectral age at different locations in the radio source, which will help us both in characterizing the energy input of the AGN and in constraining the history of the ongoing merger.

B.2 Radio images of NGC 4472

Figure B.1 shows the GMRT 240 MHz image in which the total flux density of the source is ∼0.86 Jy with a resolution of $\sim 8'' \times 6''$. At this frequency the morphology of the radio source presents two lobes with a total extension of ∼8 kpc. The west lobe seems to be more extended while the east one includes a small jet bending towards the north.

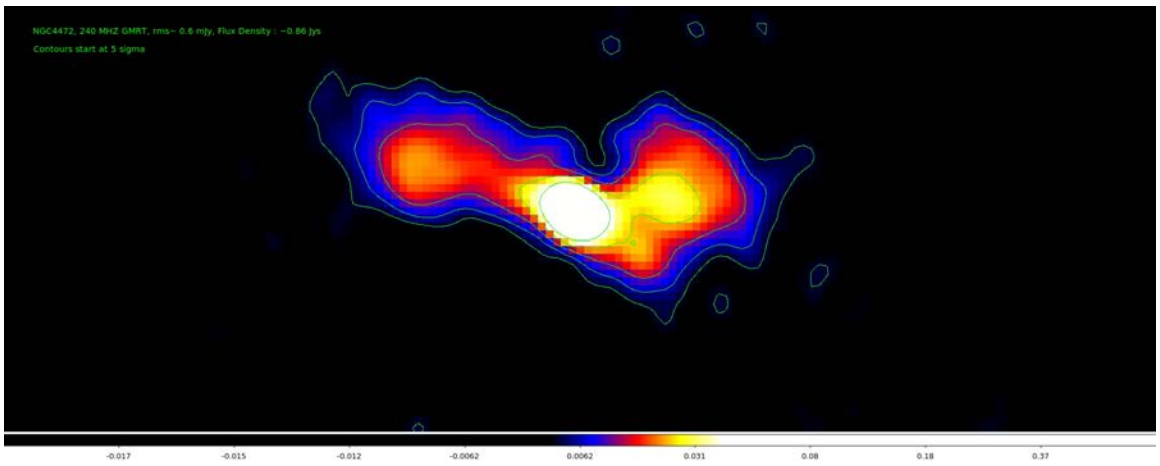

Figure B.1 GMRT 240 MHz image of NGC 4472 with $1\sigma = 0.6$ mJy beam^{-1}. The total flux density of the source at this frequency is 0.86 Jy. Contours start from 3 mJy (5 x r.m.s.) and increase by a factor of $\sqrt{2}$.

The GMRT 610 MHz radio image shown in Figure B.2 has an rms of ∼60 μJy. The total flux density of the source at this frequency is 0.5 Jy with a resolution for robust 0 of about $5.70'' \times 4.50''$. The morphology of the source at this frequency is very similar to the one at 240 MHz with the bending east jet being more profound. On the other hand, the presence of a west jet is not obvious with the lobe dominating the emission.

In Figure B.3 the GMRT 1.4 GHz image the resolution (using the parameter *robust*3) is $\sim 4'' \times 4''$. At this very high resolution only the core of the radio emission is detected. The resolution was reduced to a desirable level using the task 'uvtaper' [1] in AIPS to detect the emission from the lobes/jets. The final resolution achieved for this frequency for uvtaper 15 15 is $15.8'' \times 14.5''$ with an rms of ∼1 mJy beam^{-1} at this resolution, with the total flux density of the source at 1.4 GHz being ∼0.25 Jy.

The east jet is only just detected at this frequency while on the west side a discontinuity in the radio emission is present.

The frequency of 1.4 GHz was also analysed from VLA. The resolution of Figure B.4

[1] uvtaper is the task used in AIPS to specify widths in u and v directions of gaussian function used, to weight down long baseline data points -increase resolution-

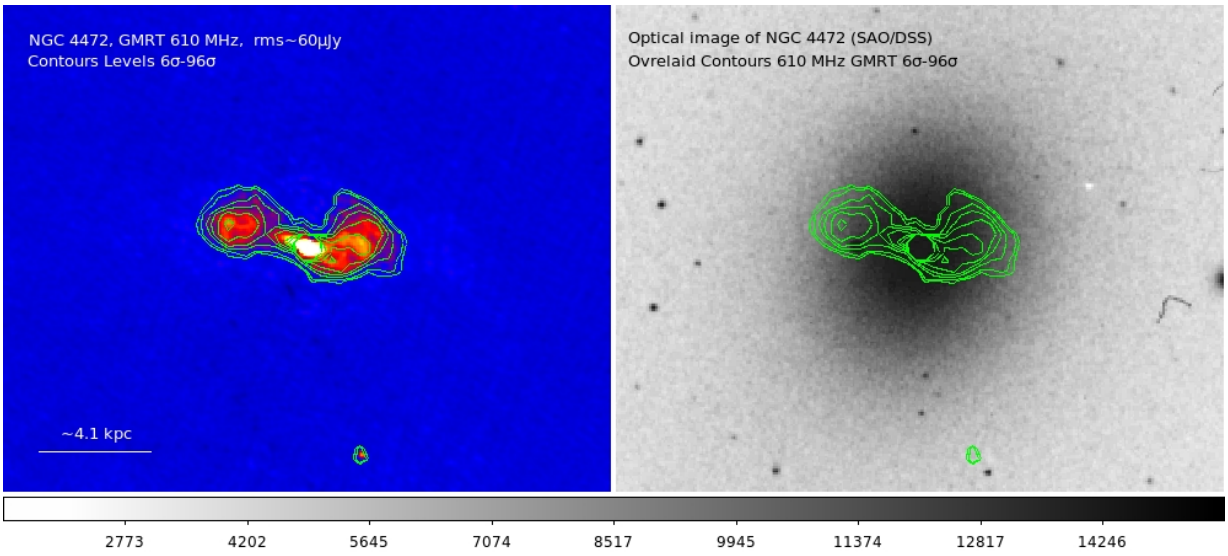

Figure B.2 On the left: Radio image of NGC 4472 at 610 MHz with an rms of ∼60 μJy beam^{-1}. Contour levels start at 6σ and rise by factor of $\sqrt{2}$. On the right: Optical DSS image overlaid by 610 MHz GMRT radio contours in green, starting at 6σ and rising by factor of $\sqrt{2}$.

is $14.2^{''} \times 11.8^{''}$ with an rms of ∼80 μJy beam^{-1} at this resolution. The total flux density is also found here to be ∼0.25 Jy. The analysis for this frequency, included the combination

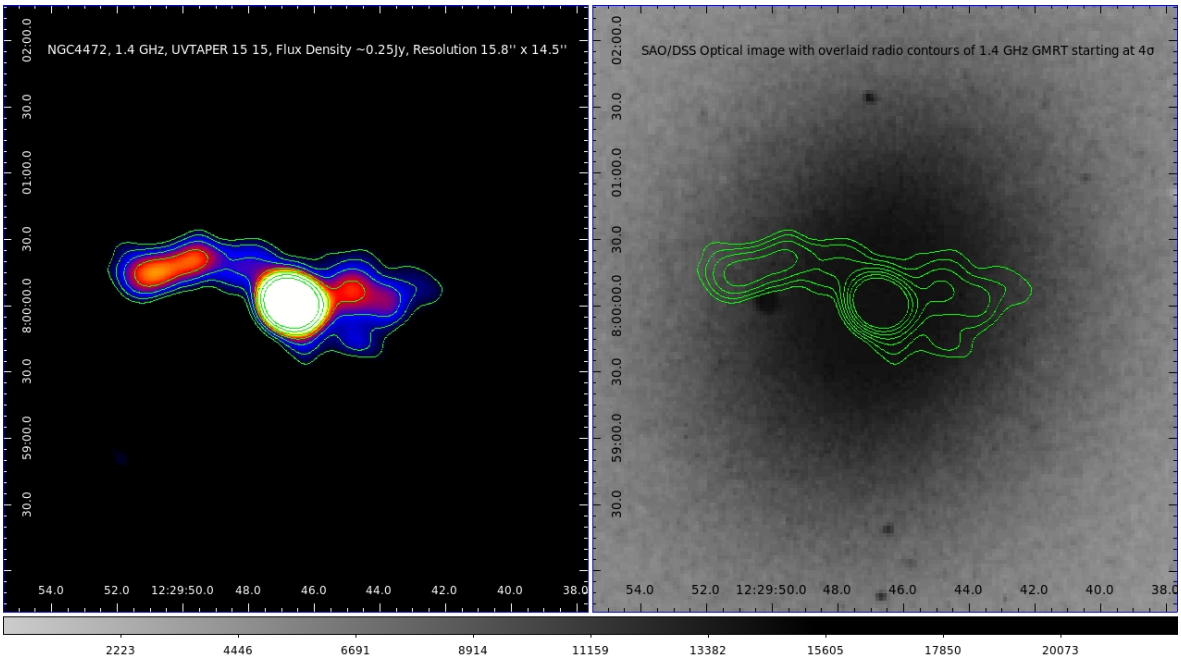

Figure B.3 On the left: Radio image of NGC 4472 at 1.4 GHz with rms ∼1 mJy beam^{-1} with contour levels starting at 4σ and rising by a factor of $\sqrt{2}$. On the right: Optical DSS image overlaid by 1.4 GHz GMRT radio contours in green, starting at 4σ and rising by factor of $\sqrt{2}$.

of two separate VLA datasets using the task 'DBCON' in AIPS. The project code of the archival VLA datasets was XX0013 (C Array) for both leading to a total observation time on source of $\sim$ 152 mins.

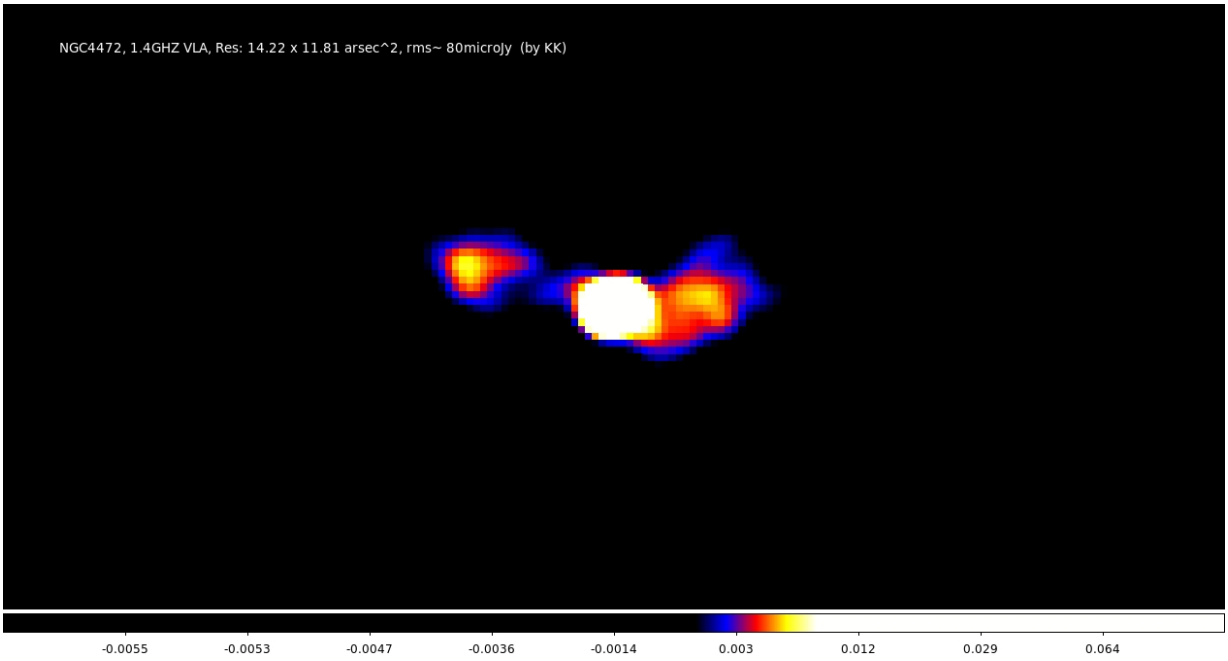

Figure B.4 1.4 GHz VLA Radio image of NGC 4472 with rms $\sim$80 μJy beam^{-1}.

The 1.4 GHz image from VLA (res: $14.2'' \times 11.8''$) was then combined with the GMRT 1.4 GHz image of uvtaper 20 20 (res: $12'' \times 11''$) of an rms of $\sim$ 0.5 mJy beam^{-1}. Both images were processed in order to have the same resolution, pixels, beam position angle and were combined using the task in AIPS 'comb'. The GMRT image was processed in order to have the same characteristics as the VLA one. The combination resulted in a 1.4 GHz image of $14.2'' \times 11.8''$ resolution with a total rms of $\sim$ 0.3 mJy beam^{-1}. The result is seen in Figure B.5 where the bent east jet is clearly detected along with emission from the west lobe.

B.3 NGC 4472, *XMM-Newton* X-ray (0.5 − 1 KeV) − 610 MHz GMRT comparison

XMM-Newton observation of M49 (NGC 4472) reveals a bright (L_X 10^42 erg s^{-1}) gaseous corona, and a long (>100 kpc), diffuse 'tail' (Fig. B.5), which is believed to be the result of ram-pressure stripping due to infall into the Virgo cluster (Irwin and Sarazin 1996, Biller

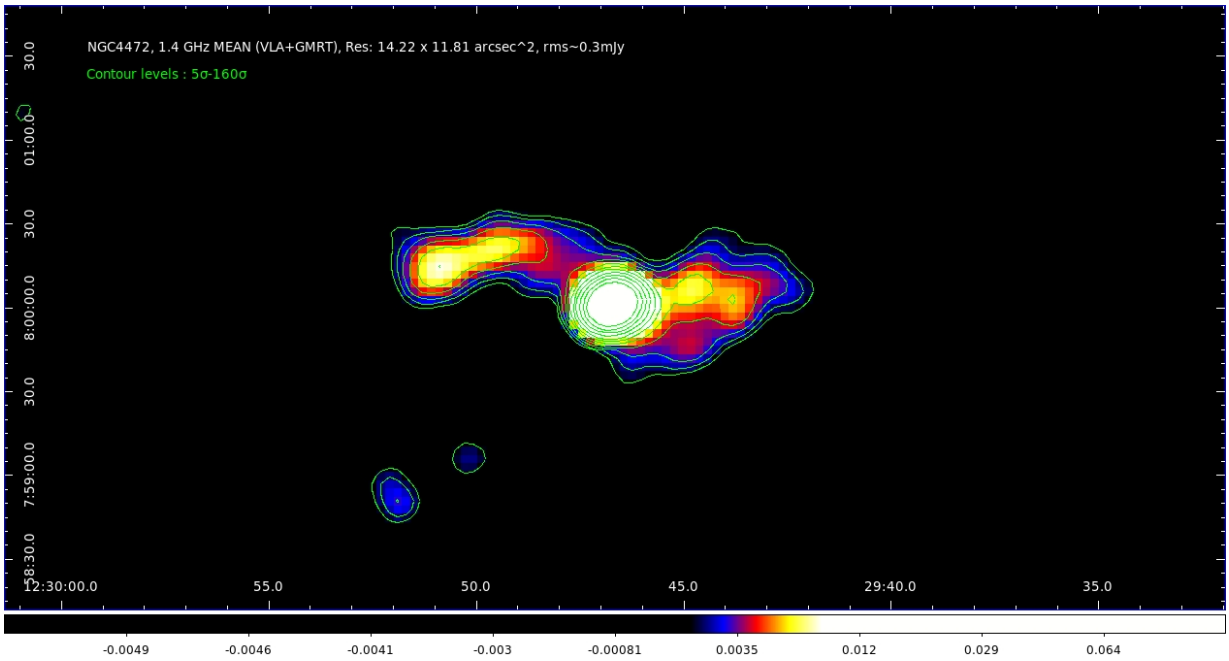

Figure B.5 Combined VLA+GMRT Radio image of NGC 4472 at 1.4 GHz with rms $\sim$ 0.3 mJy beam^{-1}. Contour levels start at 5σ and rise by factor of $\sqrt{2}$.

et al. 2004, Kraft et al. 2011). The surface brightness discontinuity to the north and the ram-pressure stripped tail to the south are both visible in Fig. B.6 where also prominent cavities on either side are visible from the overlaid 610 MHz contours.

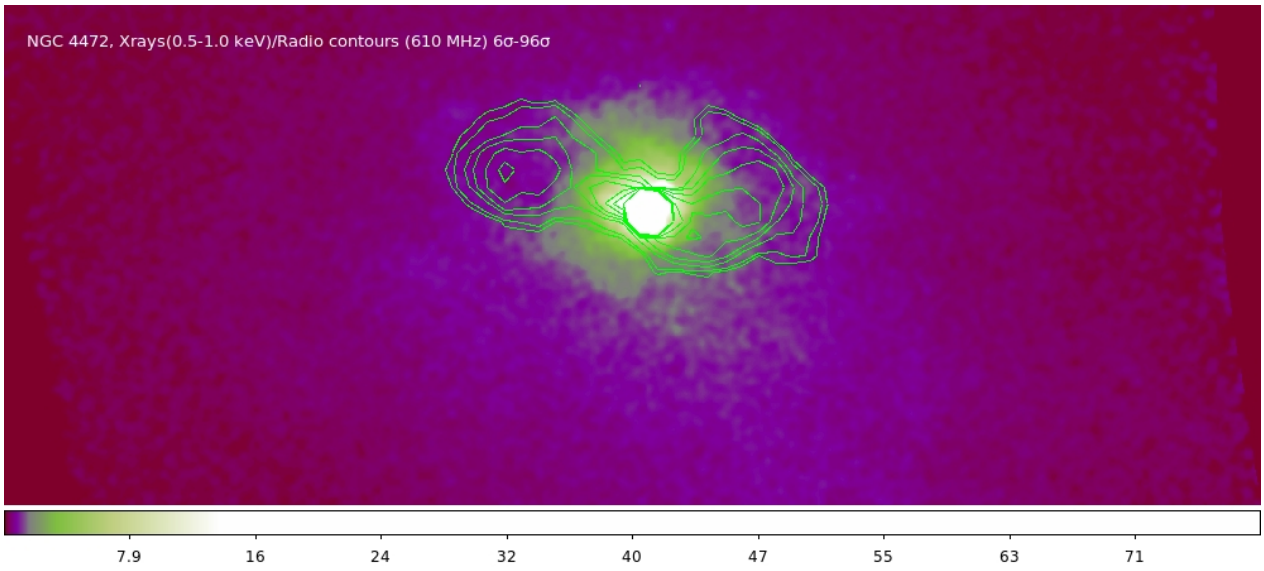

Figure B.6 Smoothed *XMM-Newton* X-ray image in the 0.5 - 1.0 KeV band (100 ks) with overlaid radio contours of NGC 4472 at 610 MHz with rms $\sim$60 μJy. Contour levels start at 6σ and rise by factor of $\sqrt{2}$.

B.4 Spectral index Maps

B.4.1 610 MHz − 1.4 GHz

We obtained the 610 MHz − 1.4 GHz spectral index distribution over the source of NGC 4472 by producing two images using the same uvrange, the same cellsize and then corrected for the primary beam attenuation (task 'PBCOR' in AIPS) and restored with the same beam of $14.2'' \times 11.8''$. The total spectral index between 610 MHz and 1.4 GHz was calculated to be $\alpha^{1.4GHz}_{610MHz} \sim 0.56$ using the negative sign convention of the formula : $S_\nu \propto \nu^{-\alpha}$.

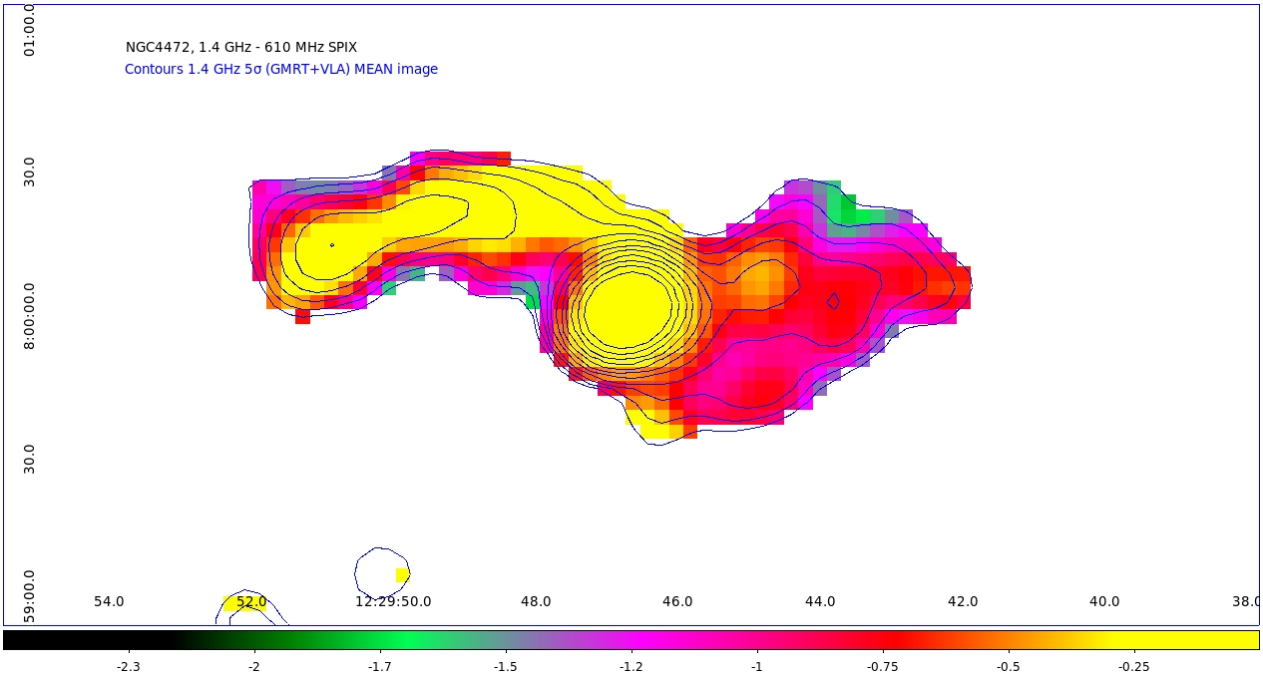

Figure B.7 Spectral index map of NGC 4472 between 1.4GHz and 610 MHz. The contour levels are of 1.4 GHz MEAN (VLA+GMRT) starting at 5 sigma

As Figure B.7 shows, the spectral index in the core and along the west jet remains the same, and relatively flat as expected. On the est lobe the steepening of the spectral index probably indicates the ageing of the emission. Possible indication of the jet orientation is also seen.

B.4.2 240 MHz - 610 MHz

The same procedure as above was followed for the image of 235 MHz − 1.4 GHz spectral index distribution over the source. The total spectral index between 240 MHz and 1.4 GHz

was calculated to be $\alpha_{235MHz}^{1.4GHz} \sim 0.62$ using the negative sign convention of the formula: $S_\nu \propto \nu^{-\alpha}$.

In Figure B.8 a steeper spectral index for the core of the galaxy is seen with a uniform spectral index at both lobes.

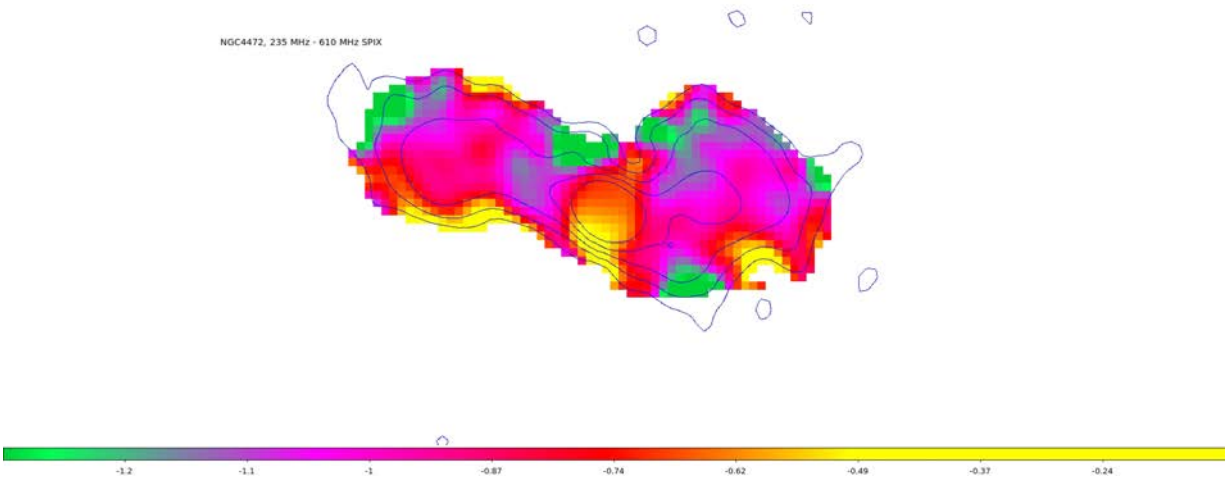

Figure B.8 Spectral index map of NGC 4472 between 1.4GHz and 235 MHz. The contour levels are of 1.4 GHz MEAN (VLA+GMRT) starting at 5 sigma

Appendix C

Origin of the X–ray, radio and HI structures in the NGC 5903 galaxy group

NGC 5903 group exhibits interesting features because of its two huge elliptical galaxies that have indications of recent interactions. The first one, NGC 5898, presents numerous tidal tails (Tal et al., 2009), while the second one, NGC 5903, is filled with ionised gas. The most interesting features of the group are observed in the radio, as previous VLA 1.4 GHz observations reveal a huge $\sim$100 kpc trail of H I emission extending north-south across NGC 5903, with a bending that indicates the H I filament is a product of a tidal interaction that removed the gas from the spiral galaxy ESO 514-5 (Appleton et al., 1990).

The TGSS 150 MHz image reveals the most extended radio emission seen for this system to date and suggests that at the outskirts of NGC 5903 the H I and continuum radio emission are anti-correlated (Gopal-Krishna et al., 2012). The analysis of the group from GMRT at 235 and 610 MHz (Figure C.1) shows the extension of the brightest emission southwest of NGC 5903 with more diffuse, low intensity emission extending to the east.

The spectrum of the emission is very steep; combining our recent GMRT 610 and 235 MHz data with archival data we find a spectral index of $\alpha_{235}^{1400} = 1.08 \pm 0.10$ for the main part of the emission (see Fig. C.2), and a spectral index $>$1.5 for the eastern component seen only at 150 MHz. There is no indication of flattening in the powerlaw at low frequencies, suggesting that the emission is very old ($>$120-350 Myr).

There are two possible scenarios that can be suggested to explain the situation in the group: 1) The steep-spectrum radio structure is a product of a close interaction between ESO 514-5 and NGC 5903, that could possibly have warmed up teh gas of the H I filament or, alternatively, 2) the continuum emission may be the remnant of old radio lobes, with their spectral index steepened by synchrotron losses.

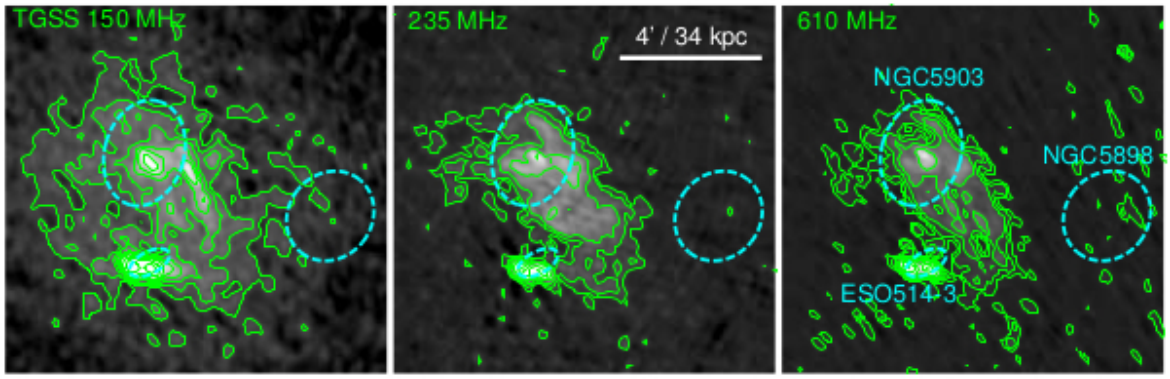

Figure C.1 GMRT radio continuum images of NGC 5903 in the TGSS 150 MHz (left), 235 MHz (centre) and 610 MHz (right) bands. The scale and alignment of the images is identical. Dashed cyan ellipses mark the D25 contours of major galaxies. The TGSS image has contours overlaid as in Fig. 1. The resolution of the 235 and 610 MHz images has been matched, with HPBW=19.9×12.1 , and the images have r.m.s. noise levels of 0.6 mJy/Beam and 0.2 mJy/beam respectively. Contours start at 3×r.m.s. and increase in steps of factor 2.

The results shown in Figures C.1 and C.2 indicate a similar radio morphology between 235 and 610 MHz with the emission at 235 MHz being slightly more extended. We are in the process of creating 150-610 MHz spectral index maps of the diffuse radio emission, which will hopefully give more information on the internal structure and relationship to the galaxy, its AGN, and the HI filament. The analysis of the XMM data will determine whether a diffuse hot IGM is present. Combination of the radio continuum and X-ray data along with the H I observations will certainly reveal the true nature of the processes that govern this rare and important system.

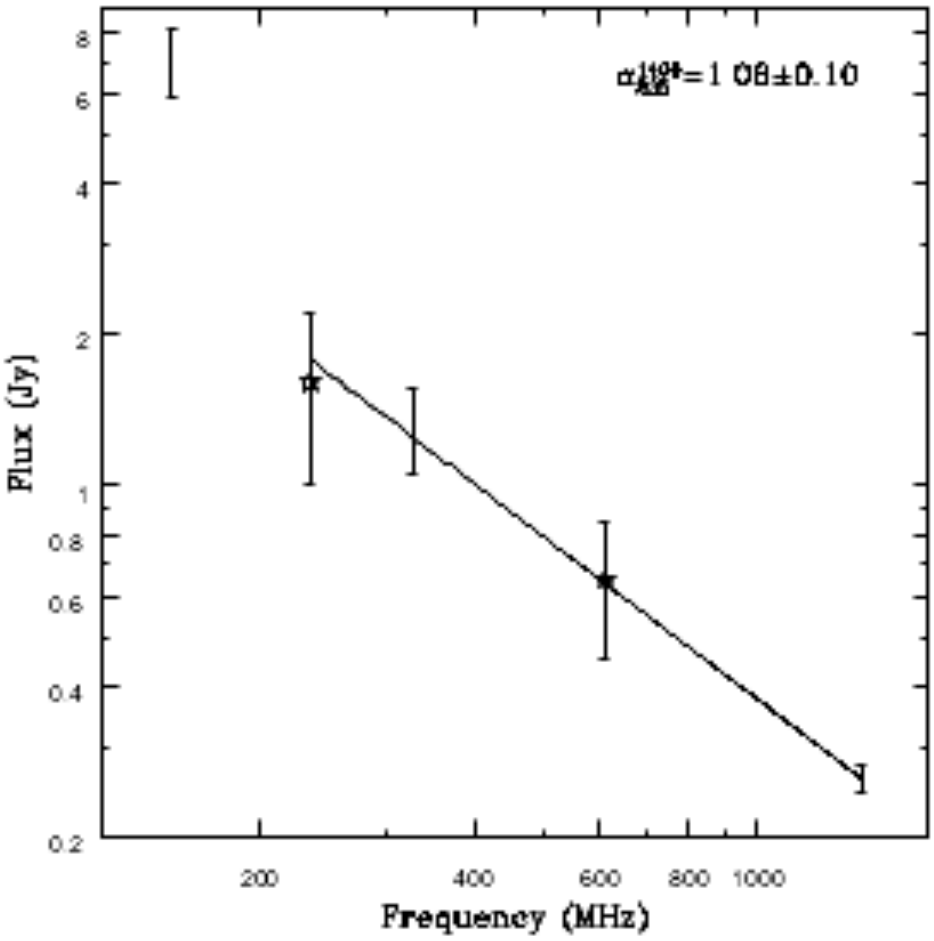

Figure C.2 Radio spectrum of NGC 5903. Points marked with stars indicate the fluxes from our new GMRT 610 and 235 MHz data, other points are drawn from the literature (Gopal-Krishna et al. 2012). The solid line indicates the best-fitting 235 MHz-1.4 GHz spectral index. The TGSS data point falls above the 150 MHz flux expected from the spectral index fit, probably because of the greater extent of the emission at this lowest measured frequency.